PHYSIK-DEPARTMENT

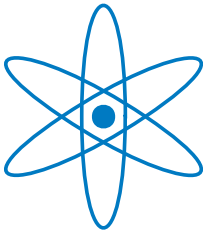

A Trigger Control System for COMPASS and A Measurement of the Transverse Polarization of Λ and Ξ Hyperons from Quasi-Real Photo-Production

Dissertation

von

Boris Grube

TECHNISCHE UNIVERSITÄT
MÜNCHEN

Fakultät für Physik der Technischen Universität München
Physik Department E18

A Trigger Control System for COMPASS and A Measurement of the Transverse Polarization of Λ and Ξ Hyperons from Quasi-Real Photo-Production

Boris Grube

Vollständiger Abdruck der von der Fakultät für Physik der Technischen Universität München zur Erlangung des akademischen Grades eines

Doktors der Naturwissenschaften (Dr. rer. nat.)

genehmigten Dissertation.

Vorsitzender:	Univ.-Prof. Dr. W. Weise
Prüfer der Dissertation:	
	1. Univ.-Prof. Dr. St. Paul
	2. Hon.-Prof. Dr. S. Bethke

Die Dissertation wurde am 17.01.2006 bei der Technischen Universität München eingreicht und durch die Fakultät für Physik am 13.03.2006 angenommen.

Abstract

The Trigger Control System of the COMPASS experiment at the CERN SPS distributes the first level trigger together with a unique event identifier and a very precise reference clock, that synchronizes the readout electronics, over a passive optical fiber network to 152 front-end modules. All signals are transmitted over a single optical fiber. The system in addition generates the readout dead-time and provides advanced management functions.

The second part presents an analysis of the transverse polarization of Λ and Ξ hyperons in quasi-real photo-production based on COMPASS data. Averaged over the whole kinematical range the Λ shows a significantly positive polarization of $+3.38 \pm 0.32(\text{stat.}) \pm 0.13(\text{sys.})$ %. The $\bar{\Lambda}$ exhibits a slightly negative polarization of $-1.51 \pm 0.39(\text{stat.}) \pm 0.10(\text{sys.})$ %. Both polarizations are studied in dependence on the kinematical variables x_F, p_T, y_B, and Q^2. Ξ^- and $\bar{\Xi}^+$ are within the errors unpolarized.

Kurzfassung

Das Trigger Control System für das COMPASS Experiment am CERN SPS verteilt das Triggersignal zusammen mit einer eindeutigen Ereigniskennung und einem hochpräzisen Taktsignal zur Synchronisation der Ausleseelektronik über ein passives optisches Netzwerk zu 152 Auslesemodulen. Alle Signale werden dabei über eine einzige optische Faser übertragen. Das System generiert außerdem die Auslesetotzeit und verfügt über erweiterte Managementfunktionen.
Der zweite Teil präsentiert eine Analyse der COMPASS Daten zur Messung der transversalen Polarisation von Λ und Ξ Hyperonen in quasi-reeller Photoproduktion. Über die gesamte Kinematik gemittelt zeigt das Λ eine signifikant positive Polarisation von $+3.38 \pm 0.32(\text{stat.}) \pm 0.13(\text{sys.})$ %, das $\overline{\Lambda}$ mit $-1.51 \pm 0.39(\text{stat.}) \pm 0.10(\text{sys.})$ % eine leicht negative. Beide Polarisationen werden in Abhängigkeit von den kinematischen Variablen x_F, p_T, y_B und Q^2 untersucht. Ξ^- und $\overline{\Xi}^+$ sind im Rahmen der Messungenauigkeit unpolarisiert.

Contents

1 Introduction **1**

2 COMPASS Experiment **3**

2.1 Physics Program – A Brief Overview 4

2.1.1 Muon Program 4

2.1.2 Hadron Program 12

2.2 Setup 13

2.2.1 Beam 13

2.2.2 Spectrometer 15

2.2.3 Polarized Target 20

3 Data Acquisition System **25**

3.1 Front-End Electronics 27

3.2 Concentrator Modules 29

3.3 Readout Computers and Data Buffering 30

3.4 Event Building and Filtering 32

3.5 DAQ Software 33

3.6 Performance 35

4 Trigger System **37**

4.1 DIS Trigger – Target Back-Pointing 39

4.2 Quasi-real Photon Trigger – Energy Loss 40

4.3 Hadron Trigger – HCAL Energy Deposit 42

4.4 Veto System 44

4.5 Trigger Hardware 45

5 Trigger Control System **47**

5.1 System Architecture 47

5.2 Optical Distribution Network and Signal Encoding 49

5.3 TCS Controller 52

5.4 TCS Receiver . . . 57
5.5 MultiDAQ Mode . . . 61
5.6 Dead-time Generation . . . 63
5.7 Special Event Types and Calibration and Monitoring Triggers . . . 64
5.8 TCS Server – Control and Configuration of the TCS . . . 67
5.9 TCS Performance and Summary . . . 69

6 Transverse Hyperon Polarization **71**
6.1 Hyperon Polarization Data – A brief Overview . . . 74
6.2 Theoretical Models . . . 77
6.2.1 Parton Recombination Model by DeGrand and Miettinen . . . 77
6.2.2 Polarizing Fragmentation Functions . . . 84

7 Data Analysis **91**
7.1 Hard- and Software Environment for Data Analysis . . . 92
7.1.1 The ROOT Framework . . . 92
7.1.2 CORAL – Reconstruction of COMPASS raw Data . . . 92
7.1.3 Physics Analysis of COMPASS Data . . . 95
7.2 Event Selection . . . 96
7.2.1 V^0 and Ξ Event Topology . . . 99
7.2.2 Definition of the Coordinate System . . . 102
7.2.3 Selection of V^0 Events . . . 104
7.2.4 Selection of Λ and $\overline{\Lambda}$ Events . . . 107
7.2.5 Selection of Ξ^- and $\overline{\Xi}^+$ Events . . . 117
7.3 Extraction Method for Hyperon Polarization – Double Bias Canceling . . . 125
7.4 Background Subtraction . . . 130
7.4.1 Λ Background Subtraction . . . 130
7.4.2 Ξ Background Subtraction . . . 140

8 Results **141**
8.1 Average transverse Polarization of Λ and Ξ Hyperons . . . 141
8.2 Study of Systematics . . . 143
8.2.1 Systematics of the Background Subtraction . . . 144
8.2.2 Systematics of the Bias Canceling . . . 148
8.2.3 Stability of the Setup . . . 150
8.2.4 Systematics due to the Setup . . . 156
8.3 Kinematical Study of Λ and $\overline{\Lambda}$ Polarization . . . 167
8.3.1 x_F and p_T dependence of Λ and $\overline{\Lambda}$ Polarization . . . 167

8.3.2 Q^2 and y_B dependence of Λ and $\overline{\Lambda}$ Polarization 175
8.4 Summary and Discussion 183
8.4.1 Comparison with HERMES Results 184
8.4.2 Comparison with Hadro-Production Data 186
8.4.3 Comparison with theoretical Predictions 187
8.4.4 Outlook 189

Appendix

A TCS Controller VME Registers **191**
A.1 Basic Registers 191
A.2 Read-only Status Registers 192
A.3 MultiDAQ Time Slices 192
A.4 Variable Dead-Time 193
A.5 Fixed Dead-Time 194
A.6 Artificial Trigger Sequencer 194
A.7 Pulse Sequencer 195

B Λ and $\overline{\Lambda}$ Polarization in kinematical Bins **197**

List of Figures **211**

List of Tables **215**

Bibliography **217**

Own Contributions **229**

Acknowledgements **231**

Chapter 1

Introduction

In our current understanding of nature we think, that on the microscopic level matter is composed out of two types of particles: leptons and quarks. These particles interact with each other via the exchange of different kinds of bosons, that belong either to the electro-weak or to the strong interaction. This so-called standard model describes the subnuclear phenomena with amazing precision. Nevertheless many questions are not or only insufficiently answered.

One of these still not fully understood fields is the structure of hadronic matter. The theory of strong interaction, which describes the interaction of quarks via the exchange of gluons, in its current form cannot be applied to the low energy, so-called non-perturbative, region, which includes bound hadronic states. From experiment it is known that free quarks cannot exist; up to now only systems consisting of a quark and an anti-quark ($q\bar{q}$ mesons) or of three quarks (qqq baryons) were observed. This is referred to as confinement and the details of this mechanism are a field of current research.

Another open question is the role of the spin in high energy reactions. Contrary to the naïve expectation experiments showed that the dynamics of high energy interactions depends significantly on the spin degrees of freedom. This is a very active field of research and at almost all accelerators spin experiments are performed or planned. Beside the measurement of the nucleon spin structure also data on polarization effects in hyperon production are of great interest.

COMPASS is a modern high-luminosity fixed target experiment to investigate the hadron structure at different scales using various beams and targets. Chapter 2 introduces the setup and also dwells on some items of the broad physics program, which covers all of the aforementioned issues.

COMPASS measures cross section asymmetries with high precision and plans to search for rare processes which demands high interaction rates. The resulting high particle rates required not only the development of novel detector technologies but also major advancements in the readout and the recording of the detector data. Therefore the COM-

PASS data acquisition system employs LHC type technologies to allow high trigger and data rates at minimum dead-time.

The thesis consists basically of two parts: The first part describes the Trigger Control System (TCS) of the COMPASS experiment, which is an essential hardware component that connects the trigger system with the data acquisition system. The TCS distributes the trigger decision and synchronizes the readout electronics of the various detectors in the experiment. Chapter 3 introduces the data acquisition system thereby following the data flow from the front-end electronics at the detectors via the readout computers to the tape storage in the computing center. Chapter 4 explains which trigger conditions are applied and how the trigger decision is generated from hodoscope and calorimeter signals. Finally chapter 5 describes the Trigger Control System starting with a system overview and then detailing the hardware and software components.

The second part presents the analysis of the transverse polarization of inclusively produced Λ and Ξ hyperons that is based on the COMPASS muon beam data of the years 2002, 2003, and 2004. After an experimental and theoretical overview in chapter 6 chapter 7 describes the event selection criteria that were applied to the data sample and explains the method utilized to extract the hyperon polarization. Chapter 8 finally presents the results of the analysis.

Chapter 2

COMPASS Experiment

The Common Muon and Proton Apparatus for Structure and Spectroscopy (COMPASS) [COM96] is a multi-purpose state-of-the-art fixed target spectrometer at the CERN[1] SPS[2]. COMPASS has a multifaceted physics program that utilizes muon as well hadron (π, p, and K) beams with high intensity on nuclear targets. The name of the experiment reflects that it is actually a merger of two originally independent projects – the Hadron Muon Collaboration (HMC) and the CHarm Experiment with Omni-Purpose Spectrometer (CHEOPS).

The proposed HMC project [HMC95] was standing in the tradition of a series of successful muon-scattering fixed target experiments at CERN. The EMC, NMC, and SMC (European, New, and Spin Muon Collaboration) experiments made important contributions to the measurement of the spin structure of the nucleon. The muon program of COMPASS will continue these efforts by studying the scattering of polarized muons off polarized nucleons.

The COMPASS hadron program is rooted in the CHEOPS proposal [CHE95] and covers the search for exotics, the study of the hadron structure and the spectroscopy of charmed baryons.

After a commissioning run in 2001 COMPASS took first physics data in 2002. Apart from a hadron beam pilot run end of 2004 all physics data up to now were taken with a polarized muon beam.

Section 2.1 first gives a brief introduction into the COMPASS physics thereby focusing mainly on the muon program. Afterwards section 2.2 introduces the beam, the spectrometer, and the polarized target.

[1] European Laboratory for Particle Physics, Geneva, Switzerland
[2] Super Proton Synchrotron (SPS)

2.1 Physics Program – A Brief Overview

2.1.1 Muon Program

In the Quark-Parton Model (QPM) the nucleon consists of point-like spin-1/2 particles that interact strongly via the exchange of gluons. The quantum numbers of the nucleon are determined by three so-called valence quarks that are embedded in a sea of quark-antiquark fluctuations. QCD calculations of Ellis and Jaffe [Ell74] showed that in the QPM 60 % of the nucleon spin is due to the valence quarks. However, in the late 80's the EMC experiment [EMC89] discovered that in reality only a small fraction of the nucleon spin originates from the quarks, which gave rise to the so-called *spin crisis*. The result was confirmed by other experiments and today we know that the contribution of the quark spins is about 25 %.

The main goal of the COMPASS muon program is to improve the understanding of the decomposition of the nucleon spin in terms of contributions of its constituents. The following subsections will outline some of the measurements that are currently performed or that are planned for the future. Further information can be found in the COMPASS proposal [COM96] and the references therein.

2.1.1.1 Spin Dependent Deeply Inelastic Scattering

In COMPASS a longitudinally polarized muon beam (see subsection 2.2.1) impinges on a fixed nuclear target (see subsection 2.2.3) that can be polarized either in longitudinal (parallel to the beam) or in transverse direction (perpendicular to the beam). The simplest process that can be measured is the inclusive muon scattering $\vec{\mu}\,\vec{N} \longrightarrow \mu' X$ which is depicted in the Born approximation in fig. 2.1. The kinematics of this reaction is usually described using the dimensionless Lorentz-scalars

$$x_B \equiv \frac{Q^2}{2P\cdot q} \overset{\text{Lab}}{=} \frac{Q^2}{2M_N\,\nu} \quad \text{and} \quad y_B \equiv \frac{P\cdot q}{P\cdot k} \overset{\text{Lab}}{=} \frac{\nu}{E} \tag{2.1}$$

where $Q^2 \equiv -q^2 = -(k-k')^2$ is the negative four-momentum squared of the virtual photon and $\nu \equiv E - E'$ its energy. E and E' are the energies of the incoming and outgoing lepton, M_N is the nucleon mass.

The so-called Bjorken scaling variable x_B is related to the invariant mass W of the hadronic final state X by

$$W^2 = (P+q)^2 = \frac{1-x_B}{x_B}\,Q^2 + M_N^2 \tag{2.2}$$

Conservation of energy ($E \geq E'$) and baryon number ($W \geq M_N$) demand that both y_B, which is the relative energy transfer of the photon in the laboratory frame, and x_B lie between 0 and 1. According to eq. (2.2) x_B is a measure for the (in)elasticity of the scattering

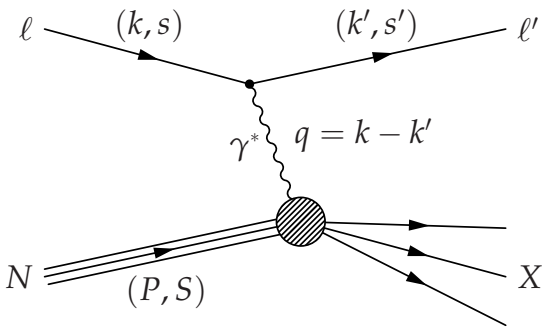

Figure 2.1: Inclusive scattering of a lepton ℓ with spin s and four-momentum $k = (E, \vec{k})$ off a target nucleon N with spin S and four-momentum $P = (M_N, \vec{0})$ into an outgoing lepton ℓ' and an unobserved hadronic final state X via the exchange of a virtual photon with four-momentum q (Born approximation).

process, where $x_B = 1$ corresponds to the elastic case.

In semi-inclusive scattering, where one or more additional hadrons h_i are detected in the final state, another dimensionless Lorentz-scalar z_{h_i} is defined

$$z_{h_i} \equiv \frac{P \cdot p_{h_i}}{P \cdot q} \overset{\text{Lab}}{=} \frac{E_{h_i}}{\nu} \tag{2.3}$$

where p_{h_i} and E_{h_i} are the four-momentum and the energy of the respective outgoing hadron. Also z_{h_i} is restricted to values between 0 and 1 and corresponds in the laboratory frame to the fractional energy that the hadron carries with respect to the virtual photon.

The muon scattering cross sections can be calculated in the kinematical domain of the so-called Deeply Inelastic Scattering (DIS), where the limit $Q^2 \to \infty$ is taken at fixed x_B. This is done in order to avoid the nucleon resonances, that lie in the region $W \lesssim 2.5$ GeV/c^2. Since

$$x_B = \frac{1}{1 + \dfrac{W^2 - M_N^2}{Q^2}} \tag{2.4}$$

in the DIS limit any hadronic state with fixed mass W is shifted to $x_B = 1$ and can therefore be disregarded. In addition at large Q^2 the nucleon is probed with a high resolving power, since the wavelength $\hbar/\sqrt{Q^2}$ is short. Q^2 also defines a hard scale, at which the coupling constant α_s of the strong interaction becomes small, so that it is possible to apply perturbative QCD (pQCD), that is to make a power expansion in α_S. Moreover the QCD terms can be sorted according to their powers in $1/Q^2$ – the so-called twist expansion.

In the quark-parton model x_B can be interpreted as the momentum fraction that the quark carries, if the nucleon is viewed in the so-called Infinite Momentum Frame (IMF), in which it is moving fast, so that the transverse motion of the quarks can be neglected. In leading order of α_s and leading twist three distribution functions $q(x_B)$, $\Delta q(x_B)$, and $\delta q(x_B)$ are needed to describe the spin structure of the nucleon: The momentum distribution $q(x_B)$ represents the probability to find a quark with flavor q and momentum fraction x_B in the nucleon. The helicity or polarized quark distribution $\Delta q(x_B) = q^{\overrightarrow{\Rightarrow}}(x_B) - q^{\overleftarrow{\Rightarrow}}(x_B)$ is the difference of the probability densities to find a quark with flavor q, momentum fraction x_B and spin parallel and anti-parallel to that of the nucleon, which is polarized longitudinally with respect to the virtual photon direction. Similarly $\delta q(x_B) = q^{\uparrow\Uparrow}(x_B) - q^{\downarrow\Uparrow}(x_B)$ is the transverse quark spin distribution in a transversely polarized nucleon. All three distributions are of equal importance and are related to the unpolarized structure function $f_1(x_B)$, the polarized one $g_1(x_B)$, and the transversity $h_1(x_B)$, that parameterize the hadronic tensor in the DIS cross section.

$$f_1(x_B) = \frac{1}{2}\sum_q e_q^2\, q(x_B), \quad g_1(x_B) = \frac{1}{2}\sum_q e_q^2\, \Delta q(x_B), \quad \text{and} \quad h_1(x_B) = \frac{1}{2}\sum_q e_q^2\, \delta q(x_B) \tag{2.5}$$

where the sum goes over all quark and antiquark flavors.

The structure functions f_1 and g_1 are related to the measurable parallel and transverse lepton cross section asymmetries $A_\parallel$ and $A_\perp$:

$$A_\parallel = \frac{\mathrm{d}\sigma^{\overleftarrow{\Rightarrow}} - \mathrm{d}\sigma^{\overleftarrow{\Leftarrow}}}{\mathrm{d}\sigma^{\overleftarrow{\Rightarrow}} + \mathrm{d}\sigma^{\overleftarrow{\Leftarrow}}} = \frac{1}{P_B \cdot P_N \cdot f}\,\frac{N^{\overleftarrow{\Rightarrow}} - N^{\overleftarrow{\Leftarrow}}}{N^{\overleftarrow{\Rightarrow}} + N^{\overleftarrow{\Leftarrow}}} = \frac{1}{P_B \cdot P_N \cdot f}\, A_\parallel^{\mathrm{meas}} \tag{2.6}$$

$$A_\perp = \frac{\mathrm{d}\sigma^{\leftarrow\Downarrow} - \mathrm{d}\sigma^{\leftarrow\Uparrow}}{\mathrm{d}\sigma^{\leftarrow\Downarrow} + \mathrm{d}\sigma^{\leftarrow\Uparrow}} = \frac{1}{P_B \cdot P_N \cdot f}\,\frac{N^{\leftarrow\Downarrow} - N^{\leftarrow\Uparrow}}{N^{\leftarrow\Downarrow} + N^{\leftarrow\Uparrow}} = \frac{1}{P_B \cdot P_N \cdot f}\, A_\perp^{\mathrm{meas}} \tag{2.7}$$

where $\overleftarrow{\rightarrow}$ indicates the longitudinal spin direction of the beam lepton and $\overleftarrow{\Rightarrow}$ that of the target nucleon. $\Uparrow$ and $\Downarrow$ represent the two directions of the transverse spin of the target nucleon. $\mathrm{d}\sigma$ stands for the differential cross section of the respective inclusive reaction. In the experiment the cross section asymmetries $A_\parallel$ and $A_\perp$ are determined from the particle number asymmetries $A_\parallel^{\mathrm{meas}}$ and $A_\perp^{\mathrm{meas}}$, which are reduced by the muon beam polarization $P_B \approx 0.75$, the target polarization $P_N \approx 0.5$, and the fraction of polarized material in the target $f \approx 0.4$. An up-to-date review of the theoretical and experimental status in deeply inelastic scattering is given by Filippone and Ji in [Fil01].

2.1.1.2 Gluon Polarization

As already mentioned above, experiments showed that the polarization $\Delta\Sigma$ of all quarks and antiquarks inside the nucleon is only a small fraction of the nucleon spin. Possible other contributions could arise from the gluon helicity ΔG and the angular momenta of

quarks and gluons, L_q and L_G:

$$\frac{1}{2} = \frac{1}{2}\Delta\Sigma + L_q + \Delta G + L_G \quad \text{where} \quad \Delta\Sigma = \sum_q \int_0^1 \mathrm{d}x_B \, \Delta q(x_B) \tag{2.8}$$

All terms in the above sum have a clear physical interpretation, but apart from the quark spin they are gauge and frame dependent.

One of the primary goals of COMPASS is the measurement of the contribution ΔG of the gluon spin to the nucleon helicity. In muon scattering the virtual photon cannot interact directly with the gluons in the target nucleon. This requires at least a second order process where the γ^* couples to the gluon via an intermediate quark line. The so-called Photon-Gluon Fusion (PGF) process $\gamma^* G \longrightarrow q\,\bar{q}$ is depicted in fig. 2.2. From the PGF process the gluon polarization $\Delta G/G$ can be extracted by measuring the cross section helicity asymmetry

$$A_\parallel^{\mathrm{PGF}} = \frac{\mathrm{d}\sigma^{\overleftarrow{\Rightarrow}}_{\mathrm{PGF}} - \mathrm{d}\sigma^{\overleftarrow{\Leftarrow}}_{\mathrm{PGF}}}{\mathrm{d}\sigma^{\overleftarrow{\Rightarrow}}_{\mathrm{PGF}} + \mathrm{d}\sigma^{\overleftarrow{\Leftarrow}}_{\mathrm{PGF}}} = \frac{\mathrm{d}\Delta\sigma^{\parallel}_{\mathrm{PGF}}}{\mathrm{d}\sigma_{\mathrm{PGF}}} \tag{2.9}$$

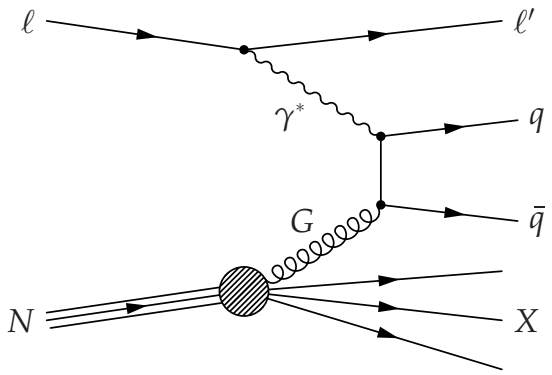

Figure 2.2: The photon-gluon fusion diagram.

In the experiment the PGF reactions have to be selected via the final state, that is one has to perform a semi-inclusive measurement. The "golden channel" is the production of open charm [Glü88], where a $c\bar{c}$ pair is produced and one of the charm quark fragments into a D^0 or D^{*+} meson or the respective anti-meson, which finally is detected in the experiment. The mesons are reconstructed via their invariant mass in the decays $D^0 \longrightarrow K^-\,\pi^+$ and $D^{*+} \longrightarrow D^0\,\pi^+_{\mathrm{soft}}$ plus the respective charge-conjugated decays. Since in leading order heavy quarks are produced predominantly via PGF and contributions from the sea quarks or from the fragmentation of light quarks are small, open charm allows a nearly background-free measurement of the gluon polarization via the cross section asymme-

try of $c\bar{c}$ production for target polarization parallel and anti-parallel to that of the muon beam

$$A_{\parallel}^{\gamma^* N\to c\bar{c}} = \frac{\mathrm{d}\Delta\sigma_{\parallel}^{\gamma^* N\to c\bar{c}}}{\mathrm{d}\sigma^{\gamma^* N\to c\bar{c}}} = \frac{\int_{4m_c^2}^{2M_N\nu}\mathrm{d}\hat{s}\ \Delta\sigma_{\parallel}^{\gamma^* N\to c\bar{c}}(\hat{s})\,\Delta G(x_G,\hat{s})}{\int_{4m_c^2}^{2M_N\nu}\mathrm{d}\hat{s}\ \sigma^{\gamma^* N\to c\bar{c}}(\hat{s})\,G(x_G,\hat{s})} \approx \hat{a}_{\parallel}^{\gamma^* N\to c\bar{c}}\frac{\Delta G}{G} \tag{2.10}$$

where $\hat{s}$ is the squared invariant mass of the $c\bar{c}$ pair and $x_G = \hat{s}/(2M_N\nu)$ the momentum fraction carried by the gluon in the limit of quasi-real virtual photons with small Q^2. Q^2 is not required to be large, because the hard scale is set by the charm mass, so that the asymmetry can be factorized into the hard asymmetry $\hat{a}_{\parallel}^{\gamma^* N\to c\bar{c}}$ and the soft asymmetry $\Delta G/G$. This in addition allows to calculate the polarized photon-gluon cross section $\Delta\sigma_{\parallel}^{\gamma^* N\to c\bar{c}}$ in pQCD, so that $\Delta G/G$ can be extracted directly and without model dependence. The disadvantage of this channel is that open charm has a small cross section and is in addition experimentally difficult to detect.

Another possibility of tagging PGF events are hadron pairs from the current fragmentation region with large transverse momenta p_T with respect to the virtual photon [Bra98c]. Here the cross section is much larger and the hard scale is defined by p_T. On the other hand the measured cross section asymmetry of high-p_T pair production

$$A_{\parallel}^{\gamma^* N\to h^+h^- X} = R_{\mathrm{PGF}}\,\hat{a}_{\parallel}^{PGF}\,\frac{\Delta G}{G} + A_{\parallel}^{\mathrm{BG}} \tag{2.11}$$

includes non-negligible background contributions $A_{\parallel}^{\mathrm{BG}}$ from non-PGF processes. The dominant background contributions come from leading order DIS, where the D^0 meson is produced in the fragmentation of the scattered quark, furthermore from QCD Compton, in which a gluon and a quark jet are produced, and from resolved photons, where the quark substructure of the photon enters into the process. Since the background contamination $A_{\parallel}^{\mathrm{BG}}$ and the fraction of PGF events R_{PGF} cannot be measured independently of the gluon polarization, they have to be calculated in Monte-Carlo simulations. Consequently the results for $\Delta G/G$ are model-dependent. A first analysis based on the 2002 and 2003 data gives a gluon polarization of $\Delta G/G = 2.4 \pm 8.9(\mathrm{stat.}) \pm 5.7(\mathrm{sys.})$ % at $\langle x_G\rangle = 0.095$ [COM05a]. According to model calculations the result favors low gluon polarization.

2.1.1.3 Transversity

The transversity distribution is the last missing fundamental piece of the polarized nucleon structure. Although the transverse spin structure function h_1 is of leading twist, it cannot be accessed in DIS, because it is a chiral odd object. h_1 involves helicity flips of the quarks which are suppressed, since chirality is conserved in hard interactions. In polarized Semi-Inclusive DIS (SIDIS) with transversely polarized target h_1 can be combined with an also chiral odd fragmentation function. In this case the transversity shows up in the azimuthal distribution of single hadrons and of the plane containing hadron pairs

as well as in the transverse polarization of spin-1/2 baryons, e.g. Λ hyperons (see subsection 2.1.1.4). An in-depth review of the present knowledge concerning transversity is given by Barone, Drago, and Ratcliffe in [Bar02].

In inclusive single hadron production $\mu^{\leftarrow} N^{\Uparrow} \longrightarrow \mu' h X$ with transversely polarized target two entirely different mechanisms, the Collins and the Sivers effect, give rise to single-spin azimuthal asymmetries. The Collins effect predicts an azimuthal asymmetry in the fragmentation $q^{\uparrow} \longrightarrow h X$ of a transversely polarized quark into a spinless hadron with finite transverse momentum $\vec{p}_T$ with respect to the quark direction. Since the polarization of the struck quark correlates with the transverse momentum, the quark prefers to fragment in a certain direction.

The fragmentation of a quark q with momentum $\vec{p}_q$ and transverse polarization $\vec{P}_q$, where $\vec{p}_q \cdot \vec{P}_q = 0$, into a hadron h with momentum $\vec{p}_h$, is described by the fragmentation function

$$D_{h/q}(\vec{p}_q, \vec{P}_q; z_h, \vec{p}_T) = \hat{D}_{h/q}(z_h, p_T) + \frac{1}{2}\Delta D_{h/q^{\uparrow}}(z_h, p_T)\, \frac{\vec{P}_q \cdot (\vec{p}_q \times \vec{p}_T)}{|\vec{p}_q \times \vec{p}_T|} \tag{2.12}$$

where $\hat{D}_{h/q}(z_h, p_T)$ is the unpolarized fragmentation function and $\Delta D_{h/q^{\uparrow}}(z_h, p_T)$ the Collins function, that describes the spin dependent part of the hadronization [Ans00b]. Since in the quark-parton model z_h is the fraction of the quark momentum carried by the hadron, the hadron momentum is $\vec{p}_h = z_h\, \vec{p}_q + \vec{p}_T$, where $\vec{p}_q \cdot \vec{p}_T = 0$.

If the fragmentation process is invariant under parity, only the quark polarization component perpendicular to the plane defined by $\vec{p}_q$ and $\vec{p}_T$ contributes to the spin dependent part of $D_{h/q}$, so that in general

$$\frac{\vec{P}_q \cdot (\vec{p}_q \times \vec{p}_T)}{|\vec{p}_q \times \vec{p}_T|} = P_q\, \sin(\varphi_h - \varphi_{s'}) = P_q\, \sin\Phi_C \tag{2.13}$$

where $\varphi_{h,s'}$ are the azimuthal angles of the outgoing hadron and of the spin of the fragmenting quark around the $\vec{p}_q$ direction (see fig. 2.3). Φ_C is the so-called Collins angle.

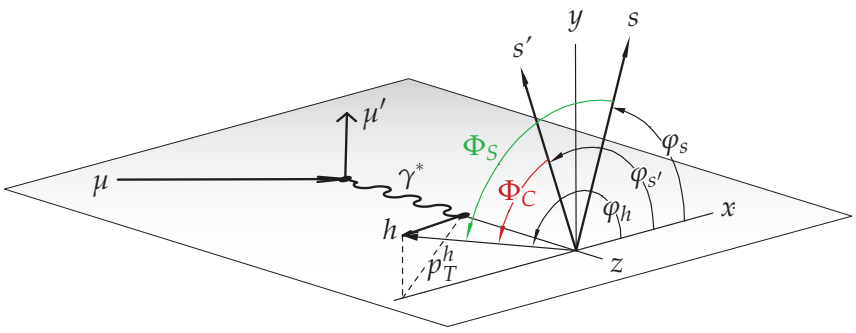

Figure 2.3: Definition of Collins and Sivers angle. (from [COM05b])

With fragmentation function (2.12) it is possible to define a single quark spin asymmetry for the process $q^{\uparrow} \longrightarrow h\,X$

$$A_{h/q} = \frac{D_{h/q}(\vec{P}_q) - D_{h/q}(-\vec{P}_q)}{D_{h/q}(\vec{P}_q) + D_{h/q}(-\vec{P}_q)} = \frac{\Delta D_{h/q^{\uparrow}}(z_h, p_T)}{2\hat{D}_{h/q}(z_h, p_T)} \cdot \sin\Phi_C \tag{2.14}$$

In leading order and neglecting the intrinsic motion of the quarks inside the target nucleon, the photo-absorption process $\gamma^* q \longrightarrow q'$ can be described in the Breit-frame as a head-on collision of photon and quark, where the struck quark bounces back and fragments into a jet that contains the detected hadron. The polarization of the fragmenting quark is determined by the initial quark polarization and the orientation of the lepton scattering plane. Since the transversity describes the transverse quark polarization in a transversely polarized target nucleon, it connects the single quark spin asymmetry $A_{h/q}$ with the single target spin asymmetry $A^C_{h/N}$ that is accessible in the experiment.

$$A^C_{h/N} = \frac{\mathrm{d}\sigma^{\mu\, N^{\Downarrow}\to\mu'\, h\, X} - \mathrm{d}\sigma^{\mu\, N^{\Uparrow}\to\mu'\, h\, X}}{\mathrm{d}\sigma^{\mu\, N^{\Downarrow}\to\mu'\, h\, X} + \mathrm{d}\sigma^{\mu\, N^{\Uparrow}\to\mu'\, h\, X}} = P_N \cdot f \cdot D_T \cdot A_C \cdot \sin\Phi_C \tag{2.15}$$

$$\text{with} \quad D_T = \frac{2(1-y_B)}{1+(1-y_B)^2} \quad \text{and} \quad A_C = \frac{\sum_q e_q^2\, \delta q(x_B)\, \Delta D_{h/q^{\uparrow}}(z_h, p_T)}{2\sum_q e_q^2\, q(x_B)\, \hat{D}_{h/q}(z_h, p_T)}$$

where D_T is the transverse spin transfer coefficient from the initial to the struck quark and A_C the Collins asymmetry. To enrich hadrons that originate from the struck quark only the leading hadron is considered. From eq. (2.15) it is clear, that in SIDIS only the product of transversity and Collins function, which are both unknown, can be accessed directly.

The Sivers effect [Siv90] is caused by the intrinsic motion of the quarks inside the nucleon. It predicts an azimuthal modulation of the intrinsic transverse momentum $\vec{k}_\perp$ of the unpolarized quarks in a transversely polarized nucleon. The transverse momentum of the struck quark, which is correlated with the nucleon polarization through the Sivers function, is inherited by the produced leading hadron. The Sivers function $f_{1T}^{\perp}$ describes the unpolarized quarks in a transversely polarized nucleon and requires quark orbital angular momentum. Since the photon scatters off unpolarized quarks, the orientation of the lepton scattering plane is irrelevant and the fragmentation of the scattered quark is described by the known unpolarized fragmentation function $\hat{D}_{h/q}(z_h, k_\perp)$.

$$A^S_{h/N} = \frac{\mathrm{d}\sigma^{\mu\, N^{\Downarrow}\to\mu'\, h\, X} - \mathrm{d}\sigma^{\mu\, N^{\Uparrow}\to\mu'\, h\, X}}{\mathrm{d}\sigma^{\mu\, N^{\Downarrow}\to\mu'\, h\, X} + \mathrm{d}\sigma^{\mu\, N^{\Uparrow}\to\mu'\, h\, X}} = P_N \cdot f \cdot A_S \cdot \sin\Phi_S \tag{2.16}$$

$$\text{with} \quad A_S = \frac{\sum_q e_q^2\, f_{1T}^{\perp q}(x_B, k_\perp)\, \hat{D}_{h/q}(z_h, k_\perp)}{\sum_q e_q^2\, q(x_B, k_\perp)\, \hat{D}_{h/q}(z_h, k_\perp)}$$

where A_S is the Sivers asymmetry and $\Phi_S = \varphi_h - \varphi_s$ the azimuthal angle between the outgoing hadron and the transverse target polarization (see fig. 2.3).

Although they appear in the same process, it is possible to disentangle the Sivers and the Collins effect. First results based on the 2002 data [COM05b] show, that both asymmetries are small and within the errors compatible with zero, which is in good agreement with existing phenomenological models.

2.1.1.4 Λ and $\bar{\Lambda}$ Polarization

COMPASS also studies the muo-production of polarized Λs and $\bar{\Lambda}$s. In the simplest process $\mu N \longrightarrow \mu' \Lambda^{\Uparrow} X$, the inclusive production of polarized Λ s by scattering of an unpolarized beam off an unpolarized target, the polarization is related to properties of the hadronization process and is still not fully understood. The measurement of the Λ polarization in this reaction is a main topic of this thesis and is described in detail from chapter 6 on.

With the polarized beam and target of the COMPASS setup it is in addition possible to study the dynamics of the spin transfer from partons to Λ hyperons. The longitudinal spin transfer from the target to the outgoing Λ hyperon can be measured with longitudinally polarized target in the semi-inclusive reaction $\mu^{\rightarrow} N^{\Rightarrow} \longrightarrow \mu' \Lambda^{\Rightarrow} X$. In the current fragmentation region of SIDIS the spin transfer is related to the fragmentation functions $\hat{D}_{\Lambda/q}$ and $\Delta D_{\Lambda/q}$, where in particular the latter is only poorly known. The unpolarized fragmentation function $\hat{D}_{\Lambda/q}(z_h)$ describes the spin-independent fragmentation of a quark with flavor q into a Λ hyperon with momentum fraction z_h. The helicity transfer from the quark to the Λ is given by the polarized fragmentation function $\Delta D_{\Lambda/q}(z_h) = D_{\Lambda^{\Rightarrow}/q^{\rightarrow}}(z_h) - D_{\Lambda^{\Leftarrow}/q^{\rightarrow}}(z_h)$.

In leading order of pQCD and neglecting the intrinsic motion of the quarks inside the target nucleon the longitudinal Λ polarization is given by

$$
\begin{aligned}
P_L^{\Lambda} &= \frac{\mathrm{d}\sigma^{\mu^{\rightarrow} N^{\Rightarrow} \rightarrow \mu' \Lambda^{\Rightarrow} X} - \mathrm{d}\sigma^{\mu^{\rightarrow} N^{\Rightarrow} \rightarrow \mu' \Lambda^{\Leftarrow} X}}{\mathrm{d}\sigma^{\mu^{\rightarrow} N^{\Rightarrow} \rightarrow \mu' \Lambda^{\Rightarrow} X} + \mathrm{d}\sigma^{\mu^{\rightarrow} N^{\Rightarrow} \rightarrow \mu' \Lambda^{\Leftarrow} X}} \\
&= \frac{\sum_q e_q^2 \left[P_B \cdot D_L(y_B) \cdot q(x_B) + P_N \cdot f \cdot \Delta q(x_B)\right] \Delta D_{\Lambda/q}(z_h)}{\sum_q e_q^2 \left[q(x_B) + P_N \cdot f \cdot P_B \cdot D_L(y_B) \cdot \Delta q(x_B)\right] \hat{D}_{\Lambda/q}(z_h)} \\
&\quad \text{with} \quad D_L(y_B) = \frac{1-(1-y_B)^2}{1+(1-y_B)^2}
\end{aligned}
\tag{2.17}
$$

where $D_L(y_B)$ is the amount of longitudinal polarization transferred from the incident muon beam to the virtual photon [Ans00a].

Beside the measurement of the polarized fragmentation function one can combine the information about the Λ and the $\bar{\Lambda}$ to test the quark-antiquark symmetry of the strange sea quarks in the nucleon, that is whether $s(x_B) = \bar{s}(x_B)$ and $\Delta s(x_B) = \Delta\bar{s}(x_B)$ [Ans01d].

The transverse polarization transfer can be studied in the semi-inclusive reaction $\mu N^{\Uparrow} \longrightarrow \mu' \Lambda^{\Uparrow} X$ with transversely polarized target. This gives information about transversity and about the transversity fragmentation function $\Delta_T D_{\Lambda/q}(z_h) =$

$D_{\Lambda^\Uparrow/q^\uparrow}(z_h) - D_{\Lambda^\Downarrow/q^\uparrow}(z_h)$, that is – like the Collins function (see previous subsection) – a chiral odd object and defined analog to the longitudinal case [Ans02a].

$$
\begin{aligned}
P_T^\Lambda &= \frac{\mathrm{d}\sigma^{\mu\, N^\Uparrow \to \mu'\, \Lambda^\Uparrow\, X} - \mathrm{d}\sigma^{\mu\, N^\Downarrow \to \mu'\, \Lambda^\Uparrow\, X}}{\mathrm{d}\sigma^{\mu\, N^\Uparrow \to \mu'\, \Lambda^\Uparrow\, X} - \mathrm{d}\sigma^{\mu\, N^\Downarrow \to \mu'\, \Lambda^\Uparrow\, X}} \\
&= P_N \cdot f \cdot D_T(y_B) \frac{\sum_q e_q^2\, \delta q(x_B)\, \Delta_T D_{\Lambda/q}(z_h)}{\sum_q e_q^2\, q(x_B)\, \hat{D}_{\Lambda/q}(z_h)} \\
&\quad \text{with} \quad D_T(y_B) = \frac{2(1-y_B)}{1+(1-y_B)^2}
\end{aligned}
\tag{2.18}
$$

Also here both functions, the transversity and the transversity fragmentation function, are unknown, so that one can directly access only the product of the two. But compared to the Collins function, the transversity fragmentation function does not depend on the transverse momentum p_T and might be easier to model. D_T is the same spin transfer coefficient as in the Collins asymmetry (2.15).

2.1.2 Hadron Program

The hadron program will probe the structure of hadrons at low and very low Q^2 using high intensity beams of pions, kaons, or protons. One of the first reactions that will be studied is the Primakoff scattering, where a pion beam scatters in the Coulomb field of a high Z nucleus thereby producing a real photon. From the interaction of the pion with the electromagnetic field of the virtual photon one can extract the electric and magnetic polarizabilities of the pion, which are related to the forces that keep the quark and the antiquark together. COMPASS will significantly improve the existing data on the polarizability of the pion and moreover will be able to make a first measurement of the kaon polarizability.

Another field is the spectroscopy of light mesons, where COMPASS wants to search for exotic states, that is for states that do not (only) consist of quark and antiquark. These states may arise from the excitation of gluonic degrees of freedom in bound quark systems, which are the so-called hybrids, or may consist of pure glue, the so-called glueballs. Some models also predict the existence of multi-quark states. Exotic states can be identified unambiguously, if they have quantum numbers that cannot be realized by $q\bar{q}$ states. The expected mass of these exotic states lies in the range between 1.0 and 2.2 GeV/c^2, which makes their observation challenging, because this mass region is already populated by many conventional meson states with different radial and angular excitations. In order to extract the quantum numbers, in particular spin and parity, of the various produced states from the data, the angular distributions of three- or more-body final states are measured and are then subject to a Partial Wave Analysis (PWA). This analysis technique decomposes the final state in terms of partial waves and allows to identify the resonances and their quantum numbers, but requires data samples with large statistics.

In a later stage COMPASS plans to search for doubly charmed baryons, which only recently were observed by the SELEX experiment [SEL02]. Charm systems are interesting, because of the heavy mass of the c quark, which lies between 1.15 and 1.35 GeV/c^2. The large charm mass introduces a hard scale, which allows to apply pQCD in the form of the so-called Heavy Quark Effective Theory (HQET). Similar to the charmonium case, the measurement of the mass spectrum of the doubly charmed baryons gives information about the confining potential. Experimentally this is a very challenging project and will require major upgrades of the apparatus.

2.2 Setup

COMPASS is a two-stage forward spectrometer with high momentum resolution and is able to detect particles in a large angular and momentum range. The layout of the detectors and the employed technologies are optimized for high particle rates, so that the spectrometer is capable of detecting the scattered muon in a large kinematical range down to very small angles. This is necessary, because the virtual photon has to be reconstructed also at low Q^2, where the cross section for PGF events is enhanced. The semi-inclusive measurements require in addition a large hadron acceptance and a good particle identification, which is performed by electromagnetic and hadronic calorimeters plus a Ring Imaging CHerenkov (RICH) detector.

After a description of the COMPASS beam in subsection 2.2.1 subsection 2.2.2 introduces the spectrometer layout with a short characterization of the various detector components. Finally subsection 2.2.3 explains the polarized target.

2.2.1 Beam

The COMPASS physics program utilizes of a variety of beams on different target types. All beams are created out of the primary 400 GeV/c proton beam delivered by the CERN SPS with a rate of up to $1.2 \cdot 10^{13}$ protons per cycle. The SPS accelerator cycle, also called spill cycle, consists of injection, acceleration, and extraction and is in total 16.8 s long. The duration of the beam extraction, the so-called on-spill time, is 4.8 s. By switching off the acceleration elements shortly before extraction, the protons are debunched, so that their flux has a random and more or less uniform time distribution.

This analysis uses data obtained with a beam of longitudinally polarized positive muons. To produce this tertiary beam, the SPS proton beam is directed onto the production target T6 [Ath80], which is situated at the beginning of the M2 beam line [Dob94] (see fig. 2.4). Out of the created secondary particles, which are mainly pions and kaons, the bending magnets B1 to B3 select positively charged particles at forward production angles with a momentum in the range of ± 10 % around 177 GeV/c.

This secondary beam enters the 600 m long decay line, where part of the π^+ and K^+ decay weakly via $\pi^+, K^+ \rightarrow \mu^+ + \nu_\mu$. In the rest frame of the spin-0 meson the spins of the

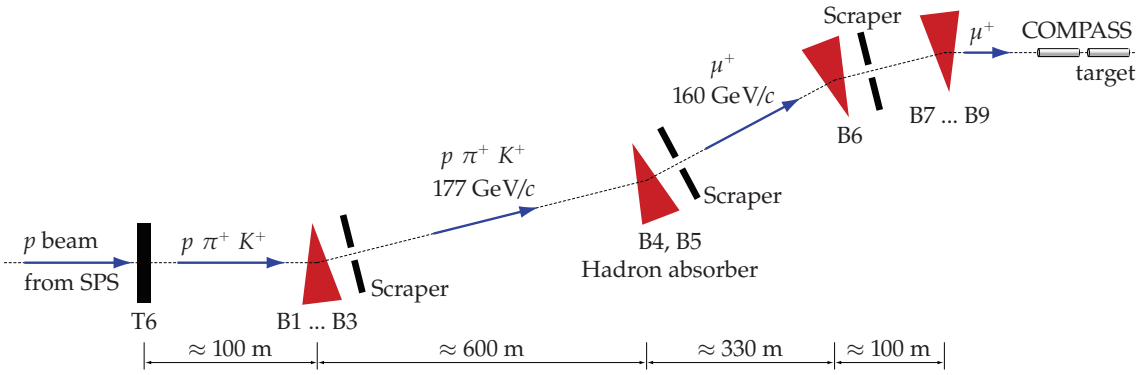

Figure 2.4: Schematic side-view of the M2 beam line at the CERN SPS as used for the muon program. The scrapers are special collimators made of magnetized iron that deflect low momentum particles away from the beam (from [Hod02])

outgoing μ^+ and ν_μ have to be aligned in opposite directions. The neutrino is always left-handed and practically massless. Consequently it has negative helicity which means that its spin is aligned oppositely to its momentum, so that the direction of the muon spin is fixed. The longitudinal muon polarization depends on the angle between the muon momentum and the meson direction in the meson rest frame. By setting a lower limit for the muon momentum one can thus choose the sign and magnitude of the beam polarization. Beam flux and energy considerations lead to a selection of forward muons with a momentum of 160 GeV/c in the laboratory frame. The muons arrive at the experiment with a longitudinal polarization of -75 ± 4 %, a value obtained from simulations which were confirmed to be sufficiently precise by measurements of the SMC experiment [Ada00] that used the same beam line.

At the end of the decay line a 9.9 m long beryllium absorber filters out the hadronic components while minimizing the multiple coulomb scattering for the muons. The muon momentum selection is performed by the bending magnets B4 and B5 that are part of the double-bend structure which lifts the beam from the SPS underground level to that of the experimental hall. At the end of the line the beam is focused onto the COMPASS target by a quadrupole magnet.

The resulting 160 GeV/c polarized muon beam has an intensity of $2.8 \cdot 10^8$ μ^+/spill with a momentum spread of about 3 % r.m.s. The divergence of the beam is 0.7 mrad in the horizontal and 0.9 mrad in the vertical plane leading to a beam spot size of $8.9 \times 7.6\,\mathrm{mm}^2$ r.m.s. in the target. The large spot size is not only due to the tertiary nature of the beam, but also because of the large penetration ability of the muons, which hampers the beam collimation and which is also the reason for the pronounced muon halo, which consists of muons that deviate from the nominal beam trajectory and pass through elements of the beam optics.

By moving out the beryllium absorber and adjusting the currents of the bending magnets the beam line can also bring the secondary hadron beam into the experimental area. A

clean meson beam of 95 % π^- and 4.5 % K^- with intensities larger than 10^7 particles/spill is obtained by selecting negatively charged particles in the first magnetic filter B1 to B3 thereby removing the beam protons. For the hadron pilot run in 2004 a meson beam with 190 GeV/c momentum was used.

By using a lead converter it is also possible to generate a low intensity tertiary electron beam with a momentum of $30 - 60$ GeV/c for calibration purposes.

The momentum of the beam particles is measured by the so-called Beam Momentum Station (BMS). This detector system consists of four planes of horizontal hodoscope slabs with a height of 5 mm and two planes of horizontal scintillating fibers. The planes are arranged around the bending magnet B6 60 to 140 m upstream of the target and allow to track the beam particles in the vertical plane, so that for each projectile the momentum is measured with a resolution of about 0.5 %.

2.2.2 Spectrometer

To provide both a large acceptance and a good momentum resolution, COMPASS was designed as a two stage spectrometer in which the first stage measures the particles with lower momentum and the second one the remaining high momentum particles. The two stages have a similar layout: A dipole magnet, surrounded by tracking detectors, is used for momentum measurement followed by electromagnetic and hadronic calorimeters, which determine the energy of the particles, and at the downstream end of the stage a muon identification and tracking system (see fig. 2.5). The absorbing detectors of the first stage have a central hole that matches the acceptance of the second stage. The first part of the spectrometer additionally is equipped with a ring imaging Cherenkov detector for particle identification. As the RICH information is not used in this analysis (see also subsection 7.2.1), the description of this detector is omitted here. Details may be found in [Alb04].

2.2.2.1 Magnets

Two dipole magnets, SM1 and SM2, generate magnetic fields whose main component is aligned vertically downwards, so that they deflect charged particles in the same direction thereby enlarging the dispersion and thus the angular separation of particles with different momenta. This property is used by the trigger system, which selects events based mainly on geometrical criteria, one of them being the deflection of the scattered muon in the magnetic fields (see section 4.2).

The magnet SM1 of the first spectrometer stage has a field integral along the beam axis of 1 Tm and a large angular acceptance of ± 180 mrad. Particles with a momentum of $\gtrsim$ 0.4 GeV/c are able to pass through the magnet and can be detected by the tracking devices on both sides of SM1. The poles of SM1 are slant towards the target to change

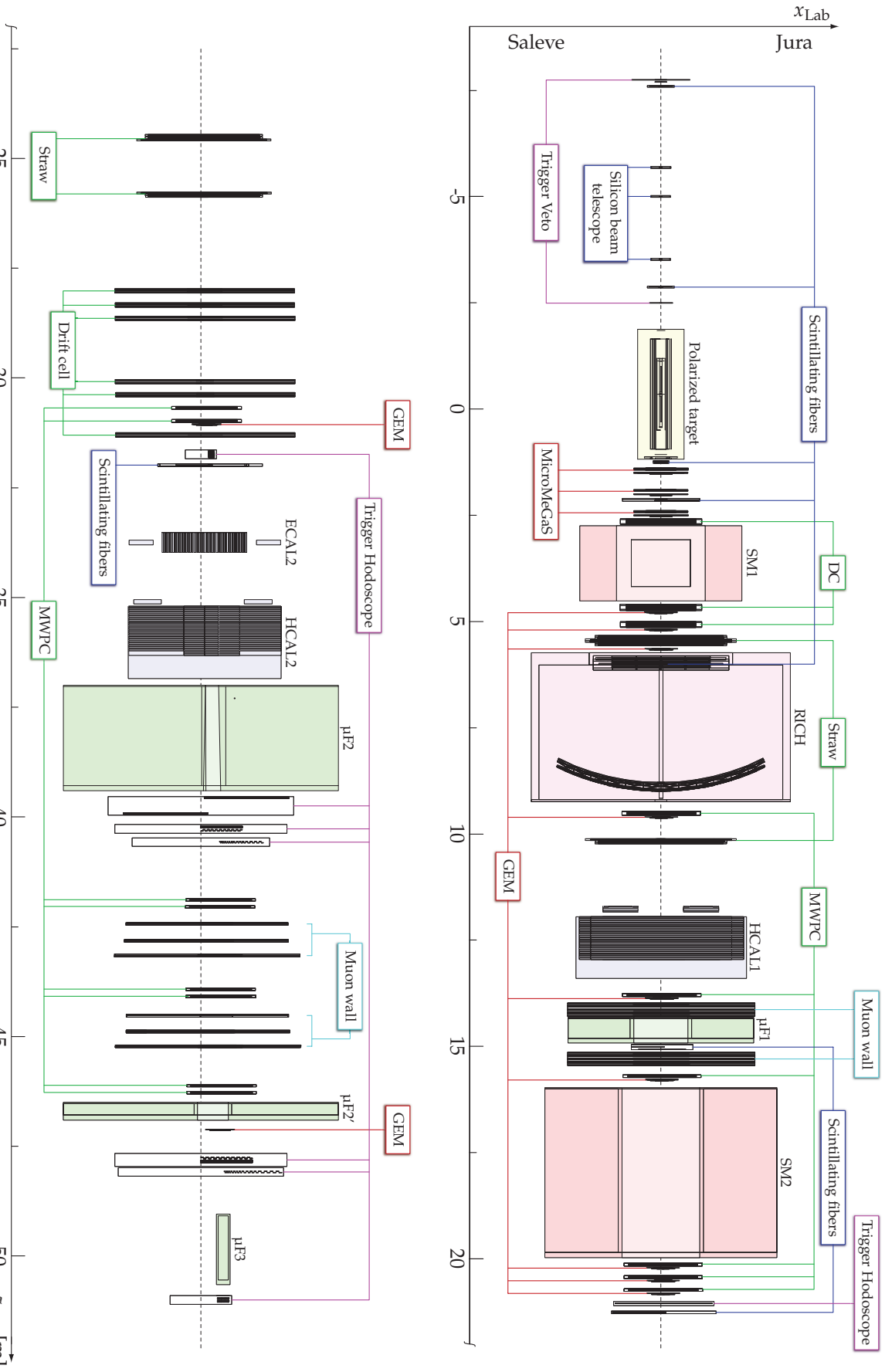

Figure 2.5: Top view of the COMPASS muon beam setup as of 2004

the field shape such, that tracks from the target are perpendicular to the field lines. Because the gap of the magnet is rather large (width 152.5 cm, height 172 cm) compared to its depth (110 cm), SM1 has a quite far reaching fringe field. The field of SM1 was measured using a Hall probe with a resolution of $4 \times 8 \times 8\,\mathrm{cm}^3$ and the result was stored in a field map consisting of three-dimensional measurement points with the associated three-dimensional field vectors, which is interpolated linearly to get the field at an arbitrary position.

The dipole magnet SM2 of the second spectrometer stage has a bending power of 4.4 Tm and an aperture of ± 30 mrad, so that particles with a momentum of $\gtrsim 4$ GeV/c can be reconstructed. The field of SM2 is quite smooth, which allows for polynomial parameterization.

There is an additional solenoid in the target of the spectrometer, which creates a field of 2.5 T along the beam axis, that is needed to preserve the longitudinal polarization of the target (see subsection 2.2.3). The fringe field of the solenoid interferes with that of SM1, which complicates the track finding in the region between the target and SM1 (see subsection 7.1.2). Because of the symmetry of the solenoid field, the field map stores only the radial component and the one along the beam axis. For transverse target polarization and to rotate the polarization of the target there is an additional dipole magnet with a field of 0.5 T in vertical direction.

2.2.2.2 Tracking System

Like in any fixed target experiment the particle flux in COMPASS is highest at the beam center and decreases going outwards. To cope with the high intensities near the beam and to cover at the same time a large acceptance, the tracking system consists of several specialized detector types with different rate capabilities and resolutions. The tracking detectors are categorized into three classes: the Very Small Area Trackers (VSAT) with active areas of 16 to 150 cm^2, the Small Area Trackers (SAT) with 1000 to 1600 cm^2 and the Large Area Trackers (LAT) with 1.4 to 13.5 m^2. The different detector types are combined to staggered arrangements in which the central inactive areas of the larger detectors are covered by smaller detectors with higher rate capability and better resolution. This way the different detectors complement one another which also leads to a more homogeneous angular and momentum resolution.

The beam tracking is done by VSAT detectors before the target: Two stations of scintillating fiber detectors together with a silicon microstrip telescope provide the beam definition, where the fibers mainly contribute the timing and the silicons the precise spatial information.

The silicon telescope [Ang05b] consists of three detector stations each made up of two silicon wafers which have an active area of $5 \times 7\,\mathrm{cm}^2$ and a double sided readout, so that each wafer measures two orthogonal projections. The two detectors of a station provide projections with horizontal (0 °), vertical (90 °), 5 °, and 95 ° orientation. The fine strip

pitch of the silicon wafers of only 50 µm results in a spatial resolution of better than 14 µm. The time resolution is below 2 ns per projection.

The scintillating fibers [Bis02, Hor02, Web04] have a lower spatial resolution of 130 to 250 µm but provide a precise time tag for the event with a time resolution of 350 to 500 ps per plane. Apart from the two fiber stations before the target another six stations with different geometrical configuration measure the beam trajectories in the spectrometer. Depending on their position the detectors use radiation hard scintillating fibers of different diameters ranging from 0.5 to 1 mm and have active areas between $4 \times 4\,\mathrm{cm}^2$ and $12 \times 12\,\mathrm{cm}^2$, where the dimensions increase towards the downstream end of the spectrometer. The fibers have orientations in the horizontal, vertical, and $+45^\circ$ direction.

Further away from the beam trajectory the particle flux is lower, so that micropattern gaseous detectors can be employed as SATs. In COMPASS two novel types of gaseous detectors are used: the Micro Mesh Gaseous Structure (MicroMeGaS) and the Gas Electron Multiplier (GEM). Both combine a high rate tolerance with a good spatial resolution, which makes them usable down to a distance of 2.5 cm away from the beam center.

The MicroMeGaS [Ber05a] are located between the target and the first spectrometer magnet SM1, a region with a large number of hadrons from the interactions in the target. The three stations have in total 12 planes with projections in the vertical, horizontal, and $\pm 45^\circ$ direction. The active area is $40 \times 40\,\mathrm{cm}^2$ with a central dead zone of 5 cm diameter, a spatial resolution of about 70 µm, and a time resolution of 9 ns.

The 22 GEM detectors [Ket02, Wei03] are distributed over both stages of the spectrometer and are organized in 11 stations. The GEM detectors have a two-dimensional orthogonal readout which not only provides two projections per detector, but in addition information about the correlation of the two projections via the signal amplitudes, which can be used to reduce ambiguities in the track reconstruction. A station consists of two detectors that are rotated by 45° with respect to each other, providing one projection in horizontal, vertical, and $\pm 45^\circ$ direction, respectively. The detectors have a spatial resolution of approximately 50 µm, a time resolution of about 12 ns, and an active area of $32 \times 32\,\mathrm{cm}^2$ with an insensitive area of 5 cm diameter in the center. The GEMs cover the dead zones of the large area trackers (MWPC, Straw, and DC; see below) to which they are directly mounted. At the far downstream end of the spectrometer one GEM station improves the tracking of muons with very small scattering angles that passed through the holes of the MWPCs situated after the second muon filter µF2.

Upstream of SM1 the large area tracking is done by one station of Drift Chambers (DC) [Per01]. The modules have a sensitive area of $1.2 \times 1.2\,\mathrm{m}^2$ with an inactive zone of 30 cm diameter. A station consists of eight layers providing two projections in horizontal, vertical, and $\pm 20^\circ$ direction with a spatial resolution of about 200 µm.

Another two drift chamber stations are situated downstream of SM1 followed by a pair of Straw drift tube stations with the RICH detector in-between. The Straw tube chambers [Pla05, Ilg03] are the main large area trackers and provide the large acceptance and

high resolution needed to track the slow hadrons in this region which are strongly deflected by SM1. The detector stations are organized in double-layer planes, in which the second layer is shifted by one tube radius with respect to the first, which helps resolving left-right ambiguities. The active area is about $3.2 \times 2.6\,\mathrm{m}^2$ with a $20 \times 20\,\mathrm{cm}^2$ hole in the center. The nine planes provide horizontal, vertical, and $\pm 10^\circ$ projections, which have a spatial resolution of approximately 270 µm. Another pair of Straw stations with six planes in total serves as LAT in the second spectrometer stage after SM2, where it improves the reconstruction of muons, which are scattered at large angles.

Refurbished Multi-Wire Proportional Chambers (MWPC) [Bar98] from the CERN OMEGA spectrometer with an active area of $1.7 \times 1.2\,\mathrm{m}^2$ and a spatial resolution of about 580 µm provide in total 34 planes which support the large area tracking in the second part of the first spectrometer stage (three stations) as well as in the second stage (eight stations). The wires have vertical, horizontal, and $\pm 10^\circ$ orientation. The diameter of the central dead zone increases with the beam cross sectional area from 16 cm to 22 cm for the more downstream chambers.

The last component of the large area tracker system are the six stations of drift chambers which were formerly used by the EMC/SMC experiments [Bra76, Cer02]. With a drift cell size of 4 cm they provide a spatial resolution of 2 mm over a large sensitive area of $5.2 \times 2.6\,\mathrm{m}^2$. The total 24 detector planes have wire orientations along the horizontal, the vertical, and $\pm 30^\circ$ direction. To reduce the occupancy the insensitive area was enlarged to diameters of 0.5 m and 1 m, respectively.

2.2.2.3 Calorimetry

After the tracking detectors the electromagnetic calorimeters (ECAL) measure the energy of photons an electrons. Although it is intended to have ECALs in both stages of the spectrometer, up to 2004 only the second stage was equipped. As of 2004 ECAL2 consists of 3000 lead-glass blocks from the GAMS calorimeter[3] [Bin86, Ald85] with a size of $3.8 \times 3.8 \times 45\,\mathrm{cm}^3$. It has an energy resolution of $(5.5/\sqrt{E[\mathrm{GeV}]} \oplus 1.5)$ % and a spatial resolution of $(6/\sqrt{E[\mathrm{GeV}]} \oplus 0.5)$ mm. The ECAL information is not used in this analysis.

The energy of hadrons is measured by hadronic calorimeters (HCAL) which are of the sampling type with several alternating layers of iron and plastic scintillator. HCALs are installed in both spectrometer stages. They are required to have a good energy resolution and have to cope with counting rates of 10^5 to $10^6\ \mathrm{s}^{-1}$ per block. HCAL1 [Gav04] has an active area of $4.2 \times 3.0\,\mathrm{m}^2$ with a central hole of $1.2 \times 0.6\,\mathrm{m}^2$ and is made of blocks with a size of $15 \times 15 \times 100\,\mathrm{cm}^3$. The sensitive area of HCAL2 has a size of $4.4 \times 2.0\,\mathrm{m}^2$ and a central opening of $0.4 \times 0.4\,\mathrm{m}^2$. It consists of cells with a dimension of $20 \times 20 \times 120\,\mathrm{cm}^3$. The energy resolution is $(60/\sqrt{E[\mathrm{GeV}]} \oplus 7.6)$ % for HCAL1 and $(65/\sqrt{E[\mathrm{GeV}]} \oplus 5)$ % for HCAL2. Due to the smaller block size, HCAL1 provides a better spatial resolution between 4 and 14 mm.

[3]The GAMS project consisted of two hodoscope spectrometers, GAMS2000 at IHEP (Protvino) and GAMS4000 at CERN.

The HCAL's short response time and good time resolution of the order of 1 ns allows to use them in the trigger decision to enrich events with hadrons in the final state (see section 4.3).

In addition to the energy measurement the calorimeters are part of the particle identification. The HCALs are shielded by ECAL2 or a lead wall equivalent to 18 radiation lengths, respectively, thus separating the electromagnetically and strongly interacting particles.

2.2.2.4 Muon Identification and Tracking

The precise identification and tracking of muons is essential for the trigger decision and for the reconstruction of the primary interaction (see chapter 4 and subsection 7.1.2). To this end two sets of muon tracking detectors are installed, both of them screened from hadrons and electrons by calorimeters and passive absorbers, so-called muon filters.

The first muon filter μF1, a 60 cm thick iron layer, is located at the end of the first spectrometer stage in front of SM2 and is sandwiched between two muon detector modules made of Iarocci type chambers [Iar83] operated in proportional mode with an active area of $4.8 \times 4.1\,\mathrm{m}^2$ and a large central hole of $1.4 \times 0.9\,\mathrm{m}^2$. Each module has four double-layers providing horizontal and vertical projections. Because of the multiple coulomb scattering in the iron absorber, the tracking does not have to be very precise, so that the spatial resolution of about 2.9 mm is sufficient.

The second muon filter μF2 is a 240 cm thick concrete absorber which is followed by two Muon Wall stations constructed out of steel drift tubes [Ant90] with a diameter of 3 cm. The chambers have a sensitive area of $4.4 \times 2.1\,\mathrm{m}^2$ with a dead region of $0.9 \times 0.7\,\mathrm{m}^2$ in the center. A station is made of six double-layers with projections in horizontal, vertical, and -15° direction.

The trigger hodoscopes at the end of the spectrometer (see chapter 4) are shielded by the muon filters μF2', an iron wall of 50 cm thickness, and μF3, a 160 cm long iron block, where the latter absorbs the hadrons that passed through the beam opening of μF2 and μF2'. Both μF2' and μF3 are not illuminated by the beam in order to not contaminate the trigger with secondaries from the interaction of the beam muons with the absorber material.

2.2.3 Polarized Target

The muon program requires both a polarized beam and a polarized target. The data used in this analysis were taken using solid ^{6}LiD as target material. The smallness of the nuclear magneton does not allow to polarize the nucleons directly by Zeeman splitting, because even for strong magnetic fields of several Tesla the interaction energy of the hyperfine splitting is much lower than the thermal energy at temperatures realizable at

moderate cost, which are in the order of some hundred mK. In COMPASS the target material is polarized via Dynamic Nuclear Polarization (DNP) [Abr78] using two separate microwave systems.

The simplest possible system that may be subject to dynamic nuclear polarization consists of an electron spin $\uparrow$ and a proton spin $\Uparrow$. In a strong external magnetic field the energy level of the electron is split into two pairs of levels (see fig. 2.6). The separation of the two pairs is given by the Larmor frequency of the electron's magnetic moment ω_L^e, which is nearly three orders of magnitude larger than the splitting of the two upper and lower levels, that is determined by the Larmor frequency ω_L^p of the magnetic moment of the proton. At temperatures below 1 K only the lower two states, in which the electron spin is aligned opposite to the external magnetic field, are populated. By irradiating the material with resonant microwaves of the frequency $\omega_L^e + \omega_L^p$ $(\omega_L^e - \omega_L^p)$ transitions $|\downarrow\Uparrow\rangle \rightarrow |\uparrow\Downarrow\rangle$ $(|\downarrow\Downarrow\rangle \rightarrow |\uparrow\Uparrow\rangle)$ can be induced in which both spins are flipped. The electron spin relaxes after a short period of the order of milliseconds, whereas the relaxation time of the proton is about 10^6 times larger. This leads to an increased population of one of the lower energy levels and thus to a negative (positive) polarization of the proton.

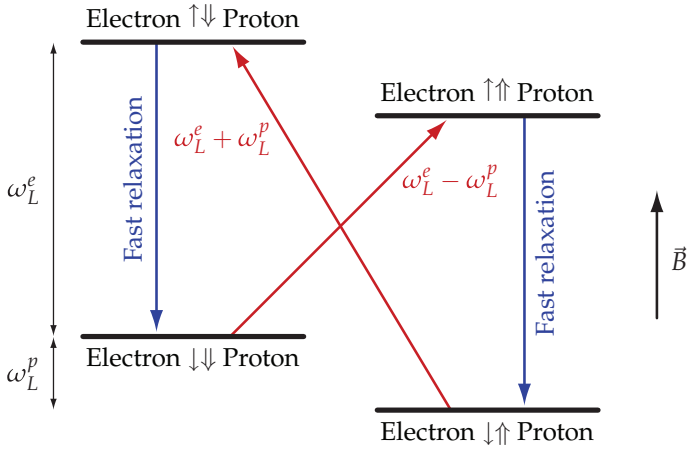

Figure 2.6: Dynamic nuclear polarization in an electron-proton spin system: In a strong external magnetic field B the energy level of the electron splits into four levels, which correspond to the different possible spin alignments of the electron ($\uparrow$) and the proton ($\Uparrow$). (from [Mal96])

The simplified scenario described above does not explain why the actually forbidden double spin-flip transitions are feasible. The reason is, that due to a dipole-dipole interaction of the protons and the electrons, the so-called "solid effect", the pure states are mixed, so that each level contains contributions from both proton spin alignments.

Until 2004 COMPASS used the target magnet system of the SMC experiment (see fig. 2.7). The microwaves polarize paramagnetic centers[4] in the target material, which transfer their polarization with the help of the DNP mechanism to the polarizable nucleons. The nucleons of the atoms around the paramagnetic centers are polarized by spin diffusion, due to spin-spin interactions of the nuclei.

To build up and sustain the polarization, the target material is surrounded by a superconductive solenoid which creates a very homogeneous field of 2.5 T. Thermal relaxation is avoided by cooling the ^{6}LiD down to temperatures of 80 to 100 mK using a ^{3}He$-^4$He dilution refrigerator. At this low temperatures the target operates in the so-called frozen spin mode with relaxation times larger than 1000 h. The polarization is measured by means of Nuclear Magnetic Resonance (NMR) and it usually exceeds the design value of 50 %.

The target is split up into two cylindrical cells each 60 cm long with a diameter of 3 cm (see fig. 2.7). The cells are polarized in opposite directions, so that both relative alignments of target and beam polarization are measured at the same time. To neutralize the effect of different acceptances of the up- and downstream target cells, the target polarization is inverted every 8 h. Additional systematic influences of the solenoid field are suppressed by reversing the orientation of the target cell polarization with respect to the direction of the solenoid field in larger time intervals, which is done by exchanging the microwave frequencies in the two cells. The data taking is organized in a way that all possible combinations of polarization and field direction are of equal statistics.

In order to be able to invert the direction of the polarization an additional dipole magnet with a maximum transverse field of 0.5 T in vertical direction is integrated into the target. The fields of the solenoid and the dipole magnet are ramped in a coordinated way, so that the total field vector is slowly rotated by 180 $^\circ$ taking along the target spins. The dipole magnet is also used to keep the target in transverse polarization, which is needed for the transversity measurements (see subsection 2.1.1.3). Data taken with transverse target polarization are not considered in this analysis.

In future measurements with NH_3 as target material (proton target) are planned, which in combination with the ^{6}LiD data (deuteron target) will allow to extract information about the neutron spin structure.

[4] Impurities with a single valence electron.

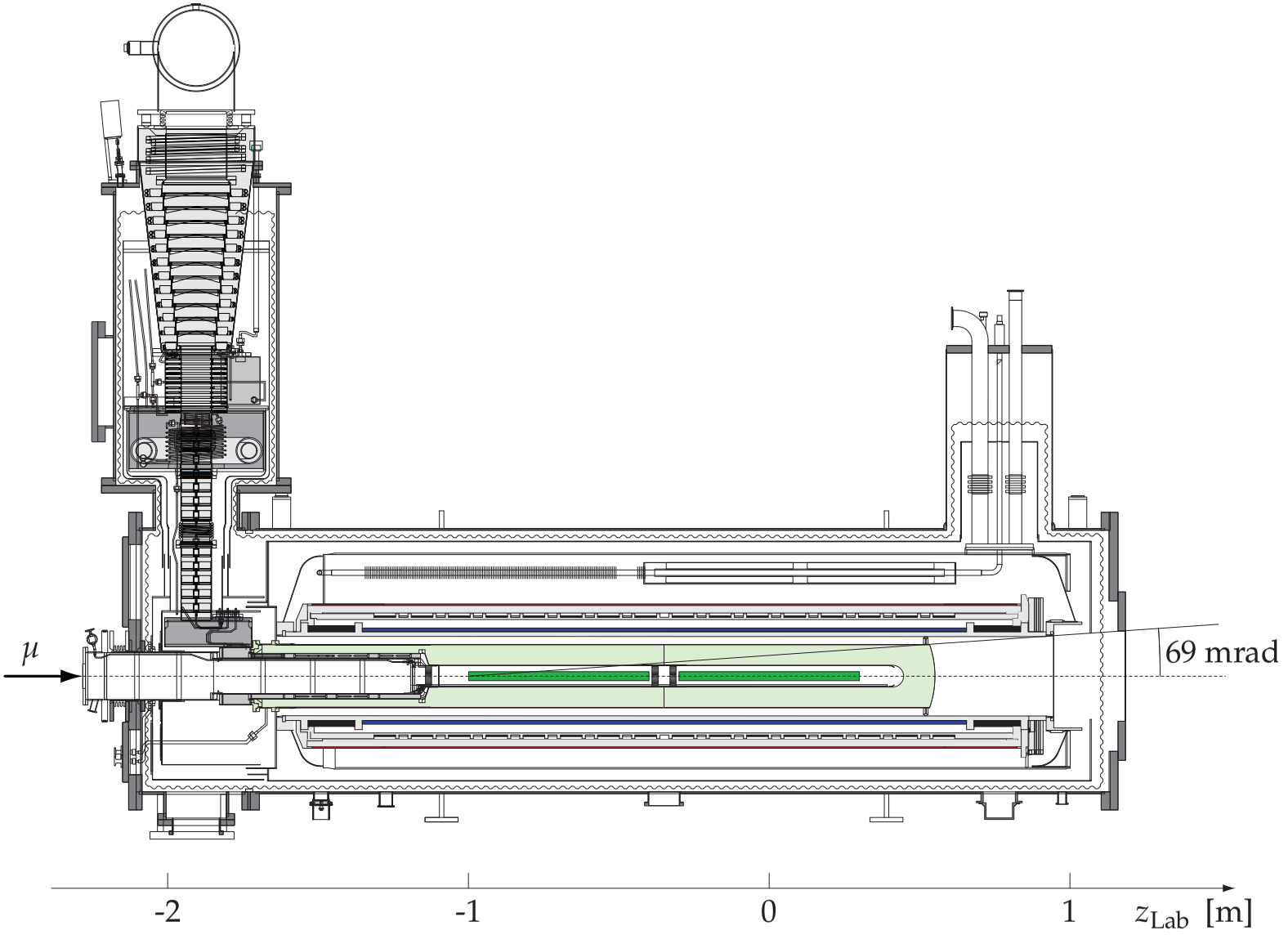

Figure 2.7: Side view of the COMPASS polarized ^{6}LiD target. The components relevant for this analysis are colored: the two target cells in green, surrounded by the microwave cavity in light green and the solenoid in blue plus the dipole magnet in red. (from [Tak02])

Chapter 3

Data Acquisition System

The main challenge for the design of the COMPASS Data AcQusition (DAQ) was to build a system, that reads out a large number of channels, distributed over the various detector systems of the approximately 50 m long spectrometer setup, at a maximum on-spill trigger rate of 10^5 s^{-1} and with a dead-time as low as possible. To cope with the expected high peak data rates of up to 4 GByte/s, the system has a pipelined architecture and the signals are digitized and concentrated as close to the detectors as possible, which not only simplifies the processing and transport of the detector data, but additionally lowers the readout noise. Most of the data links utilize optical fibers, which provide high data bandwidths, are insensitive to electromagnetic noise, and simplify the electrical grounding of the apparatus. Moreover the system was demanded to be upgradable, so that it can be adapted to the requirements of the different physics programs. This led to a modular system design, in which the modules, that are connected by a tree-like hierarchical network, merge the digital data streams of the various equipments at different levels.

The COMPASS DAQ [Sch04] consists of several subcomponents (see fig. 3.1): The front-end electronics (see section 3.1) processes and digitizes the analog detector signals. The digital data are accumulated in concentrator modules (see section 3.2) and are sent via optical fibers to ReadOut Buffer computers (ROB) (see section 3.3), where they are cached in order to take advantage of the SPS spill cycle. The EVent Builder computers (EVB) (see section 3.4) receive the data fragments of the various sub-detector systems, that belong to the same trigger, from the readout computers and assemble them to event data blocks. Before the events are transferred to the Central Data Recording (CDR), where they are written to tape, they are preselected by the online filter (see section 3.5), a software running on the event builder PCs.

The high performance of the DAQ system is achieved by a cost-effective combination of custom made modules with standard off-the-shelf components. The custom modules are based on reconfigurable logic devices, so-called Field Programmable Gate Arrays (FPGA). FPGAs are multipurpose reconfigurable circuits that were introduced in 1985 by Xilinx [Xil]. They consist of a regular array of configurable logic blocks, which are interconnected by a routing network. The logic blocks are able to perform simple

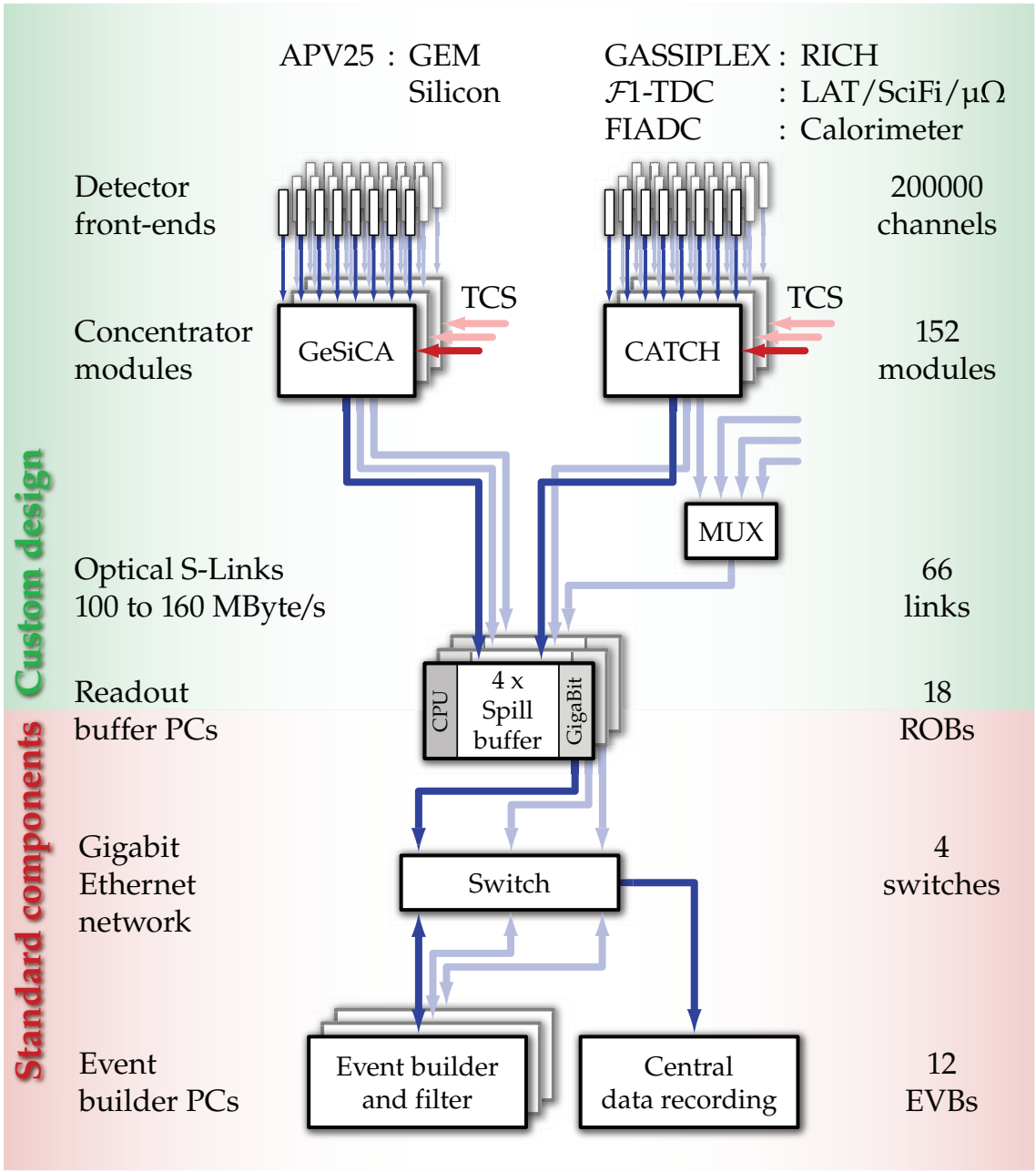

Figure 3.1: General structure of the COMPASS data acquisition system. The data flow from the front-end electronics to the central data recording is indicated by the arrows. The given numbers represent the setup as of 2004.

logical operations using look-up tables based on static RAM. Switching boxes determine, how the routing network connects the different logic blocks. By configuring the look-up tables and the switching boxes the FPGA can be adapted to perform specific algorithms. The algorithms are usually formulated in a high level hardware description language like VHDL[1] and then translated by vendor specific logic synthesis tools into a firmware file that is downloaded into the FPGA device. The complexity of the algorithm is only constrained by the available hardware resources (number of logic blocks) and by the required speed.

3.1 Front-End Electronics

The detectors in COMPASS use different types of front-end electronics chosen according to the special requirements of the particular detector type. The photon chambers of the RICH detector are read by the GASSIPLEX chip, whose analog signals are digitized by the BORA board. All gas drift type detectors and the scintillation detectors use the $\mathcal{F}1$ TDC[2] for measuring their signal times. The signals of the gas drift detectors are amplified, shaped, and discriminated either by the MAD4 [Gon01], the ASD8 [New93], or by the SFE16 chip [Del00], whereas the trigger hodoscopes use a custom made discrimination logic (see section 4.5). The GEM and silicon microstrip detectors share a common readout electronics based on the APV25 chip, which is read by an ADC[3] card. The signals of the calorimeters are digitized by classical fast integrating ADCs. In 2004 part of the ECAL2 was equipped with a newly developed sampling ADC readout.

With its 83,000 channels the RICH is the detector with the largest number of channels in COMPASS. It utilizes MWPCs with segmented CsI-coated cathodes to detect the Cherenkov photons. The pads are read by the GASSIPLEX chip [San94], an analog signal processor ASIC[4] developed at CERN and especially modified for COMPASS. The chip has 16 input channels of which each is equipped with an analog amplifier, a filter, and a shaper with a peaking time of 1.2 µs. The 16 channels are multiplexed to an analog output line which introduces some noise. To prevent that this multiplexer noise disturbs the measurement, a minimum dead-time of 5 µs is required. The analog data are digitized with a 10 bit dynamic range by the BORA boards [Bau03], which also perform a zero suppression by threshold subtraction.

The $\mathcal{F}1$ TDC [Fis00, Fis99] is a joint development of the University of Freiburg and the company ACAM for COMPASS. The $\mathcal{F}1$ is an ASIC manufactured in a 0.6 µm sea-of-gates process with a pipelined architecture and a dead-time-free readout. The central

[1] The VHSIC Hardware Description Language (VHDL), where VHSIC is an acronym for Very-High-Speed Integrated Circuit, is a strongly typed high level language comparable to C, but specialized in describing concurrently interacting processes.

[2] A Time to Digital Converter (TDC) converts input pulses into a digital representation of their time indices.

[3] An Analog to Digital Converter (ADC) converts continuous analog signals into a sequence of discrete digital values that correspond to the signal amplitude.

[4] Application Specific Integrated Circuit (ASIC)

part of the TDC is an asynchronous ring oscillator made of 19 identical delay elements that are controlled by a PLL[5], which stabilizes the individual gate propagation delays and thus the oscillator frequency.

The $\mathcal{F}1$ can be operated in three different modes: In the standard mode the chip offers eight input channels with a digitization unit of about 120 ps at a dynamic range of 16 bit. This mode is used for the 12,500 MicroMeGaS channels and the 22,100 channels of LAT other than MWPC. The 25,600 MWPC channels require less precise time information and therefore use the latch mode, which provides 32 input channels split into groups of four. Each group is connected to an input register that stores the hits, which arrive within a programmable time window, whose start is defined by the first arriving pulse in the group of channels. At the end of the time window the $\mathcal{F}1$ writes out the hit pattern in the input register together with its time stamp, that has a precision of about 5 ns. For very precise time measurements at high rates the $\mathcal{F}1$ provides a third mode, that is used by most of the 5600 scintillating fiber channels. In the high resolution mode the digitization time is only 60 ps and the hit buffer depth is doubled. The number of input channels on the other hand is reduced to four. The $\mathcal{F}1$ is able to perform data sparsification by writing out only those hits, that were found to be coincident with the trigger pulse within a programmable time window.

The GEM and silicon tracking detectors use the APV25[6] [Fre01, Jon99] chip, a development of the CCLRC[7] for the silicon tracker of CMS[8], which is a LHC experiment currently under construction at CERN. The APV25 has 128 input channels, each of them equipped with a shaping amplifier and a pipeline able to store the analog signals for up to 4 µs. A multi-event buffer renders the readout dead-time free, but limits the average trigger rate to 10 triggers in 200 µs[9]. At the output stage the 128 channels are multiplexed into one analog output line, which makes the readout system for the in total 45,000 channels very compact.

The analog signals from the APVs are digitized with a 10 bit dynamic range by ADC cards, that also apply the channel calibration, the so-called pedestal subtraction, and perform a zero suppression with common mode noise correction (see [Gru01a]). A striking feature of the APV based readout is its ability to not only extract the amplitude but also the timing of the signal by reading three consecutive samples at the rising edge of the signal pulse. This way the very precise spatial information of the double sided silicon microstrip detectors is complemented by a time information with a resolution of better than 2 ns per projection [Ang05b].

[5] A Phase Locked Loop (PLL) is a closed-loop control system that maintains a fixed phase relationship between a generated signal and a reference signal (see also section 5.2).

[6] The Analog Pipeline Voltage type (APV) chip is manufactured in a radiation hard 0.25 µm Complementary Metal-Oxide-Semiconductor (CMOS) process.

[7] Council for the Central Laboratory of the Research Councils (CCLRC), Great Britain

[8] Compact Muon Solenoid (CMS), see [CMS]

[9] This value may be improved by a factor of two and thus reaching the 10^5 s^{-1} design value by operating the output multiplexer of the APV at 40 instead of 20 MHz.

The signals of the calorimeters are digitized by gated Fast Integrating ADC (FIADC) modules [Kon05], which have 12 bit dynamic range and are able to handle up to three consecutive events within 30 µs.

3.2 Concentrator Modules

The concentrator modules are a central part of the readout chain. They process the digital data of the detector front-ends and provide the interface to the trigger control system which supplies the trigger signal, the reference clock, and the event labels (see section 5.4). The clock is distributed to the connected front-ends, so that they operate synchronously and may use it as a reference for time measurements. In the same way the trigger signal is forwarded to initiate the readout in the front-end electronics.

The concentrator modules buffer the data, that arrive after each trigger from the front-ends, and packetize them into well-defined blocks [Fis03]. The blocks are labeled with additional header information, which include the unique event identifier provided by the TCS, and are sent via optical fibers to the readout computers in the counting room. The event label is used later at the event building stage to assemble the data fragments that belong together (see section 3.4). The optical links have a typical length of 100 to 200 m. They follow the S-Link[10] standard [vdB97] developed at CERN and offer data bandwidths of 100 MByte/s (fibre channel implementation), 128 MByte/s (single G-Link), and 160 MByte/s (double G-Link).

Furthermore the concentrator modules provide a common interface to load firmware and configuration data into the various types of front-end modules. The configuration data and firmware files are handled by the ConfigServer software [Kuh06], which retrieves its information from a central database. The concentrator modules are housed in crates, which beside power and cooling, provide a VMEbus[11] interface for communication. Each crate is equipped with a VMEbus controller, a special computer through which the VMEbus devices may be accessed. A client process, that runs on the VME computers, communicates with the ConfigServer via standard local area network and provides an interface to the concentrator modules connected to the VMEbus. In combination with a web front-end for the configuration database this system allows an efficient management of the large amount of configuration data.

COMPASS uses two types of concentrator modules (see fig. 3.2): the COMPASS Accumulate, Transfer, and Control Hardware (CATCH) and the GEM and Silicon Control and Acquisition module (GeSiCA). The CATCH is a development of the University of

[10] The Simple-Link interface specification defines a protocol for simple buffered data transmission. As the standard only specifies the logical interface, several implementations using different physical layers are available.

[11] The VERSAmodule Eurocard bus (VMEbus) is a standard maintained by the Institute of Electrical and Electronics Engineers (IEEE) and is defined in ANSI/IEEE 1014-1987 [IEE]. VMEbus uses an asynchronous signaling scheme, the connected modules do not share a common clock. The VMEbus implementation used in COMPASS supports 32 bit wide data transfers and 24 bit addressing.

Freiburg [Sch02, Grü02]. The front-end specific components sit on separate mezzanine cards, that communicate with the CATCH motherboard via well-defined links. This makes the CATCH a rather versatile module and it is used for nearly all front-end types, except for those that are based on the APV chip. The APV front-ends of the GEM and silicon detectors are read by GeSiCA modules [Gru01b, Gru01a]), which provide similar functionality, but are adapted to the special requirements of the highly integrated APV readout.

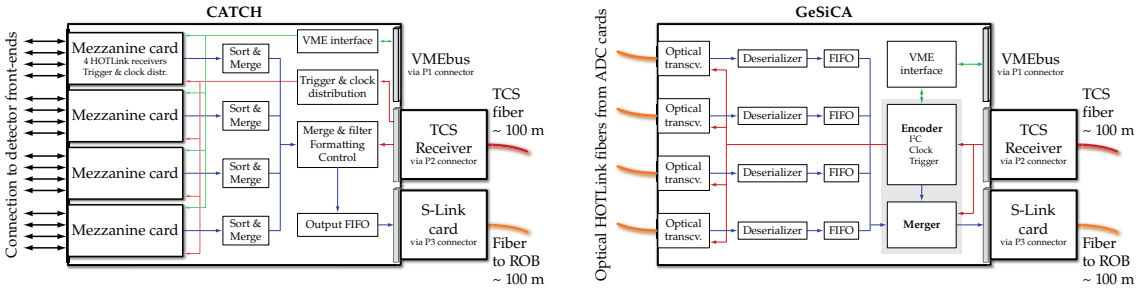

Figure 3.2: (a) Schematic of the CATCH module. (b) the same view of the GeSiCA. (from [Fis00] and [Gru01a], respectively)

Because the data rates produced by the various detectors are quite different an additional S-Link multiplexing device was developed. The S-Link Multiplexer [Kon05, Ang05a] merges the S-Link data streams of up to four concentrator modules into one S-Link output stream, which allows to lower the number of required optical connections by exploiting the available bandwidth of the S-Links more efficiently.

3.3 Readout Computers and Data Buffering

The readout computers are equipped with custom made PCI[12] extension cards, so-called Spillbuffers (see fig. 3.3), that receive the data from the concentrator modules via the optical S-Links. To take advantage of the SPS spill cycle (see subsection 2.2.1) the cards have large buffer memories, from which the data are transferred to the event builder computers via Gigabit Ethernet[13]. The SPS has a duty cycle with 4.8 s of beam extraction, during which detector data arrive at a high rate, and a 12 s long off-spill period, where the beam is off. The buffers lower the bandwidth requirements for the event building

[12]The Peripheral Component Interconnect (PCI) bus is an industry standard maintained by the PCI Special Interest Group [PCI]. Depending on the hardware the bus offers bandwidths from 133 MByte/s (32 bit, 33 MHz) to 533 MByte/s (64 bit, 66 MHz). Nowadays practically all personal computers use this bus, or its designated successor PCI Express, to connect the CPU with extension devices like mass storage controllers, network adapters, graphics cards, and the like.

[13]Ethernet is a widely used communication standard for Local Area Networks (LANs) specified in IEEE 802.3 [IEE]. The standard defines various communication speeds (Fast Ethernet with 100 Mbit/s, Gigabit Ethernet with 1 Gbit/s, and 10 Gigabit Ethernet with 10 Gbit/s) using various physical media like twisted pair cable (e.g. 100/1000BASE-T) and multi-mode fiber (e.g. 100BASE-FX and 1000BASE-SX).

network (see section 3.4) to about 30 % of the mean on-spill data rate by averaging the input rate over a whole SPS cycle.

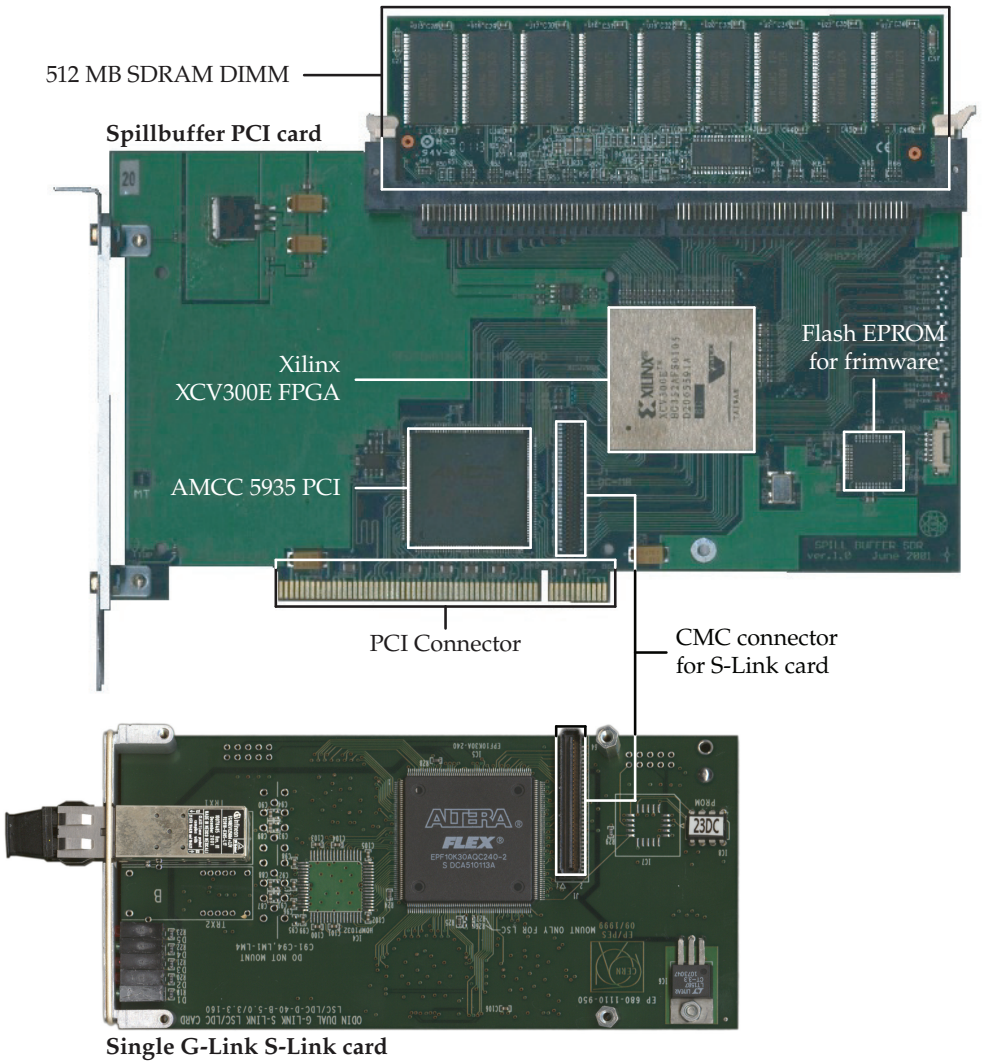

Figure 3.3: The Spillbuffer card with an unmounted single G-Link S-Link mezzanine card. (from [Sch04])

The S-Link transceiver, that provides the interface to the concentrator modules, sits on a separate mezzanine card, which is connected to the Spillbuffer card via an IEEE 1386 Common Mezzanine Connector (CMC). This way the Spillbuffer is independent of the utilized S-Link implementation (100, 128, or 160 MByte/s).

The data flow is controlled by a Xilinx FPGA which receives the incoming S-Link data from the mezzanine card and writes them into the buffer memory. The buffer is a standard SDRAM DIM module[14] with a capacity of 512 MByte, so that the altogether 66 Spillbuffers provide a buffer of 33 GByte size, which is sufficiently large to store more data

[14]The Synchronous Dynamic Random Access Memory Dual In-line Memory Module (SDRAM DIMM) is a widely used industry standard developed by the Joint Electron Device Engineering Council (JEDEC) [JED]

than arrive during one spill. The FPGA accesses the memory as a FIFO[15] buffer, from which the host computer reads the data via standard PCI bus. The PCI interface is based on an AMCC chip, that is controlled by the FPGA and that allows to transfer the data via DMA[16] from the Spillbuffer memory directly into the memory of the host PC.

The 18 readout buffer PCs consist of standard server components and are optimized for data throughput. They are equipped with two PCI busses: One bus with 32 bit and 33 MHz connects the four Spillbuffer cards mounted per ROB, the other one with 64 bit and 66 MHz the Gigabit Ethernet interface. This separation allows the reading from the Spillbuffers and the writing of the data to the event building network to be performed simultaneously without additional overhead or loss of bandwidth. The data streams are controlled by two Intel Pentium III CPUs which are equipped with altogether 1 GByte of ECC SDRAM memory.

3.4 Event Building and Filtering

The event building is the last stage of data concentration. In this process each ROB sends its sub-events to a single EVB, which is chosen in a round robin scheme, so that all data fragments, that belong to the same event, arrive at the same event builder, where they are assembled to event data blocks. The consistency of the data fragments is insured by means of the TCS event labels, which were added to the data stream by the concentrator modules.

For the event building it is necessary that each EVB communicates with each ROB, which requires an event building network that provides sufficient bandwidth and avoids collisions by balancing the network traffic. This is achieved by a hierarchical network structure in which a backbone switch interconnects the three front-end switches that connect all DAQ computers (see fig. 3.4). To each front-end switch four EVBs are attached, matching the number of backbone uplinks and thus equalizing the network load. A further load balancing is achieved by connecting the ROBs according to their average data output. In total the event building network offers 36 1000BASE-T ports for DAQ computers and provides a bandwidth of 12 GBit/s.

The 12 event builder PCs are equipped with two AMD Athlon MP CPUs at 1.6 GHz with 1 GByte of ECC DDR-SDRAM plus an IDE RAID 5 storage system[17] with a net capacity of 640 GByte. The altogether 7.68 TByte of disk space are used to buffer the data before

[15] The First In First Out (FIFO) buffer is a special kind of data buffer, that conserves the order the data are coming in. It is normally used to decouple data processing units.

[16] The Direct Memory Access (DMA) allows certain hardware components to directly read from or write to main memory areas. Because the CPU is not involved, DMA transfers are very efficient.

[17] A Redundant Array of Independent/Inexpensive Disks (RAID) is a system that connects multiple hard disks to increase capacity, fault tolerance, data integrity and/or throughput with respect to a single disk. There are different so-called RAID levels that determine how the data are distributed over the disks thereby favoring some of the aforementioned aspects. RAID 5 is the most widely used level. It distributes the data evenly over all disks and generates additional parity information that is stored on a separate disk. RAID 5 thus increases both performance and fault tolerance.

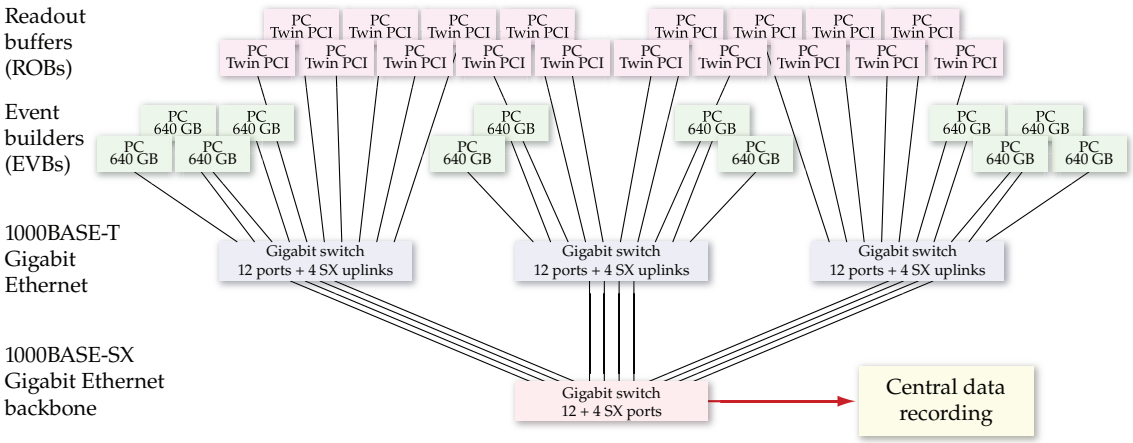

Figure 3.4: The event building network. (from [Sch04])

they are transferred asynchronously via a Gigabit uplink to the central data recording in the CERN computing center, so that in case of problems with the tape recording the experiment is able to keep taking data for up to two days.

3.5 DAQ Software

The data flow in the acquisition system is controlled by the DATE software [DAT01], which was developed by the ALICE DAQ group. DATE provides a complete framework for distributed network based data acquisition with software components for readout of detector data, event building, run control, information logging, and event sampling. The various software components were adapted to fit the COMPASS environment.

The DATE Local Data Collector (LDC) software, which runs on the readout buffer PCs, reads the sub-event data from the Spillbuffer cards, checks and reformats the data, before it sends them to an event builder computer, that is determined in a round robin scheme based on the unique TCS event label. The Global Data Collector (GDC) software, running on the EVBs, receives the sub-events and re-packetizes them to event data blocks, which then a daemon transfers to the central data recording, where they are stored on tape by the CASTOR hierarchical storage manager[18]. The meta-data are managed by an Oracle 9i database.

Since the bandwidth to the central data recording and also to the tapes itself is limited, higher trigger and thus data rates are only achievable by filtering the data stream after event building and before it is written to disk and tape. The online filter is essentially

[18]The CERN Advanced STORage Manager (CASTOR) is a hierarchical storage management system developed at CERN [CAS], in which the high-capacity but slow tape storage is complemented by a fast hard disk storage of lower capacity. CASTOR manages the files in a directory structure and automatically migrates them between the front-end disks and the back-end tape system.

a software trigger, that discards events which are uninteresting for the physics analysis, thus increasing the purity of the trigger, while at the same time keeping the efficiency practically unchanged. The purity is defined as the ratio between the number of good events and the total number of recorded events, whereas the efficiency is the ratio of the number of recorded good events to the number of all good events. The online filter also helps to lower the dead-time introduced by the veto system, as part of the veto can be shifted to the software stage. Last but not least the purification of the data also leads to a more efficient utilization of the storage space on tape.

For the COMPASS experiment the online filter software Cinderella was developed [Kuh06, Nag05]. As the event building uses only about 20 % of the available CPU time on the event builder machines, the first generation of Cinderella exploits the remaining computing power of the altogether 24 CPUs. At a trigger rate of 50,000 events/spill each event builder PC has about 4 ms time to make a decision. This low tight time budget permits only simple operations like decoding of the detector information and time correlation of some detectors.

The Cinderella filter software is implemented as a multithreaded[19] application in which the various tasks are performed by separate threads (see fig. 3.5), so that Cinderella is able to scale in multiprocessor environments. The input thread reads the DATE data stream via a TCP/IP socket[20] and writes it into a large buffer memory that decouples Cinderella from fluctuations of the incoming data flow. The events in the buffer are read by the filter thread, which tags them with the filter decision, made by a configurable chain of filter modules. The output thread waits for tagged events and writes the good ones into an output buffer after adding some meta-information, which allow to reconstruct the filter decision for offline performance monitoring. The filter thread is monitored by the watchdog thread, which restarts the filter in case it got stuck and ensures that the decision time does not exceed a certain limit.

The muon beam physics requires the knowledge of the primary interaction point of the beam muon with the target nucleon, which renders events, where no beam trajectory could be reconstructed, useless. In addition to the existence of the beam track also its momentum must be known and the time of the trajectory has to match the trigger time in order to ensure that the triggered event was caused by the beam particle. The beam reconstructability criterion combines the information of the beam momentum station, the scintillating fiber detectors, and the silicon beam telescope, all of them situated upstream of the target (see subsections 2.2.1 and 2.2.2). The filter decision is implemented by means of a conditional coincidence algorithm.

In the hadron pilot run Cinderella cleaned up the diffractive trigger by applying a multiplicity cut on the tracks after the target. In diffractive production the scattering of the

[19] In a multithreaded application multiple threads of execution run in parallel either on one CPU using time slicing or on multiple CPUs by multiprocessing. Modern operating systems have a scheduler that manages the threads and usually supports both schemes.

[20] A TCP/IP socket implements the communication between two processes utilizing the TCP network transport layer. Using this kind of sockets makes it possible to run the two processes on different machines.

beam particle creates short-lived hadrons, which decay already in the target. Due to charge conservation and since the production of doubly charged particles is very improbable, the number of charged tracks after the target is always odd and larger than one. The track multiplicity is estimated based on the hit multiplicities in the silicon detectors, that were situated right after the target, by a coincident multiplicity algorithm.

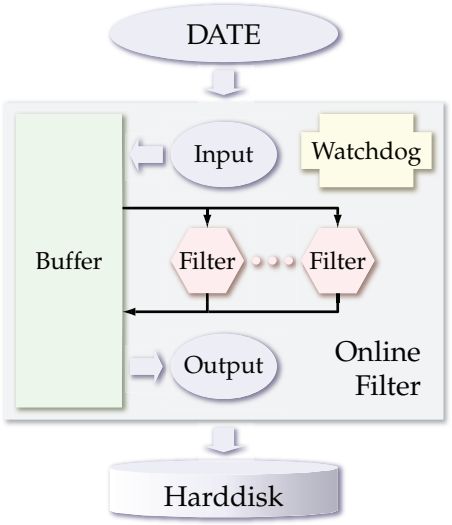

Figure 3.5: Architecture of the online filter. (from [Sch04])

A positive side-effect of Cinderella is, that it provides a real-time feedback of the quality of the recorded data by means of the filter reject rates, that are calculated after each SPS spill and that instantaneously indicate detector problems, thus complementing the standard online monitoring.

3.6 Performance

The muon program requires only moderate trigger rates: In the 2004 beam-time typically 50,000 events were recorded per spill corresponding to a trigger rate of 10^4 s^{-1} at a read-out dead-time of about 5 %. With an average event size of 35 kByte [Kuh05] this equals to an on-spill data rate of 365 MByte/s which due to the buffering results in a sustained data rate of 104 MByte/s before the online filter. Cinderella was employed to enrich events with reconstructible beam trajectories for circa 80 % of the recorded $13.6 \cdot 10^9$ events of which it discarded 23 % at an efficiency of 99.6 % thus reducing the data rate to tape to 80 MByte/s.

For the comparatively short 2004 hadron pilot run the trigger rate was adjusted such, that the Gigabit Ethernet link to the CDR, which provides a bandwidth of 120 MByte/s, was saturated. With an average event size of 25 kByte [Kuh05] trigger rates of $1.8 \cdot 10^4$ s^{-1} or 86,000 per spill were reached corresponding to on-spill data rates of 450 MByte/s and a sustained rate of 130 MByte/s before the filter. The multiplicity condition of the online

filter was applied to part of the recorded data and reduced the number of diffractive events by 45 % thereby lowering the total data rate to tape by 10 % to 117 MByte/s.

Tests demonstrated that the full DAQ system is able to sustain data rates of up to 180 MByte/s to disk.

In the future it is planned to have a dedicated Cinderella computer farm with much more computing power providing processing times in the order of 100 ms per event. This will allow to implement elaborate calorimetric triggers and tracking in the target region, thus rendering reduction factors of ten and larger possible, so that trigger rates close to the design value of 10^5 s^{-1} may be reached. In addition the connection to the central data recording will be upgraded to 10 Gigabit Ethernet, which will not influence the tape writing speed, but will make the data transfer easier.

Chapter 4

Trigger System

The trigger system stands at the beginning of the readout chain. It makes the decision, whether an event is read out or whether it is discarded. Typically trigger systems have several levels, which use different kind of information to generate the trigger decision. COMPASS uses two trigger levels: The First Level Trigger (FLT) is implemented in hardware and if an event fulfills a certain logical condition, the trigger condition, it initiates the readout of the front-end electronics of the detectors. The FLT discards uninteresting events and enriches certain wanted classes of events. In addition it provides time information, so that the scattered muon can be unambiguously associated with the incoming beam muon. A further selection of the events is performed by the online filter software Cinderella, which runs on the readout computers (see section 3.5). Since it has the full information about the event at its disposal, the online filter is able to make more elaborate decisions, which a hardware trigger would not be capable of.

This section is intended to give a short introduction into the COMPASS first level trigger system with the focus on the basic principles. A more detailed description can be found in [Ber05b], [Leb03] and [Leb02].

Since the data of all detectors have to be buffered until the trigger arrives, the first level trigger decision has to be generated within a short time. Apart from two exceptions the detector front-ends have a pipelined architecture, which allows them to cope with large trigger latencies. The main limitation for the trigger latency is set by the hadronic calorimeters, which use a classical readout scheme where the analog data are stored in delay cables, thus limiting the trigger latency to values smaller than 500 ns. The second exception is the RICH detector, which employs integrating amplifiers with a peaking time of about 1 µs for the readout of its photon chambers. Both detectors are supplied with a dedicated fast trigger signal with a latency smaller than 500 ns.

The trigger is formed by (anti)coincidence of the signals of various detectors. This requires detectors that have a short response time and a good time resolution. For this reason plastic scintillation counters with photo-multiplier readout were chosen. They have a response time in the order of 30 ns and a time resolution of better than 1 ns. The signals of these detectors are combined by a custom made coincidence logic (see section 4.5).

The trigger system for the muon program mainly uses information about the scattered muon to generate its decision. High energy muons are well suited for trigger purposes, because they are able to penetrate large amounts of material. They therefore can easily be separated from other particles by absorbers, the so-called muon-filters (see subsection 2.2.2). The trigger selects two classes of muon scattering events: deeply inelastic scattering events (see subsections 2.1.1.1, 2.1.1.3, and 2.1.1.4) and photon-gluon fusion events (see subsection 2.1.1.2). In both cases the goal is to reach a high trigger efficiency in combination with a high purity in order to collect as many interesting events as possible. Purity and efficiency are, on the other hand, conflicting goals, so that compromises have to be made for the relevant physics channels, which also take into account the available bandwidth and rate capability of the data acquisition system.

In DIS events the virtual photon has a negative four-momentum squared Q^2 of at least $0.5\,(\mathrm{GeV}/c)^2$. The DIS trigger (see section 4.1) selects these type of events over a x_B range as large as possible. The maximum measurable Q^2 is limited by the dimensions of the opening of the second spectrometer magnet SM2 to values below $60\,(\mathrm{GeV}/c)^2$. Events with larger Q^2 can only be reconstructed in the first spectrometer stage.

Beside the DIS physics the main goal of the muon program is the extraction of the gluon polarization $\Delta G/G$ from photon-gluon fusion events. For PGF events the hard scale, that allows to apply perturbative QCD, is not the Q^2 of the virtual photon but the center of mass energy $\sqrt{\hat{s}}$ of the photon-gluon system. For small Q^2 the flux of virtual photons and thus the PGF cross section is proportional to $1/Q^2$. This means that PGF events are predominantly reactions, where a quasi-real photon with $Q^2_{\mathrm{min}} \approx m_\mu^2\, y_B^2/(1-y_B) < Q^2 < 0.5\,(\mathrm{GeV}/c)^2$ is exchanged resulting in small scattering angles of the scattered muon.

The production of open charm in PGF events requires a center of mass energy $\sqrt{\hat{s}}$ of the photon-gluon system larger than twice the charm quark mass m_c. For quasi-real photons the center of mass energy is related to the energy ν of the virtual photon and the Bjorken scaling variable x_G of the gluon by $\hat{s} \approx 2M_N\,\nu\,x_G > 4m_c^2$. This condition implies, that the photon must have a minimum energy ν_{min} of 32 GeV for $x_G < 0.1$ corresponding to a minimum relative energy loss y_B^{min} of the incoming muon of about 0.2. Cutting on larger y_B in addition selects the more interesting PGF events with larger polarization of the virtual photon. The main background processes are Bremsstrahlung, elastic muon-electron scattering, and halo muons. Their contribution is suppressed by using information from the hadronic calorimeters in the trigger, which on the other hand may introduce a bias in the event selection, because of the different acceptance for positive and negative hadrons.

The COMPASS trigger system selects the full Q^2 range including the region of quasi-real photo-production (see section 4.2) and in addition looks for final state hadrons in the forward region (see section 4.3). The whole acceptance is covered by four hodoscope systems named “Inner”, “Ladder”, “Middle” and “Outer” (see fig. 4.1). Each subsystem has an optimized granularity to fulfill the resolution and rate requirements. The background caused by halo muons is suppressed by an additional veto system (see section 4.4) which introduces dead-time. The logical condition, which connects the information from the different subsystems to form the trigger, is a compromise between the conflicting re-

quirements of minimum bias (no hadronic information), minimum dead-time (no veto), and maximum allowed data rate to CDR.

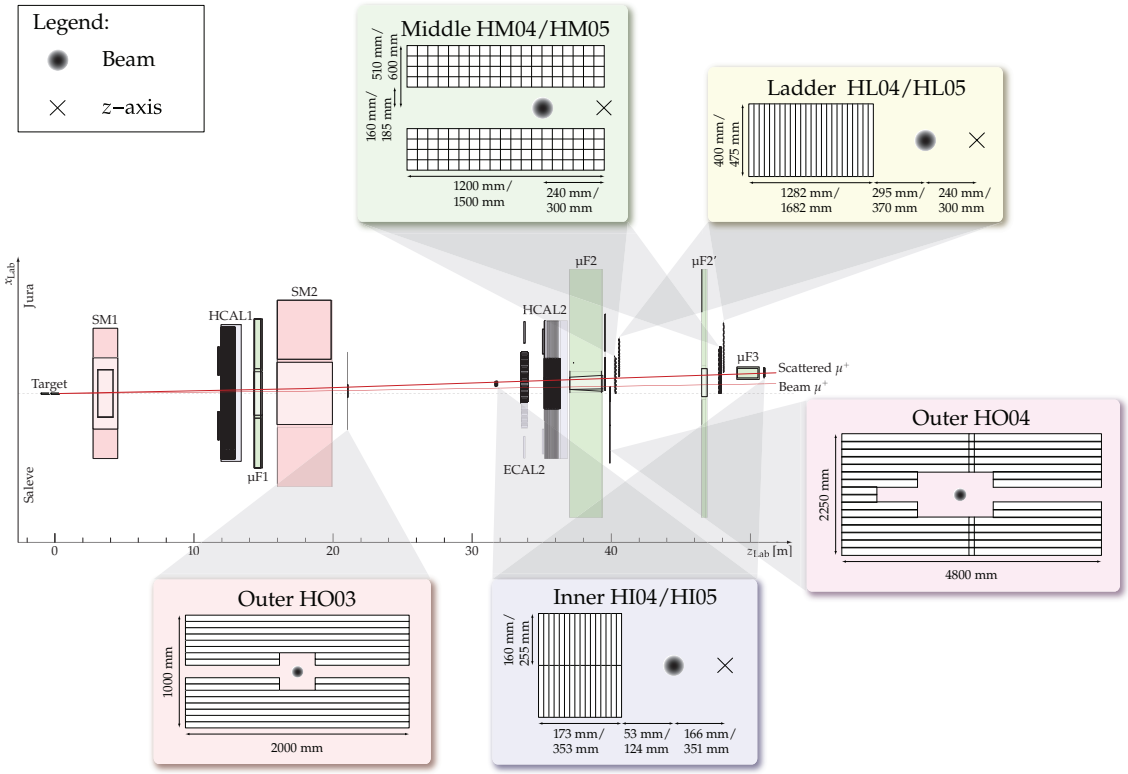

Figure 4.1: Top view of the trigger hodoscope setup: The vertically segmented "Inner" and "Ladder" hodoscope systems perform the energy loss trigger, the horizontal segments of the "Outer" hodoscopes are used for the geometrical DIS trigger. The "Middle" hodoscopes have vertical as well as horizontal segments and thus contribute to both triggers. Each subsystem consists of two planes. The "Inner" hodoscopes have the most fine grained structure, because they measure the smallest deflection angles. The boxes show geometry and dimensions of the different hodoscopes. (from [Leb02])

4.1 DIS Trigger – Target Back-Pointing

The hodoscope system of the DIS trigger selects events with a Q^2 between 0.5 and 50 $(\mathrm{GeV}/c)^2$ in the full y_B-range from 0 to 0.9. To distinguish between scattered and halo muons, the system singles out events in which the scattered muon has crossed the target. This geometrical trigger, that determines the position of the scattered muon in the target region, can be implemented in a straightforward way only in the y_{Lab}-direction perpendicular to the bending plane of the spectrometer magnets by requiring the coincidence of two horizontal hodoscope segments (see fig. 4.2).

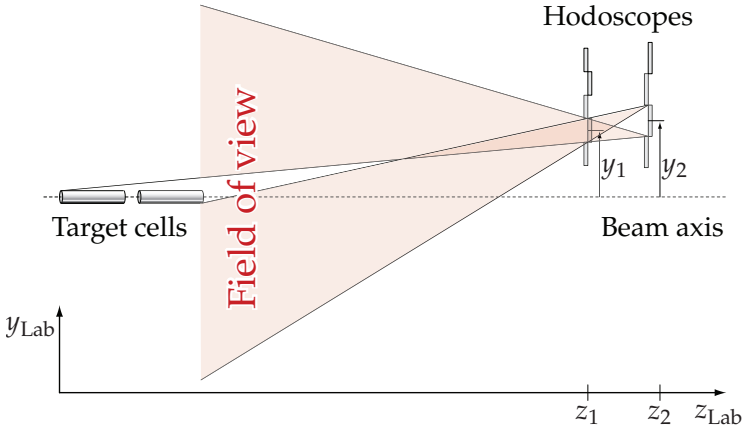

Figure 4.2: Selection of DIS events with geometrical trigger: By requiring the coincidence of pairs of horizontal hodoscope segments the origin of the scattered muons is constrained to the field of view which includes the target. (from [Leb02])

The field of view of the two hodoscope segments defines the volume, which the trigger cannot distinguish from the target. Its size is given by the size of the hodoscope slabs, which is limited by the multiple scattering caused by the absorbers, that the muons have to cross before they reach the hodoscopes.

Since COMPASS measures inclusive DIS events, no hadronic calorimeter information can be used to suppress the background. Instead a special veto system rejects muons, which cross the field of view of the DIS trigger but not the target (see section 4.4).

4.2 Quasi-real Photon Trigger – Energy Loss

The PGF trigger selects events with a certain minimum energy loss for muon scattering angles down to zero. The trigger determines the energy loss of the muon from its horizontal deflection in the magnetic field of the spectrometer magnets. Since the outgoing muon has an additional scattering angle θ, a single measurement of the horizontal distance x_{Lab} from the beam axis in the bending plane of the spectrometer is not sufficient. Therefore the x_{Lab}-measurements of two vertically segmented hodoscope planes positioned at z_1 and z_2 are combined, so that both the deflection angle α and the projection θ_x of the scattering angle into the bending plane can be determined. The two spectrometer magnets can be treated as one effective magnet with a field integral of $\int B_{\text{tot}}\,\mathrm{d}\ell = \int B_{\text{SM1}}\,\mathrm{d}\ell + \int B_{\text{SM2}}\,\mathrm{d}\ell$ situated at $z_M = (z_{\text{SM1}} \int B_{\text{SM1}}\,\mathrm{d}\ell + z_{\text{SM2}} \int B_{\text{SM2}}\,\mathrm{d}\ell) / \int B_{\text{tot}}\,\mathrm{d}\ell$. The bending of the scattered muon trajectory in the magnetic field equals to a momentum kick of $\Delta p_x \approx 0.3\,\text{GeV}/\text{Tm} \int B_{\text{tot}}\,\mathrm{d}\ell$ in the x_{Lab}-direction at the effective coordinate z_M.

From fig. 4.3 it is evident that

$$x_{1,2} = x_0 + (z_M - z_0)\tan\theta_x + (z_{1,2} - z_M)\tan(\theta_x + \alpha)$$
$$\text{with} \quad \tan(\theta_x + \alpha) = \frac{x_2 - x_1}{z_2 - z_1} \quad \text{and} \quad \sin\alpha = \frac{\Delta p_x}{p'} \tag{4.1}$$

where x_0 and z_0 are the coordinates of the primary interaction point, $x_{1,2}$ the coordinates of the scattered muon, measured by the two segmented hodoscope planes at $z_{1,2}$, and p' the momentum of the scattered muon.

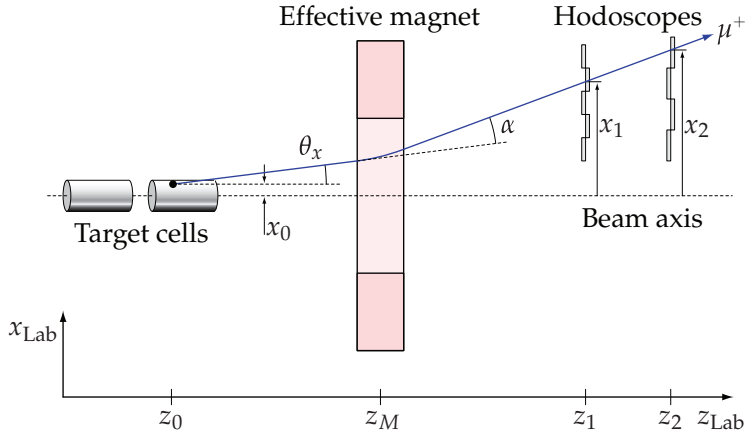

Figure 4.3: Determination of the scattered muon energy by measuring its deflection angle in the bending plane of the spectrometer with two vertically segmented hodoscope planes. To simplify the calculations the two spectrometer magnets are combined to one effective magnet at position z_M. (from [Leb02])

Applying the small angle approximation to eq. (4.1) and setting without loss of generality $z_0 = 0$ the momentum of the scattered muon is given by

$$\frac{1}{p'} = \frac{1}{\Delta p_x \, z_M}\left(x_0 + \frac{z_1 \, x_2 - z_2 \, x_1}{z_2 - z_1}\right) \tag{4.2}$$

For large beam muon momenta p the relative energy transfer y_B is in good approximation

$$y_B = \frac{p - p'}{p} \quad \text{with an error of} \quad \delta y_B = (1 - y_B)\sqrt{\left(\frac{\delta p'}{p'}\right)^2 + \left(\frac{\delta p}{p}\right)^2} \tag{4.3}$$

This means that, if the beam momentum p, the momentum kick Δp_x, and the coordinates $z_{1,2,M}$ and x_0 are known, the condition of a minimum energy transfer y_B can be translated into a coincidence condition for certain $x_{1,2}$ hodoscope segments.

The quasi-real photon trigger only looks at the energy loss. Consequently it cannot distinguish good events from background events like elastic muon-electron scattering, (quasi)elastic radiative scattering off target nucleons, or events where the beam muon already arrives with a lower energy. All three processes are strongly enhanced in the

low-y_B region. The large-y_B part of the background is rejected by using the fact, that no final state hadrons are associated with the background events (see section 4.3).

In order to suppress the low-y_B background the uncertainty of the energy transfer δy_B has to be as low as possible in the region of $y_B \approx 0.2$, so that the cut $y_B > 0.2$ is sufficiently sharp. According to eq. (4.3) this requires a good resolution of the measurement of the scattered muon momentum p'. The p' resolution is obtained from eq. (4.2) by Gaussian error propagation:

$$\frac{\delta p'}{p'} = \frac{p'}{\Delta p_x \, z_M} \sqrt{\delta x_0^2 + \left(\frac{z_2}{z_2 - z_1}\right)^2 \delta x_1^2 + \left(\frac{z_1}{z_2 - z_1}\right)^2 \delta x_2^2} \tag{4.4}$$

The coordinate x_0, the impact parameter of the beam muon at the target position, is unknown but limited by the target geometry and taken into account by the uncertainty δx_0, which by using the known size of the horizontal beam waist is estimated to $\delta x_0 \approx 8\,\text{mm}$. The uncertainty of the horizontal coordinates x_1 and x_2 is dominated by the dimensions of the vertical hodoscope segments, whereas the effect of multiple scattering of the outgoing muons in the muon filters is negligible for most of the hodoscopes planes. In order to optimize the p' resolution, the widths of the segments of the hodoscope planes are chosen to be proportional to the z_{Lab}-coordinate thus equalizing the contributions of the last two terms in eq. (4.4).

The quasi-real photon trigger system consists of several hodoscope subsystems with different dimensions, granularity and z_{Lab}-positions. Since the resolution of the energy transfer δy_B is proportional to $1 - y_B$ (cf. eq. (4.3)), the influence of the p' resolution is suppressed for larger y_B. This means that fine grained pairs of hodoscope planes with the second plane close to the muon filter are only required for the region $y_B \approx 0.2$ ("Inner" hodoscope system; cf. fig. 4.1). In total the y_B-uncertainty of the system is about 27 % in the region of $y_B \approx 0.2$.

4.3 Hadron Trigger – HCAL Energy Deposit

Using only the information about the energy loss y_B of the muon the hodoscope trigger cannot distinguish events, where the muon lost its energy in an interesting scattering process, from those, where the lower muon energy is due to other reasons. Most background processes have in common, that the outgoing muon looks like a scattered muon, but that no hadrons are produced. This means that by requiring an energy deposit in the hadronic calorimeters (see subsection 2.2.2), that is correlated with the hodoscope information, the background is suppressed and PGF events are enriched.

Hadrons create showers in the HCAL with a typical size in the order of the hadron's interaction length (several tens of centimeters), so that the energy deposit is spread over several HCAL cells, that form a cluster. The hadron energy is the sum of the amplitudes of all HCAL cells that belong to the cluster. Obtaining this cluster sum for the trigger

decision is non-trivial, because no tracking information for the charged hadrons is available and in addition the trigger must include neutral hadrons, so that the position of the cluster center is unknown at the trigger level. On the other hand to determine the full hadron energy by summing up cell amplitudes, the hadron must have hit the center of the summation region. The solution to this dilemma is the subdivision of the calorimeter into predefined blocks of several cells.

For COMPASS a summation of 4×4 HCAL blocks was chosen, because a hadron, hitting the center of such a block, will deposit at least 85 % of its energy. To make sure that a hadron always hits the central region of one of these predefined blocks, the subdivision of the calorimeter is repeated several times with a slightly shifted grid. In COMPASS four layers of summation blocks are used (see fig. 4.4 and [DvH]).

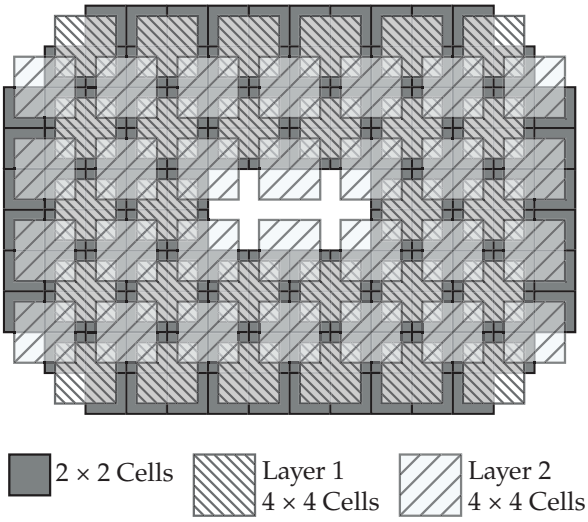

Figure 4.4: HCAL1 cluster summation in the hadronic trigger: To reduce the number of signals first the responses of 2×2 HCAL1 blocks are summed up. The resulting "sum-of-4" signals are combined to "sum-of-16" signals, which represent 4×4 blocks. This is done in four different ways to cover all possible combinations. Two of these summation layers are illustrated in the figure. (from [Ber05b])

The hadronic trigger fires, if one of the summation blocks is above threshold. The hadron threshold is determined by the muon energy deposit, because the flux of halo muons through the HCALs is not negligible. The threshold has to be set to a value, where the muon background is largely suppressed without lowering the HCAL efficiency too much.

Because of the required low trigger latency, the hadronic trigger cannot use the digitized information from the HCALs. Therefore a separate analog system for cluster summation, pulse height discrimination, and fast timing was built (see section 4.5).

4.4 Veto System

Due to its tertiary nature and the large penetration ability of the muons, the beam has a quite high emittance and a high flux of halo muons outside of the target, which under some conditions may cause unwanted triggers. The purity of the DIS trigger (see section 4.1) depends on the precision of the measurement of the muon position in the target, which is limited by the length of the target and the multiple scattering in the muon-filters, so that halo muons in the target vicinity can be mistaken as scattered muons thus causing unwanted triggers. In case of the quasi-real photon trigger halo muons contribute to the background, because the impact parameter x_0 of the incoming muon is unknown.

Both effects are suppressed by the veto system, which signals the presence of certain classes of halo muons and blocks the trigger through an anti-coincidence. The system is located upstream of the target with the hodoscopes V1 and V2 as the main components (see fig. 4.5). These two planes have a hole around the beam axis and limit the impact parameter for incoming muons to $\pm 2\,\mathrm{cm}$ and also their angle with respect to the beam axis to $\theta < 6.7\,\mathrm{mrad}$. Since the acceptance of the DIS trigger starts only at $4\,\mathrm{mrad}$, the scintillating fiber stations SF1 and SF2 are utilized to extend the veto down to $5.3\,\mathrm{mrad}$.

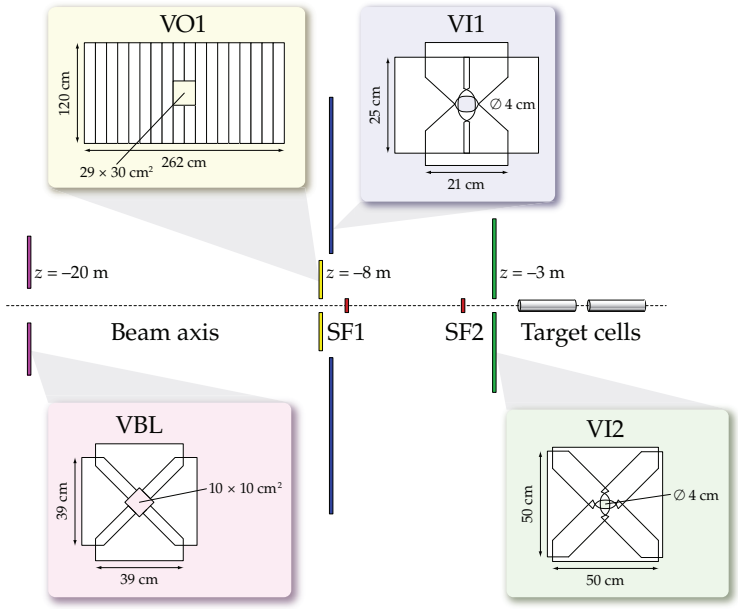

Figure 4.5: The veto system consists of three hodoscopes: two main hodoscopes V1 and V2 that are supplemented by V_{BL} further upstream. In the vicinity of the beam axis the fiber stations SF1 and SF2 provide additional veto information. The boxes show geometry and dimensions of the different hodoscopes. (from [Leb02])

The veto system reduces the trigger rate, but this advantage is bought at the expense of introducing dead-time. Under the assumption that the veto rate R_{veto} is approximately constant, the dead-time is given by the product of R_{veto} and the duration of the veto gate signal T_{veto}. R_{veto} is determined by the diameter of the hole, that the hodoscope

planes have around the beam axis. This diameter has a lower limit, because otherwise the veto rate would be too high. The minimum T_{veto} is limited by the time resolution of the veto *and* the trigger system. To minimize the dead-time, the hodoscopes of the veto system are segmented which allows to select individual time windows for the different elements. Smaller segments with better time resolution are placed in the region close to the beam axis, whereas in the outer region larger elements are used.

4.5 Trigger Hardware

The whole trigger system consists of approximately 1000 electronic channels, which are processed by the trigger electronics, which is built out of custom made VME based modules.

The signals from the photo-multipliers, that are used to readout the scintillators, are digitized by Constant Fraction Discriminator (CFD) [1] modules, developed by IPN Orsay. Each module has two CFDs plus a mean-timer, which is used for the hodoscope elements that are read out from both sides, to compensate the propagation time of the light in the scintillator depending on the point of impact of the muon. 32 discriminator modules sit on one discriminator board, that is able to process the signals of 32 scintillators, which are read out on both sides, or of 64 scintillators with single-sided readout, corresponding in both cases to a full hodoscope plane.

The digital information of the CFDs goes from the discriminator boards via flat cable to coincidence matrices, which perform the y_B-cut (quasi-real photon trigger) and the target pointing (DIS trigger). The coincidence matrix is implemented as a full custom ASIC with 32 input rows and columns and sits on a VME card, that forms the coincidences for a pair of hodoscope planes. Each of the 1024 possible coincidences between the input signals can be switched independently. The matrix patterns are computed from the known geometry of the hodoscopes and the cut condition. A minimum pulse width of 1.2 ns is required by the coincidence units. Accidental coincidences are suppressed by timing in all input channels via programmable delay and pulse shaping units, that sit at each of the 64 input channels on the matrix board. This way the time skew between the different input channels is lowered allowing to set a narrow coincidence window. The delay may be set in 32 steps over a range of 9 ns and is implemented using five inverter chains (2, 4, 8, 16, and 32 inverters in series).

The output of the coincidence matrices for the various pairs of hodoscope planes, the signals from the HCAL summation logic, and the veto signal enter then the last stage of coincidence, which finally forms the first level trigger signal, that serves as the input signal for the Trigger Control System.

[1] The CFD generates a logic signal, if the amplitude of its input signal reaches a certain fraction of the peak height. If the rise time of the signal is independent of its peak height the output of the CFD gives a walk-free timing signal [Leo94].

Chapter 5

Trigger Control System

5.1 System Architecture

The trigger control system connects the trigger logic (see chapter 4) with the data acquisition system (see chapter 3). The TCS fans out the trigger decision generated by the coincidence matrices, that are located in the counting room, to each of the 152 concentrator modules (see section 3.2) via a passive optical fiber network with a latency below 1.5 µs[1]. The same path is also used to distribute the precise 38.88 MHz TCS reference clock, that synchronizes all front-end electronics and serves as the time reference for the TDCs. In addition the fiber links transmit the TCS event labels and other control information. A special encoding scheme (see section 5.2) allows to send all this information over a single optical fiber, which greatly reduces cost and improves reliability.

Fig. 5.1 shows the architecture of the trigger control system, which consists of four main components: The central module of the system is the TCS controller (see section 5.3). It receives the trigger signal from the trigger logic, generates the corresponding TCS event labels, and sends both information over serial lines to the TTCex transmitter module, which generates the serial bit stream for the laser diodes that drives the passive fiber network (see section 5.2). The TCS event label consist of three numbers: the spill number in the current run[2], the event number in the spill, and the event type. The first two numbers together with the run number uniquely identify each event.

The optical fibers end at the TCS receiver cards (see section 5.4) that are connected to the back of each concentrator module. The receivers decode and deserialize the bit stream and recover the TCS clock. The trigger and clock signals are directly forwarded to the concentrator modules. The event labels are buffered and can be accessed by the concentrator modules through a well-defined interface.

[1] The trigger latency is dominated by the signal propagation time in the fiber.

[2] The term "run" denotes the time interval between the start and the stop of the data acquisition system or the data taken during that period, respectively. Runs are counted by the DATE run control, which increments the run number whenever the DAQ is started.

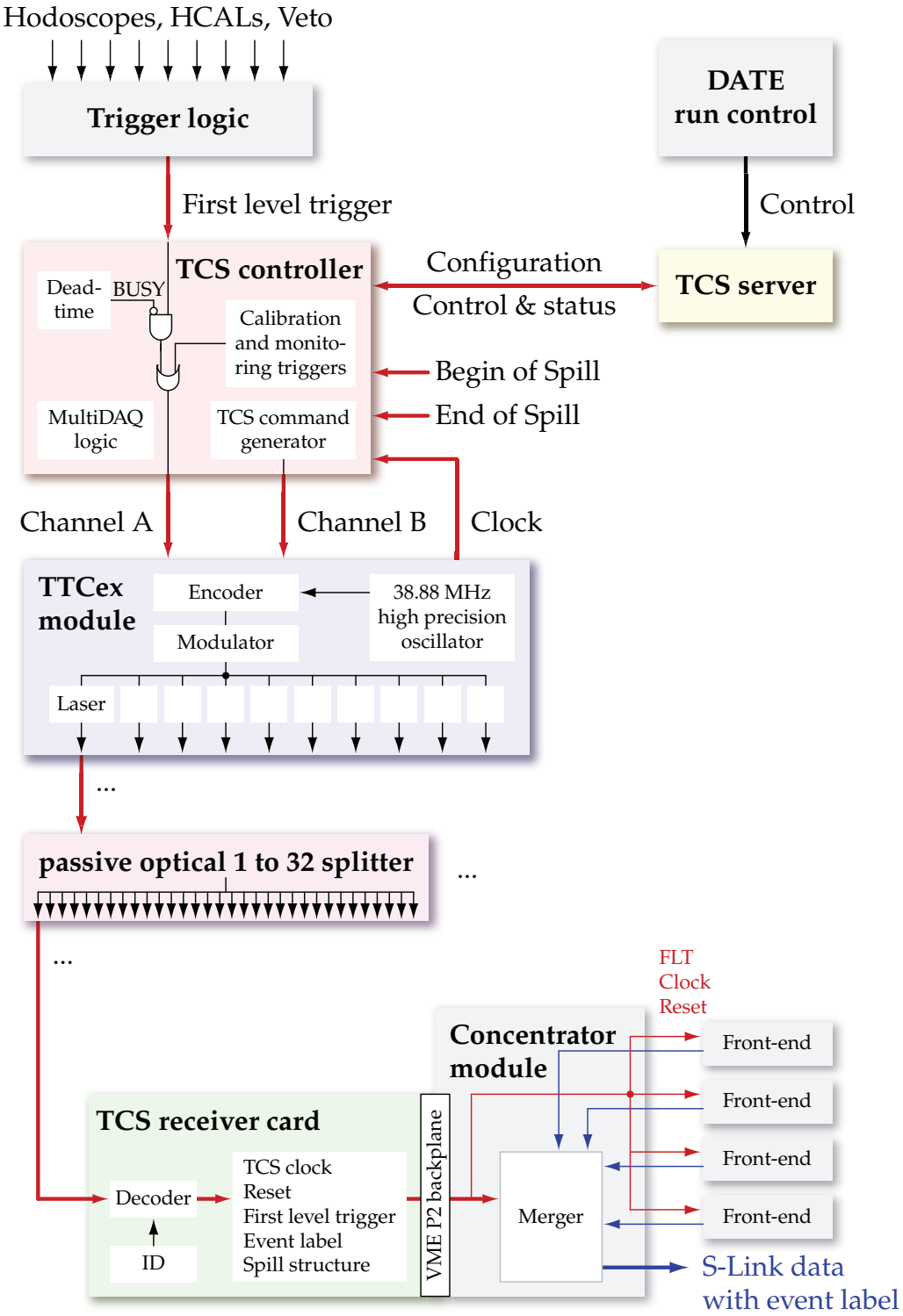

Figure 5.1: Architecture of the trigger control system.

The whole system is controlled and configured by the TCS server (see section 5.8), a software that interfaces the TCS controller via VMEbus and that also communicates with the DATE run control of the experiment.

In addition to the distribution of the trigger together with the associated event label the TCS offers several other functions and features: It broadcasts the Begin Of Spill (BOS) and End Of Spill (EOS) signals, which are used to synchronize the data acquisition with the SPS spill structure and it ensures, that the Begin Of a Run (BOR) and the End Of a Run (EOR) are always performed at the beginning of a spill. To synchronize the concentrator modules and the connected front-end electronics, in particular the TDCs, the TCS distributes a signal that allows to synchronously reset all readout electronics. The TCS controller also generates the readout dead-time by vetoing triggers, that cannot be accepted by part of the readout system (see section 5.6). For calibration and monitoring purposes the controller is able to produce artificial triggers, for which the TCS receivers can generate an optional pre-trigger pulse that precedes the trigger with a defined timing (see section 5.7). The receivers have an identification number, so that they may be accessed and configured individually. This way it is also possible to en/disable certain equipments in the data taking, which is a prerequisite for the partitioning of the data acquisition system into practically independent subsystems. This so-called MultiDAQ mode simplifies testing and debugging (see section 5.5).

The system presented here is the continuation of a former work [Gru01a]. The TCS controller hardware was replaced by a new and improved design providing much more FPGA and I/O resources, which were utilized to extend and advance the TCS functionality in particular concerning the MultiDAQ mode and the vetoing of the external trigger signals.

5.2 Optical Distribution Network and Signal Encoding

The TCS is a fan out system with one central data source, the TCS controller, from which the data are transmitted unidirectionally to all connected receivers. Since the controller is the only data source and as the TCS functions do not require a feedback channel, all TCS information is transmitted over a single optical fiber, which simplifies the system design. The optical signals from the TTCex transmitter are distributed to the connected TCS receivers by a simple and robust passive optical fiber network. Furthermore the receivers need to be equipped only with one opto-electronic receiver per card, which reduces cost and power consumption. The hardware for the optical distribution network as well as the encoding scheme, used for the signal transmission, are based on developments of the CERN RD12 collaboration for the Timing, Trigger, and Control (TTC) system of the LHC experiments [Tay02]

The TCS clock serves as a reference for all TDC measurements in the experiment. Therefore its jitter[3] must be well below the time resolution of the TDCs. In the high resolution

[3] In general the term "jitter" denominates the (in most cases unwanted) variation of one or more signal

mode the $\mathcal{F}1$ chip provides a digitization unit of 60 ps (see section 3.1), so that the design goal for the TCS was to achieve a clock jitter below 50 ps r.m.s.

The whole fiber network is driven by ten powerful synchronously operating laser diodes mounted on the TTCex transmitter module. The optical signals of the TTCex outputs may be fanned out further to up to 320 destinations, dispersed over the whole length of the spectrometer setup, using passive optical 1 to 32 splitters. The TTCex transmitter is equipped with laser diodes of a special type[4], that have a temperature-compensated bias and modulation current control [Tay]. A feedback loop stabilizes the optical output level against temperature changes and ageing effects.

The transmission of the reference clock, the trigger, and the event label together with other control information over a single fiber is implemented using Time-Division Multiplexing (TDM). In the two channel TDM employed here, two bit streams denoted as channel A and B are interleaved to one bit stream, which is encoded biphase mark at 155.520 Mbit/s. This is a rate of the standard Sonet OC-3 (CCITT SDH STM-1)[5]. The biphase mark encoding uses signal *transitions* instead of signal levels to transmit logical ones and zeros. A signal transition is interpreted as a '0', no transition as a '1'. To allow a precise recovery of the TCS clock on the TCS receivers, regular fixed signal transitions are inserted in-between the data transitions. At a rate of 155.520 Mbit/s four transitions occur during one TCS clock cycle of 25.72 ns: two fixed transitions, corresponding to the 38.88 MHz clock, and two data transitions, that allow to transport one out of four possible symbols (see fig. 5.2). The DC offset of the biphase mark encoded signal is well bounded, which reduces the jitter introduced by time walk.

Fig. 5.3 shows a schematic view of the encoder circuitry in the TTCex module. The central part is a phase locked loop that stabilizes the 38.88 MHz clock signal, generated by an on-board oscillator, and that ensures the low jitter of the TCS clock. The PLL utilizes a Voltage Controlled Oscillator (VCO), whose frequency is tuned by a DC signal. This phase error signal is generated by the loop filter out of a difference signal, that is provided by the phase detector which compares the phases of the external and the feedback clock. The phase error signal shifts the feedback frequency closer to that of the external oscillator. Because the feedback path divides the frequency of the VCO output by four, the VCO is running at 155.52 MHz. The inherent inertia of the closed loop feedback system levels out short-term fluctuations of the input clock thus resulting in a low jitter of

characteristics. Here the phase jitter, which describes the distribution of the clock phase, is the interesting parameter.

[4]Multi-sourced InGaAsP low-threshold multiple-quantum-well hermetic-package Fabry-Perot laser with a wavelength of 1280 to 1330 nm and a spectral width of 4 nm at -20 dBm.

[5]The Synchronous Optical NETwork (SONET) is a data transmission architecture, from which in 1988 the Comité Consultatif International Télégraphique et Téléphonique (CCITT, later renamed to International Telecommunications Union - Telecommunications Standardization Sector (ITU-TSS)) derived the Synchronous Digital Hierarchy (SDH) standard. SDH defines a transmission system, which can be used as a physical transport medium in networking applications. "Synchronous" means that all transitions of the digital signals occur exactly at the same rate and that all clock signals in the synchronous network are derived from one primary reference clock. The Optical Carrier level 3 (OC-3) and the Synchronous Transport Module level 1 (STM-1) are building blocks of the SDH describing the transport of data at a rate of 155.520 Mbit/s over an optical fiber.

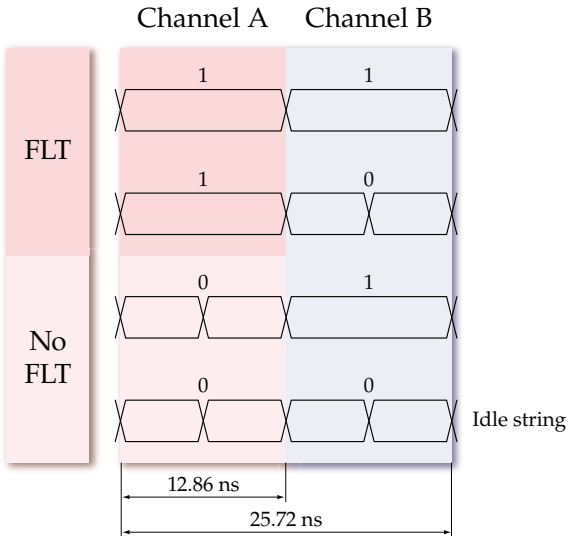

Figure 5.2: The four possible symbols, that can be transmitted during one TCS clock cycle using two-channel time division multiplexing with a biphase mark encoding. (from [Tay98])

the 38.88 MHz TCS clock output. This clock also switches the input multiplexer between the channels A and B generating a bit stream, that is latched with the 77.76 MHz clock generated inside the PLL. The encoder then utilizes both the 77.76 and the 155.52 MHz clock signal to convert the logical levels into signal transitions and to add the fixed clock transitions. The encoded bit stream goes via a driver to the laser modulator.

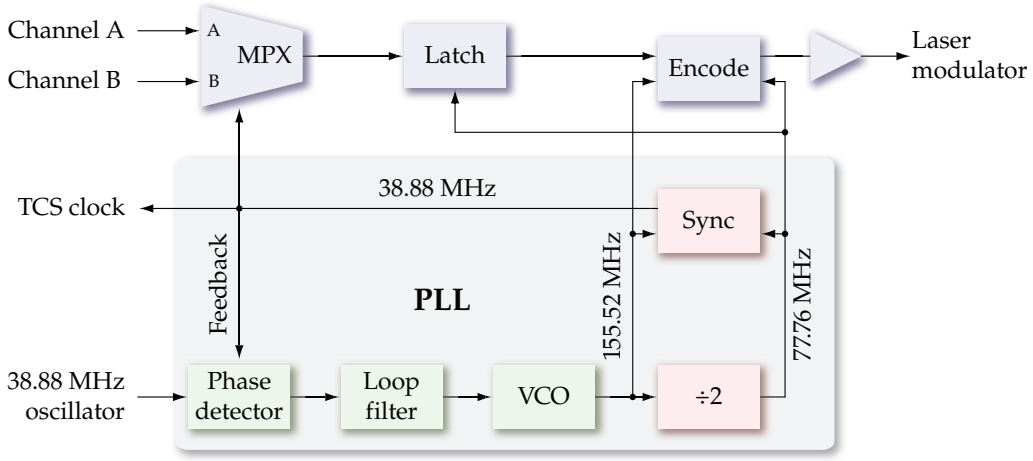

Figure 5.3: TTCex encoder circuitry. (from [TTC])

The two TDM data channels transmit different information: Channel A exclusively transports the first level trigger and delivers a one bit decision every 25.72 ns. This way the trigger latency is kept low and at a *constant* value, which is important for the latency compensation in the front-end electronics.

The triggers may arrive at any time during a TCS clock interval. The necessary synchronization of the trigger pulse to the TCS clock cycle introduces an uncertainty of the trigger time at the front-end stage of 25.72 ns. This is in particular relevant for the APV25 based readout of the GEM and silicon detectors, which by means of three consecutively sampled signal amplitudes reconstruct the time of the traversing particle [Ang05b]. The time reconstruction is performed during the offline analysis of the data (see subsection 7.1.2) and requires the knowledge of the trigger time within the TCS clock cycle. This so-called TCS phase is measured by dedicated TDCs.

All other TCS information are sent completely independently from the trigger via channel B. This way the event label information can be distributed asynchronously with respect to the trigger, which simplifies the communication, since the latency of the event labels is not required to be constant. The data transmission on the B channel is performed in terms of datagrams called "commands" (see fig. 5.4). The beginning of a command is indicated by a start bit, that synchronizes the data transfer, and is followed by the 20 bit long command itself. The datagram is trailed by a 6 bit ECC[6] checksum.

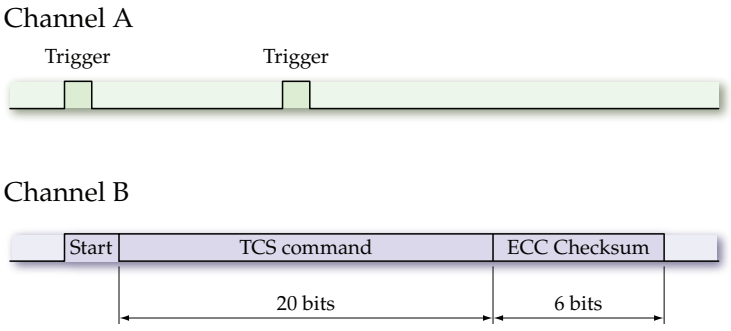

Figure 5.4: Data transferred via channel A and B. (from [Gru01a])

The TCS command set (see [Gru01a]) distinguishes broadcast commands, that are executed by all TCS receivers, and addressed commands, processed only by receivers with a certain ID and ignored by all others. Broadcasts are used to distribute the event label information and to synchronize the readout modules with the SPS spill structure. Addressed commands allow to configure the TCS receivers.

5.3 TCS Controller

The TCS controller is the central part of the trigger control system. The controller processes the SPS spill cycle signals as well as the first level trigger from the trigger logic and generates the channel A and B bit streams, that go through the TTCex transmitter module

[6] With an Error Correction Code (ECC) data are encoded in a way that the decoding stage is able to detect certain transmission errors. Here a simple Hamming code is utilized, which can be operated in two modes: either it *detects* all possible triple bit errors or it *corrects* all single bit and detects all double bit errors.

to the fiber network. Furthermore the module generates the readout dead-time by blocking the first level trigger and produces artificial triggers for calibration and monitoring purposes (see section 5.7). A VMEbus interface facilitates the communication with the TCS server, which initiates the starting and stopping of the system, configures the TCS, and reads back status information (see section 5.8). The controller runs synchronously to the TCS clock provided by the TTCex module. A schematic view of the module is shown in fig. 5.5.

In order to transmit the trigger through channel A, the FLT processor synchronizes the first level trigger pulses from the trigger logic to the 38.88 MHz TCS clock and vetoes the trigger with the internal BUSY signal (see fig. 5.6), that is generated by the dead-time logic (see section 5.6) and by other subcomponents. The FLT processor also counts the number of events in a spill and the number of spills in a run. At each beginning of a spill the event number is reset, so that the first event in a SPS cycle has always the number 1. At the same time the controller sends out a broadcast command, that resets the receivers, the concentrator modules, and the connected front-end electronics. This synchronizes the front-ends and ensures, that at the beginning of a spill the system is in a well-defined state, which makes the DAQ more robust: In case a non-lethal DAQ error (e.g. buffer overflow in a front-end) happens during a spill, the above reset scheme will recover the system at the beginning of the next spill, so that in the worst case only a fraction of the spill data are corrupt or lost. Likewise at each start of a run the spill number is reset to 1.

The spill and event numbers are read by the command generator, which generates all TCS commands in the controller. For each trigger a broadcast command is sent out containing the 20 bit event number and a 5 bit event type. The event type allows to tag physics events, various monitoring and calibration triggers, and special triggers, that mark the SPS spill structure in the data stream (see section 5.7). To distinguish events of different spills, the 11 bit wide spill number is broadcast to all receivers at the beginning of a spill together with the reset command. The TCS receivers use the event type plus the spill and event numbers to generate the event labels.

As mentioned in section 5.2, the data transmissions on channel B is done in form of TCS commands, which are either of the broadcast or addressed type. To prioritize the different commands the output interface is equipped with three FIFO buffers, each of them able to buffer up to 512 TCS commands, before they are serialized and transmitted via channel B. The commands from the command generator are so-called "fast" commands and have the highest priority. The second so-called "slow" command buffer is accessible via VMEbus. Whatever the TCS server writes into this FIFO, will be transmitted to the receivers. Slow commands have a lower priority and are sent out only when the fast command FIFO is empty. This way activities of the TCS server may not degrade the system performance. The third buffer, the configuration FIFO, is intended to buffer the addressed TCS commands, that configure the TCS receivers. Like the slow command FIFO it is filled by the TCS server, but the buffered commands are sent out by the controller only at well-defined moments (see section 5.8). This feature is required by the MultiDAQ mode: When a SubDAQ is started while others are already running, there is

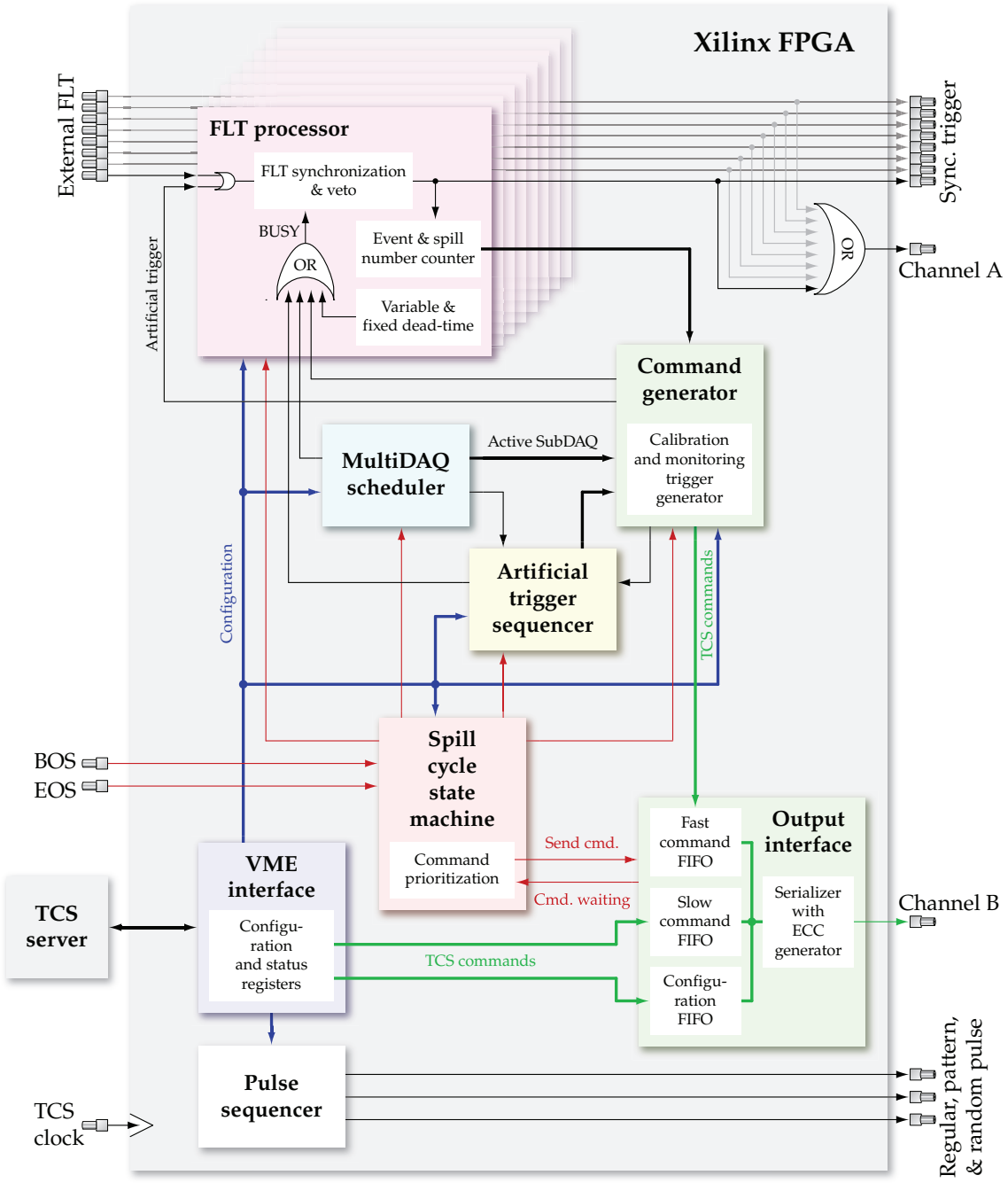

Figure 5.5: Schematic view of the TCS controller.

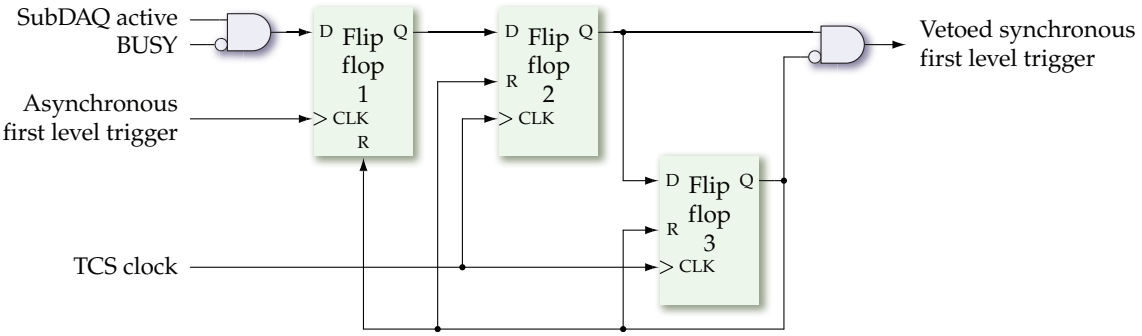

Figure 5.6: Trigger synchronization and veto logic: To avoid glitches, the FLT signal is not directly gated with a logical "and". Instead the veto is applied to the data input of flip-flop 1, which detects the rising edge of the trigger. The edge signal is then synchronized by flip-flop 2 to the TCS clock. The third flip-flop ensures a minimum dead-time of two TCS clock cycles. This period is needed by the dead-time generation logic to process the incoming trigger and to set the BUSY signal accordingly.

only a short time window at the beginning of each spill, during which the receivers may be configured such, that the system is again in a consistent state when the triggers arrive (see section 5.5).

All processes in the controller are synchronized to the SPS spill cycle by the spill structure state machine. This central component controls the command generation, the scheduling in the MultiDAQ mode (see section 5.5), and the generation of calibration and monitoring triggers (see section 5.7). It also defines, when slow commands may be sent out and at which point the configuration FIFO is emptied.

The TCS controller hardware, as shown in fig. 5.7, is a 6U high VME card with 16 LEMO inputs and outputs, that are all connected to a powerful Xilinx FPGA. Except for of the signals to and from the TTCex transmitter, which use the ECL[7] standard to be less sensitive to noise, all inputs and outputs follow the NIM[8] standard. The VMEbus interface is provided by a CPLD[9] chip, which is also able to configure the FPGA via VME. The module is quite versatile: It may not only be used as a TCS controller but, depending on the FPGA firmware that is loaded, it may also act as a programmable pre-scaler[10] [Kon05]. Furthermore tests were performed to implement an FPGA-based TDC [Kon05, Ang05a].

[7]The Emitter Coupled Logic (ECL) is a standard signal format for differential digital signals.

[8]The Nuclear Instrument Module (NIM) logic is a standard for fast digital signals, widely used in high energy physics.

[9]The Complex Programmable Logic Device (CPLD) is a reconfigurable logic device comparable to the FPGA, but with a different internal architecture, that utilizes so-called macro cells. The big advantage of the CPLD over to the FPGA is its non-volatile configuration memory, so that it does not have to be loaded after each power cycle.

[10]A pre-scaler is a device, that lowers the pulse rate of a signal by forwarding only every nth incoming pulse.

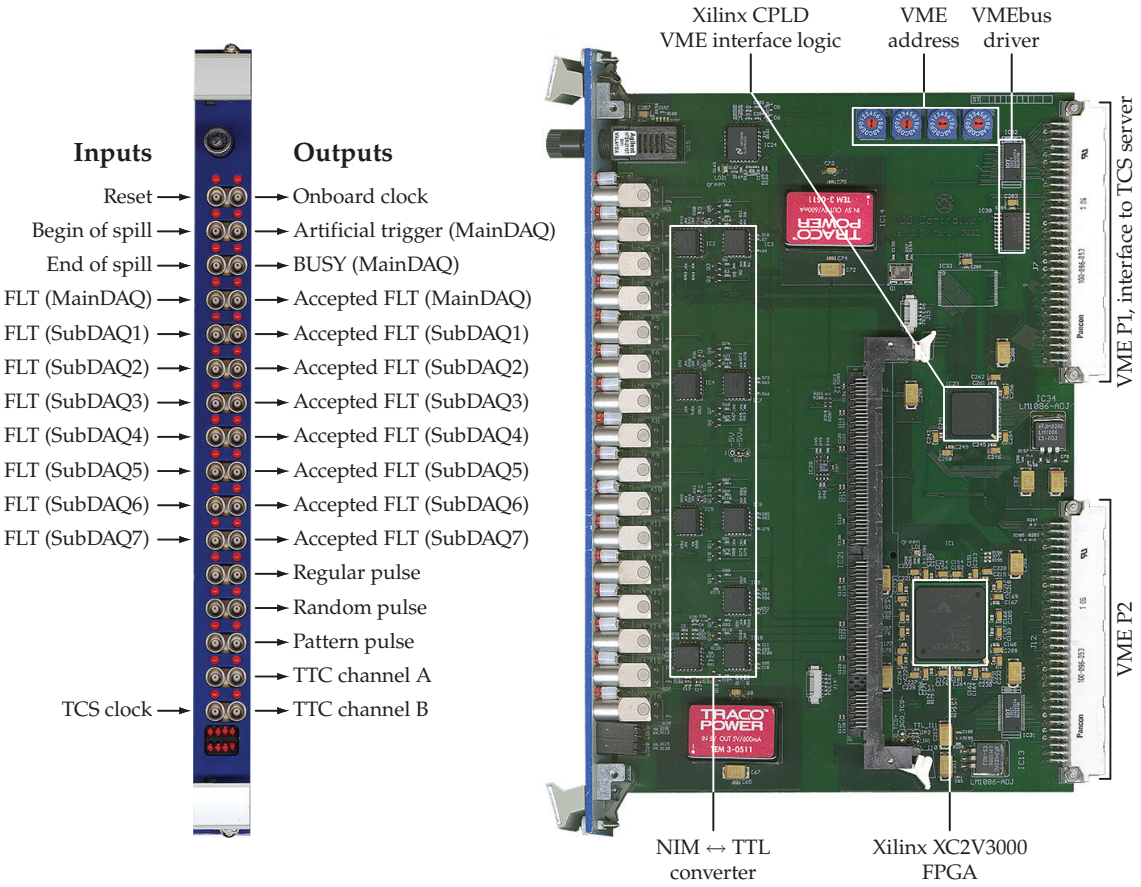

Figure 5.7: The TCS controller module.

If programmed with the TCS controller firmware, the module offers 12 inputs: Apart from the ones for the TCS clock and the SPS spill cycle signals, there are eight independent trigger inputs, which may be used in the MultiDAQ mode (see section 5.5), where the TCS partitions the readout system into definable disjoint subsets of concentrator modules, that form independent DAQ subsystems, so-called SubDAQs. The maximum eight SubDAQs are operated quasi-concurrently using time-sharing in which the TCS ensures that only the receivers of the particular SubDAQ react on the trigger pulses of the respective LEMO input.

On the output side all 16 LEMO jacks are assigned to signals: Two outputs bring out the channel A and B bit streams and are connected to the TTCex module. Each of the eight trigger inputs has a corresponding output, which provides either the vetoed and synchronized triggers or the artificial triggers. The former might be used to measure the TCS phase, that is the time difference of the synchronized trigger pulse to the first level trigger. For one SubDAQ, the so-called MainDAQ (see section 5.5), there are additional outputs for the artificial triggers, that are generated by the controller, and for the BUSY signal, which is used internally to veto the FLTs and which goes to a pre-scaler module.

For test and lab setups the controller is equipped with a simple pulse sequencer, which provides three different types of pulse sequences, that may be used instead of a real trigger source. Besides regular pulses with a configurable frequency in the range from 37.08 Hz to 38.88 MHz the controller may generate pulse patterns with configurable length. These patterns are read from a 32 bit$\times$512 RAM, which is accessible via the VME-bus. Each of the maximum 16384 bits defines the output signal for a time interval equivalent to the TCS clock period. The minimum period between two pulses is thus 25.72 ns, the largest possible time interval is 421.4 µs. The pseudo-random pulses may be used as a crude replacement for a random noise generator. The rate of these pulses may be reduced by setting a pre-scale factor, that orders the sequencer to send out two out of n pulses, where n may range from 2 to $2^{24} - 1$.

5.4 TCS Receiver

The TCS receiver processes the TDM biphase mark encoded data stream, sent by the TTCex module through the optical fiber network, and provides an interface to the concentrator modules CATCH and GeSiCA via the VME P2 backplane. Fig. 5.8 shows a schematic view of the TCS receiver.

In a first step the receiver recovers the clock from the 155.52 Mbit/s bit stream, that the opto-electronic receiver gets from the TTCex transmitter. This is performed by a clock recovery chip that is equipped with a PLL. The chip puts out a low jitter 155.52 MHz clock, from which the 38.88 MHz TCS clock is derived by fourfold downsampling performed in two steps. The TCS clock is used by the receiver itself and is forwarded to the readout modules, which fan out the clock signal to the front-end electronics. To keep the clock jitter as low as possible, the optical receiver and the clock recovery chip are powered

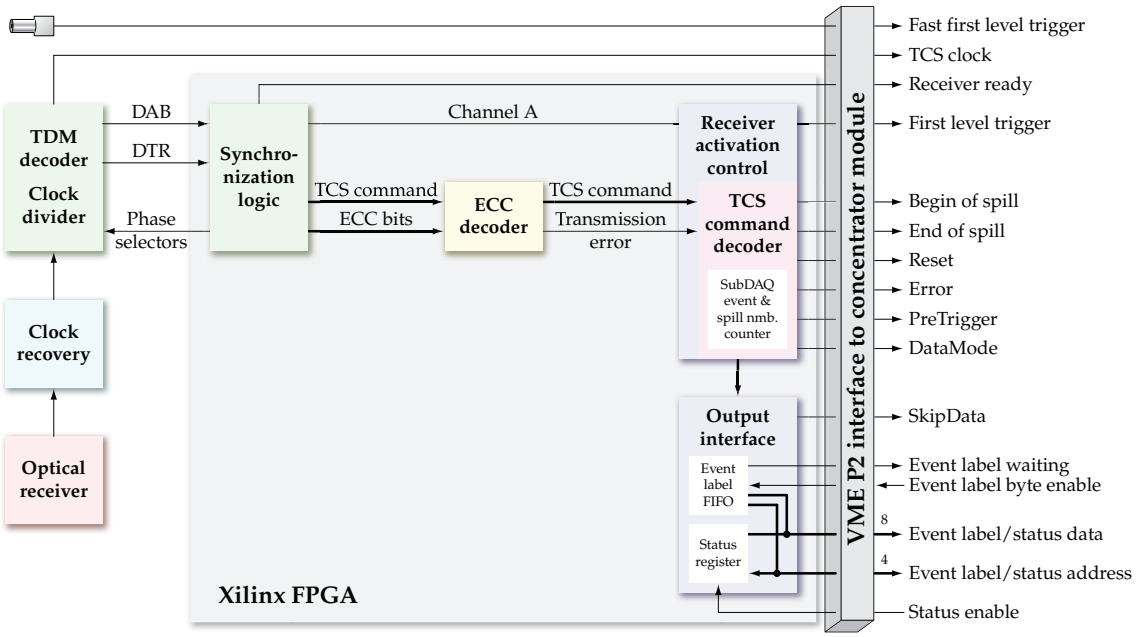

Figure 5.8: Schematic view of the TCS receiver.

separately through a DC-DC converter, which decouples them from the power supply of the rest of the board, thus reducing the noise on the power lines. The clock processing circuitry in addition uses differential signals to keep the low jitter level.

The clock recovery chip also performs the biphase mark decoding of the bit stream. In order to decode the 155.52 Mbit/s still TDM encoded bit stream, the clock downsampling circuitry is equipped with two cascaded multiplexers, that allow to switch the phase of the intermediate 77.76 MHz clock as well as that of the 38.88 MHz TCS clock. Fig. 5.9 shows how the TDM decoding is accomplished by picking up the wanted data bits with flip-flops, that are driven by the different clock phases.

The receiver synchronizes itself to the optical link on the channel level by identifying and decoding the two time division multiplexed channels A and B. The identification of the channels relies on the fact that the A channel transports only the first level trigger signal, whereas channel B transmits all the broadcast and addressed commands, so that there are much more '1's on channel B than on A. To make the channel identification possible even when the system is idle, the TCS controller in this case regularly generates so-called dummy commands, which just produce some traffic on the B channel, but are otherwise ignored by the receivers. The synchronization on the command level utilizes the start bit that precedes every command

When the receiver successfully has established the synchronization to the optical link, it forwards the triggers from channel A via the VME P2 connector to the concentrator module and executes the broadcast and addressed commands from the B channel. Due

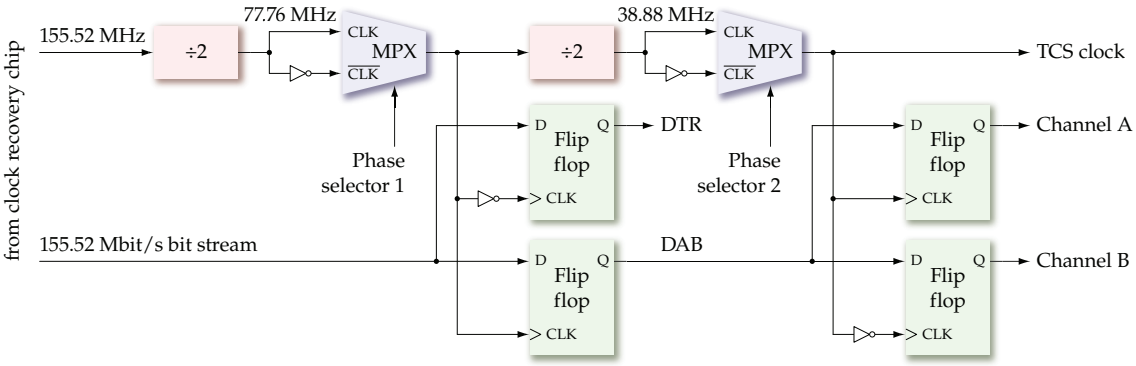

Figure 5.9: Decoding of the time division multiplexed bit stream in the TCS receiver: By choosing the phase of the 77.76 MHz clock correctly the DTR signal will always be zero, because it corresponds to the fixed clock transitions, which in the biphase mark encoding stand for '0'. The DAB signal then contains the information of the channels A and B which is recovered by choosing the phase of the TCS clock correctly.

to requirements introduced by the MultiDAQ mode (see section 5.5), the receiver has to be activated by a certain sequence of TCS commands before it is fully functional.

For each arriving trigger the receiver generates an event label consisting of six bytes (see table 5.1), which are buffered in a FIFO that is able to store up to five labels. A signal notifies the concentrator module when event labels are waiting in the FIFO. By asserting an "enable" signal the concentrator may request the label byte by byte where the byte number is indicated by four address lines.

	Bit assignment							
Byte No.	7	6	5	4	3	2	1	0
0x0	Spill # [2..0]				Event type [4..0]			
0x1	Spill # [10..3]							
0x2	Event # [7..0]							
0x3	Event # [15..8]							
0x4	0000				Event # [19..16]			
0x5	Error byte [7..0]							

Table 5.1: Byte format of the event label generated by the TCS receiver. The definition of the error byte is given in table 5.2.

The same address lines may be used in the opposite direction by the concentrator module to access status information like the error register, the TCS receiver ID, and configuration values which are summarized in table 5.3.

Bit No.	Description
0	Event label FIFO full
1	Event number overflow
2	—
3	ECC transmission error
4	—
5	—
6	TDM synchronization error
7	—

Table 5.2: Definition of the TCS error byte.

	Bit assignment							
Byte No.	7	6	5	4	3	2	1	0
0x0	Receiver ID [7..0]							
0x1	000			ECC mode	000			Enable
0x2	Error byte [7..0]							
0x3	DAQ mask [7..0]							
0x4	SkipData mask [7..0]							
0x5	SkipData mask [15..8]							
0x6	SkipData mask [23..16]							
0x7	SkipData mask [31..24]							
0x8	DataMode mask [7..0]							
0x9	DataMode mask [15..8]							
0xA	DataMode mask [23..16]							
0xB	DataMode mask [31..24]							
0xC	Coarse PreTrigger delay [7..0]							

Table 5.3: Read-only status registers in the TCS receiver: The enable bit indicates whether the receiver is in the "enabled" state (see section 5.5). The error byte is the same as in the event label. The DAQ mask shows to which of the eight SubDAQs the receiver is assigned. The SkipData and DataMode masks define the level of certain signals, that are associated with the various calibration and monitoring trigger types (see section 5.7). The last register contains the delay of the pre-trigger pulse which is used in the same context.

To distinguish different receivers, they are equipped with an 8 bit TCS receiver ID, which is defined by a DIL-switch on the card. Whenever the receiver decodes an addressed TCS command, it compares the receiver ID, specified in the command, with its own ID and executes the addressed command, if both IDs match, otherwise it is ignored.

The TCS receiver hardware, as shown in fig. 5.10, is a 3U VME card, which is plugged into the VME P2 backplane. Apart from the VME P2 connector and the optical receiver the card is equipped with two LEMO connectors: One brings out the TCS clock as a NIM signal, which may be used to synchronize external equipment. The other connector is an input for the so-called fast trigger signal and is directly connected to a pin of the VME P2 connector. The fast trigger signal brings the first level trigger pulse on a faster path to the readout module and is used by the readout electronics of the RICH detector, which requires a small trigger latency.

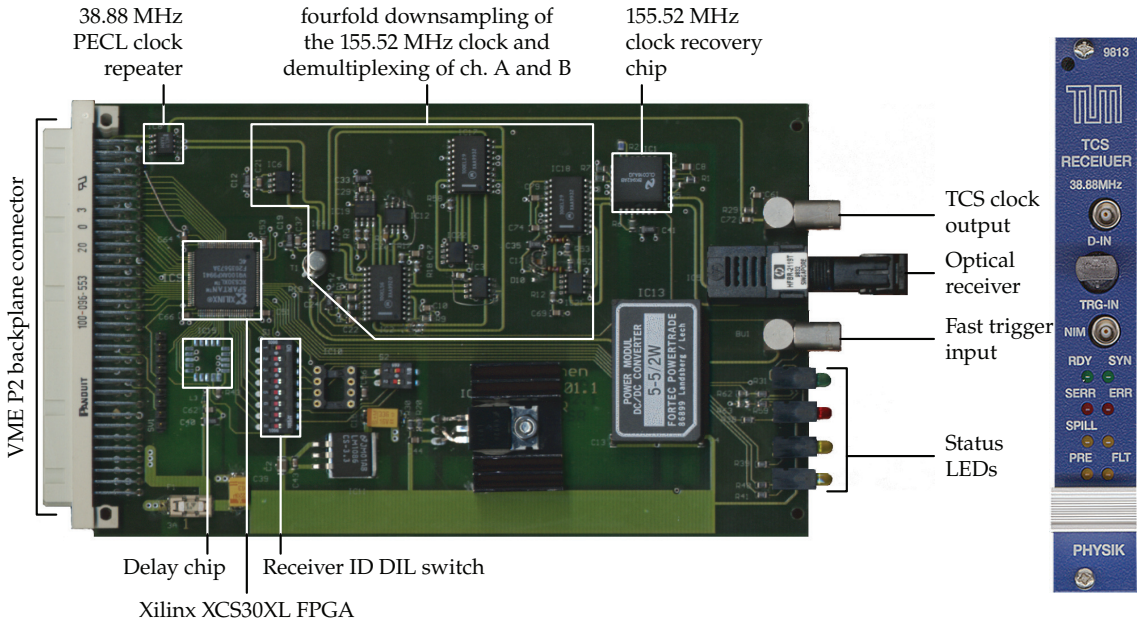

Figure 5.10: The TCS receiver card. (from [Gru01a])

For online calibration purposes the TCS system provides artificially generated calibration and monitoring triggers. In this context the receiver provides several signals which are described in detail in section 5.7.

5.5 MultiDAQ Mode

The MultiDAQ mode was implemented to simplify the testing and debugging of the data acquisition system or of (parts of) detectors. In this mode the whole DAQ system is partitioned into up to eight logically independent subsystems that do not interfere with

each other. These SubDAQs are operated quasi-concurrently by using a time-division scheme in which each SubDAQ is active for a configurable time interval, the so-called time slice, during which it allocates the TCS exclusively. The MultiDAQ scheduler in the TCS controller cycles through all running SubDAQs in ascending order granting them the configured time slice. This way it is ensured, that at each instant in time only one SubDAQ receives triggers. The eight time slices are set by the TCS server and may range from 25.72 ns to 26.97 ms in steps of 25.72 ns.

The various SubDAQs may be stopped and started without any restrictions. One may include/exclude SubDAQs into/from data taking while the other SubDAQs keep on running unaffected by this action. The starting and stopping of a particular SubDAQ is always performed at the beginning of a spill.

The SubDAQs share the TCS hardware resources, but are logically completely independent. Every SubDAQ has its own spill and event number counters and receives only the triggers from that TCS controller input, that is assigned to the particular SubDAQ (see section 5.3). The only exception to this are the first and last events in the run and in the cycle, respectively, plus the last event in the spill. These artificial events (see section 5.7) are generated at the beginning and at the end of the spill, respectively, and mark the SPS spill cycle in the data stream. They have to be received by *all* running SubDAQs, which causes some complications, since the same artificial event has different event numbers in the various SubDAQs. A similar problem arises for the broadcasting of the spill numbers of the different SubDAQs. There are two conceivable solutions to this: Either the controller generates multiple broadcasts, that contain the various event and spill numbers, respectively, or the event and spill numbers are counted locally in the TCS receivers. Here the second approach was implemented in a way that the spill and event numbers of one particular SubDAQ, the so-called MainDAQ, are still counted centrally in the TCS controller, whereas for all other seven SubDAQs these numbers are counted in the TCS receivers. This way the MainDAQ remains more fault tolerant, because there is only one source for the event header information.

The implementation of the MultiDAQ mode required additional logic in the TCS controller, that is able to freeze and save the state of certain subcomponents in the controller at the end of the time slice of the currently active SubDAQ. The state is then replaced by the saved state of that SubDAQ, that will be active during the forthcoming time slice. In addition the execution of the various TCS commands had to be made either interruptible or atomic depending on the priority of the performed action, so that the state of the controller as well as that of the receivers is well-defined before and after switching of the SubDAQ. To prevent that external first level triggers interfere with the switching of the SubDAQs, the triggers are blocked during the whole process. This extra dead-time can be minimized by choosing the largest possible time slices for the involved SubDAQs.

In the MultiDAQ mode the TCS receivers have to know to which SubDAQ they are assigned, which SubDAQs are running, and which one is currently active. Based on this information the receiver has to be either fully functional, when its SubDAQ is active, or has to ignore incoming triggers and certain TCS commands. To allow in addition the se-

lective (de)activation of certain equipments in data taking, the receiver features four activation levels: After power-up the receiver is in the "off" state in which the trigger output is blocked and in which it ignores all TCS commands other than "reset" and "switch on", which are generated by the TCS server. The "switch on" command lifts the receiver into the "enabled" state. By default the receiver is attached to no SubDAQ. When the receiver is "enabled", the TCS server may assign the receiver to a certain SubDAQ by an addressed command. The receiver then waits for a broadcast command from the controller, that announces which SubDAQs are running, and goes to the "running" state, if its own SubDAQ is in this set. In the "running" state the receiver decodes all TCS commands but still block its trigger output and ignores event label broadcasts. This restriction is lifted, when the controller announces the beginning of the time slice of the receiver's SubDAQ with a broadcast command, thus putting the receiver into the "active" state where it is fully functional. In order to avoid complicating things by introducing a special case, this activation procedure is performed also when only one SubDAQ is running.

5.6 Dead-time Generation

The lower limit for the readout dead-time is mainly defined by the RICH front-end electronics (see section 3.1): To prevent the noise, that is introduced by the output multiplexer of the GASSIPLEX chip, from affecting the detector signal a minimum dead-time of 5 µs after each event is required, during which the TCS controller has to veto the first level trigger. This so-called fixed dead-time after each trigger may be configured by the TCS server in steps of the TCS clock period in the range from 51.44 ns to 1685.6 µs, so that also test and calibration setups with high dead-time settings are supported.

Although most of the detector front-ends have a pipelined design and are thus dead-time free, they have different rate capabilities due to differently sized buffers. To ensure that these rate limits are not exceeded even at high trigger rates, the controller monitors the trigger rate and is able to generate a so-called variable dead-time, that is combined with the fixed dead-time by a logical "or". The maximum allowed trigger rate is defined by the number of first level triggers during a certain time interval. The number of triggers may range from 0 to 255 and the time window may be configured by the TCS server between 25.72 ns and 1685.6 µs in steps of the TCS clock period. If the number of allowed triggers is bigger than one, the minimum time between two triggers is determined by the fixed dead-time as defined above.

In the MultiDAQ mode (see section 5.5) the dead-times of all eight DAQs may be configured independently. This gives more flexibility and, for example, allows to test an equipment at low trigger share and high dead-time settings, while operating the rest of the system at nominal conditions, or vice versa perform high rate tests on parts of the apparatus.

In order to lower the readout induced dead-time, the MainDAQ is able to generate two independent variable dead-times, that are combined by a logical "or". This allows to

set one variable dead-time such, that the largest front-end buffers are fully used, while the second dead-time prevents the smaller buffers from overflowing. This way the rate capabilities of the different front-ends are exploited more efficiently.

Another type of dead-time is generated by the so-called throttling. This TCS feature is employed to ensure a stable operation of the DAQ system even at its limits. The throttling blocks part of the triggers at the beginning of a spill on a spill-by-spill basis to prevent the DAQ from aborting the run, due to buffer overflows in the ROB computers. To this end the DATE local data collector software, that runs on the readout buffer PCs, monitors the filling of the buffers. If on the spill-average there are more incoming data than the system is able to transfer to the event builders, the DATE run control lowers the amount of data for the next spill appropriately. Therefore it calculates the approximate on-spill time interval, that corresponds to the accumulated amount of excess data in the buffers, using the known mean trigger rate and event size. The TCS server is then ordered to write the calculated time interval into a dedicated VME register in the controller, which then vetoes the trigger at the beginning of the next spill. The time interval during which the triggers are blocked may be set in steps of 200 ms ranging from 0 to 51 s. The throttling is only active for exactly one spill and affects all SubDAQs. In case the buffers keep filling up, the readout control has to order the throttling repeatedly.

5.7 Special Event Types and Calibration and Monitoring Triggers

The 5 bit event type field, that is part of the event label generated for each first level trigger by the TCS controller, allows to distinguish up to 32 different types of events. The most important event type is the physics event. This tag is assigned to all events that are triggered by the external first level trigger logic. All other event types distinguish different artificial triggers generated by the TCS controller. The First and Last Event in the SPS Cycle (FEC and LEC), and in the Run (FER and LER) as well as the Last Event in the Spill (LES) mark the SPS spill structure in the data stream (see fig. 5.11). The other 26 event types may be used for calibration and monitoring purposes. Table 5.4 summarizes the various event types.

The calibration and monitoring triggers are intended to be used to sample detector data at a low rate under conditions, that allow a monitoring of the detector performance and/or calibration. A prime example is the monitoring of the photomultiplier calibration in the hadronic calorimeters by injecting a light pulse of known magnitude and reading the resulting PMT response.

The calibration and monitoring triggers may be either requested one-by-one by the TCS server via the VMEbus or may be generated more efficiently by the TCS controller itself. In the latter case the controller allows to define for each of the 26 calibration and monitoring trigger types an individual rate, with which this trigger type is generated

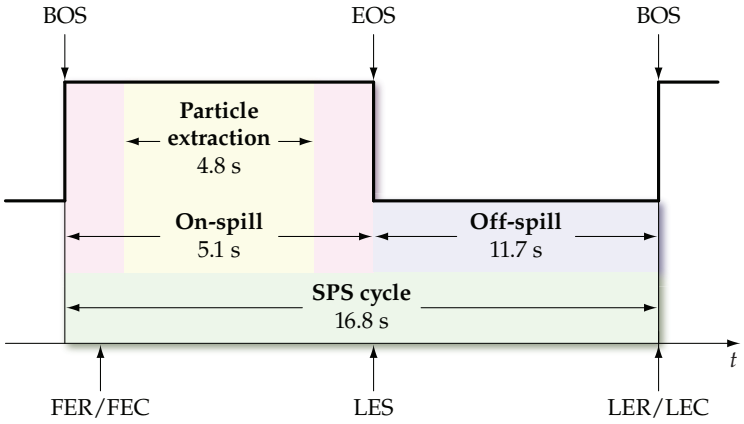

Figure 5.11: Tagging of the SPS spill structure by artificial events. (not to scale)

Event type	Description
0x00	Physics event
0x01	Calibration and monitoring event 1
⋮	⋮
0x1A	Calibration and monitoring event 26
0x1B	Last event in the spill
0x1C	First event in the run
0x1D	Last event in the run
0x1E	First event in the cycle
0x1F	Last event in the cycle

Table 5.4: TCS event types.

either only during the on- or off-spill time or continuously. The periods of the calibration and monitoring triggers may be set in a range from 3.371 ms to 863.0 ms in steps of 3.371 ms. The automatic generation of calibration and monitoring triggers by the controller covers the most common applications and avoids timing problems, that would occur in a software driven scenario especially concerning the MultiDAQ mode (see further below).

On the TCS receiver side the calibration and monitoring triggers are accompanied by three additional signals: PreTrigger, SkipData, and DataMode. The pre-trigger functionality may be illustrated by the HCAL example given above. The flash LED has to be triggered by a pulse *before* the calibration and monitoring trigger arrives and initiates the readout of the front-end electronics. This pulse is provided by the PreTrigger signal.

The TCS controller ensures a fixed timing between the pre-trigger and the trigger pulse: First the controller asserts the BUSY signal to prevent that FLTs interfere with the procedure. Then it transmits the calibration and monitoring trigger command, that announces the arrival of a certain trigger type to the TCS receivers. A fixed time interval of 6558.6 ns after the command was received by the receivers, the controller generates the artificial trigger. In the TCS receivers the TCS command from the controller initiates the generation of the pre-trigger pulse, which may be delayed by a configurable time period, so that the time interval between the pre-trigger and the subsequent artificial trigger may be set in a range from 0 to 6558.6 ns in steps of 25.72 ns. By equipping the receiver with an optional delay chip, the step size may be decreased by a factor of 256 to 100.5 ps.

When the receiver sets the SkipData bit, the connected concentrator module is ordered to discard the front-end data for the particular event and to only generate headers. This allows to record data only for those detectors, for which the calibration and monitoring trigger is useful thereby saving space on tape.

The DataMode signal may be used to switch the front-end for the calibration and monitoring trigger into a different readout mode. To measure, for example, the pedestals of the GEM or the silicon detectors so-called latch all data are needed where the zero suppression in the ADC cards is switch off.

For each TCS receiver ID the three signals described above may be dis/enabled independently for the 26 calibration and monitoring trigger types. Also the pre-trigger timing can be set individually for the different IDs, but is the same for all artificial trigger types.

Some difficulties arise from the MultiDAQ mode: The switching between the different SubDAQs is performed on the millisecond scale, so that it is nearly impossible to synchronize the TCS server software with the time slices of the various SubDAQs, which, however, would be necessary in order to request the calibration and monitoring triggers for the right SubDAQ. To circumvent this problem, the TCS controller takes care, that requests for calibration and monitoring triggers are executed at the correct moment thereby creating a little overhead, since the controller has to wait for the right SubDAQ to become active.

5.8 TCS Server – Control and Configuration of the TCS

The TCS server [Sch05] fulfills two functions: In the first place it controls and configures the whole trigger control system via the VMEbus interface of the TCS controller and secondly it provides a remote interface via standard local area network, so that other processes like the DATE run control are able to access TCS functions.

The TCS configuration is defined by a set of text files, that are read by the TCS server and have a simple syntax[11], where an option identifier is followed by one or more arguments. Table 5.5 lists all valid option strings and their meaning.

Option string		Argument(s)
`TCScontroler`		VME address of the TCS controller
`TCSconfig`		TCS controller configuration (defines register 0x24 in table A.1)
`TCSreset`		TCS reset broadcast command
`Timeslice`	[0-8]	Time slices of the eight SubDAQs in units of the TCS clock period
`DeadtimeF`	[0-8]	Fixed dead-time of the eight SubDAQs in units of the TCS clock period
`DeadtimeN`	[0-8]	Variable dead-time: number of triggers for the eight SubDAQs
`DeadtimeW`	[0-8]	Variable dead-time: time interval for the eight SubDAQs in units of the TCS clock period
`DeadtimeSN`		2nd variable dead-time of the MainDAQ: number of triggers
`DeadtimeSW`		2nd variable dead-time of the MainDAQ: time interval in units of the TCS clock period
`Receiver`nnn	[0-N]	List of $N-1$ addressed TCS commands for receivers with ID nnn
`Include`		Name of the configuration file to include

Table 5.5: Supported option strings in the TCS server configuration file: If an option requires more than one argument, the parameters are given as a zero terminated list whose length is defined by the numbers in the brackets.

The configuration files define both the configuration of the controller as well as that of the receivers. The controller is configurable by setting various registers, that are directly accessible by the TCS server through the VMEbus. A complete list of the controller registers can be found in appendix A. The TCS receivers are configured indirectly by writing a set of addressed TCS commands either into the slow command or into the configuration FIFO, where the latter is the standard procedure. While parsing the configuration files, the TCS server constructs an internal logical representation of the TCS in form of a data structure, that is utilized for error handling and to check the consistency of the configuration.

[11] The syntax is the same as for the configuration files of the COMPASS reconstruction software CORAL [COR].

The second task of the TCS server is to provide a network interface for other processes in the DAQ, so that they may access the TCS status information and may issue requests to be executed by the TCS server. The TCS server in particular executes the requests from the run control to start and stop SubDAQs. The communication interface is implemented in form of a network socket[12] with a simple character based command interface. The client process, which may be for example the run control or just a telnet client, opens a connection via a certain network port on the machine, that is running the TCS server and issues a single command character which is optionally followed by one or more parameters. The server executes the command, eventually sends back reply data, and closes the connection. Table 5.6 collects all the supported commands.

Command	Argument(s)	Description
I	—	(Re)configure the TCS
Z	—	Reset the TCS receivers and the connected front-end electronics
R	N	Start SubDAQ N
S	N	Stop SubDAQ N
P	—	Veto all external triggers
C	—	Remove the veto from all external triggers
L	Period	Order the controller to veto triggers at the beginning of the next spill (throttling)
T	N	Activate the artificial trigger sequencer with certain event type,
	event type	period, and mode on SubDAQ N
	period	
	mode	
B	—	Returns spill status: '1' = on-spill, '0' = off-spill
N	—	Returns spill number of the MainDAQ
?	—	Returns extensive status summary

Table 5.6: Socket based remote interface provided by the TCS server.

The two most important commands are "R" and "S" which order the TCS to start and stop a SubDAQ, respectively. The start command is issued by the DATE run control when the user has hit the start button. When the TCS server receives this command it first waits until the end of the SPS extraction by polling the spill status register of the TCS controller. During the 11.7 s long off-spill time the server writes a set of TCS commands into the configuration FIFO of the controller. This set contains TCS commands that reset the receivers and their connected front-end electronics. They are followed by commands that configure the particular receivers, assign them to the requested SubDAQ, and enable them. The SubDAQ is then started by setting its time slice to a non-zero value. From this point on the TCS controller takes over: It waits, until the start of the next SPS cycle is announced

[12] A socket is a software component that represents one end of a bi-directional communication link between two processes. Network sockets establish the inter-process communication utilizing the transport layer of standard network protocols like TCP, so that the two processes may run on different machines.

by the begin of spill signal and generates the last event in the cycle for the other running SubDAQs (see section 5.7). Then the controller sends out the TCS commands, buffered in the configuration FIFO, thus putting the TCS receivers into a defined state. Thereafter the controller resets all concentrator modules and front-end electronics with a broadcast command, before it broadcasts the new spill number. In the last step the artificial first event in the run is generated, the controller removes the veto from the FLT input, and waits for triggers.

When the user hits the stop button the run control sends the stop command to the TCS server, which waits until the end of the SPS extraction and sets the time slice of the requested SubDAQ to zero. The TCS controller waits for the next begin of the spill signal and generates the artificial last event in the run. Then it blocks all FLTs for this SubDAQ by setting the BUSY signal and sends a reset broadcast to all concentrator modules.

As was mentioned in section 5.5 the artificial events, that mark the beginning and the end of a spill/run in the data stream, require a special treatment, because they have to be received by *all* running SubDAQs, but the controller sends only one broadcast. Beside complications related to the counting of the event and spill numbers, this also concerns the event types, where again the MainDAQ is treated differently from the other SubDAQs. The start and stop procedures are performed as described above for the MainDAQ or in case only a single SubDAQ is started/stopped while all others are off. If one or more SubDAQs are running and another SubDAQ is started/stopped, the controller generates artificial FEC and LEC events instead of FER and LER. Vice versa running SubDAQs will receive FER/LER events instead of FEC/LEC, when the MainDAQ is started/stopped. This way the spill structure is always marked correctly in the MainDAQ.

5.9 TCS Performance and Summary

As the trigger control system is an essential part of the readout chain, the TCS was one of the first electronic components, that was installed in the experiment. Since the COMPASS commissioning run in the year 2000, the TCS was improved and extended in several stages and, although the core functionality of the system is quite simple, the feature extensions, that arose from the experience of running the system, added quite some complexity to the TCS, in particular on the controller side. This was the main reason why a new controller hardware was necessary to overcome the limitations of the old hardware.

Nevertheless the TCS proved to be one of the most reliable electronics components. All design goals were met: The trigger control system is able to handle trigger rates well above 100 kHz and the jitter between the recovered TCS clocks of two receivers was measured to 41 ps r.m.s. [Gru01a], well below the required 50 ps r.m.s.

Chapter 6

Transverse Hyperon Polarization

Hyperons are an ideal probe to measure polarization effects in high energy reactions. Due to the parity violation of their weak decay, the polarization of the hyperons is reflected in the angular distribution of their decay daughters. This eminent property of the hyperons, referred to as their *self-analyzing* weak decay, allows a direct extraction of their polarization from the asymmetry of the angular distribution of one of its daughter particles.

If the hyperon H is produced in an unpolarized inclusive reaction like $A\,B \longrightarrow H^{\uparrow}\,X$ and if the interaction in the production process is parity conserving, the hyperon can only be polarized parallel to the normal $\hat{n}$ of the production plane, spanned by the incoming beam particle and the outgoing hyperon $\hat{n} \propto \vec{p}_{\text{beam}} \times \vec{p}_H$. This is referred to as *transverse* polarization (see fig. 6.1).

The Λ for example is the lightest hyperon and has a non-leptonic decay mode into two charged particles $\Lambda \longrightarrow p\,\pi^-$ (see fig. 6.2a) with a branching ratio of 64 %. In the rest frame of the Λ with the z-axis along its spin direction ($J_\Lambda = 1/2,\ m_\Lambda = +1/2$) angular momentum conservation allows two waves to contribute to the decay amplitude [Per87]: a parity violating s-wave, where proton and pion have no relative angular momentum ℓ and where proton- and Λ-spin are parallel ($m_\Lambda = m_p = +1/2$), and a parity conserving p-wave, where proton and pion have a relative angular momentum of one unit ($\ell = 1$). The p-wave consists of two components: One with $m_\ell = +1$, where the spins of proton and Λ are anti-parallel ($m_\Lambda = -m_p = +1/2$), and another with $m_\ell = 0$, where the spins are parallel. Hence the total wave function is given by

$$\psi = \psi_s + \psi_p \quad \text{with} \quad \psi_s = A_s\, Y_0^0\, \chi^+ \quad \text{and} \quad \psi_p = A_p \left[\sqrt{\frac{2}{3}}\, Y_1^1\, \chi^- - \sqrt{\frac{1}{3}}\, Y_1^0\, \chi^+ \right] \tag{6.1}$$

where Y_l^m are the spherical harmonics, $A_{s,p}$ the complex amplitudes, and $\chi^{\pm}$ the spin wave functions of the two possible spin states of the decay proton with respect to the Λ spin.

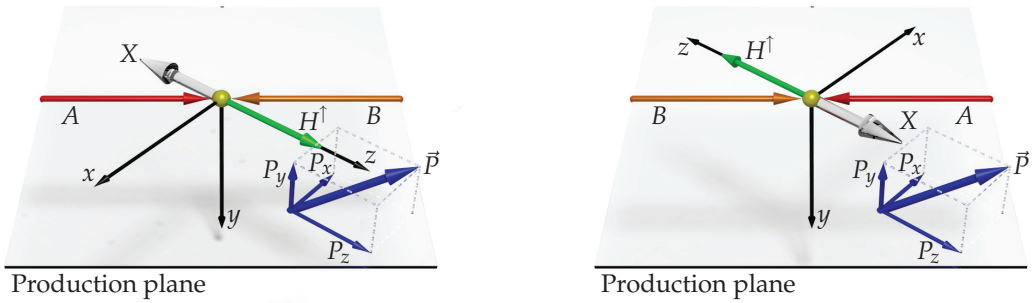

(a) **(b)**

Figure 6.1: (a) Production of a polarized hyperon in the unpolarized inclusive reaction $A\,B \longrightarrow H^\uparrow\,X$. The coordinate system is defined by the reaction and chosen such, that the y-axis is along the normal of the production plane and the z-axis along the hyperon direction. The polarization $\vec{P}$ of the hyperon is assumed to have an arbitrary orientation with components P_x, P_y, and P_z with respect to the coordinate axes. (b) The same process after the parity operator $\mathbb{P}$ was applied: It is evident, that, if the coordinate system is chosen in the same way as in (a), the x- and z-components of the polarization flip sign, whereas the y-component stays unchanged, because the production plane normal still points in the same direction. If the process is parity conserving, both P_x and P_z average to zero, so that the polarization is always transverse to the production plane.

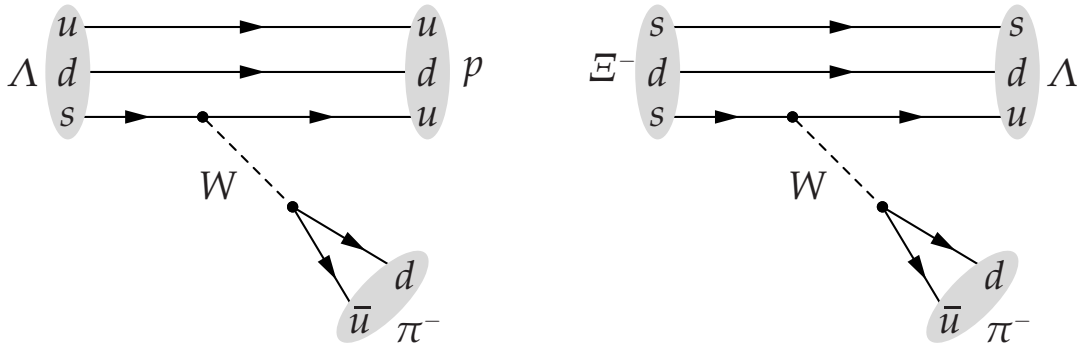

(a) **(b)**

Figure 6.2: (a) Decay of the Λ hyperon into proton and pion and (b) that of the Ξ^- hyperon into Λ and pion both via exchange of a W boson.

Eq. (6.1) together with the orthonormality of the spin wave functions and the definition of the spherical harmonics gives the angular distribution:

$$\frac{\mathrm{d}N}{\mathrm{d}\cos\theta} \propto \psi\psi^* = \frac{1}{4\pi}\left[|A_s|^2 + |A_p|^2 - (A_s^* A_p + A_s A_p^*)\cos\theta\right] \tag{6.2}$$

where θ is the polar angle of the proton with respect to the quantization axis in the hyperon's rest frame. Without loss of generality one of the complex phases can be chosen to be real: $A_s \in \mathbb{R}$. This simplifies the interference term in eq. (6.2) and gives

$$\frac{\mathrm{d}N}{\mathrm{d}\cos\theta} \propto (1 + \alpha\cos\theta) \quad \text{with} \quad \alpha \equiv -\frac{2A_s\,\Re(A_p)}{|A_s|^2 + |A_p|^2} \tag{6.3}$$

The interference of the *s*- and *p*-waves, which due to parity violation are both allowed in the weak decay, causes the decay baryon to be preferentially emitted either along or opposite to the spin direction of the hyperon, depending on the sign of α. α is the so-called decay asymmetry parameter and describes the details of the weak decay process. In order to have a non-vanishing asymmetry parameter, both amplitudes A_s and A_p have to be non-zero. Table 6.1 summarizes the decay asymmetry parameters of some hyperon decays.

Hyperon	Decay channel	Branching ratio	Asymmetry parameter α
Λ	$p\,\pi^-$	63.9±0.5 %	0.642±0.013
Λ	$n\,\pi^0$	35.8±0.5 %	0.65±0.05
Σ^+	$p\,\pi^0$	51.57±0.30 %	$-0.980\pm^{0.017}_{0.015}$
Σ^+	$n\,\pi^+$	48.31±0.30 %	0.068±0.013
Σ^-	$n\,\pi^-$	99.848±0.005 %	−0.068±0.008
Ξ^0	$\Lambda\,\pi^0$	99.522±0.032 %	−0.411±0.022
Ξ^-	$\Lambda\,\pi^-$	99.887±0.035 %	−0.458±0.012
Ω^-	$\Lambda\,K^-$	67.8±0.7 %	−0.026±0.023
Ω^-	$\Xi^0\,\pi^-$	23.6±0.7 %	0.09±0.14

Table 6.1: Decay asymmetry parameters of some hyperon decay channels: Due to the convention to use the angular distribution of the decay baryon to determine the polarization, the asymmetry parameter of the respective charge-conjugated decay has the opposite sign, assuming $\mathbb{CPT}$-invariance. (from [PDG04])

Eq. (6.3) describes the angular distribution in a frame, where the axis, with respect to which the angle θ is defined, was chosen to be always along the spin of the hyperon. In a measurement such a frame is not possible to realize, instead an analyzer direction $\hat{n}$ is chosen, along which the polarization P is measured. For a spin-1/2 particle the polarization is defined as

$$P \equiv \langle \vec{\sigma} \cdot \hat{n} \rangle = \frac{N^\uparrow - N^\downarrow}{N^\uparrow + N^\downarrow} \tag{6.4}$$

where $\vec{\sigma}$ is the spin operator and $N^{\uparrow(\downarrow)}$ the number of particles with spin along (opposite) to the quantization axis. In this analysis the production plane normal is used as the analyzer to measure the transverse hyperon polarization P_T^H. Redefining the angle θ to be taken with respect to the production plane normal $\hat{n}$ gives the measurable angular distribution, that now includes the transverse polarization:

$$\frac{\mathrm{d}N}{\mathrm{d}\cos\theta} = \frac{N_0}{2}\left(1 + \alpha_H P_T^H \cos\theta\right) \tag{6.5}$$

Due to the self-analyzing weak decay, a possible transverse polarization of the hyperon manifests itself as an up-down asymmetry of the distribution of the daughter particles with respect to the production plane.

The production of polarized hyperons via a certain production channel can be described in terms of spin-flip and spin-non-flip forward amplitudes A_F and A_N [Sof99]. According to the generalized optical theorem the polarization is given by

$$P_T^H = \frac{\Im(A_N A_F^*)}{|A_N|^2 + |A_F|^2} \tag{6.6}$$

Hence a polarization different from zero requires both amplitudes to be non-vanishing and to have moreover a non-zero phase difference. At high energies, however, a large number of possible reaction channels contribute to the production cross section with comparable magnitudes and various relative phases. Therefore the polarization in inclusive high energy processes is expected to be small, since in the weighted mean over all contributing channels the relative phases interfere randomly.

Moreover pQCD calculations [Kan78] show, that the quark helicity flip amplitudes vanish at high energies, mainly because for massless quarks the QCD Lagrangian is chiral invariant, so that the quark helicities are conserved in hard interactions.

The following two sections will first shortly summarize the experimental results on hyperon polarization, gathered so far, and then introduce two of the models, that are proposed to explain the data.

6.1 Hyperon Polarization Data – A brief Overview

The story of hyperon polarization in high energy reactions started over 30 years ago at Fermilab where Λ hyperons, produced by a 300 GeV/c proton beam in the unpolarized inclusive reaction $p\,\mathrm{Be} \longrightarrow \Lambda\, X$, were found to have a sizeable polarization opposite to the normal of the production plane [Bun76]. Considering the arguments given in the previous section, this discovery came as a surprise. It was the first indication, that the spin seems to be an important factor in high energy hadronic reactions.

The finding of the transverse Λ polarization initiated a systematic and detailed study of polarization effects in hyperon production. From numerous experiments, which covered a wide kinematical range and used a large variety of beams and targets, both unpolarized, one knows, that most hyperons are produced polarized along the normal of the production plane. At present measurements of the hyperon polarization contribute the largest data set on spin effects in high energy hadronic reactions. In the following a short overview of the experimental results is given. More detailed information can be found in [Pan90, Lac92, Hel96, Bra98b].

The bulk of data on hyperon and anti-hyperon polarization was collected in proton-beam experiments, where it was found, that the various hyperons show a similar behavior: The absolute value of the hyperon polarization rises approximately linearly with the transverse momentum p_T of the hyperon, starting at zero for $p_T = 0$ GeV/c, as required by rotational symmetry, and reaching a plateau at $p_T \approx 1$ GeV/c. Up to the highest measured transverse momenta of $p_T \approx 3.5$ GeV/c no drop of the polarization, as expected by pQCD, was seen. In the plateau region the polarization rises almost linearly with the Feynman variable[1] x_F of the hyperon. The polarization is virtually independent of the beam energy and shows only a weak dependence on the atomic mass number A of the target.

In particular the polarization of the Λ hyperon was studied in great detail in the current fragmentation region by proton-beam experiments at Fermilab [Bun76, Hel78, Lun89, Ram94] and at CERN [Erh79, Smi87, Fan99], which measured a *negative* polarization, that is opposite to the production plane normal. Other proton beam experiments showed, that nearly all hyperons are produced polarized with a comparable magnitude of the polarization of about 20 % at large x_F in the plateau region, where $p_T > 1$ GeV/c: $P_T^{\Lambda} \approx P_T^{\Xi^-}$ [Ram86, Dur91] $\approx P_T^{\Xi^0}$ [Hel83] $\approx -P_T^{\Sigma^0}$ [Duk87] $\approx -P_T^{\Sigma^+}$ [Wil87] $\approx -P_T^{\Sigma^-}$ [Wah85] (cf. also fig. 6.3a). The only exception is the Ω^- with $P_T^{\Omega^-} \approx 0$ [Luk93]. For the anti-hyperons the picture is less clear: Whereas the $\overline{\Lambda}$ is produced unpolarized [Hel78, Lun89, Ram94, Bra98a, Fan99], $\overline{\Sigma}^-$ and $\overline{\Xi}^+$ exhibit a polarization with the same sign as the respective hyperons: $P_T^{\overline{\Sigma}^-} \approx 10$ % [Mor93] and $P_T^{\overline{\Xi}^+} \approx -10$ % [Ho91] (see fig. 6.3b).

$\overline{\Lambda}$s produced by anti-protons [Gou86] as well as Λs produced by a neutron beam [Ale00] show a similar behavior like Λs from proton induced reactions. The same is true for the exclusive diffractive process $p\,p \longrightarrow p\,(\Lambda\,K^+)$, except that the Λ exhibits a remarkably strong negative polarization below -60 % [Hen92].

The behavior of the hyperon polarization changes, if the strange quark content of the outgoing hyperon is not produced from the sea, like in proton induced reactions, but

[1] The Feynman variable x_F is the fraction of the incident beam momentum $p_{z,\max}$ carried by the hyperon in the beam direction $x_F \equiv p_z / p_{z,\max}$. x_F is not Lorentz-invariant and usually defined in the center-of-mass system of beam and target. In this system x_F is given by $x_F \approx 2p_{z,\mathrm{cm}}/\sqrt{s}$, where $\sqrt{s}$ is the center-of-mass energy. x_F may range from -1 to 1, where positive values mean that the hyperon goes into the forward hemisphere and thus probably stems from the beam particle. Therefore this kinematical domain is called current or beam fragmentation region. In a similar way negative x_F indicate, that the hyperon production is dominated by the target and is thus called target fragmentation region.

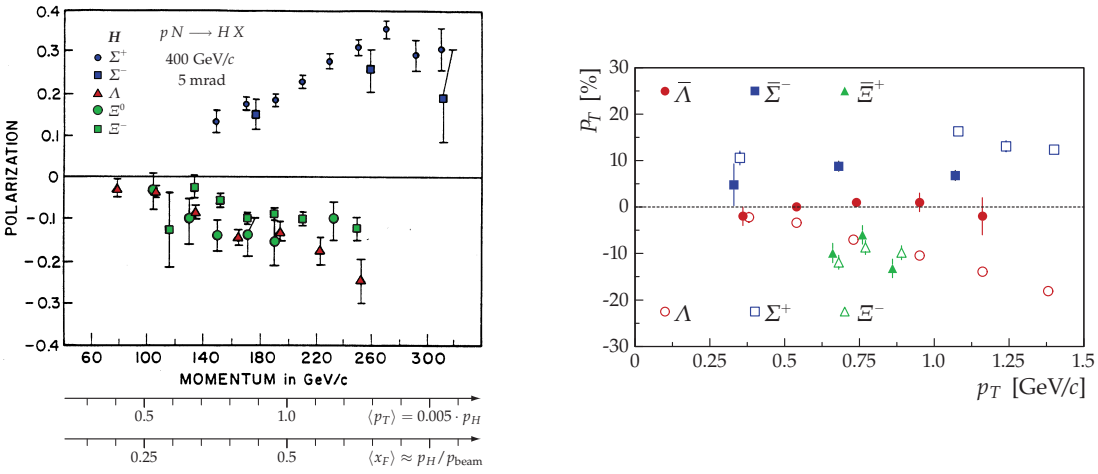

Figure 6.3: Polarization of various hyperons and anti-hyperons measured in proton induced inclusive reactions: (a) Polarization of hyperons from a 400 GeV/c proton beam as a function of their momentum, which, due to the fixed scattering angle, is proportional to their transverse momentum p_T as well as to their longitudinal momentum fraction x_F. (b) Polarization of anti-hyperons in dependence of p_T. For comparison the hyperon polarizations measured by the same experiments are shown as well. (from [Bra98b])

is instead brought in by the beam particle: Λs produced by a K^- beam show a sizeable *positive* polarization in the current fragmentation region, opposite to the one observed in proton data [Gou86, Chu75, Abr76]. $\overline{\Lambda}$s from a K^+ beam [Aji83] behave similarly. The same phenomenon was observed for Λs from a Σ^- beam, where in addition a first possible hint for the breakdown of the polarization at large p_T was seen [Ada04a]. Whereas Ξ^- hyperons from proton beams have a sizeable negative polarization, they were found to be unpolarized, if produced by a beam consisting mainly of n, Λ, and Ξ^0 [Woo96]. In the same beam the Ω^- showed a small positive polarization. If produced by a Σ^- beam, the Ξ^- polarization on the other hand exhibits a behavior very similar to that of the proton data [Ada04b], whereas Ξ^-s produced by K^-s have a large positive polarization [Ben85].

Λs from pion beams exhibit a small negative polarization [Ben83] and $\overline{\Lambda}$s [Bar94] are produced unpolarized.

Two older experiments [Ast82, Abe84] studied the Λ and $\overline{\Lambda}$ polarizations in photoproduction with photon energies between 20 and 70 GeV. Both experiments are limited by statistics and measured polarizations compatible with zero. Nevertheless they seem to indicate a small *positive* Λ polarization. This was confirmed by a HERMES measurement [Brü02, Gre02, Bel01] in quasi-real photo-production, which resulted an average Λ polarization of $+5.5\%$ and an $\overline{\Lambda}$ polarization of -4.3 % (see also subsection 8.4.1).

6.2 Theoretical Models

The previous section showed that the transverse polarization of hyperons is a complex phenomenon. Within the current framework of perturbative QCD the polarization cannot be calculated from first principles, because the hyperon production in proton induced reactions in the current fragmentation region at small transverse momenta is a soft process. A number of models try to explain the experimental data using different polarization mechanisms: [Hel78] proposes that polarized $s\bar{s}$ pairs are created by polarized gluon bremsstrahlung. In [And83] the $s\bar{s}$ pairs originate from the breaking of a stretched color flux tube. Since the s quark has a transverse momentum the $s\bar{s}$ pair has to have angular momentum, which is balanced by the quark spins. In analogy to multiple Coulomb scattering [Szw81] considers the polarization of massive s quarks by multiple scattering in quark-gluon matter. [DeG81a] developed a model that explains the polarization with the Thomas precession of the participating quark spins.

Beside these semi-classical models there are also some, that are based on Regge theory. In the triple-Regge model [Bar92] the Λ production is described by three processes: direct production, intermediate baryon dissociation via Σ and Σ^*, and electromagnetic decay of Σ^0. The one pion exchange model [Sof92] is based on the dominance of the pion exchange in hadronic amplitudes and reduces the Λ production to the reaction $\pi\, p \longrightarrow K\, \Lambda$ with reggeized off-shell pions.

None of the proposed theoretical models is able to describe all observed polarization phenomena in a consistent way. Up to now the details of the mechanism, that creates the polarization, are not understood. A more in-depth discussion of the proposed models and the current theoretical developments is given in [Sof99, Fel99].

The following subsection 6.2.1 introduces the recombination model by DeGrand and Miettinen as a typical example for a semi-classical model. Notwithstanding its simplicity, it is able to predict at least on a qualitative level many observed hyperon polarizations. Subsection 6.2.2 presents a recent phenomenological approach to describe the Λ polarization in deeply inelastic scattering by applying pQCD factorization schemes, that separate the non-perturbative polarizing process into a measurable quantity.

6.2.1 Parton Recombination Model by DeGrand and Miettinen

In the parton recombination model developed by DeGrand and Miettinen [DeG81b, DeG81a, DeG85] the polarization in inclusive baryon fragmentation is reduced to the polarization in the underlying partonic subprocess. The model considers the scattering of a baryon B with momentum p_B on a target, thereby producing baryon B' with momentum $p_{B'}$. B' carries a longitudinal momentum fraction x_F with respect to B and has a small transverse momentum p_T. The polarization is measured along the normal $\hat{n}$ of the production plane, that is also the scattering plane and is spanned by the two baryons $\hat{n} \propto \vec{p}_B \times \vec{p}_{B'}$.

The beam baryon is considered in an infinite momentum frame, where its wave function can be decomposed into partonic wave functions. The three valence partons determine the flavor quantum numbers and carry the major part of the baryon momentum, whereas the numerous sea partons contribute only a small part to the momentum and possess no net quantum numbers. The production of fast baryons with large x_F is described as a recombination of beam valence quarks with sea quarks under the assumption of minimum complexity of the quark transitions and SU(6) spin-flavor symmetry. This means that B and B' share the maximum possible number of valence quarks and that these valence quarks have the same wave functions in the fragmenting and in the outgoing baryon. The production of B' via baryon resonances is neglected, so that the predictions are valid only for "promptly" produced baryons.

There are three classes of recombination processes: If two valence partons from the beam baryon B recombine with one sea parton to form B', as it is the case for the Λ production by a proton beam, where the ud diquark of the beam proton recombines with an s quark from the sea, this is called VVS recombination. In VSS recombination B and B' share only one valence parton like in the Ξ^- production by protons, where the d quark from the proton recombines with an ss diquark from the sea. The case, where B and B' have no valence quarks in common, so that all valence partons of the outgoing baryon have to be created from the sea, is called SSS recombination, which applies to all anti-baryons produced by baryons.

The sea partons are supposed to be unpolarized. The polarization is built up in the process of recombination, where certain spin directions are preferred. It turns out that nearly all polarization data can be explained at least qualitatively by a simple rule: *Slow (sea) partons recombine preferentially with their spin down with respect to the production plane, while fast (valence) partons recombine with their spin up*. DeGrand and Miettinen propose that this correlation of spin and momentum is caused by the change of the parton momentum during the recombination process, which is not collinear to the parton momentum and therefore leads to a Thomas precession of the parton's spin.

An "algebraic" model for the polarization can be constructed using the standard SU(6) spin-flavor wave functions for the baryons to describe the VVS and VSS recombinations in terms of the exchange of quarks and pairs of quarks between the fragmenting and the outgoing baryon. Considering the structure of the two recombination processes it is convenient to represent the baryons as a combination of quark and diquark, where the internal diquark interaction is neglected.

$$\left|B\, s_B\, m_B\right\rangle = \sum_{s_D=0,1} \sum_{m_q+m_D=m_B} \left(D\, s_D\, m_D\; q\, m_q \middle| B\, s_B\, m_B\right) \left|D\, s_D\, m_D\right\rangle \left|q\, m_q\right\rangle \tag{6.7}$$

where B, D, and q are the flavor quantum numbers of the baryon, the diquark, and the quark, respectively. s_i and m_i with $i = B, D, q$ are the respective spins and their components along the quantization axis, which is the normal $\hat{n}$ of the production plane. $\left(D\, s_D\, m_D\; q\, m_q \middle| B\, s_B\, m_B\right)$ stand for the SU(6) Clebsch-Gordan coefficients.

In the VVS recombination process one valence quark q of the beam baryon's wave function is replaced by a different quark q' from the sea. The model assumes, that there exists a $\boldsymbol{T}$-matrix amplitude for this process, which can be factorized in a valence quark term $\boldsymbol{V}$ and a sea quark term $\boldsymbol{S}$ with $\boldsymbol{T} = \boldsymbol{VS}$, so that

$$\begin{aligned}(6.8)\quad \left\langle B'\, s_{B'}\, m_{B'};\ q\, m_q \middle| \boldsymbol{T} \middle| B\, s_B\, m_B;\ q'\, m_{q'} \right\rangle = \\ \sum_{s_D=0,1} \sum_{\substack{m_q+m_D=m_B \\ m_{q'}+m_D=m_{B'}}} \left(D\, s_D\, m_D\ q\, m_q \middle| B\, s_B\, m_B\right) \left(D\, s_D\, m_D\ q'\, m_{q'} \middle| B'\, s_{B'}\, m_{B'}\right) V^D_{s_D\, m_D} S^{q'}_{m_{q'}}\end{aligned}$$

where $V^D_{s_D\, m_D}$ is the amplitude, that parameterizes the recombination of the diquark state $|s_D\, m_D\rangle$ to the outgoing baryon B', and $S^{q'}_{m_{q'}}$ the respective amplitude of the sea quark q' with spin projection $m_{q'}$. The two brackets in the sum again represent the SU(6) Clebsch-Gordan coefficients, that determine the contribution of the quark and diquark states to the initial and final baryon states. Since only unpolarized beams are considered, the Clebsch-Gordans for the beam baryon drop out, when the polarization is calculated, and are therefore omitted in the following calculations. From eq. (6.8) the cross section is calculated as the incoherent sum of the squared amplitudes over all possible spin states of q and q':

$$(6.9)\qquad \sigma(B \to B') \propto \sum_{s_D=0,1} \sum_{m'_q+m_D=m_{B'}} \left| \left(D\, s_D\, m_D\ q'\, m_{q'} \middle| B'\, s_{B'}\, m_{B'}\right) V^D_{s_D\, m_D} S^{q'}_{m_{q'}} \right|^2$$

This is a usual parton model simplification. The interference terms are assumed to be negligible, because the outgoing spectator valence quarks have different spin states, that do not overlap.

To describe the data the amplitudes are parameterized:

$$(6.10)\qquad \left|S_{\uparrow\downarrow}\right|^2 = \mathcal{A}(1 \mp \varepsilon), \qquad \left|V_{00}\right|^2 = \mathcal{B}, \qquad \left|V_{1m_D}\right|^2 = \mathcal{B}(1 + m_D\, \delta)$$

where ε and δ are small parameters, which depend on x_F and p_T of the outgoing baryon. The experimental data suggest that $\varepsilon \approx \delta$. In the parameterization the signs of ε and δ are chosen such, that the cross section is enhanced, if the valence partons from the beam particle's wave function recombine with spin up and the sea partons with spin down.

The simplest example is that of $p \longrightarrow \Lambda$ (cf. fig. 6.4a): Since the valence ud diquark in the Λ is in a spin-0 singlet state, the spin of the Λ is determined by the spin of the s quark:

$$(6.11)\qquad \begin{aligned} P_T^\Lambda &= \frac{\sigma(p \to \Lambda^\uparrow) - \sigma(p \to \Lambda^\downarrow)}{\sigma(p \to \Lambda)} \quad \text{with} \quad \sigma(p \to \Lambda^{\uparrow(\downarrow)}) \propto \left|V^{ud}_{00}\right|^2 \left|S^s_{\uparrow(\downarrow)}\right|^2 \\ P_T^\Lambda &= -\varepsilon \end{aligned}$$

The VSS recombination can be described in the same way by exchanging the roles of quark and diquark. The outgoing baryon is produced by replacing the valence diquark D

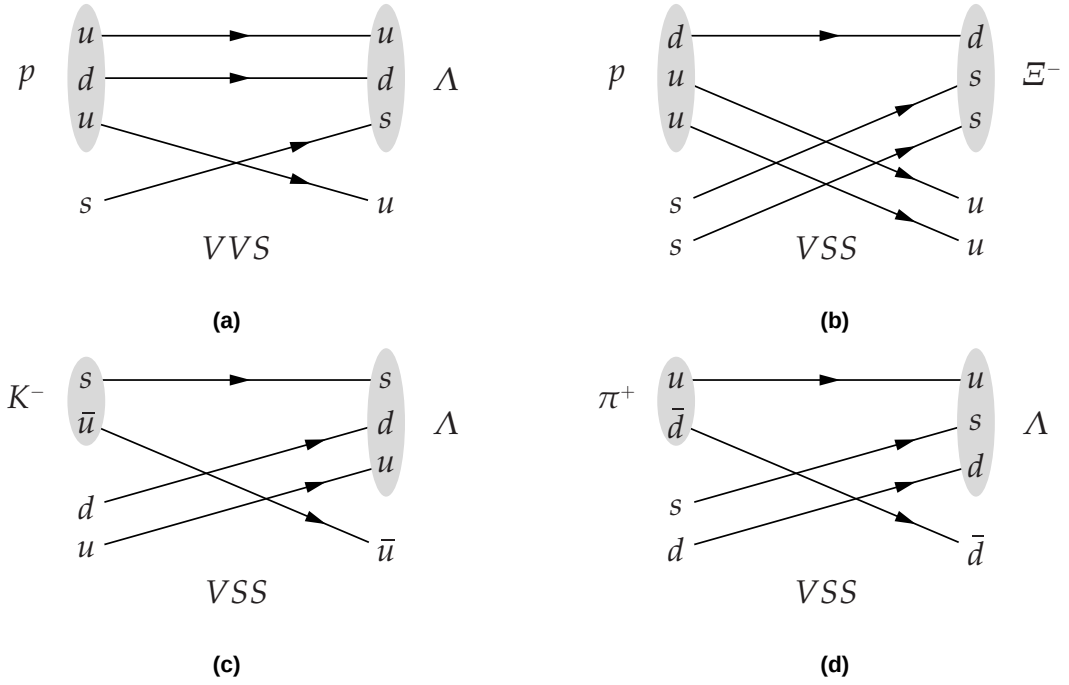

Figure 6.4: Schematic illustration of some VVS and VSS recombination processes.

of the beam baryon by the diquark D' from the sea, which recombines with the valence quark, that is shared by B and B'. The corresponding $\boldsymbol{T}$-matrix amplitude reads:

$$\begin{aligned}(6.12)\quad &\left\langle B'\, s_{B'}\, m_{B'};\ D\, s_D\, m_D \middle| \boldsymbol{T} \middle| B\, s_B\, m_B;\ D'\, s_{D'}\, m_{D'} \right\rangle = \\ &\sum_{\substack{s_D=0,1 \\ s_{D'}=0,1}} \sum_{\substack{m_D+m_q=m_B \\ m_{D'}+m_q=m_{B'}}} \left(D\, s_D\, m_D\ q\, m_q \middle| B\, s_B\, m_B\right) \left(D'\, s_{D'}\, m_{D'}\ q\, m_q \middle| B'\, s_{B'}\, m_{B'}\right) V^q_{m_q} S^{D'}_{s_{D'}\, m_{D'}}\end{aligned}$$

The cross section is again calculated as the incoherent sum of the squared amplitudes over all spin states of D and D'.

$$(6.13)\qquad \sigma(B \to B') \propto \sum_{s_{D'}=0,1} \sum_{m_{D'}+m_q=m_{B'}} \left| \left(D'\, s_{D'}\, m_{D'}\ q\, m_q \middle| B'\, s_{B'}\, m_{B'}\right) V^q_{m_q} S^{D'}_{s_{D'}\, m_{D'}} \right|^2$$

The same parameterization as in the VVS case is used, but the signs of ε and δ are reversed in order to comply with the recombination rule, that sea quarks recombine as a matter of preference with spin down and valence quarks with spin up:

$$(6.14)\qquad \left|V_{\uparrow\downarrow}\right|^2 = \mathcal{A}(1 \pm \varepsilon), \qquad \left|S_{00}\right|^2 = \mathcal{B}, \qquad \left|S_{1m_D}\right|^2 = \mathcal{B}(1 - m_D\, \delta)$$

The process $p \longrightarrow \Xi^-$ is an example for a VSS recombination (see fig. 6.4b). In the SU(6) Ξ^- wave function the ss diquark is in a spin-1 state. Using eq. (6.13) and (6.14) the Ξ^- polarization can be calculated

$$
\begin{aligned}
P_T^{\Xi^-} &= \frac{\sigma(p \to \Xi^{-\uparrow}) - \sigma(p \to \Xi^{-\downarrow})}{\sigma(p \to \Xi^-)} \\
&\text{with} \quad \sigma(p \to \Xi^{-\uparrow}) \propto \frac{1}{3}\left|S_{10}^{ss}\right|^2 \left|V_\uparrow^d\right|^2 + \frac{2}{3}\left|S_{11}^{ss}\right|^2 \left|V_\downarrow^d\right|^2 \\
&\text{and} \quad \sigma(p \to \Xi^{-\downarrow}) \propto \frac{1}{3}\left|S_{10}^{ss}\right|^2 \left|V_\downarrow^d\right|^2 + \frac{2}{3}\left|S_{1-1}^{ss}\right|^2 \left|V_\uparrow^d\right|^2 \\
P_T^{\Xi^-} &= -\frac{1}{3}(\varepsilon + 2\delta)
\end{aligned}
\tag{6.15}
$$

For SSS recombination processes like $p \longrightarrow \bar{\Lambda}$ the model predicts zero polarization, because the involved sea partons do not exhibit a strong momentum hierarchy. There are equally many configurations in which the same parton is both faster and slower than the diquark, so that the effect cancels on the average.

The same scheme also predicts the polarization of leading baryons in meson fragmentation: The reaction $K^- \longrightarrow \Lambda$ can be described as a VSS recombination of the valence s quark from the kaon with a spin-0 singlet ud diquark from the sea (see fig. 6.4c). In analogy to eq. (6.11) the Λ polarization is calculated to be $P_T(K^- \to \Lambda) = +\varepsilon$. The same polarization is expected in the reaction $K^+ \longrightarrow \bar{\Lambda}$. Both predictions are in agreement with the experimental findings. The VSS recombination scheme also applies to the production of leading Λs by pion and K^+ beams, where the valence quark is a u or d quark, respectively (cf. fig. 6.4d), and predicts in all three cases a negative polarization of $P_T(\pi^\pm \to \Lambda) = P_T(K^+ \to \Lambda) = -\delta/2$.

The results for the meson fragmentation are directly related to the polarization of leading baryons produced in quark fragmentation. Assuming that the fragmenting quarks are produced in helicity eigenstates, the Λ polarization in s quark fragmentation should be the same as in K^- fragmentation $P_T(s \to \Lambda) = P_T(K^- \to \Lambda)$. The same is true for u/d and $\pi^\pm$ fragmentation: $P_T(u, d \to \Lambda) = P_T(\pi^\pm \to \Lambda)$.

The above results are universal in the sense, that no assumption on the actual polarization mechanism, that determines the two parameters ε and δ, is made. Table 6.2 compares some predictions with experimental results and shows that for the considered reactions at least the sign of the polarizations is predicted correctly. For part of the processes also the relative magnitudes are reproduced.

In order to explain the rule, that fast partons recombine preferentially with spin up and slow partons with spin down, which was used to derive the results discussed above, DeGrand and Miettinen propose a simple semi-classical model. The simplest case is again that of Λ production by a proton beam ($p \longrightarrow \Lambda$): The recombining s quark stems from the sea of the beam proton and has thus only a small momentum fraction of $x_B^s \approx 0.1$. During the recombination process this quark becomes a valence quark of the outgoing Λ

Transition	Predicted P_T^H	Observed P_T^H	Energy [GeV]
$p \longrightarrow \Lambda$	$-\varepsilon$	-0.1 . . . -0.2	24 . . . 2000
$p \longrightarrow \bar{\Lambda}$	0	0	24 . . . 2000
$p \longrightarrow \Sigma^+$	ε	0.1 . . . 0.2	400
$p \longrightarrow \Sigma^-$	$\varepsilon/2$	0.15 . . . 0.3	400
$p \longrightarrow \Xi^0$	$-\varepsilon$	-0.1 . . . -0.2	400
$p \longrightarrow \Xi^-$	$-\varepsilon$	-0.1 . . . -0.2	400
$K^+ \longrightarrow \bar{\Lambda}$	ε	>0.4 for x_F>0.3	32, 70
$K^- \longrightarrow \Lambda$	ε	0.4	14
$\pi^- \longrightarrow \Lambda$	$-\varepsilon/2$	-0.05	18

Table 6.2: Comparison of predictions of the DeGrand and Miettinen model, where $\delta = \varepsilon$, with experimental data from inclusively produced hyperons by unpolarized beams as of 1985. (from [DeG85])

in which it carries a large momentum fraction of about $1/3$. Because the Λ carries a large longitudinal fraction x_F of the beam proton momentum p_B, the s quark experiences an increase of its longitudinal momentum from $x_B^s\, p_B$ to $1/3\, x_F\, p_B$. The transverse momentum $k_\perp$ of the s quark on the other hand remains approximately unchanged during the recombination process $k_\perp^p \approx k_\perp^\Lambda$ and is roughly parallel to the transverse momentum p_T of the outgoing Λ. This means that the change of momentum of the s quark is not collinear to its momentum which, due to the fermion nature of the quark causes a Thomas precession of the s quark's spin (see fig. 6.5).

It is assumed that the recombination process can be described by equations of motion in a confining scalar force field. The evolution of the rest frame of the s quark can be expressed as a series of infinitesimal Lorentz boosts without rotation. The infinitesimal boosts are not collinear and, since the product of two noncollinear boosts is equivalent to a boost plus a rotation (also known as Wigner rotation), the rest frame experiences an additional rotation – the Thomas precession.

The Thomas precession is a purely relativistic kinematical effect and appears as an extra term in the effective Hamiltonian, that describes the recombination process:

$$U = \vec{s}_s \cdot \vec{\omega}_T \quad \text{with} \quad \vec{\omega}_T = \frac{\gamma}{\gamma+1}\frac{1}{m_s}\vec{F} \times \vec{v} \tag{6.16}$$

where $\vec{s}_s$ is the spin vector, m_s the mass, $\vec{v}$ the velocity, and γ the Lorentz factor of the s quark. $\vec{F}$ is the force, that changes the quark momentum and $\vec{\omega}_T$ the angular velocity of the Thomas precession [Jac99]. In the infinite momentum frame $\gamma/(\gamma+1) \approx 1$.

According to eq. (6.16) the Thomas precession vanishes only, if $\vec{F}$ and $\vec{v}$ are parallel. The force $\vec{F}$ is directed along the beam direction, so that the angular velocity $\vec{\omega}_T$ of the Thomas precession points in the direction of the production plane normal $\hat{n} \propto \vec{p}_B \times \vec{p}_\Lambda \propto \vec{F} \times \vec{v}$. The additional term $U = \vec{s}_s \cdot \vec{\omega}_T$ in the Hamiltonian changes the energy of the final state

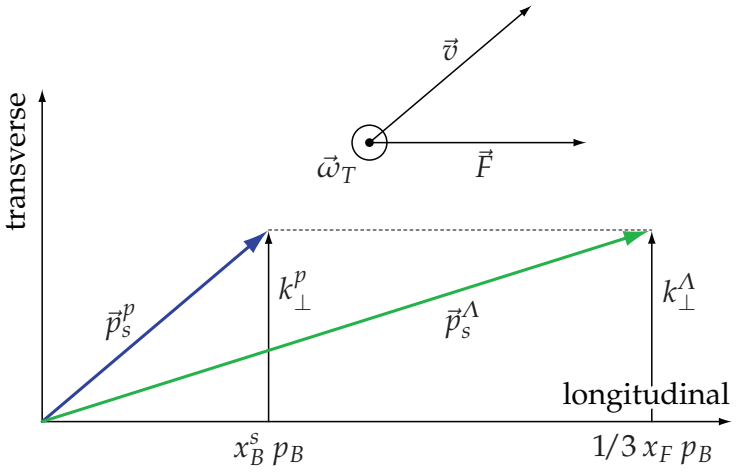

Figure 6.5: Thomas precession in the semi-classical parton recombination model for $p \longrightarrow \Lambda$: In the initial state of the beam proton the s quark has the momentum $\vec{p}_s^{\,p}$ with a small longitudinal component $x_B^s\, p_B$. In the final state of the outgoing Λ hyperon the quark momentum $\vec{p}_s^{\,\Lambda}$ has a larger longitudinal component $1/3\, x_F\, p_B$. Since the transverse momentum components $k_\perp^p$ and $k_\perp^\Lambda$ of the s quark remain unchanged, the total change of the s quark momentum and thus the accelerating force $\vec{F}$ is along the longitudinal direction and is not collinear to $\vec{p}_s^{\,p}$ or $\vec{p}_s^{\,\Lambda}$. The angular velocity of the resulting Thomas precession is parallel to $\vec{F} \times \vec{v}$ and points in direction of the production plane normal.

and hence the scattering amplitude: If the spin of the s quark is aligned in the direction of the production plane normal, U is positive and the energy of the final state is increased, so that the scattering amplitude is suppressed. For oppositely aligned spin U is negative and the scattering amplitude is enhanced. In total a *negative* polarization of the s sea quark is energetically favored. Since $|\vec{F} \times \vec{v}|$ is to first order proportional to p_T, the model also explains the dependence of the polarization on the transverse momentum.

The same arguments can be applied to the valence partons as well. In the recombination $p \longrightarrow \Sigma^+$, for example, the spin-1 uu valence diquark looses momentum, when it goes from the beam proton to the Σ^+ hyperon. The diquark is decelerated from $p_D^p = 2/3\, p_B$ to $p_D^{\Sigma^+} = 2/3\, x_F\, p_B$, so that the angular velocity $\vec{\omega}_T$ of the Thomas precession now is directed opposite to the normal of the production plane. Hence the same mechanism leads to *positive* polarization of the valence diquark.

Despite its simplicity the model of DeGrand and Miettinen is able to predict the relative signs of various hyperon polarizations and for part of the transitions also the relative magnitudes. It fails to explain the non-vanishing polarizations of the $\bar{\Sigma}^-$ and $\bar{\Xi}^+$ anti-hyperons. Whereas the p_T dependence of the polarization is at least qualitatively reproduced by the semi-classical Thomas precession model, this is not true for the observed x_F behavior. Yamamoto *et al.* [Yam97] have extended the model using a relativistic formulation of the parton-parton interaction, that describes the relativistic quark kinematics including the dynamics of the spin polarization. Based on experimentally extracted momentum distribution functions for quarks and diquarks, the so-called Quark ReCom-

bination (QRC) model is able to describe the p_T as well as the x_F dependence for various transitions.

6.2.2 Polarizing Fragmentation Functions

Anselmino *et al.* propose a phenomenological approach to the problem of transverse Λ polarization in the current fragmentation region of deeply inelastic scattering (see subsection 2.1.1.1), that is based on pQCD and factorization schemes and includes effects from spin and from intrinsic transverse momentum $\vec{k}_\perp$ [Ans02b, Ans01a, Ans03, Ans01c, Ans01b]. The central idea is the introduction of a new kind of fragmentation function, the so-called *polarizing fragmentation functions* (pFF), that were first described by Mulders and Tangerman [Mul96] and that are thought to describe a universal feature of the hadronization process, which makes them independent of the nature of the hadronic target. The pFFs have an interpretation in the parton picture, a formal definition, and are free of ambiguities concerning initial-state interactions. In the twist expansion, that is the expansion in inverse powers of the momentum transfer Q of the virtual photon, which is the perturbative hard scale, these functions contribute to the leading terms. One can either extract the pFFs from experimental data in the appropriate kinematical range (i.e. from proton-proton scattering at large center-of-mass energy and high transverse momentum of the produced hyperon) or they can be modelled based on plausible assumptions. The results can be used to make consistent predictions for other processes like the unpolarized SIDIS reaction $\mu\, N \longrightarrow \mu'\, \Lambda^\uparrow\, X$, that is considered here and that allows a clean test of the universality hypothesis.

The scattering process is analyzed in the center-of-mass frame of the virtual photon and the target nucleon neglecting the intrinsic motion of the partons inside the target nucleon N. The process is considered in leading order in the power expansion of the strong coupling constant α_s and in leading twist in the $1/Q$ power expansion. The basic assumption is, that the Λ polarization is built up during the fragmentation of an *unpolarized* quark, which is described by the polarizing fragmentation functions. In order to not violate the rotational invariance of the pFFs, the Λ has to have a non-zero transverse momentum $\vec{k}_\perp$ with respect to the fragmenting quark. Due to the above simplifications the fragmenting quark is collinear to the virtual photon and the kinematics is limited to the beam fragmentation region, where $x_F > 0$. The intrinsic transverse momentum $\vec{k}_\perp$ of the Λ is equal to the transverse momentum $\vec{p}_T$ of the Λ with respect to the virtual photon (see fig. 6.6). For small transverse momenta one is thus directly sensitive to the $\vec{k}_\perp$ dependence of the polarizing fragmentation functions. For larger $\vec{p}_T$ hard pQCD corrections are required.

The fragmentation of an unpolarized quark q with momentum $\vec{p}_q$ into an unobserved rest X and a polarized Λ with momentum $z_h\, \vec{p}_q + \vec{k}_\perp$, where $\vec{p}_q \cdot \vec{k}_\perp = 0$, and polarization

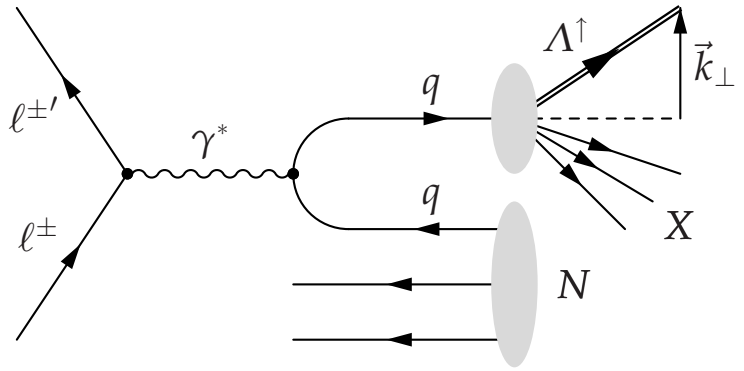

Figure 6.6: Illustration of the Λ production in SIDIS at leading order and leading twist: In this approximation the intrinsic transverse momentum $\vec{k}_{\perp}$ of the Λ is equal to its transverse momentum $\vec{p}_T$, which is a directly measurable quantity.

direction $\uparrow$ is described by the fragmentation function $\hat{D}_{\Lambda^{\uparrow}/q}(z_h, \vec{k}_{\perp})$. The unpolarized fragmentation function is independent of the direction of $\vec{k}_{\perp}$ and is given by

$$\hat{D}_{\Lambda/q}(z_h, k_{\perp}) = \hat{D}_{\Lambda^{\uparrow}/q}(z_h, \vec{k}_{\perp}) + \hat{D}_{\Lambda^{\downarrow}/q}(z_h, \vec{k}_{\perp}) \tag{6.17}$$

In like manner one can define the *polarizing* fragmentation function by taking the difference of the two density numbers:

$$\Delta D_{\Lambda^{\uparrow}/q}(z_h, \vec{k}_{\perp}) = \hat{D}_{\Lambda^{\uparrow}/q}(z_h, \vec{k}_{\perp}) - \hat{D}_{\Lambda^{\downarrow}/q}(z_h, \vec{k}_{\perp}) \tag{6.18}$$

By requiring parity invariance it is possible to separate the dependence of $\Delta D_{\Lambda^{\uparrow}/q}(z_h, \vec{k}_{\perp})$ on the direction of $\vec{k}_{\perp}$, since, due to the same reasons as given in fig. 6.1 (page 72), the only component of the polarization vector $\vec{P}_{\Lambda} = \uparrow$, that contributes to the polarizing fragmentation function, is the one parallel to $\vec{p}_q \times \vec{k}_{\perp}$.

$$\Delta D_{\Lambda^{\uparrow}/q}(z_h, \vec{k}_{\perp}) = \Delta D_{\Lambda^{\uparrow}/q}(z_h, k_{\perp}) \, \frac{\vec{P}_{\Lambda} \cdot (\vec{p}_q \times \vec{k}_{\perp})}{|\vec{p}_q \times \vec{k}_{\perp}|} \tag{6.19}$$

Because of rotational invariance of the fragmentation process around the direction of the fragmenting quark, the density numbers for the different spin directions of the Λ are related by:

$$\hat{D}_{\Lambda^{\uparrow(\downarrow)}/q}(z_h, \vec{k}_{\perp}) = \hat{D}_{\Lambda^{\downarrow(\uparrow)}/q}(z_h, -\vec{k}_{\perp}) \tag{6.20}$$

Applying this relation to eq. (6.17) and (6.18) the polarizing fragmentation function is found to be antisymmetric in $\vec{k}_\perp$, whereas the unpolarized one is, as expected, symmetric.

$$\hat{D}_{\Lambda/q}(z_h, k_\perp) = \hat{D}_{\Lambda^\uparrow/q}(z_h, \vec{k}_\perp) + \hat{D}_{\Lambda^\uparrow/q}(z_h, -\vec{k}_\perp) \tag{6.21}$$

$$\Delta D_{\Lambda^\uparrow/q}(z_h, \vec{k}_\perp) = \hat{D}_{\Lambda^\uparrow/q}(z_h, \vec{k}_\perp) - \hat{D}_{\Lambda^\uparrow/q}(z_h, -\vec{k}_\perp) \tag{6.22}$$

As will be shown later, $\hat{D}_{\Lambda/q}(z_h, k_\perp)$ and $\Delta D_{\Lambda^\uparrow/q}(z_h, \vec{k}_\perp)$ can be measured and according to eq. (6.21) and (6.22) they can be used to calculate the fundamental fragmentation function

$$\hat{D}_{\Lambda^\uparrow/q}(z_h, \vec{k}_\perp) = \frac{1}{2}\hat{D}_{\Lambda/q}(z_h, k_\perp) + \frac{1}{2}\Delta D_{\Lambda^\uparrow/q}(z_h, k_\perp)\, \frac{\vec{P}_\Lambda \cdot (\vec{p}_q \times \vec{k}_\perp)}{|\vec{p}_q \times \vec{k}_\perp|} \tag{6.23}$$

Unlike e.g. the Collins function (see subsection 2.1.1.3), the polarizing fragmentation functions are chiral even objects. Therefore the measured observable, the transverse Λ polarizations P_T^Λ in SIDIS, cannot depend on the orientation of the lepton scattering plane, so that P_T^Λ will *not* average to zero, when integrated over all directions of the scattered lepton. Another consequence is, that the polarization can be measured both in neutral and charged current reactions.

To find an analytical expression for the transverse Λ polarization, the neutral current SIDIS reaction $\mu\, N \longrightarrow \mu'\, \Lambda^\uparrow\, X$ is analyzed in the center-of-mass frame of the virtual photon and the target nucleon. The coordinate system is chosen such, that the z-axis is in the direction of the incoming virtual photon. The x-axis is taken along the transverse momentum p_T of the Λ with respect to the photon. The transverse polarization is measured with respect to the $+y$-axis, which is given by $\vec{z} \times \vec{x}$ and thus normal to the production plane. This way $\vec{k}_\perp$ is always perpendicular to the analyzer (cf. eq. (6.19)).

The transverse Λ polarization is measured as an asymmetry of inclusive cross sections

$$P_T^\Lambda(x_B, y_B, z_h, p_T) = \frac{\mathrm{d}\sigma^{\Lambda\uparrow} - \mathrm{d}\sigma^{\Lambda\downarrow}}{\mathrm{d}\sigma^{\Lambda\uparrow} + \mathrm{d}\sigma^{\Lambda\downarrow}} \quad \text{where} \quad \mathrm{d}\sigma^{\Lambda\uparrow(\downarrow)} = \frac{\mathrm{d}\sigma^{\mu\, N \longrightarrow \mu'\, \Lambda^{\uparrow(\downarrow)}\, X}}{\mathrm{d}x_B\, \mathrm{d}y_B\, \mathrm{d}z_h\, \mathrm{d}^2\vec{p}_T} \tag{6.24}$$

is the differential cross section for the inclusive production of Λs, that are polarized along the $\uparrow$ ($\downarrow$) direction. By neglecting electroweak interference effects, which are very small in the relevant kinematical region, the cross section can be factorized into two parts: One term describes the scattering of the electroweak virtual boson on a parton. It is proportional to the quark distribution function $q(x_B)$ of the nucleon and to the elementary cross section of the process $\ell\, q \longrightarrow \ell'\, q'$ where the pair (ℓ, ℓ') can be any of $(\ell^\pm, \ell^\pm)$, (ν, ν), and $(\bar{\nu}, \bar{\nu})$ for neutral current reactions and (ν, ℓ^-), $(\bar{\nu}, \ell^+)$, (ℓ^-, ν), and $(\ell^+, \bar{\nu})$ for charged current reactions, respectively. The second factor is the polarizing fragmentation function $\hat{D}_{\Lambda^{\uparrow(\downarrow)}/q'}$. In total $\mathrm{d}\sigma^{\Lambda\uparrow(\downarrow)}$ can be written

$$\mathrm{d}\sigma^{\Lambda\uparrow(\downarrow)} = \sum_{q,q'} q(x_B)\, \frac{\mathrm{d}\hat{\sigma}^{\ell\, q \longrightarrow \ell'\, q'}}{\mathrm{d}y_B}\, \hat{D}_{\Lambda^{\uparrow(\downarrow)}/q'}(z_h, p_T) \tag{6.25}$$

where the sum goes over all allowed quark and antiquark flavor combinations q, q', which in the case of neutral currents requires an additional $\delta_{q\,q'}$ term in the partonic cross section $\mathrm{d}\hat{\sigma}^{\ell\,q\longrightarrow\ell'\,q'}\,/\,\mathrm{d}y_B$. The above factorization relies on the universality hypothesis, which postulates, that the Λ polarization from unpolarized quark fragmentation is independent of the initial state.

With eq. (6.24) and (6.25) the transverse Λ polarization in unpolarized SIDIS with a charged lepton beam is given by

$$
\begin{aligned}
P_T^{\Lambda} &= \frac{\sum_q e_q^2\, q(x_B)\, \dfrac{\mathrm{d}\hat{\sigma}^{\ell q}}{\mathrm{d}y_B}\, \Delta D_{\Lambda^\uparrow/q}(z_h, p_T)}{\sum_q e_q^2\, q(x_B)\, \dfrac{\mathrm{d}\hat{\sigma}^{\ell q}}{\mathrm{d}y_B}\, \hat{D}_{\Lambda/q}(z_h, p_T)} \\
&= \frac{4u\,\Delta D_{\Lambda^\uparrow/u} + d\,\Delta D_{\Lambda^\uparrow/d} + s\,\Delta D_{\Lambda^\uparrow/s} + 4\bar{u}\,\Delta D_{\Lambda^\uparrow/\bar{u}} + \bar{d}\,\Delta D_{\Lambda^\uparrow/\bar{d}} + \bar{s}\,\Delta D_{\Lambda^\uparrow/\bar{s}}}{4u\,\hat{D}_{\Lambda/u} + d\,\hat{D}_{\Lambda/d} + s\,\hat{D}_{\Lambda/s} + 4\bar{u}\,\hat{D}_{\Lambda/\bar{u}} + \bar{d}\,\hat{D}_{\Lambda/\bar{d}} + \bar{s}\,\hat{D}_{\Lambda/\bar{s}}}
\end{aligned}
\tag{6.26}
$$

where in the second line factors coming from the elementary partonic cross sections have been cancelled out in the nominator and denominator.

Expression (6.26) can be simplified by assuming isospin symmetry, that is $(\Delta)D_{\Lambda^{(\uparrow,\downarrow)}/d} = (\Delta)D_{\Lambda^{(\uparrow,\downarrow)}/u}$. Furthermore contributions from sea quarks can be neglected, since terms of the form $\bar{q}(\Delta)D_{\Lambda^{(\uparrow)}/\bar{q}}$ are non-leading in the distribution as well as in the fragmentation functions and are thus doubly suppressed. A good approximation for P_T^{Λ} is therefore

$$
P_T^{\Lambda}(\ell^{\pm}\,N \longrightarrow \ell^{\pm}\,\Lambda^{\uparrow}\,X) \approx \frac{(4u+d)\,\Delta D_{\Lambda^\uparrow/u} + s\,\Delta D_{\Lambda^\uparrow/s}}{(4u+d)\,\hat{D}_{\Lambda/u} + s\,\hat{D}_{\Lambda/s}}
\tag{6.27}
$$

The polarization of the $\overline{\Lambda}$ can be calculated from eq. (6.26) by assuming invariance under charge conjugation, that is the fragmentation functions for Λ and $\overline{\Lambda}$ are related by $(\Delta)D_{\Lambda^{(\uparrow,\downarrow)}/q,\bar{q}} = (\Delta)D_{\overline{\Lambda}^{(\uparrow,\downarrow)}/\bar{q},q}$:

$$
P_T^{\overline{\Lambda}} = \frac{4\bar{u}\,\Delta D_{\Lambda^\uparrow/u} + \bar{d}\,\Delta D_{\Lambda^\uparrow/d} + \bar{s}\,\Delta D_{\Lambda^\uparrow/s} + 4u\,\Delta D_{\Lambda^\uparrow/\bar{u}} + d\,\Delta D_{\Lambda^\uparrow/\bar{d}} + s\,\Delta D_{\Lambda^\uparrow/\bar{s}}}{4\bar{u}\,\hat{D}_{\Lambda/u} + \bar{d}\,\hat{D}_{\Lambda/d} + \bar{s}\,\hat{D}_{\Lambda/s} + 4u\,\hat{D}_{\Lambda/\bar{u}} + d\,\hat{D}_{\Lambda/\bar{d}} + s\,\hat{D}_{\Lambda/\bar{s}}}
\tag{6.28}
$$

Isospin symmetry can be applied here as well, but one has to be careful with neglecting terms, because they are all of the form $q(\Delta)D_{\Lambda^{(\uparrow)}/\bar{q}}$ or $\bar{q}(\Delta)D_{\Lambda^{(\uparrow)}/q}$, which means they combine leading valence and non-leading sea quark contributions, that are different in magnitude depending on the kinematical region in x_B, y_B, and z_h. Assuming that $\Delta D_{\Lambda^\uparrow/\bar{q}}$ is negligibly small eq. (6.28) simplifies to

$$
P_T^{\overline{\Lambda}}(\ell^{\pm}\,N \longrightarrow \ell^{\pm}\,\overline{\Lambda}^{\uparrow}\,X) \approx \frac{(4\bar{u}+\bar{d})\,\Delta D_{\Lambda^\uparrow/u} + \bar{s}\,\Delta D_{\Lambda^\uparrow/s}}{(4\bar{u}+\bar{d})\,\hat{D}_{\Lambda/u} + \bar{s}\,\hat{D}_{\Lambda/s} + (4u+d)\,\hat{D}_{\Lambda/\bar{u}} + s\,\hat{D}_{\Lambda/\bar{s}}}
\tag{6.29}
$$

Compared to eq. (6.27) there are additional terms from the non-leading contributions of the unpolarized fragmentation functions in the denominator, which may lead to smaller polarization for the $\overline{\Lambda}$.

In a similar way expressions for the other neutral and charged current reactions can be found:

$$P_T^{\Lambda}(\nu N \longrightarrow \nu \Lambda^{\uparrow} X) \approx \frac{(Ku + d)\,\Delta D_{\Lambda^{\uparrow}/u} + s\,\Delta D_{\Lambda^{\uparrow}/s}}{(Ku + d)\,\hat{D}_{\Lambda/u} + s\,\hat{D}_{\Lambda/s}} \tag{6.30}$$

$$P_T^{\Lambda}(\nu N \longrightarrow \ell^- \Lambda^{\uparrow} X) \approx \frac{\Delta D_{\Lambda^{\uparrow}/u}}{\hat{D}_{\Lambda/u}} \tag{6.31}$$

$$P_T^{\Lambda}(\bar{\nu} N \longrightarrow \ell^+ \Lambda^{\uparrow} X) \approx \frac{\Delta D_{\Lambda^{\uparrow}/u} + R\,\Delta D_{\Lambda^{\uparrow}/s}}{\hat{D}_{\Lambda/u} + R\,\hat{D}_{\Lambda/s}} \tag{6.32}$$

where $K = (1 - 8C)/(1 - 4C) + \mathcal{O}(C^2)$, $C = 1/3 \cdot \sin^2\theta_W$, and $R = \tan^2\theta_C$ with $\theta_{W,C}$ being the Weinberg and Cabbibo angle of the standard model.

The above equations show, that the transverse Λ polarization can in principle be measured in various unpolarized SIDIS processes and that in each process different combinations of distribution functions, unpolarized fragmentation functions, and polarizing fragmentation functions appear. In addition the various terms are modulated by factors coming from the dynamics of the elementary partonic process or from the contribution of the strange quarks, which depends on the chosen x_B-region. This gives the opportunity to separate the various contributions and to study the properties of the unpolarized and polarizing fragmentation functions utilizing the transverse Λ polarization.

Most of the experimental data on the Λ polarization contain a non-separable contamination of 20-30 % of Λs produced via the decay $\Sigma^0 \longrightarrow \Lambda\gamma$. The applied factorization scheme does not separate the Λ and Σ^0 fragmentation, so that the pFFs are effective fragmentation functions. Since the branching ratio for $\Sigma^0 \longrightarrow \Lambda\gamma$ is 100 %, the full Σ^0 fragmentation function is included.

Anselmino *et al.* obtain qualitative and generic numerical estimates for the transverse Λ and $\overline{\Lambda}$ polarization using the above formulas in combination with a Gaussian model for the explicit $k_\perp$ dependence of the fragmentation functions (see [Ans02b]). They fix the hard scale to $Q^2 = 2\,(\mathrm{GeV}/c)^2$ and use SU(3)-symmetric unpolarized Λ fragmentation functions. The calculations were performed for two different scenarios with different weights $|N_q| \leq 1$ for the polarizing fragmentation functions $\Delta D_{\Lambda^{\uparrow}/q}(z_h, k_\perp) = N_q\, f(z_h, k_\perp)$. In scenario 1 the up, down, and strange quark contributions have nearly the same weight ($N_u = N_d = -0.8$ and $N_s = 1$), whereas for scenario 2 the weights are more asymmetric ($N_u = N_d = -0.3$ and $N_s = 1$). Unless a SU(3)-asymmetric model is used, where $|N_{u,d}| \gg |N_s|$, the Λ polarization is dominated by the contributions from up and down quarks, because $\Delta D_{\Lambda^{\uparrow}/s}$ is suppressed by the strange quark distribution. Fig. 6.7 shows the numerical results for P_T^{Λ} and $P_T^{\overline{\Lambda}}$ as a function of z_h, averaged over p_T. The polarization is in both cases negative and increases strongly with z_h.

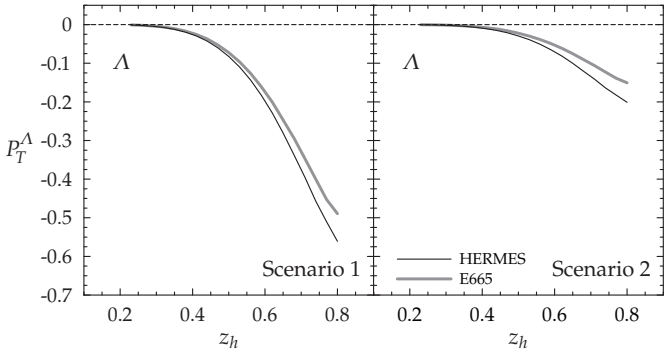

(a)

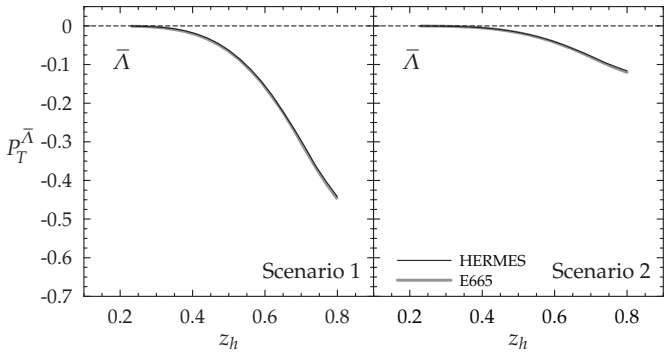

(b)

Figure 6.7: (a) Numerical results for the p_T-averaged transverse Λ polarization P_T^{Λ} as a function of z_h for the HERMES and E665 kinematics in two different scenarios described in the text. (b) shows the same for the $\bar{\Lambda}$. [Ans02b]

Chapter 7

Data Analysis

This chapter describes the methods and techniques, applied to extract the polarization of Λ and Ξ hyperons from the COMPASS muon beam data with longitudinally polarized target.

The first section 7.1 gives a brief overview of the technical issues as well as the hard- and software involved in the data analysis. Section 7.2 defines the data sample, that is analyzed, describes how the Λ and Ξ hyperons are identified by their decay topology, and introduces the coordinate system. The main part of this section details the selection of the Λ and Ξ samples by a series of cuts, which mainly aim at improving the ratio of the hyperon signal with respect to the background in order to minimize the contamination of the measured hyperon polarization by background processes with unknown polarization.

In order to suppress acceptance effects, which possibly give rise to false asymmetries, a bias canceling technique is employed, which is described in section 7.3. This method is able to correct the left-right asymmetry of the COMPASS acceptance under the assumption, that the spectrometer is symmetric with respect to its mid-plane. The slope of the acceptance corrected angular distribution is directly proportional to the polarization.

The last section 7.4 explains how the background is subtracted from the Λ and the Ξ samples in order to get the angular distributions, that are needed for the bias canceling method. Because the Λ background consists of several components and therefore has a quite complicated structure, an elaborate two-dimensional fitting procedure is employed to subtract the background.

7.1 Hard- and Software Environment for Data Analysis

7.1.1 The ROOT Framework

ROOT [Bru97, ROO] is the basic software environment used in the analysis of COMPASS data. It is an object oriented framework written in C++ and developed at CERN. The project is quite successful: Starting around 1995 as a successor for the PAW package, it is nowadays the standard tool in high energy physics and beyond.

ROOT provides routines for visualization, processing, and storage of large amount of complex data. The analysis presented here heavily relies on ROOT's histogramming capabilities including the fitting of histograms, which internally is handled by the classic MINUIT package. The second main feature of ROOT, relevant here, is its optimized data I/O, which is based on the so-called *tree* class. ROOT trees are used to store and access complex data structures efficiently on an event-by-event basis.

7.1.2 CORAL – Reconstruction of COMPASS raw Data

The COMPASS beam times in the years 2002, 2003, and 2004 resulted in 964 TByte of raw data, which contain the digitized values (amplitude and time information, scaler values) of all detectors of the spectrometer. The raw data files consist of event data blocks, which again contain several subblocks with the detector-specific data. The subblocks are identified by header words and have a particular data format depending on the type of the readout electronics.

The data taking is subdivided into different time periods: The smallest unit of event recording is the SPS *spill* (see subsection 2.2.1), which is identified by the spill number. A period of 100 (year 2002) and 200 (year 2003/04) consecutive spills, respectively, forms a *run*, that is labelled by a run number. An event is unambiguously identified by its run number, its spill number in the run, and its event number in the spill (see section 5.1). A run corresponds to about 1/2 and 1 hour of data taking, respectively, where external conditions, like temperature, air pressure, humidity etc., and the properties of the spectrometer are assumed to remain sufficiently stable. In a typical analysis a run is the smallest considered unit.

The raw detector information as such is not very convenient for physics analysis, which is better done in terms of particle trajectories with known charge and momentum. To this end the raw data are processed by the COMPASS Reconstruction and Analysis software (CORAL [COR]). This is an object oriented C++ program, that extracts the physically relevant objects like three-dimensional tracks with momentum and possibly particle identification from the detector responses, stored in the raw data.

This so-called *reconstruction* consists of several steps: First the raw data are decoded. In this process the data are checked for consistency and the detector information is extracted and filled into data structures, that represent the logical structure of the apparatus. This mapping of hardware channels to logical channels introduces an abstraction from the actual hardware realization of the detector readouts and facilitates the subsequent processing of the channel information, since each channel can directly be accessed by the detector plane it belongs to plus its logical channel number in this projection.

In the next step the logical channels with their digitized values are transformed into *hits* with three-dimensional coordinates and, if appropriate, with additional information like time and amplitude. For this purpose the channel information is corrected using the calibration data of the particular detectors like pedestals, zero times etc. For some detector types this in addition involves the combination of neighboring channels, the co-called *clustering*. The three-dimensional position of the hits is given by the alignment information, which maps the logical channel number to a position in space.

The found hits are combined to tracks, which represent possible charged particle trajectories. The *tracking* is done by the TraFDiC (Track Finding with Dictionary in COMPASS) package and is a three stage procedure: The pre-pattern step searches for track segments in different regions of the spectrometer, which the second step, the bridging, tries to connect to full tracks. In the third step the found track candidates are fitted to find the track parameters. In the following the basic principles of this procedure are outlined. Details, especially the handling of fringe field tracks and of the left-right ambiguities inherent to gas drift detectors, can be found in [Bed04].

The *pre-pattern* step tries to select sets of clusters, that match the pattern of a track segment. To this end the spectrometer is subdivided along the beam axis into several disjoint zones, in which the particle trajectories are assumed to be straight lines. The zones are defined by the position of the target, the magnets, and of the muon filters. The search is first performed in projections, which are sets of planes, that have the same azimuthal angle. Within these groups of planes a first simple search for one-dimensional track segments is performed by a "pivot planes" algorithm. This algorithm successively takes pairs of detector planes as pivots. Any pair of hits situated in both pivot planes defines a straight corridor through the planes, along which the program collects hits from the other planes. The width of the corridor, that is the maximum allowed deviation of the additional hits from the straight line connecting the two pivot points, is defined by the spatial resolution of the detector plane, to which the hit belongs. The set of one-dimensional track pieces, found by this method, is cleaned up by three selection steps: First a minimum number of clusters and a track inclination smaller than a maximum angle is demanded. Then the remaining set of track segments is sorted according to a quality function, which takes into account the number of clusters and their χ^2. In the last step the list is processed starting with the best rated track segments. Track piece candidates are removed, if they share too many hits with segments of higher quality.

The one-dimensional track segment candidates from the different projections are combined to track pieces in space using a similar method as described above: Successively

pairs of projections are chosen. For each pair the track segments are combined, which again defines straight corridors, but this time in three dimensions. Along these corridors the algorithm collects hits from all detector planes of all projections. By going to three dimensions the hits in the projections get assigned a coordinate perpendicular to their projection. In addition to the hit distance criterion hits are excluded, when their perpendicular coordinate lie outside of the active area of the respective detector plane. The set of three-dimensional track segment candidates is cleaned by a three step procedure similar to the one-dimensional case, except that no cut on the inclination angle is applied.

The last step of the pre-pattern improves the definition of the track segments and removes fake hits. This is done using a dictionary of all possible tracks through the spectrometer, which is obtained from Monte-Carlo simulations. The dictionary translates between the two different representations of tracks: a track as a set of hits and a track as a vector in the five-dimensional phase space. The dictionary is implemented as a look-up table, which is indexed by the five phase space variables: horizontal and vertical position, horizontal and vertical inclination angle, and charge over momentum. Each entry contains the corresponding set of hit coordinates. This allows a fast calculation of the χ^2 of a given phase space vector for a measured hit pattern. By interpolation also the partial derivatives of the χ^2 of the phase space vector can be calculated. Both information are used to implement a fast χ^2 minimization fit for the track parameters. The dictionary fit is performed for all track segments. If the resulting χ^2 exceeds a threshold, the relevance of the individual hits is checked and they are removed, if their contribution to the χ^2 is too large. At the end a cut on the number of hits and on the χ^2 cleans up the sample.

The second step of the track reconstruction, the so-called *bridging*, tries to build full tracks by sequentially connecting the up- and downstream track segments across all zone borders. In order to bridge the magnets, first up- and downstream track pieces are preselected by checking the compatibility of their track parameters after extrapolating them to the middle of the magnet. The preselected combinations of track segments are fitted and sorted by a quality function, which mainly takes into account the χ^2 of the fit. The sorted list is processed in direction of decreasing quality and combinations, that share an up- or downstream track piece with a higher quality track combination, are removed. The bridging of the absorbers uses a simplified version of the above procedure, in which the track combinations are not fitted. Instead the quality function directly acts on the sum of the squared differences of the extrapolated track parameters.

In the last stage of the track reconstruction the optimal track parameters and error matrices of the bridged tracks are calculated using a Kalman filter [Frü87, Wol93]. This iterative method successively adds the hits to the fit of the track and calculates the optimal track parameters and the χ^2 for each step. Between the hits the tracks are extrapolated taking into account multiple coulomb scattering, caused by the traversed material. Again χ^2 cuts are applied to improve the quality of the track sample.

After the track reconstruction CORAL initiates the *vertexing* stage, which tries to find the primary and secondary interaction points. To reconstruct the primary interaction point, first the beam and the scattered muon trajectories have to be identified, since they

constitute the anchors for the reconstruction. A track is taken as a scattered muon μ', if it has segments after the second muon filter, if the charge of the particle is positive, and if the track, extrapolated to the target center, has a distance to the beam axis of less than 2 cm. The corresponding beam muon μ is the beam track, that is closest to the scattered muon, that has a track time matching that of the μ' within ± 1 ns, and that has a point of closest approach with the μ' not too far away from the target center.

The vertexing is performed in two steps starting with a fast preselection, which looks for tracks that are likely to originate from one common point in space, the vertex, using geometrical and kinematical criteria. The mean of the coordinates of the closest approach of the tracks is taken as a first estimate on the vertex position.

The vertex and track parameters with the corresponding error matrices are calculated in the second step using the method of the inverse Kalman-filter, in which first a global fit is performed under the assumption, that all preselected tracks originate from one point in space. Based on the fit results a χ^2 value is calculated for each track. The track with the highest χ^2 is discarded and the global fit is repeated with the remaining tracks. This procedure is iterated, until the track with the highest χ^2 is below threshold. For the reconstruction of the primary vertex the beam and the scattered muon track are not allowed to be removed. At the end of the vertexing procedure the vertex coordinates and the refitted track parameters are saved.

The results of the reconstruction are written into so-called Data Summary Table (DST) files, which contain the fully reconstructed events with all their tracks and vertices (including the respective error matrices, momenta and particle identification), the calorimetric information, and other event-wise information like scaler values.

To limit the size of the DST files, that are used for physics analysis, they contain only a selected non-redundant subset of the available information and only analyzable events with at least one reconstructed vertex are stored. Hence these files are called Mini Data Summary Table (mDST). The total size of all mDST files of the COMPASS beam times 2002, 2003, and 2004 with longitudinal target polarization is 7.491 TByte, which corresponds to a reduction factor of better than 80 with respect to the raw data (cf. table 7.1).

7.1.3 Physics Analysis of COMPASS Data

The mDST files are created and analyzed using the PHysics Analysis Software Tools (PHAST [PHA]). This C++ program provides a convenient object oriented interface to the reconstructed data. The mDST data structures contain everything needed for analysis: an object, that represents the event, provides access to all the reconstructed tracks, particles, and vertices. A second object contains all meta-information of the run like magnetic fields, material maps, detector geometry etc.

The data are analyzed by a designated function, that the user has to program and that is executed by PHAST for every event. This function has access to all reconstructed data in the mDST file and can use this information to select certain events. In the analysis,

presented here, the PHAST user function selects so-called V^0 events (see subsections 7.2.1 and 7.2.3) and writes all needed information of the V^0 candidates into a ROOT tree. The resulting files are called Micro Data Summary Table (µDST).

The ROOT trees in the µDSTs are processed further using so-called *selector* classes derived from the ROOT framework. This second step applies further cuts to the V^0 events of the µDST sample and the result is saved in so-called Nano Data Summary Table (nDST), which contain only the information needed for the polarization analysis of the particle under consideration (Λ, $\overline{\Lambda}$, Ξ^-, or $\overline{\Xi}^+$).

In the last step the angular distributions of the decay baryons are extracted from the ROOT trees in the nDST files. Here last cuts, that define the different kinematical bins, but also cuts, that define certain subsets, needed for systematic studies, are applied. The polarization results as well as the parameters and constants needed for the various steps of the analysis are managed by a MySQL database.

The analysis was performed on a cluster of ten PCs, two of them file servers. The eight computing nodes provide in total 16 AMD Opteron CPUs of the 2 GHz class for data processing, which are managed by an OpenPBS batch system.

The above multi-step procedure was chosen to fulfill two requirements: flexibility in the cuts and fast data processing. The processing time of the mDST data is dominated by the I/O bandwidth of the storage system of the PC cluster. Therefore the µDST generation involves only very basic cuts, that are unlikely to change, so that this time consuming task (about 10 days for all 2002, 2003, and 2004 mDST data with longitudinal target polarization) has to be done only seldom. Since the µDST cuts are more general, this advantage is bought at the expense of a larger amount of disk space, that is needed to store the µDSTs. They consume about 261 GByte, which corresponds to a reduction factor of better than 28 with respect to the mDSTs.

The quite general information in the µDST files is used to project out the different nDSTs, needed for the Λ and Ξ polarization analysis. The cut set, that generates the nDST files from the µDSTs, includes more specific and tighter cuts, which had to be changed more frequently during the optimization process. This could be done more efficiently, because the processing time of the µDST data is considerably lower (about 12 hours for the whole set). The nDST files contain much more condensed information and are thus considerably smaller compared to the µDSTs: A total of 61 GByte equals to a reduction factor of about 4.

7.2 Event Selection

As shown in chapter 6, the polarization of hyperons is measured by exploiting the parity-violating nature of their weak decay, which leads to an asymmetric angular distribution of the decay particles. By convention the decay baryon is chosen as the reference particle

and its angular distribution in the rest frame of the hyperon is given by eq. (6.5):

$$\frac{\mathrm{d}N}{\mathrm{d}\cos\theta} = \frac{N_0}{2}\left(1 + \alpha_H\, P_T^H \cos\theta\right)$$

where P_T^H is the hyperon polarization, α_H the decay asymmetry parameter of the respective decay channel, and θ the angle of the decay baryon with respect to the normal of the production plane in the hyperon's rest frame.

In this analysis the angular distributions of the hyperon decays $\Lambda \longrightarrow p\,\pi^-$, $\overline{\Lambda} \longrightarrow \bar{p}\,\pi^+$, $\Xi^- \longrightarrow \Lambda\,\pi^-$, and $\overline{\Xi}^+ \longrightarrow \overline{\Lambda}\,\pi^+$ are measured to extract the polarization of the respective hyperons. For a precise polarization measurement the angular distributions have to be corrected for apparatus effects (see section 7.3) and for background contaminations (see section 7.4). The goal of the event selection is to extract clean Λ, $\overline{\Lambda}$, Ξ^-, and $\overline{\Xi}^+$samples with a background as low as possible without loosing too much signal.

The analysis is based on all muon beam data with longitudinal target polarization from the COMPASS beam times in the years 2002, 2003, and 2004 (see table 7.1 for a detailed overview). To ensure a constant data quality, "bad" runs and spills with obvious problems were excluded according to the official COMPASS lists [Kob]. These lists are generated by looking at the time evolution of the average number of primary vertices, beam tracks, secondary tracks, and the number of tracks associated with the primary vertex. A spill is marked as "bad", if it deviates more than 5σ from the main band, if it has too low statistics, or if it belongs to a group of spills, that exhibit a systematic shift with respect to the neighboring spills in one of the aforementioned variables. Most of such deviations are clearly correlated to detector problems or to changes of the trigger settings. The goal of this preselection is to ensure a stable ratio of the acceptances of the up- and downstream target cells, which is an essential prerequisite for the asymmetry measurements of the muon program (see subsection 2.1.1). Although the analysis of the hyperon polarization does not require a stable acceptance ratio of the target cells, it still benefits from the exclusion of problematic data, which is bought at the expense of lower statistics. In total about 13 % of the spills are marked as "bad", but they contain on the average less events than the "good" spills.

The following subsections describe the event topology of the different decays (subsection 7.2.1), the used coordinate system (subsection 7.2.2), and the event selection in more detail. The latter is presented in three subsections, starting with the V^0 pre-selection in subsection 7.2.3, followed by the Λ selection in subsection 7.2.4 and the definition of the Ξ sample in subsection 7.2.5, which are the two main branches of the analysis. Unless explicitly mentioned otherwise, the histograms, that illustrate the selection cuts, are all "raw" histograms, meaning that no background subtraction was applied. From the above defined dataset the selection cuts extract in total 1,626,000 Λs, 854,000 $\overline{\Lambda}$s, 24,900 Ξ^-s, and 14,900 $\overline{\Xi}^+$s.

Period	Raw data size [TByte]	mDST file size [GByte]	Number of events [10^6]
2002/P1C	11.5	131	112.298
2002/P2A	24.8	288	221.720
2002/P2D	18.0	174	132.367
2002/P2E	21.8	204	178.741
2002/P2F	9.2	93	82.103
2002/P2G	19.8	200	150.289
2002	105.1	1090	877.518
2003/P1A	27.0	182	113.986
2003/P1B	12.5	145	101.346
2003/P1C	15.1	161	118.994
2003/P1D	23.6	203	118.735
2003/P1E	28.5	284	188.082
2003/P1F	18.1	200	160.989
2003/P1I	22.5	272	190.069
2003/P1J	34.1	443	310.531
2003	181.4	1890	1302.732
2004/W22	46.4	558	357.351
2004/W23	29.6	363	211.769
2004/W26	22.9	376	214.748
2004/W27	13.2	215	121.716
2004/W28	17.4	232	141.682
2004/W29	16.2	213	149.199
2004/W30	20.8	315	189.594
2004/W31	22.4	293	193.569
2004/W32	30.1	416	263.554
2004/W37	32.3	450	289.969
2004/W38	35.2	547	353.968
2004/W39	19.2	307	162.321
2004/W40	19.9	229	119.779
2004	325.6	4514	2769.219
Overall	612.0	7491	4949.470

Table 7.1: Summary of the dataset used for the analysis: In contrast to the raw data and the mDST file sizes, which still include runs and spills, that are marked as bad, the number of events is given after applying the bad run and spill lists.

7.2.1 V^0 and Ξ Event Topology

The Λ, being a neutral particle, cannot be seen as a track in the spectrometer. The only way to identify Λs in COMPASS is to look for their charged decay products in the decay channel $\Lambda \longrightarrow p\,\pi^-$, which has a branching ratio of 63.9 %. The information from the RICH detector is not employed to identify the protons and pions from the Λ decays, mainly because the RICH has rather high pion and proton thresholds. Pions are identified, if their momentum is larger than circa 2.5 GeV/c for protons a momentum above 18 GeV/c is required [Alb03, Soz03]. Since the momentum distributions of the pions and protons from the Λ decays have mean values of only 2.67 GeV/c and 13.33 GeV/c (see fig. 7.1), respectively, the majority of the decay particles, in particular the protons, cannot be identified. Moreover the RICH acceptance was limited in the 2002 run and in 2003 the acceptance was not stable in time, which potentially violates the assumption, that the spectrometer is symmetric with respect to its mid-plane, an essential prerequisite of the employed analysis method (see section 7.3).

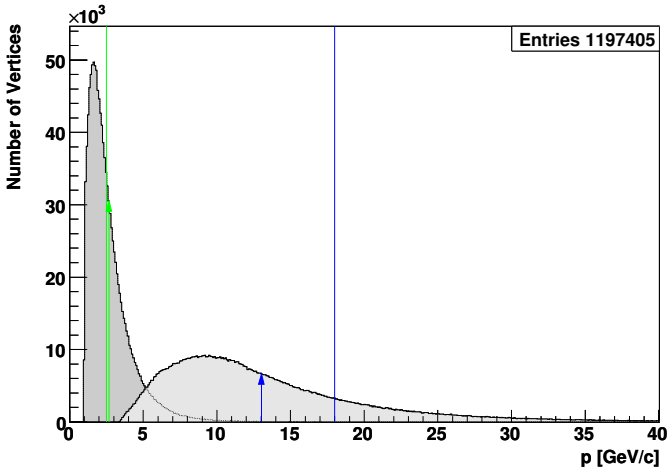

Figure 7.1: Background corrected momentum distributions of protons (light shaded histogram) and pions (dark shaded histogram) from Λ decays: The arrows indicate the mean momenta, whereas the lines mark the thresholds of the RICH (pion green, proton blue).

Consequently the Λ selection relies purely on kinematical information: Events in the spectrometer are selected, if they have two tracks of opposite charge, that within the precision of the measurement emerge from a common point in space, the Λ decay vertex, which has no incoming track and which is separated from the primary interaction point (see fig. 7.2a). The Λ is not the only particle, that decays with such kind of signature, but there is a whole class of particles, the so-called V^0 particles, that exhibit the same V-shaped decay structure.

The different particle species, that contribute to the V^0 sample, are visualized best by the so-called Armenteros-Podalanski plot, that disentangles the different V^0 decays by correlating the transverse with the longitudinal lab frame momenta of the decay daughters

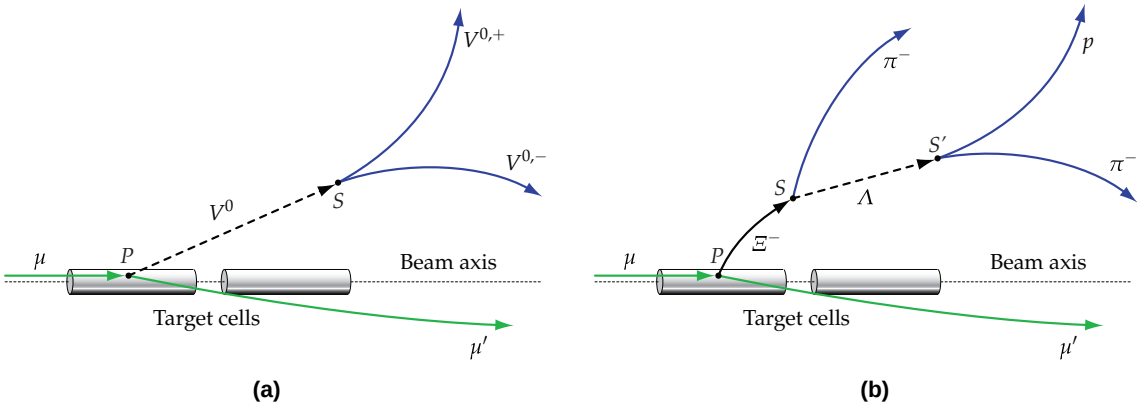

Figure 7.2: (a) V^0 event signature: An incoming beam muon scatters off a target nucleon in the primary interaction point P and creates a V^0 particle, which is neutral and thus cannot be seen by the apparatus. Some distance apart from the primary vertex the V^0 decays into two tracks of opposite charge. The resulting V-shaped structure defines the secondary interaction point S. (b) Ξ event signature: An incoming beam muon scatters off a target nucleon in the primary interaction point P and creates a Ξ hyperon, which flies some distance and decays into a charged pion and a neutral Λ. At a certain distance from the Ξ vertex S the Λ decays with a V^0 signature as defined in (a).

with respect to the V^0 direction. The transverse momentum p_T^D in the V^0 decay is determined by the mass difference of the mother and the decay particles as well as by the decay angle in the V^0 rest frame, whereas the longitudinal momenta $p_L^{\pm}$ of the daughters in addition depend on the velocity β_{V^0} of the V^0. If the measured longitudinal momenta of the daughters are combined to the momentum asymmetry $\alpha \equiv (p_L^+ - p_L^-)/(p_L^+ + p_L^-)$, the different V^0 species accumulate on elliptic arcs, that are described by

$$p_{\mathrm{Br}}^2 = (p_T^D)^2 + \frac{1}{4}\beta_{V^0}^2 m_{V^0}^2 (\alpha - \alpha_{\mathrm{Center}})^2 \tag{7.1}$$

$$\text{with} \quad \alpha_{\mathrm{Center}} = \frac{m_+^2 - m_-^2}{m_{V^0}^2} \tag{7.2}$$

$$\text{and} \quad p_{\mathrm{Br}}^2 = \frac{\left[m_{V^0}^2 - (m_+ + m_-)^2\right]\left[m_{V^0}^2 - (m_+ - m_-)^2\right]}{4m_{V^0}^2} \tag{7.3}$$

where p_{Br} is the breakup momentum of the V^0 decay in its rest frame. The center α_{Center} of the arc, at which the transverse momentum p_T^D reaches its maximum value of p_{Br}, is situated at $\alpha = 0$, if the masses of the decay particles are equal. For asymmetrically decaying V^0s the center is shifted to positive or negative values, respectively. The arc crosses the α-axis at $\alpha_{\mathrm{Center}} \pm 4p_{\mathrm{Br}}/(\beta_{V^0} m_{V^0})$.

Fig. 7.3 shows the Armenteros plot of the V^0 sample, which is the basis for the further analysis (see subsection 7.2.3). Apart from the Λ and $\overline{\Lambda}$ arcs two other prominent arcs from kaons ($K_S^0 \longrightarrow \pi^+\pi^-$) and from converted photons (predominantly $\gamma \longrightarrow e^+e^-$) are clearly visible. In this analysis only the short-lived weak eigenstate K_S^0 of the neutral kaon

is relevant, consequently the subscript "s" will be omitted in the further text. From the plot it is evident, that the disentanglement of the four V^0 species is not complete – there are regions, where the arcs overlap and in which the different particles are kinematically indistinguishable. Whereas the photons do only overlap in the low p_T^D region – and can therefore be excluded easily – the overlap of the Λ and $\overline{\Lambda}$ arcs with the kaon line is more difficult to handle, because exactly in these regions the number of Λ and $\overline{\Lambda}$ is largest (see also subsection 7.4.1).

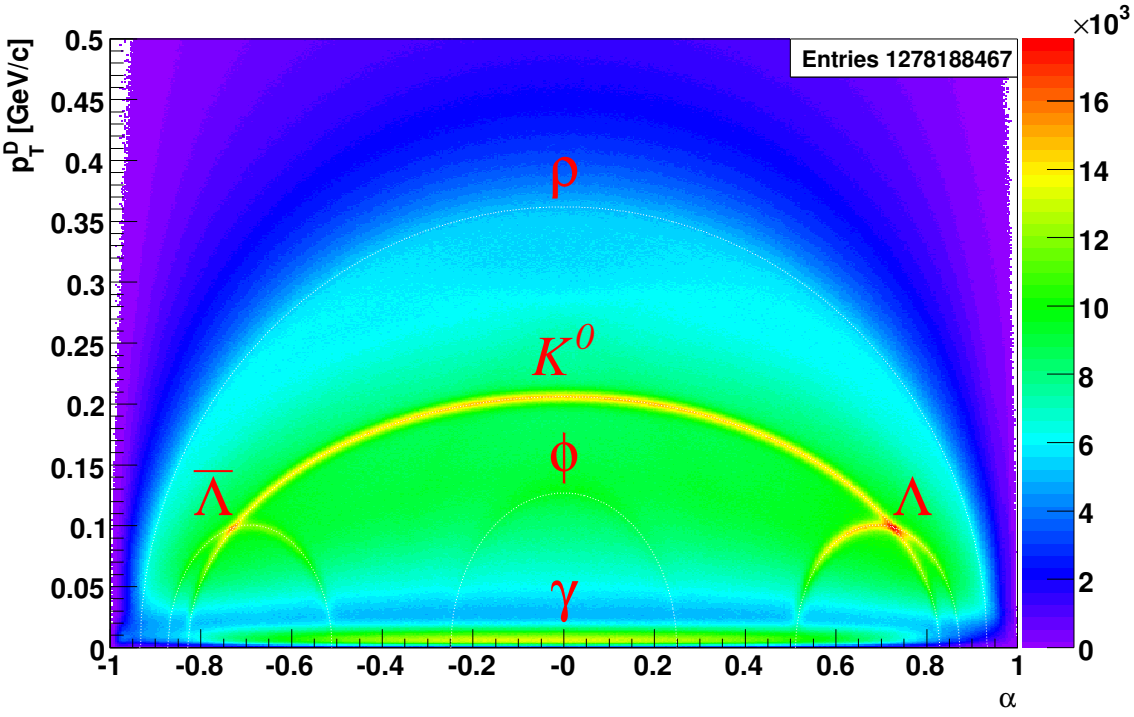

Figure 7.3: Armenteros-Podalanski plot of the V^0 sample after V^0 selection cuts (see subsection 7.2.3). Three prominent arcs from $\Lambda \longrightarrow p\,\pi^-$, $\overline{\Lambda} \longrightarrow \bar{p}\,\pi^+$, and $K_S^0 \longrightarrow \pi^+\,\pi^-$ are visible together with two faint arcs from $\rho(770) \longrightarrow \pi^+\,\pi^-$ and $\phi(1020) \longrightarrow K^+\,K^-$. The nominal positions of the arcs (assuming $\beta_{V^0} \approx 1$) are indicated by lines. The height of the arcs is defined by the breakup momentum of the V^0 decay. The decay $\gamma \longrightarrow e^+\,e^-$ has a very small phase space leading to a prominent broad line at low p_T^D.

The Ξ decays nearly exclusively into Λ and pion. Fig. 7.2b shows the event signature: In addition to the V^0 signature from the decaying Λ there is another charged track, that originates from a vertex, which lies between the primary and the Λ decay vertex. Since the Λ is a neutral particle, the Ξ decay vertex can be reconstructed only with a well-defined Λ candidate by finding the location of the closest approach of the reconstructed Λ track with that of the pion.

7.2.2 Definition of the Coordinate System

The process under investigation is the production of a hyperon H and an unobserved rest X by the interaction of a beam muon μ with a target nucleon N and the subsequent decay of the hyperon.

Fig. 7.4 illustrates this process in the laboratory frame with the help of the Λ hyperon. The incoming beam muon μ and the outgoing scattered muon μ' define the scattering plane, which is rotated with respect to the production plane by an angle φ_S around the direction of the virtual photon γ^*. The production plane is spanned by the virtual photon and the outgoing hyperon. The decay particles of the hyperon form the decay plane, which is rotated with respect to the production plane by an angle φ_D around the direction of the hyperon. Two transverse momenta are used in this analysis: the transverse momentum p_T of the hyperon with respect to the virtual photon and the momentum p_T^D of the decay daughter with respect to the hyperon direction. The latter is used to generate the Armenteros plot (see subsection 7.2.1), whereas p_T is an important kinematical variable of the hyperon production process.

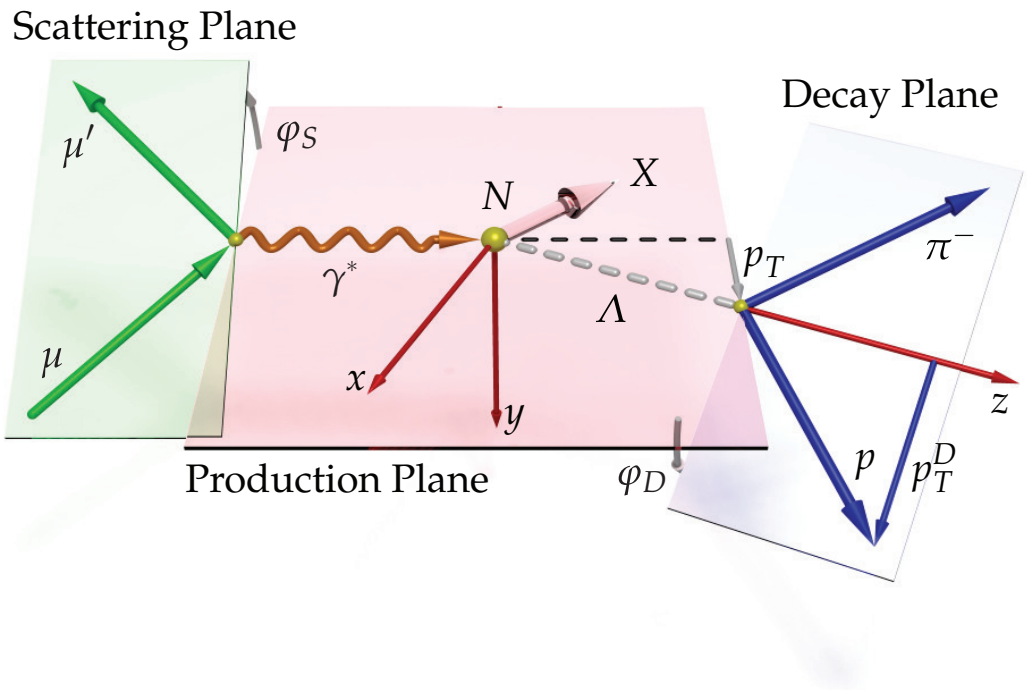

Figure 7.4: Definition of the coordinate system in the laboratory frame on the basis of the inclusive production of a Λ hyperon.

The normal of the production plane $\hat{n}$ is defined by the directions of the virtual photon and of the hyperon $\hat{n} = \vec{\gamma}^* \times \vec{H}$. It is taken as y-axis. The z-axis is defined by the direction

of the outgoing hyperon. This somewhat unusual choice (normally the beam direction, here $\vec{\gamma}^*$, is taken) is justified by the way the background from converted photons $\gamma \longrightarrow e^- e^+$ is suppressed in the case of the Λ (see subsection 7.2.4). To complete the right-handed coordinate system, the x-axis is set to $\vec{y} \times \vec{z}$.

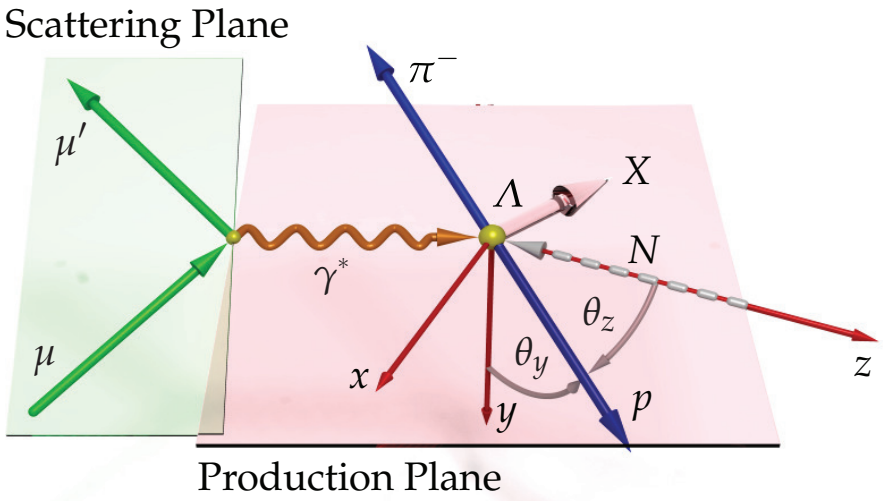

Figure 7.5: Definition of the coordinate system in the rest frame of the hyperon. The depicted process is the same as in fig. 7.4.

Fig. 7.5 shows the same process boosted into the rest frame of the hyperon, in which the angular distribution of the decay baryon is analyzed. The directions of the axes are unaffected by this transformation. The angular distribution, given by eq. (6.5), refers to the production plane normal, which is the y-axis. For the suppression of the converted photons a second angle θ_z with respect to the z-axis is needed (see subsection 7.2.4). To enhance the clarity of the notation, all values, that are defined with respect to the normal of the production plane, will be denoted with the subscript y instead of T for the rest of this chapter, so that the angular distribution reads:

$$\frac{\mathrm{d}N}{\mathrm{d}\cos\theta_y} = \frac{N_0}{2}\left(1 + \alpha_H P_y^H \cos\theta_y\right) \tag{7.4}$$

The COMPASS main reference system is defined with the z_{Lab}-axis in the mid-plane of the spectrometer and along the nominal beam axis. The y_{Lab}-axis is in the vertical direc-

tion and points upwards. To complete the right-handed coordinate system the x_{Lab}-axis points to the left (Jura direction), if looking downstream.

7.2.3 Selection of V^0 Events

A V^0 event has a at least four tracks – the beam and the scattered muon plus two charged tracks from the V^0 decay – and at least two vertices – the primary and the V^0 decay vertex. This condition is fulfilled by 45.97 % of all events.

The primary vertex has to have exactly one incoming track from the beam muon and an outgoing track, that was identified as the scattered muon. To ensure a good definition of the kinematics of the primary interaction, the event is allowed to have only one primary vertex. The identification of the scattered muon is improved by the requirement, that it traversed an amount of material, which is equivalent to a radiation length of more than 30 X_0. These cuts reduce the number of events from 45.97 % to 21.48 %.

The set of events is decreased further to 15.34 % by cutting on the target cell volume: The primary vertex is demanded to lie either in the upstream ($-100\,\mathrm{cm} < z_{\mathrm{Prim}} < -40\,\mathrm{cm}$) or in the downstream target cell ($-30\,\mathrm{cm} < z_{\mathrm{Prim}} < +30\,\mathrm{cm}$), in which its distance r_{Prim} from the z_{Lab}-axis has to be smaller than 1.4 cm, a value a little bit below the true target cell radius of 1.5 cm (see fig. 2.7). This is to compensate the imperfect alignment of the target and its movement due to the changing solenoid field. In addition the extrapolated beam muon trajectory is required to completely traverse both target cells in order to equalize the muon flux through the two cells in the selected sample (see fig. 7.6).

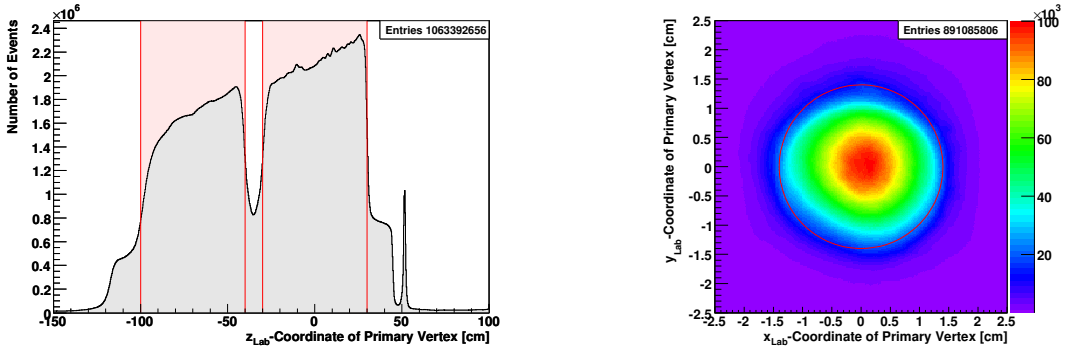

(a) (b)

Figure 7.6: Target cut: (a) Distribution of the z_{Lab}-coordinate of the primary vertex. The positions of the up- and downstream target cells are indicated by the shaded bands. The sharp peak at $z_{\mathrm{Lab}} \approx 50\,\mathrm{cm}$ is caused by the window of the target microwave cavity (see fig. 2.7 (page 23)). (b) Radial distribution of the position of the primary vertex after the cut on the z_{Lab}-position. The circle indicates the applied cut.

The above set of cuts gives a good definition of the primary vertex. In addition to the primary a secondary V^0 decay vertex is needed, which is defined as a non-primary vertex with no incoming track and exactly two outgoing tracks of opposite charge, that are not

identified as muons and which have to have an associated momentum. This condition is fulfilled by 15.27 % of all events with an average number of 3.38 V^0 vertex candidates per event. Fig. 7.7 shows the Armenteros plot of the raw V^0 sample together with the $m_{p\pi^-}$ invariant mass spectrum for the Λ hypothesis, where the positive track is assumed to be a proton and the negative one a pion. This assumption is only correct for the real Λ decays, which form a peak at the nominal Λ mass of 1115.683 MeV/c^2 [PDG04]. The goal of the cuts in this and in the following subsections is to reduce the background under the peak while retaining the signal in order to get as clean Λ and $\bar{\Lambda}$ samples as possible.

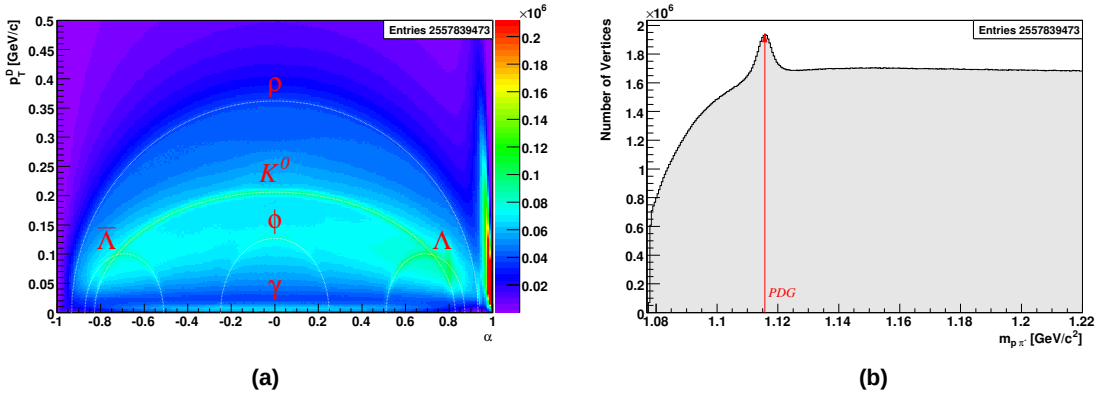

(a) (b)

Figure 7.7: Definition of the V^0 vertex: (a) Armenteros plot and (b) $m_{p\pi^-}$ invariant mass distribution of the raw V^0 sample. The structure around $\alpha \approx 1$ in the Armenteros plot is caused by unidentified halo muons. To better visualize the arcs, the Armenteros plot was clipped at 60 % of its maximum value. The arrow in (b) indicates the nominal value of the Λ mass.

The Armenteros plot in fig. 7.7 shows a prominent structure around $\alpha \approx 1$. A longitudinal momentum asymmetry of $\alpha \approx 1$ means, that the longitudinal momentum of the negative particle is negligible compared to that of the positive particle. The momentum distributions of the positive and negative V^0 daughters, as shown in fig. 7.8a and b, are similar, except that for the positive particle the distribution has a secondary peak around the beam momentum. This indicates, that positive halo muons (see subsection 2.2.1), which were not identified as muons, contaminate the V^0 sample. A cut at 140 GeV/c suppresses the halo component and reduces the number V^0 events from 15.27 % to 14.67 % and that of the V^0 vertex candidates to 93.69 %.

In order to ensure a precise measurement of the momentum of the V^0 decay particles, and thus of the reconstructed V^0 mass, the daughter trajectories are required to have passed through the first spectrometer magnet SM1 by demanding a last measured point with $z_{\text{Lab}} > 360\,\text{cm}$ (see fig. 2.5 (page 16)). Because only V^0s produced in the primary interaction are of interest, the V^0 vertex has to lie downstream of the primary vertex ($z_{V^0} > z_{\text{Prim}}$). Both cuts together decrease the number of V^0 events from 14.67 % to 11.30 % and the number of V^0 vertices from 93.69 % to 49.97 % (see fig. 7.9).

The above cuts are summarized in table 7.2. They select a sample of 559,200,000 generic V^0 events each containing on average 2.29 V^0 vertices.

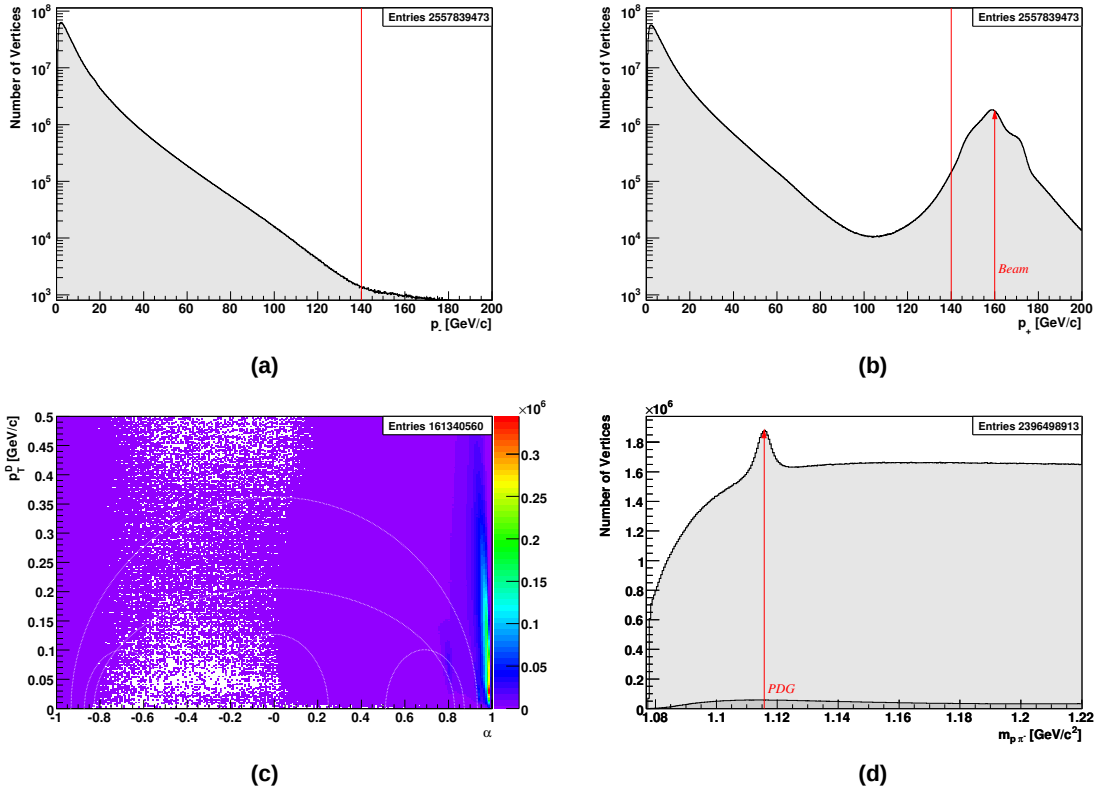

Figure 7.8: Suppression of halo muons: (a) Distribution of the momentum of the negative V^0 daughter particle. (b) shows the same for the positive particle. A peak around the beam momentum, indicated by the arrow, is clearly visible. The vertical line marks the cut on the momentum. (c) Armenteros plot of the sample, that was cut away. (d) $m_{p\pi^-}$ invariant mass distribution after the cut. The darker area shows the sample, that was cut away.

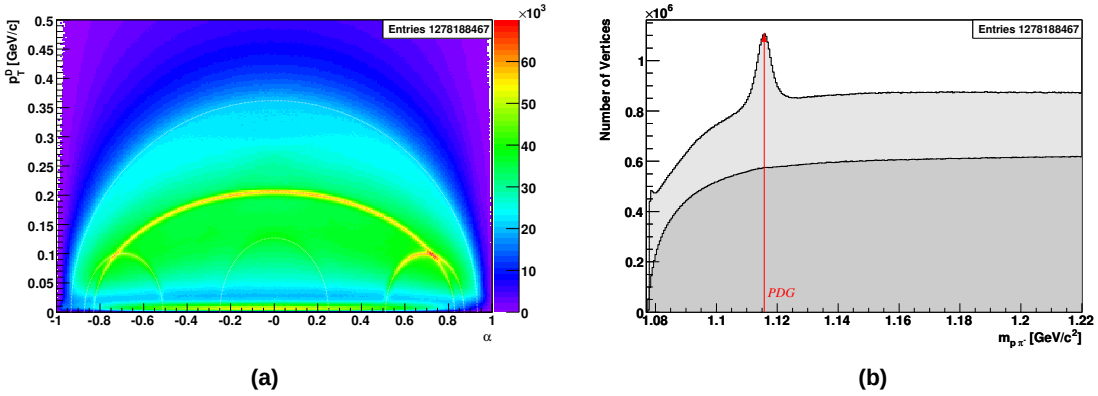

Figure 7.9: V^0 sample after selection: (a) Armenteros plot and (b) $m_{p\pi^-}$ invariant mass distribution of the final V^0 sample, which is obtained by requiring, that the V^0 daughter tracks have a last measured z_{Lab}-position larger than 360 cm and that the V^0 vertex lies downstream of the primary of vertex. The darker area in (b) shows the sample, that was cut away.

Cut	Number of Events		Number of V^0 vertices	
	[10^6]	[%]	[10^6]	[%]
Initial data set	4949.470	—	—	—
$N_{\text{Track}} \geq 4, N_{\text{Vertex}} \geq 2$	2275.498	45.97	—	—
Definition of primary vertex	1063.393	21.48	—	—
Target Cut	759.077	15.34	—	—
Definition of V^0 vertex	755.968	15.27	2557.839	—
Suppression of halo muons	725.944	14.67	2396.499	93.69
Daughters pass SM1, V^0 decay topology	559.196	11.30	1278.188	49.97

Table 7.2: Summary of the V^0 selection cuts: The table lists, how the different cuts reduce the absolute and relative number of V^0 events and vertices, respectively. In total 559,195,694 events with 1,278,188,467 V^0 vertex candidates fulfill the selection criteria.

7.2.4 Selection of Λ and $\overline{\Lambda}$ Events

The hyperon polarization manifests itself as a small asymmetry in the angular distributions of the decay daughters. The angular distributions need to be extracted with a high precision, that is the background corrections have to be kept as low as possible in order to reduce the error. Based on the preselected V^0 sample, the following cuts mainly aim at extracting clean Λ and $\overline{\Lambda}$ samples, by removing as much background as possible with the least loss of signal.

Tracks with low momentum are very sensitive to the traversed magnetic field. In the first part of the spectrometer there is a region, where the fringe fields of the target solenoid and the SM1 dipole overlap. Because of the complicated interplay of these two fields, the description of the magnetic field is less accurate in this region, which makes the track reconstruction and vertex finding more difficult and leads to a less precise momentum measurement for small momentum tracks. To avoid these problems, the momentum of the V^0 daughters is required to be larger than 1 GeV/c, which reduces the number of Λ candidates to 95.62 % of all preselected V^0 vertices (see fig. 7.10).

The signal to background ratio of the Λ hyperons depends strongly on the z_{Lab}-position of the Λ decay vertex. If the Λ decays inside the target cells, the background rises strongly, the more upstream the decay vertex lies. A good compromise between keeping as many Λs as possible and having a background as low as possible is to take decay vertices with $z_{V^0} > +0\,\text{cm}$ (see [Wie04]). There is also an upper limit to the z_{Lab}-coordinate of the V^0 vertex, which comes from the fact, that one wants to select those V^0s, where the daughters traversed the MicroMeGaS stations in front of the first spectrometer magnet. In this region the MicroMeGaS are the detectors with the highest spatial resolution and

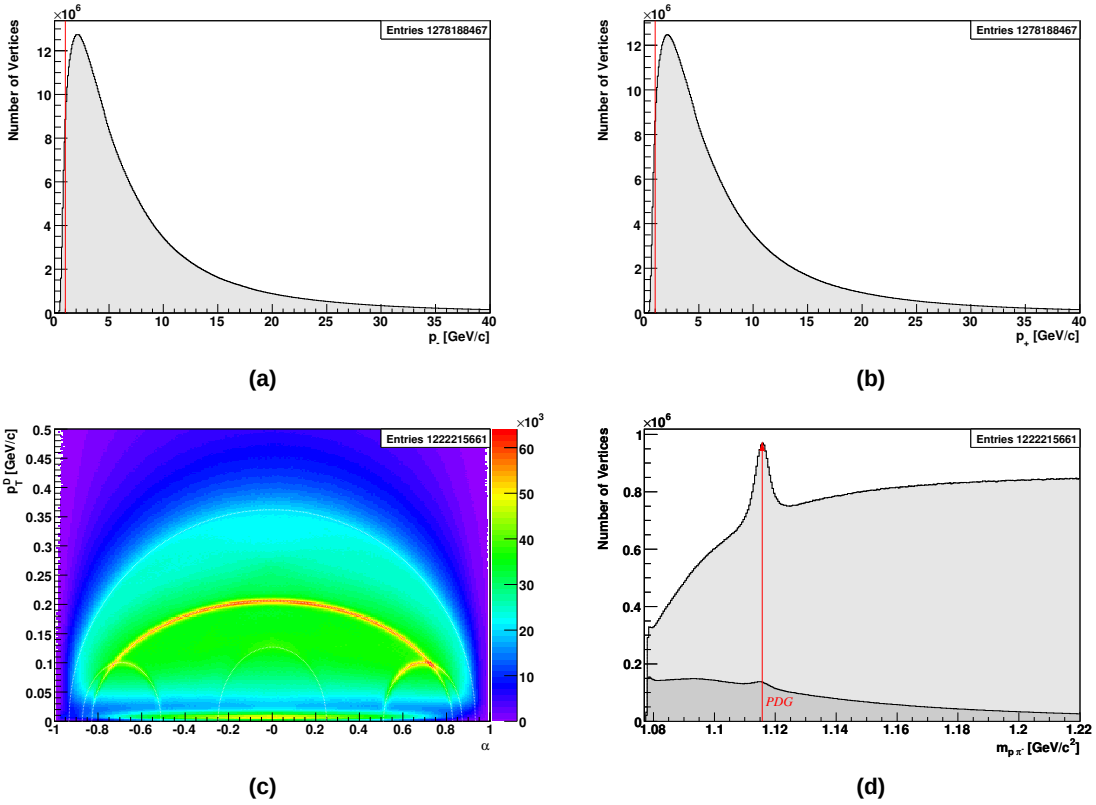

Figure 7.10: Removal of fringe field tracks: (a) Momentum distribution of the negative and (b) the positive V^0 daughter. The cut on this variable is indicated by the vertical line. (c) Armenteros plot and (d) $m_{p\pi^-}$ invariant mass distribution after the cut. The darker area in (d) shows the sample, that was cut away.

therefore provide a precise track definition leading to a good mass resolution. Consequently z_{V^0} is restricted to values smaller than 140 cm, which is the position of the first MicroMeGaS plane (see fig. 2.5 (page 16)). Both cuts together lead to a reduction of the V^0 sample from 95.62 % to 42.12 % (see fig. 7.11).

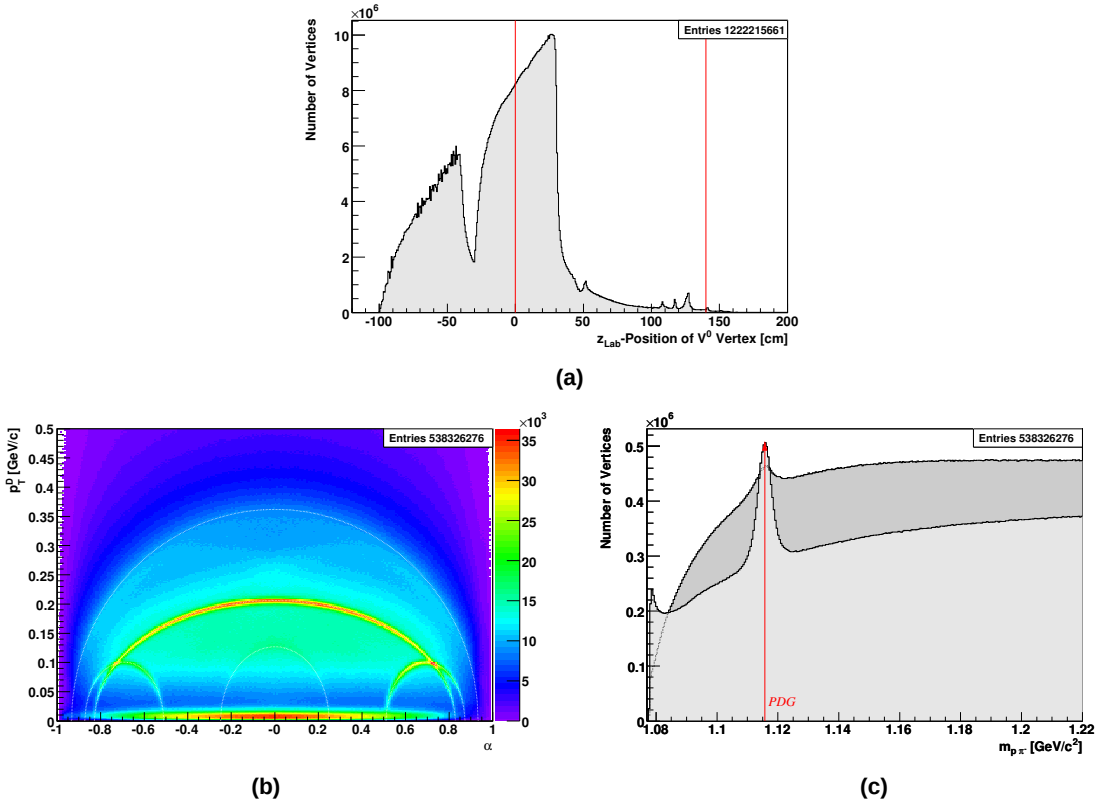

Figure 7.11: V^0 decay vertex position: (a) z_{Lab}-distribution of the V^0 vertex. The vertical lines indicate the applied cut. (b) Armenteros plot and (c) $m_{p\pi^-}$ invariant mass distribution after the cut. The darker area in (c) shows the sample, that was cut away.

Because of the finite spatial resolution of the measured charged particle trajectories, V^0 decay vertices close to the primary vertex can be the result of wrong track combinations. This effect is suppressed by demanding, that the V^0 vertex lies more than 20 cm downstream of the primary vertex, which decreases the number of V^0 vertices from 42.12 % to 11.80 % (see fig. 7.12).

The measurement of the Λ polarization has a direct interpretation in terms of the production mechanism only, if the Λs were produced directly in the primary interaction. On the other hand the Λ sample includes contributions of Λs from the decay of Ξ and Σ hyperons, which are experimentally difficult to separate. The fraction of prompt Λs can be enhanced by imposing a cut on the back-pointing of the reconstructed Λ momentum to the primary vertex (collinearity). The number of vertices is lowered from 11.80 % to 6.64 % by requiring, that the angle between the Λ momentum and the line connecting primary and Λ decay vertex is smaller than 15 mrad (see fig. 7.13). Like the previous

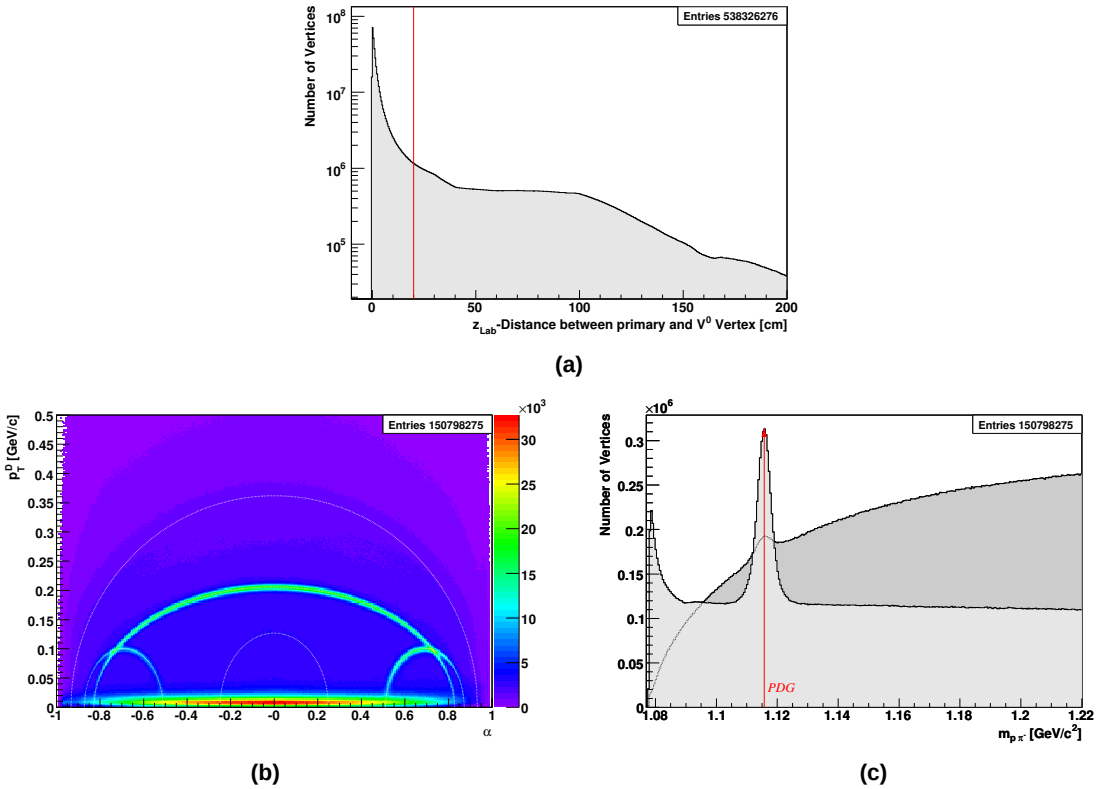

Figure 7.12: Vertex Separation: (a) Distribution of the difference of the z_{Lab}-coordinates of primary and V^0 vertex. The applied cut is indicated by the vertical line. (b) Armenteros plot and (c) $m_{p\pi^-}$ invariant mass distribution after the cut. The darker area in (c) shows the sample, that was cut away.

cut on the vertex separation this one also suppresses V^0 vertices that, due to the limited spatial resolution, were formed out of wrongly combined tracks.

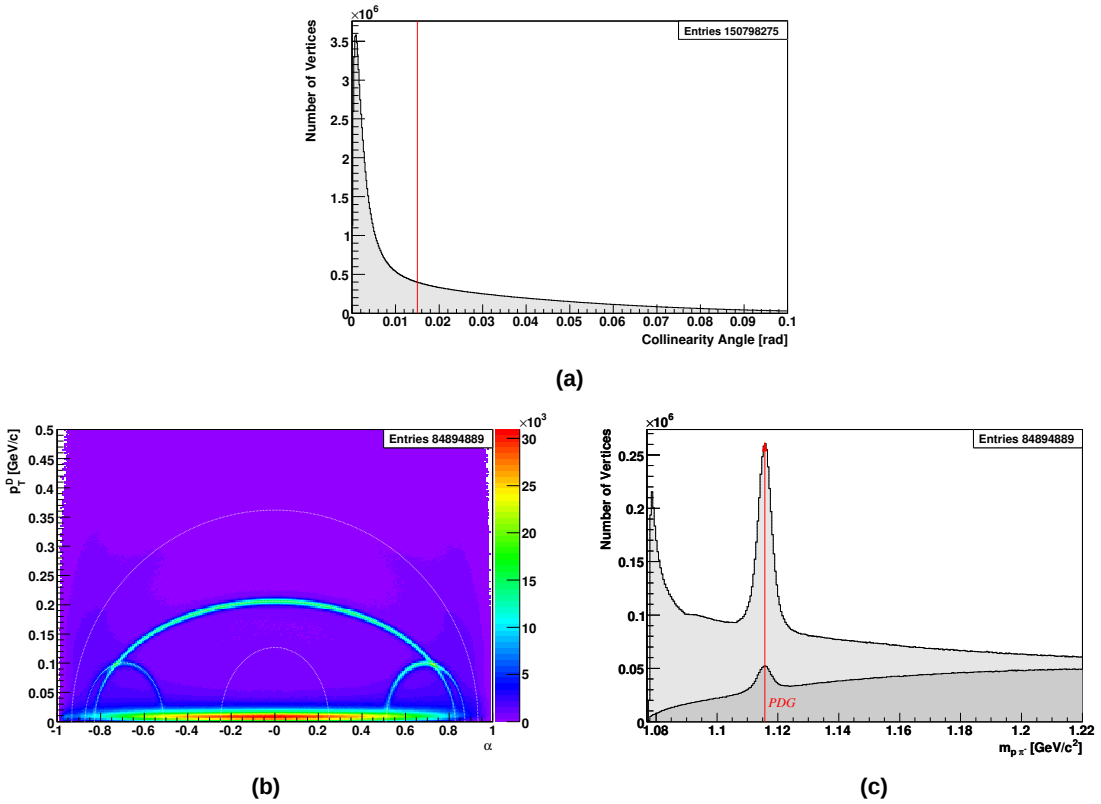

Figure 7.13: Collinearity cut: (a) Collinearity angle of the V^0 vertices. The vertical line indicates the applied cut. (b) Armenteros plot and (c) $m_{p\pi^-}$ invariant mass distribution after the cut. The darker area in (c) shows the sample, that was cut away.

In order to have a good definition of the production plane and thus of the direction of the polarization analyzer (see subsection 7.2.2), the transverse momentum p_T of the V^0 with respect to the direction of the virtual photon is demanded to be larger than 100 MeV/c, which is comparable to the resolution in this variable [Kan] and reduces the number of V^0 candidates from 6.64 % to 5.80 % (see fig. 7.14).

From fig. 7.14a it is evident, that the sample still contains a lot of converted photons, which contribute to the background under the Λ peak. This background is suppressed by discarding those vertices, where the track of the pion candidate is associated both with the secondary and the primary vertex, which, because of the separation of the two vertices, is only correct for the decays, in which the pion is emitted in or opposite to the direction of the Λ. Only a small number of true Λs is affected by the cut, since the pion for kinematical reasons is in the most cases emitted with a larger angle with respect to the Λ direction (see fig. 7.15). The same is not true for the proton daughter. A cut on

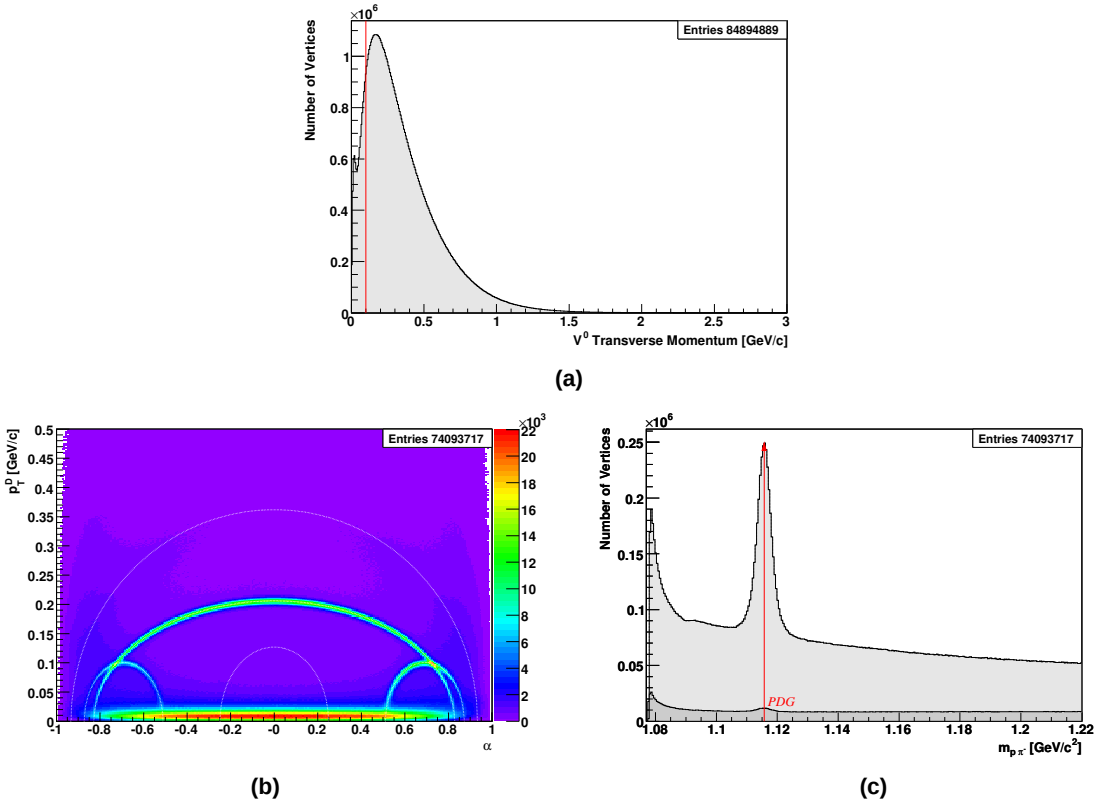

Figure 7.14: Definition of the production plane: (a) Distribution of the transverse momentum p_T of the V^0 with respect to the direction of the virtual photon. The cut on this variable is indicated by the vertical line. (b) Armenteros plot and (c) $m_{p\pi^-}$ invariant mass distribution after the cut. The darker area in (c) shows the sample, that was cut away.

the proton's association with the primary vertex would cleanup the sample further, but would also remove a considerable amount of true Λs. In total the cut lowers the number of vertices from 5.58 % to 2.46 %.

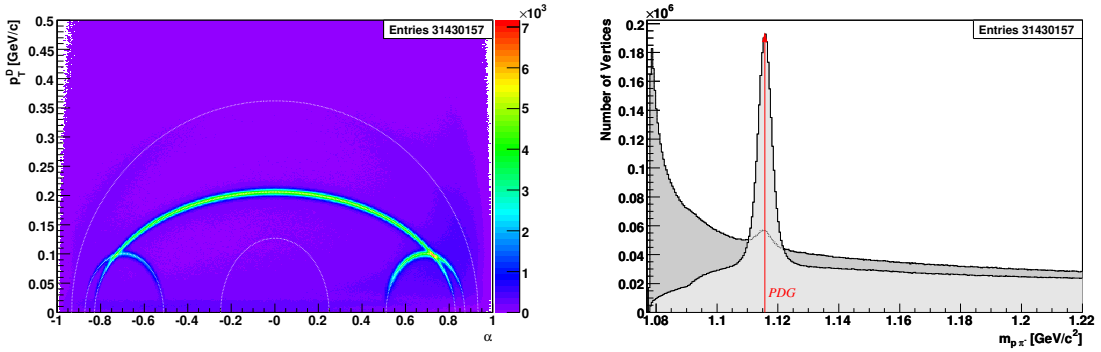

(a) (b)

Figure 7.15: Cut on pion association with the primary vertex: (a) Armenteros plot and (b) $m_{p\pi^-}$ invariant mass distribution after requiring, that the daughter pion candidate of the V^0 vertex is *not* associated with the primary vertex. The darker area in (b) shows the sample, that was cut away.

The remaining background from converted photons is usually removed by cutting away the region of low transverse momenta p_T^D, but this method has a drawback: It distorts the $\cos\theta_y$ distribution of the decay particles (see subsection 7.2.2), from which the polarization is extracted. As will be explained in section 7.3 the extraction method for the polarization assumes, that the acceptance is symmetric with respect to the mid-plane of the spectrometer and consequently is also symmetric in $\cos\theta_y$. This means that the applied cuts must not affect this symmetry, which renders the simple p_T^D cut unfavorable. But there is an alternative method to suppress the converted photons: The converted photons have small angles θ_z with respect to the reconstructed V^0 direction in the V^0 rest frame. Therefore they accumulate mainly at the edges of the $\cos\theta_z$ spectrum and are suppressed by cutting on angles with $|\cos\theta_z| < 0.8$ (see fig. 7.16a, b and c). The cut decreases the number of V^0 vertices from 2.46 % to 1.14 % and also reduces the number of Λ hyperons by a non-negligible amount, but fig. 7.16d shows, that still more background than signal is discarded. Fig. 7.16e illustrates that the $\cos\theta_z$ cut acts symmetrically in $\cos\theta_y$, so that it does not disturb the mid-plane symmetry of the acceptance.

In the 2002 data taking period the acceptance of the outer and middle trigger hodoscopes (see chapter 4) was not up-down asymmetric. Consequently events, which are exclusively defined by those hodoscopes, are excluded, which has only a small impact on the statistics and reduces the number of Λ candidates from 1.14 % to 1.12 % (see fig. 7.17).

Table 7.3 summarizes the applied selection cuts, that define the Λ and $\overline{\Lambda}$ samples used for the polarization analysis. The 14,334,000 V^0 vertices contain 1,626,000 Λs and 854,000 $\overline{\Lambda}$s. In addition a K^0 sample is extracted for systematic studies (see section 8.2) by applying the above cut set with the exception, that the association of the daughter pions with

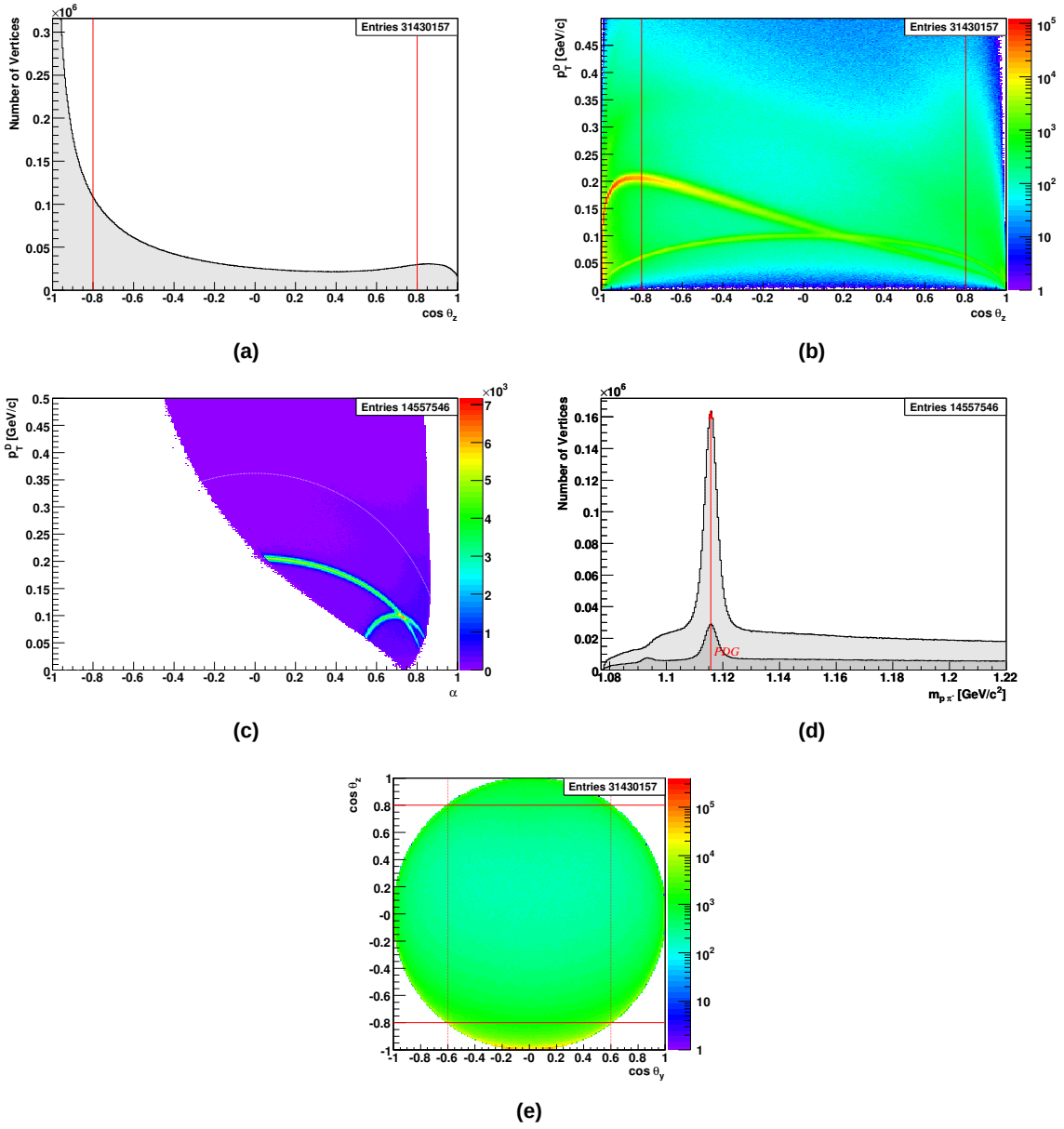

Figure 7.16: Suppression of converted photons: (a) $\cos\theta_z$ distribution of the positive decay daughter under $m_{p\pi^-}$ invariant mass hypothesis. The distribution strongly deviates from the uniform distribution, that one would expect for the Λ, which decays forward-backward symmetrically in its rest frame. The vertical lines indicate the cut in this variable. In (b) the $\cos\theta_z$ distribution is expanded with the transverse momentum p_T^D of the V^0 daughters with respect to the V^0 direction (like it is also used in the Armenteros plot), so that the contributions from the different V^0 species are disentangled (note the logarithmic z-scale): The symmetric arc is formed by the Λs, the photons accumulate at large values of $|\cos\theta_z|$, and the Kaons make the asymmetric arc, that peaks at $p_T^D \approx 0.2\,\mathrm{GeV}/c$ and $\cos\theta_y \approx -0.9$. (c) Armenteros plot and (d) $m_{p\pi^-}$ invariant mass distribution after cut on $\cos\theta_z$. The sample, that was cut away, is shown by the darker area in (d). (e) Correlation of $\cos\theta_z$ and $\cos\theta_y$: It is evident, that the cut on $\cos\theta_z$ is symmetric in $\cos\theta_y$.

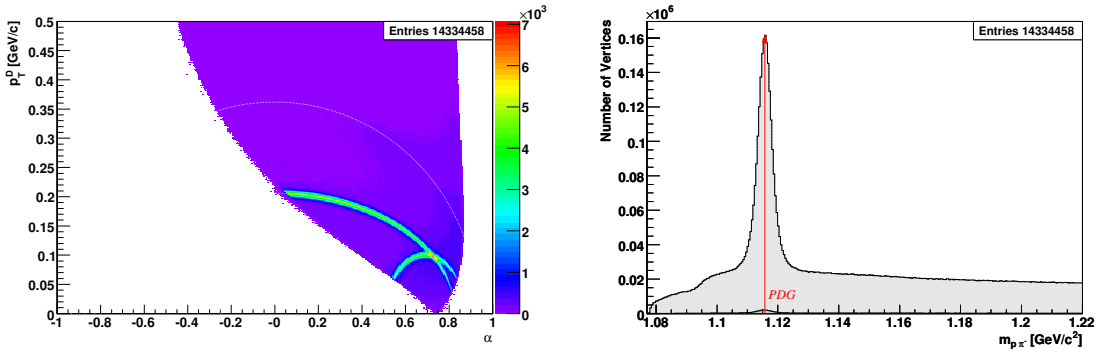

(a) (b)

Figure 7.17: Λ sample after selection: (a) Armenteros plot and (b) $m_{p\pi^-}$ invariant mass distribution of the final Λ sample after excluding events, that were exclusively triggered by the outer or the middle trigger hodoscopes. The darker area in (b) shows the sample, that was cut away.

the primary vertex is not checked. The resulting 10,547,000 K^0s partly contribute to the background under the Λ and $\overline{\Lambda}$ peak, respectively.

Cut	Number of V^0 vertices	
	[10^6]	[%]
V^0 selection cuts (see subsection 7.2.3)	1278.188	—
Removal of fringe field tracks	1222.216	95.62
V^0 vertex position	538.326	42.12
Vertex separation	150.798	11.80
Collinearity	84.895	6.64
Definition of production plane	74.094	5.80
Pion association with primary vertex	31.430	2.46
Suppression of converted photons, $\cos\theta_z$ cut	14.558	1.14
Removal of outer and middle trigger	14.334	1.12

Table 7.3: Summary of the cuts, that define the Λ and $\overline{\Lambda}$ sample: The Table shows the absolute and relative reduction of the number of Λ candidates by the different cuts. In total 14,334,458 V^0 vertices fulfill the selection criteria.

Fig. 7.18 shows the invariant mass plots for the Λ, $\overline{\Lambda}$, and K^0 hypothesis, respectively. Since the lifetimes of the three particles are rather long, their natural widths ($\Gamma_{\Lambda,\overline{\Lambda}} = 2.501$ μeV/c^2, $\Gamma_{K^0_S} = 7.351$ μeV/c^2) practically do not contribute to the measured widths, which therefore purely reflect the resolution of the spectrometer.

The Λ and $\overline{\Lambda}$ peaks still sit on a nonvanishing background, which is subtracted using two different methods: In the polarization analysis the invariant mass histograms are fitted by a function, that models signal and background as described in subsection 7.4.1. For all

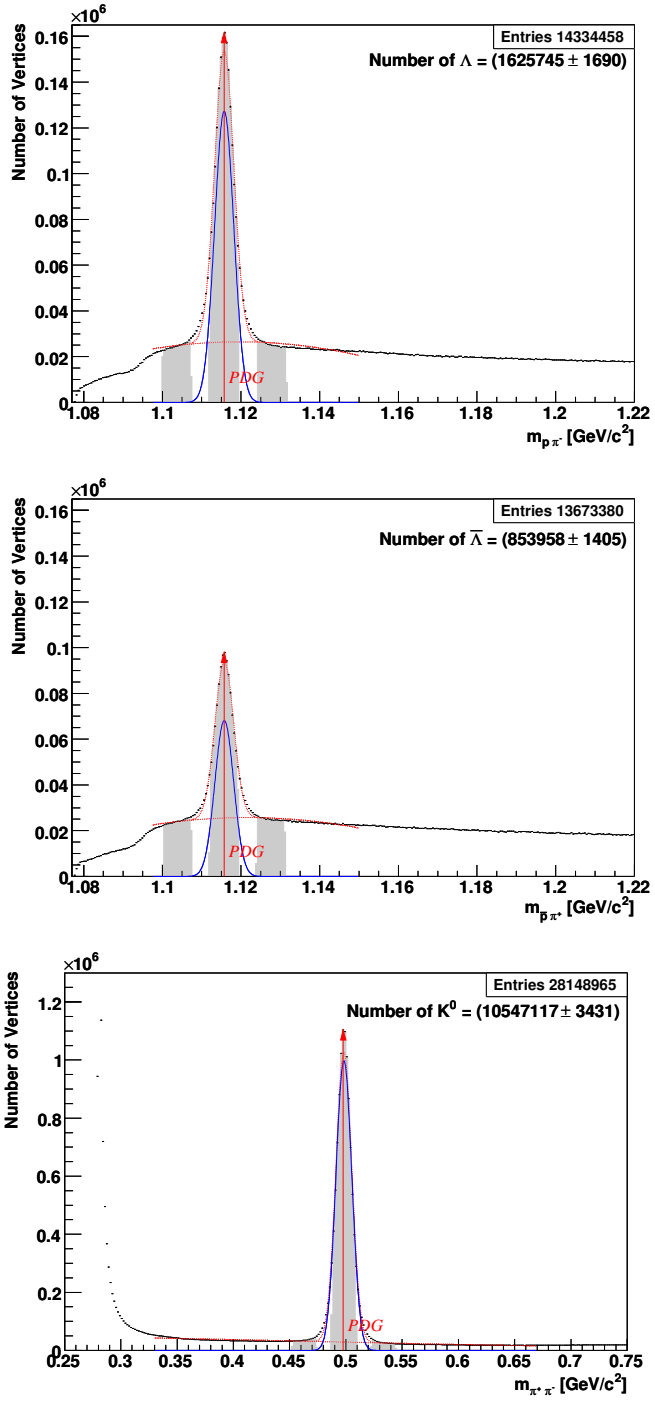

Figure 7.18: Final Λ and $\overline{\Lambda}$ samples after event selection: The upper two plots show the $m_{p\pi^-}$ and the $m_{\bar{p}\pi^+}$ invariant mass distributions, respectively. The 1,626,000 Λs in the peak have a mean mass of 1115.72 MeV/c^2, which corresponds to a deviation of $\Delta m = 40$ keV/c^2 with respect to the PDG value. The width of the Λ peak is $\sigma_\Lambda = 2.43$ MeV/c^2. The mass of the 854,000 $\overline{\Lambda}$s is measured to 1115.74 MeV/c^2 ($\Delta m = 60$ keV/c^2) with a resolution of $\sigma_{\overline{\Lambda}} = 2.38$ MeV/c^2. The lower plots depicts the $m_{\pi^+\pi^-}$ invariant mass distribution. The 10,547,000 K^0s are reconstructed with a mass of 498.24 MeV/c^2 ($\Delta m = 590$ keV/c^2) and a width of $\sigma_{K^0} = 7.02$ MeV/c^2. The fitting procedure is described in subsection 7.4.1. In all three plots the shaded bands indicate the peak- and side-band regions used for the background subtraction.

other distributions, like e.g. the transverse momentum p_T of the Λs or their momentum fraction x_F, first the kaon background is suppressed by excluding V^0s, that lie within a $\pm 2\,\sigma_{K^0}$ range around the measured K^0 mass, and then the side-band subtraction method is applied. This method combines distributions of the particular variable, taken in three invariant mass regions: a region around the mass peak (the peak-band) and two regions some distance apart from the peak (the side-bands). All three mass regions are disjoint and the side-bands lie symmetric with respect to the peak. The background corrected distribution of the variable under consideration is obtained by subtracting the side-band distributions from the peak distribution. The side-band method is able to correct for background contributions up to first order, because if the background is linear in the invariant mass, the background samples in the two side-bands average exactly to the background under the peak. For Λ and $\overline{\Lambda}$ a peak-band with a width of $3\,\sigma_{\Lambda,\overline{\Lambda}}$ is used together with $3\,\sigma_{\Lambda,\overline{\Lambda}}$ wide side-bands, that are centered at $\pm 5\,\sigma_{\Lambda,\overline{\Lambda}}$ from the peak, where $\sigma_{\Lambda,\overline{\Lambda}}$ is the width of the fitted Gaussian (see fig. 7.18).

7.2.5 Selection of Ξ^- and $\overline{\Xi}^+$ Events

The Ξ selection criteria applied in this analysis are similar to those used in the pentaquark search analysis [Age05, DeM04]. A Ξ event has to have a V^0 decay vertex and an additional pion track from the Ξ decay (cf. subsection 7.2.1). Therefore each V^0 vertex, that fulfills the general V^0 selection criteria (see subsection 7.2.3), is combined with each additional track in the event, that has a momentum associated with it and that is neither a muon nor one of the decay particles of the V^0 vertex under consideration. For each combination of V^0 and pion candidate the point of closest approach with the reconstructed V^0 candidate is computed. If a closest approach is found, the combination is considered as a Ξ vertex candidate. The data set contains in total $2.007 \cdot 10^9$ Ξ^- vertex candidates, where the pion candidate has negative charge, and $2.376 \cdot 10^9$ $\overline{\Xi}^+$ candidates, where the pion is charged positively. Fig. 7.19 shows the Armenteros plot and the $m_{\Lambda\pi^-}$ invariant mass histogram of the raw Ξ sample. The $m_{\Lambda\pi^-}$ mass histogram, like the ones further below, is generated by assuming proton and pion mass for the V^0 decay tracks and pion mass for the additional track.

Like for the Λ contaminations from unidentified halo muons are suppressed by requiring, that the momentum of the pion candidate is less than 140 GeV/c, which removes 0.07 % of the Ξ^- and 9.66 % of the $\overline{\Xi}^+$ vertices from the sample (see fig. 7.20).

Due to the topology of the Ξ decay, the point of closest approach of the V^0 and the pion candidate, which is taken as the position of the Ξ decay vertex, has to lie downstream of the primary and upstream of the V^0 decay vertex. This lowers the number the Ξ^- candidates from 99.93 % to 30.26 % and that of the $\overline{\Xi}^+$ candidates from 90.34 % to 27.39 % (see fig. 7.21).

Similarly to the V^0 selection the trajectory of the pion candidate is required to have a last measured point with a z_{Lab}-coordinate larger than 360 cm, so that the particle has to pass

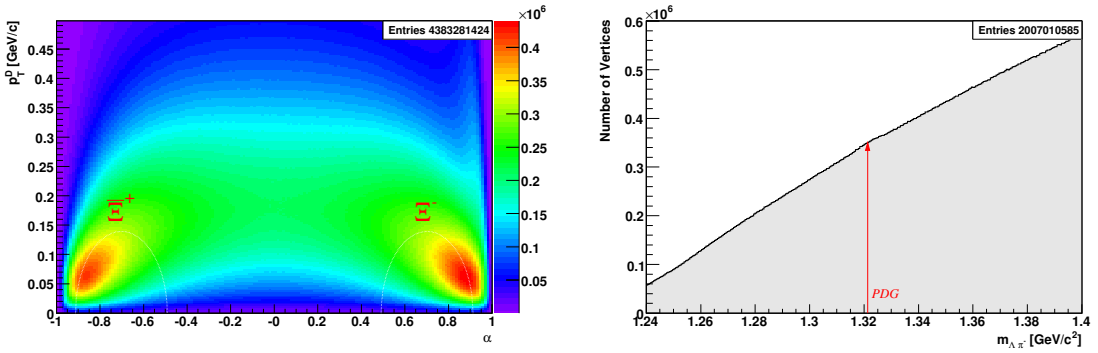

(a) (b)

Figure 7.19: Definition of Ξ vertex: (a) Armenteros plot and (b) $m_{\Lambda\pi^-}$ invariant mass distribution for the raw Ξ sample. Due to the large background, the Ξ^- and $\overline{\Xi}^+$ arcs are not visible, but their nominal position is indicated by lines.

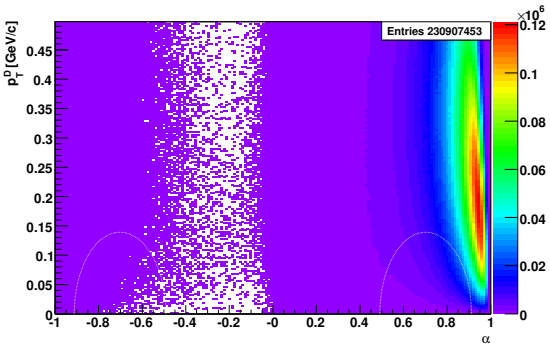

Figure 7.20: Suppression of halo muons: Armenteros plot of the sample, that is cut away by demanding the momentum of the pion candidate to be lower than 140 GeV/c.

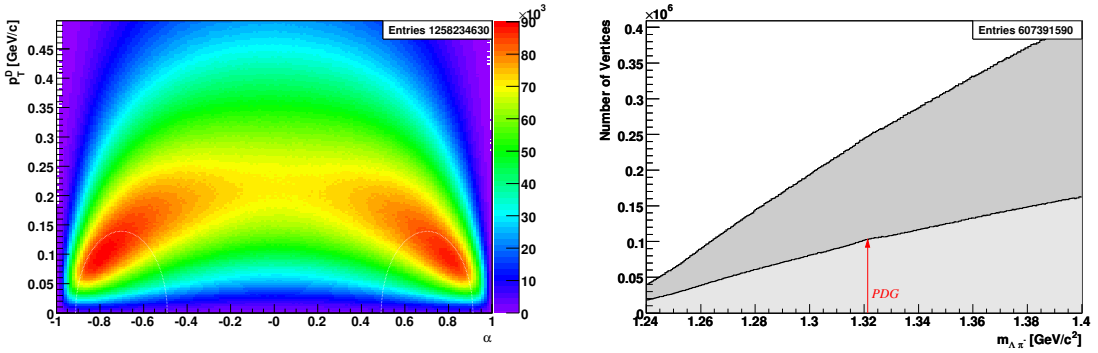

(a) (b)

Figure 7.21: Ξ decay topology: (a) Armenteros plot and (b) $m_{\Lambda\pi^-}$ invariant mass distribution after excluding Ξ vertices, that do not lie in-between the primary and the V^0 vertex. The darker area in (b) shows the sample, that was cut away.

through the first spectrometer magnet SM1 (see fig. 2.5), which ensures a precise momentum measurement and reduces the sample of Ξ^- candidates from 30.26 % to 28.89 % and that of the $\overline{\Xi}^+$ candidates from 27.39 % to 26.17 % (see fig. 7.22).

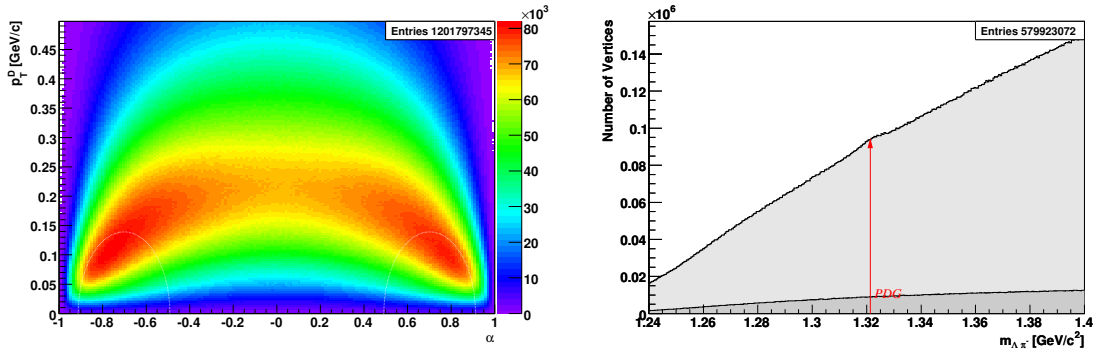

Figure 7.22: Pion passes through SM1: (a) Armenteros plot and (b) $m_{\Lambda\pi^-}$ invariant mass distribution after requiring, that the pion candidate flew through SM1. The darker area in (b) shows the sample, that was cut away.

The Ξ sample is cleaned by improving the definition of the Λ vertex. To this end some cuts of the Λ selection (see subsection 7.2.4) are applied to the V^0 vertex: The V^0 daughter tracks are required to have a momentum larger than 1 GeV/c to suppress fringe field tracks. The V^0 decay vertex has to be located in the range 0 cm $< z_{V^0} <$ 140 cm and has to lie at least 20 cm downstream of the primary vertex. A collinearity cut is *not* applied, because it would suppress Ξ decays, where the Λ has a higher transverse momentum with respect to the Ξ. The Λ vertex definition decreases the number of Ξ^- vertices from 28.89 % to 6.626 % and that of the $\overline{\Xi}^+$ vertices from 26.17 % to 6.024 % (see fig. 7.23).

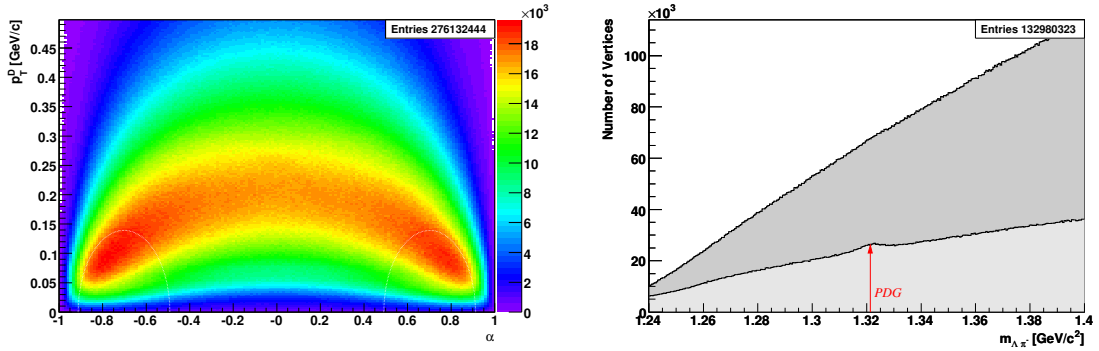

Figure 7.23: Definition of Λ vertex: (a) Armenteros plot and (b) $m_{\Lambda\pi^-}$ invariant mass distribution after the cut. The darker area in (b) shows the sample, that was cut away.

A further cleanup of the Ξ sample is achieved by cutting on the distance of closest approach (DCA) of the pion candidate track and the reconstructed V^0 track. By requiring a

DCA of less than 0.8 cm the number of Ξ^- vertices is lessened to 4.719 % and that of the $\overline{\Xi}^+$ candidates to 4.314 % (see fig. 7.24).

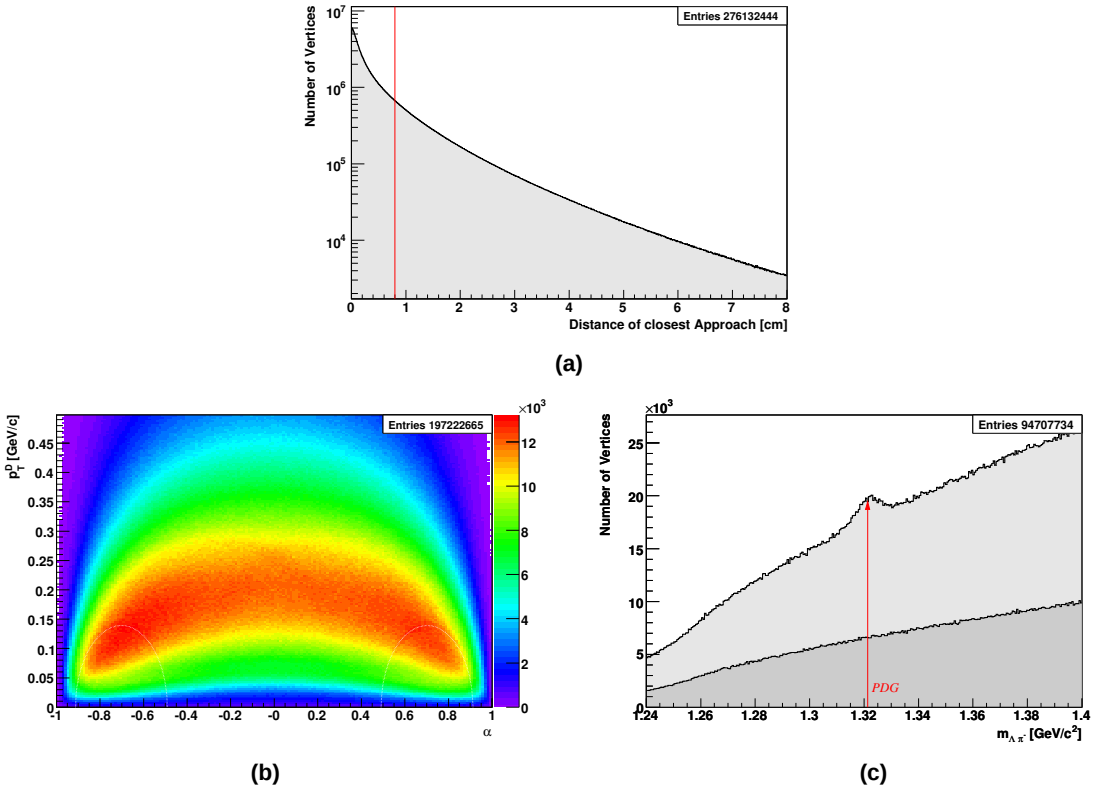

Figure 7.24: DCA of Ξ vertex: (a) DCA distribution of all pion and V^0 track before the cut, that is indicated by the vertical line. (b) Armenteros plot and (c) $m_{\Lambda\pi^-}$ invariant mass distribution after the cut. The darker area in (c) shows the sample, that was cut away.

As in the Λ selection the transverse momentum p_T of the Ξ with respect to the direction of the virtual photon is demanded to be larger than 100 MeV/c. This ensures a good definition of the production plane and thus of the direction of the polarization analyzer (see subsection 7.2.2) and decreases the Ξ^- sample to 4.500 % and the $\overline{\Xi}^+$ sample to 4.125 % (see fig. 7.25).

A great deal of background is suppressed, if the pion candidate track is required to *not* be associated with the primary vertex. Like in the Λ case this affects only a small fraction of real Ξs, where the emitted pion is nearly collinear with the Ξ, but removes all those candidates, where the Ξ decay vertex was not resolved (medium shaded histogram in fig. 7.26b). The sample is cleaned further by applying the same condition to the pion candidate from the V^0 vertex (dark shaded histogram in fig. 7.26b). The two cuts lower the number of Ξ^- candidates from 4.500 % to 1.002 % and that of the $\overline{\Xi}^+$ candidates from 4.125 % to 0.968 %.

An additional suppression of the contamination of the Λ vertices by converted photons is achieved by demanding $\left|\cos\theta_z^p\right| < 0.8$, where $\cos\theta_z^p$ is the angle of the Λ decay proton

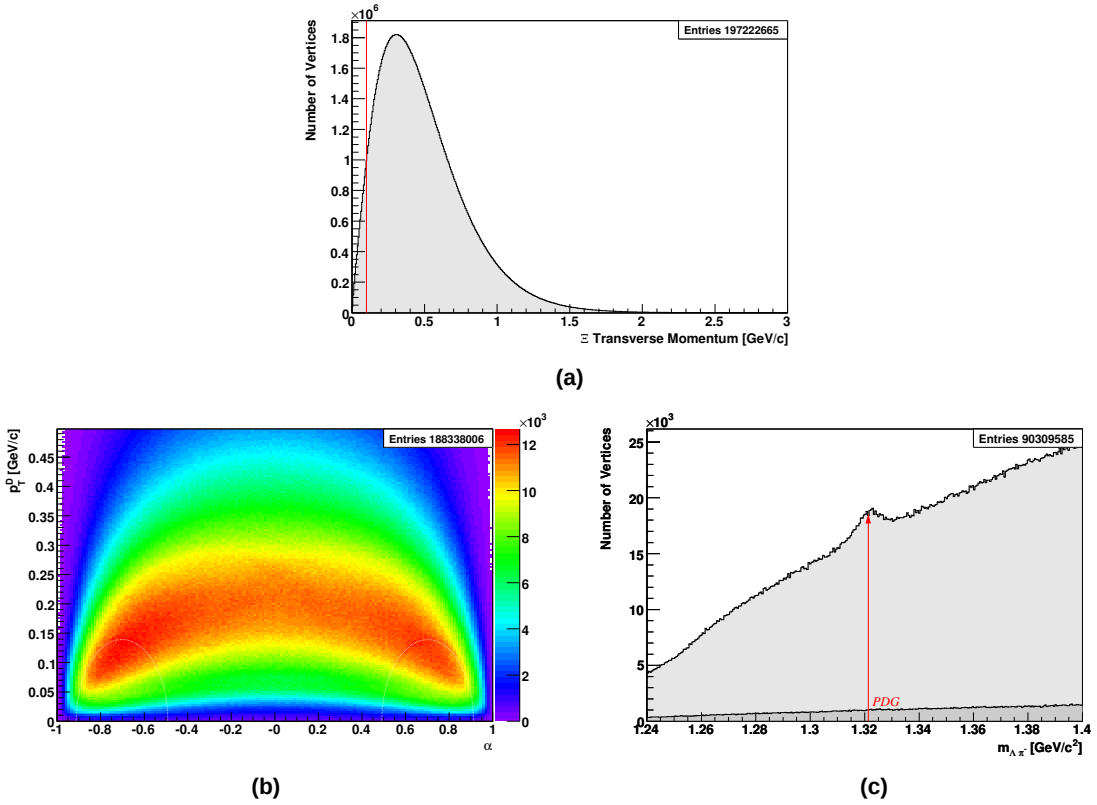

Figure 7.25: Definition of production plane: (a) Distribution of the transverse momentum p_T of all Ξ candidates with respect to the direction of the virtual photon. The cut on this variable is indicated by the vertical line. (b) Armenteros plot and (c) $m_{\Lambda\pi^-}$ invariant mass distribution after the cut. The darker area in (c) shows the sample, that was cut away.

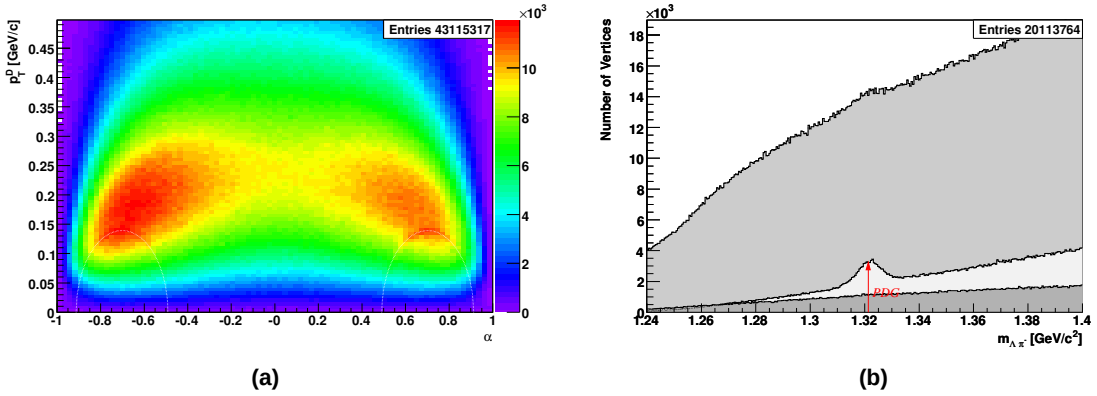

Figure 7.26: Cut on pion association with the primary vertex: (a) Armenteros plot and (b) $m_{\Lambda\pi^-}$ invariant mass distribution after excluding Ξ candidates, where the pions are associated with the primary vertex (light shaded histogram).

with respect to the Λ direction in the Λ rest frame. This cut is similar to that in the Λ selection (cf. fig. 7.16 (page 114)) and reduces the number of Ξ^- vertices from 10.02 ‰ to 3.088 ‰ and that of the $\overline{\Xi}^+$ vertices from 9.68 ‰ to 2.882 ‰ (see fig. 7.27).

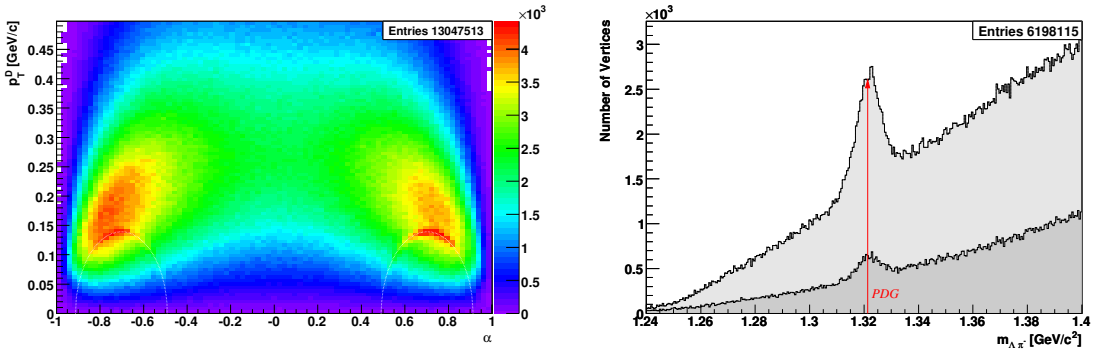

(a) (b)

Figure 7.27: Suppression of converted photons for Λ daughter: (a) Armenteros plot and (b) $m_{\Lambda\pi^-}$ invariant mass distribution after improving the Λ definition by suppressing background from converted photons with the cut $\left|\cos\theta_z^p\right| < 0.8$. The darker area in (b) shows the sample, that was cut away.

A last improvement of the background is attained by cutting on the reconstructed mass of the Λ ($\overline{\Lambda}$) daughter. All V^0 vertices, that have an invariant $m_{p\pi^-}$ ($m_{\bar{p}\pi^+}$) mass outside a $\pm 5\sigma_{\Lambda(\overline{\Lambda})}$ region around the measured Λ ($\overline{\Lambda}$) mass, are excluded. This lowers the number of Ξ^- vertices from 3.088 ‰ to 0.3594 ‰ and that of the $\overline{\Xi}^+$ vertices from 2.882 ‰ to 0.2752 ‰ (see fig. 7.28).

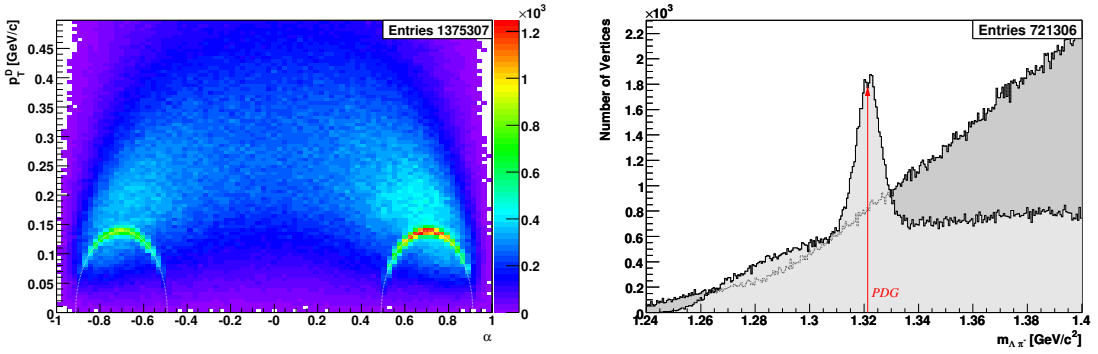

(a) (b)

Figure 7.28: Cut on invariant mass of the Λ daughter: (a) Armenteros plot and (b) $m_{\Lambda\pi^-}$ invariant mass distribution after the cut. The darker area in (b) shows the sample, that was cut away.

As was discussed already in subsection 7.2.4 the acceptance of the outer and middle trigger hodoscopes was not up-down symmetric for some data taking periods. Since this is an essential prerequisite for the polarization extraction method, events are ex-

cluded, if they are only defined by those two triggers. The number of Ξ^- vertices is reduced from 0.3594 ‰ to 0.3523 ‰.The number of $\overline{\Xi}^+$ vertices decreases from 0.2752 ‰ to 0.2694 ‰ (see fig. 7.29).

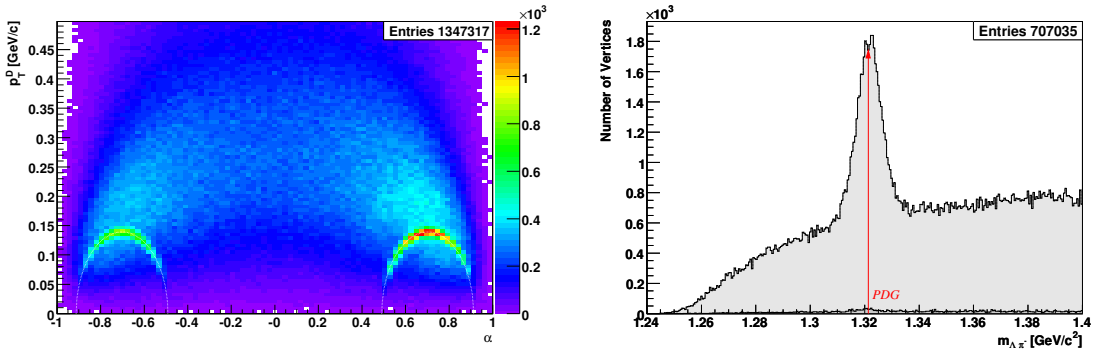

(a) (b)

Figure 7.29: Ξ sample after selection: (a) Armenteros plot and (b) $m_{\Lambda\pi^-}$ invariant mass distribution of the final Ξ sample after excluding events, that were exclusively triggered by the outer or the middle trigger hodoscopes. The darker area in (b) shows the sample, that was cut away.

Table 7.4 summarizes the Ξ selection cuts, that define the Ξ^- and $\overline{\Xi}^+$ sample, used for the polarization analysis. The final Ξ sample consists of 706,000 Ξ^- candidates, that contain 24,900 Ξ^-s, and of 638,000 $\overline{\Xi}^+$ candidates with 14,900 $\overline{\Xi}^+$s.

Cut	Number of Ξ^- vertices		Number of $\overline{\Xi}^+$ vertices	
	[10^6]	[%]	[10^6]	[%]
Definition of Ξ vertex	2007.011	—	2376.271	—
Suppression of halo muons	2005.687	99.93	2146.687	90.34
Ξ decay topology	607.392	30.26	650.843	27.39
Pion passes through SM1	579.923	28.89	621.874	26.17
Definition of Λ ($\overline{\Lambda}$) vertex	132.980	6.626	143.152	6.024
DCA of Ξ vertex	94.708	4.719	102.515	4.314
Definition of production plane	90.310	4.500	98.028	4.125
Pion association with primary vertex	20.114	1.002	23.002	0.968
Suppression of converted photons for Λ ($\overline{\Lambda}$)	6.198	0.3088	6.849	0.2882
Cut on Λ ($\overline{\Lambda}$) mass	0.721	0.03594	0.654	0.02752
Removal of outer and middle trigger	0.707	0.03523	0.640	0.02694

Table 7.4: Summary of the cuts, that define the Ξ^- and $\overline{\Xi}^+$ sample. The table specifies the absolute as well as the relative reductions of the Ξ candidate sample by the individual cuts. In total 707035 $\Xi^-$and 640282 $\overline{\Xi}^+$ vertices fulfill the selection criteria.

Fig. 7.30 shows the invariant mass distributions for the Ξ^- and the $\bar{\Xi}^+$ hypothesis, where the mass of the Λ ($\bar{\Lambda}$) decay daughter is set to the nominal PDG value. This improves the Ξ mass resolution compared to the $m_{\Lambda\pi^-}$ invariant mass plots above, that illustrate the different cuts and that use the reconstructed Λ ($\bar{\Lambda}$) mass. Also the Ξs have a rather long lifetime and therefore a small natural width ($\Gamma_{\Xi^-,\bar{\Xi}^+} = 4.019$ μeV/c^2), so that the measured widths are dominated by the resolution of the spectrometer.

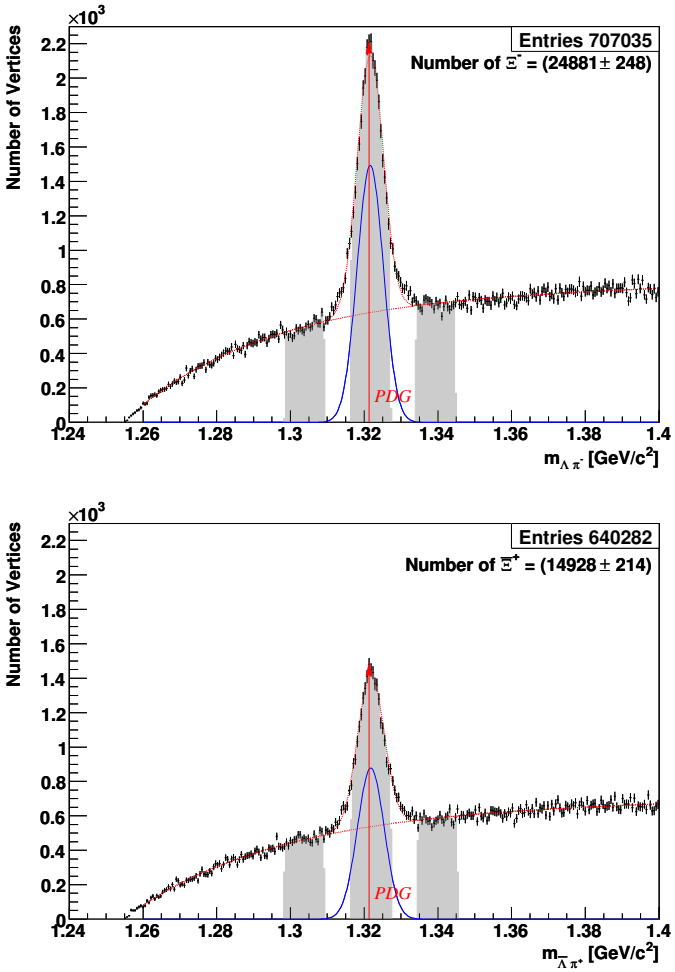

Figure 7.30: Final Ξ^- and $\bar{\Xi}^+$ samples after event selection: The upper plot shows the $m_{\Lambda\pi^-}$, the lower one the $m_{\bar{\Lambda}\pi^+}$ distribution of the final Ξ sample, where the Λ ($\bar{\Lambda}$) mass was fixed to its nominal value. The 24,900 Ξ^-s have a mean mass of 1321.7 MeV/c^2, which corresponds to a deviation of $\Delta m = 400$ keV/c^2 with respect to the PDG value. The width of the Ξ^- peak is 3.54 MeV/c^2. The mass of the 14,900 $\bar{\Xi}^+$s is measured to 1321.8 MeV/c^2 ($\Delta m = 500$ keV/c^2) with a mass resolution of 3.61 MeV/c^2. The fitting procedure is described in subsection 7.4.2. In both plots the shaded bands indicate the peak- and side-band regions used for the background subtraction.

The Armenteros plot in fig. 7.29a shows, that in contrary to the case of the Λ no other particles interfere with the Ξ^- and $\bar{\Xi}^+$ arcs, which leads to a much simpler background. Like for the Λs the angular distributions, which determine the polarizations, are extracted

by fitting the invariant mass histograms with a function, that models the Ξ peak and the background (see subsection 7.4.2). In all other cases the background subtraction is performed by applying the side-band subtraction method. For the Ξs a peak-band with a width of $3\,\sigma_{\Xi^-,\bar{\Xi}^+}$ is used together with $3\,\sigma_{\Xi^-,\bar{\Xi}^+}$ wide side-bands, that are centered at $\pm 5\,\sigma_{\Xi^-,\bar{\Xi}^+}$ from the peak (see fig. 7.30), where $\sigma_{\Xi^-,\bar{\Xi}^+}$ is the width of the fitted Gaussian.

7.3 Extraction Method for Hyperon Polarization – Double Bias Canceling

The hyperon polarization is extracted from the measured angular distribution of the decay baryon with respect to the production plane normal in the hyperon rest frame utilizing eq. (7.4) (see also chapter 6):

$$\frac{\mathrm{d}N}{\mathrm{d}\cos\theta_y} = \frac{N_0}{2}\Big(1 + \alpha_H\, P_y^H \cos\theta_y\Big) \tag{7.5}$$

where P_y^H is the hyperon polarization, α_H the decay asymmetry parameter for the particular hyperon decay channel as given in table 6.1 (page 73), and N_0 the total number of hyperons. According to the above formula the polarization can be obtained by fitting the slope of the $\cos\theta_y$ distribution.

Unfortunately this procedure is not applicable in practice, because eq. (7.5) ignores an important experimental complication – the acceptance. The acceptance describes the average detection efficiency and subsumes all effects, that may cause losses of events, as there are: geometrical acceptance of the apparatus, dead-time, (varying) detector efficiencies, efficiency of the reconstruction process, and cuts applied during the event selection, to name only the most important contributions. Due to the dipole magnets, the COMPASS spectrometer has an inherently left-right asymmetric acceptance. Depending on their charge, particles are bent into or out of the acceptance, when they fly into the left or the right part of the spectrometer.

The acceptance A enters as a factor into the angular distribution

$$\frac{\mathrm{d}N}{\mathrm{d}\cos\theta_y} = \frac{N_0}{2} A\Big(1 + \alpha_H\, P_y^H \cos\theta_y\Big) \tag{7.6}$$

A is in general a function of time and of the kinematical variables, which in the angular distributions are, apart from $\cos\theta_y$, all integrated out, so that $A = A(\cos\theta_y)$. The effect of the acceptance is clearly visible in fig. 7.31, which shows the measured $\cos\theta_y$ distribution for the Λ and the Ξ^- hyperons. The distortions of the angular distributions due to the acceptance have to be corrected, because they otherwise might cause false asymmetries, indistinguishable from the real hyperon polarization. Two different methods may be used to perform the acceptance correction: Either the acceptance function $A(\cos\theta_y)$ is extracted from Monte-Carlo simulations or the symmetry of the apparatus is exploited and

bias canceling techniques are applied, which extract the acceptance correction functions directly from the measured data by a suitable recombination of data subsamples.

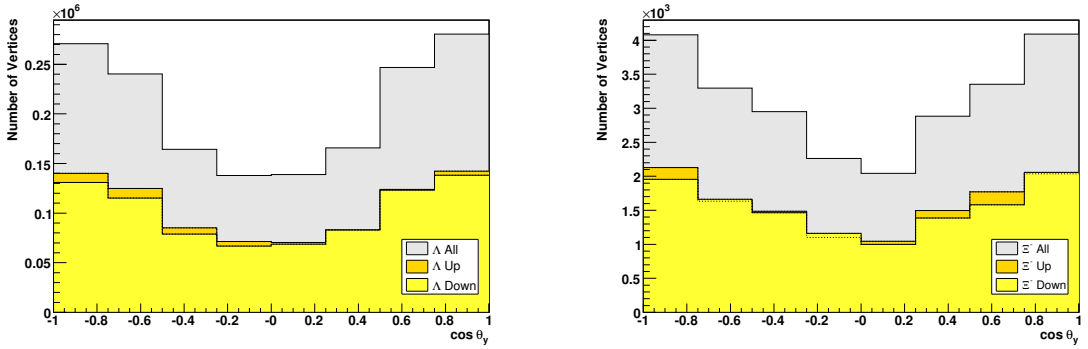

(a) (b)

Figure 7.31: (a) Background corrected $\cos\theta_y$ distributions for the Λ, used to extract the polarization. The distributions strongly deviate from a flat distribution one would expect for small acceptance effects. Instead events around $\cos\theta_y \approx 0$ are suppressed, mainly by the $\cos\theta_z$ cut (cf. fig. 7.16 (page 114)). (b) shows the same distributions for the Ξ^-.

This analysis employs a bias canceling method, which was developed by Ohlsen and Keaton [Ohl73] for the measurement of analyzing powers in spin-1/2 ion beams and which was applied to the analysis of hyperon polarization by the WA89 [Ada95] and EXCHARM [Ale00] experiments. The method corrects left-right asymmetries of the acceptance and is based on the assumption, that the apparatus is symmetric with respect to its mid-plane, which is spanned by the beam (z_{Lab}) and the left-right direction (x_{Lab}). The hyperon sample is subdivided into two subsamples: up-going hyperons with $p^H_{y_{\text{Lab}}} > 0$ and down-going hyperons with $p^H_{y_{\text{Lab}}} < 0$. Each of the two subsamples follows the angular distribution of eq. (7.6):

$$U(\cos\theta_y) = \frac{\mathrm{d}N_U}{\mathrm{d}\cos\theta_y} = \frac{U_0}{2} A_U(\cos\theta_y)\left(1 + \alpha_H\, P_y^H \cos\theta_y\right)$$
$$D(\cos\theta_y) = \frac{\mathrm{d}N_D}{\mathrm{d}\cos\theta_y} = \frac{D_0}{2} A_D(\cos\theta_y)\left(1 + \alpha_H\, P_y^H \cos\theta_y\right) \tag{7.7}$$

Provided the apparatus is perfectly up-down symmetric, the total numbers of up- and down-going hyperons U_0 and D_0 are equal.

$$U_0 = D_0 \tag{7.8}$$

If the data set is sufficiently large, it contains for a given hyperon decay always a second decay, that is mirrored with respect to the mid-plane of the spectrometer, like it is shown in fig. 7.32. In the two symmetric hyperon decays the y_{Lab}-momentum components of the involved particles have opposite signs. This may be used to establish a relation between the acceptances $A_U(\cos\theta_y)$ and $A_D(\cos\theta_y)$. Because of the sign flip in the y_{Lab}-

momentum components of the virtual photon γ^* and of the hyperon H, the x_{Lab}- and z_{Lab}-components of the "up" and "down" production plane normals $\hat{n}_{U,D}$ have opposite signs as well:

$$\hat{n}_U = \frac{\vec{p}^{\,U}_{\gamma^*} \times \vec{p}^{\,U}_H}{|\vec{p}^{\,U}_{\gamma^*}|\,|\vec{p}^{\,U}_H|} = (n_x, n_y, n_z)^T \qquad \hat{n}_D = \frac{\vec{p}^{\,D}_{\gamma^*} \times \vec{p}^{\,D}_H}{|\vec{p}^{\,D}_{\gamma^*}|\,|\vec{p}^{\,D}_H|} = (-n_x, n_y, -n_z)^T \tag{7.9}$$

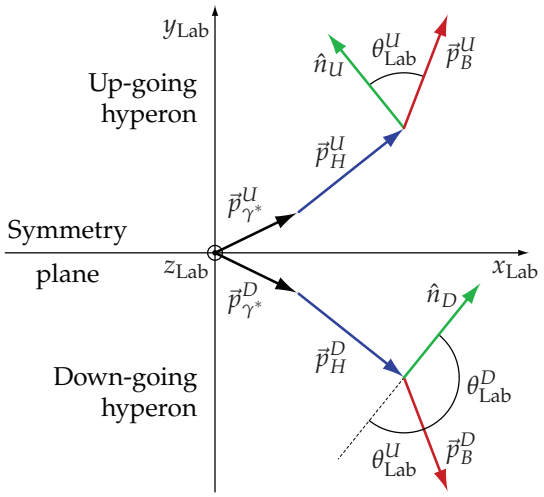

Figure 7.32: Mid-plane symmetry of the apparatus and hyperon decay: The figure shows two hyperon decays U and D in the laboratory frame, that are symmetric with respect to the mid-plane of the spectrometer. For each decay the normal $\hat{n}$ of the production plane is defined by $\vec{p}_{\gamma^*} \times \vec{p}_H$. Because of the axial vector nature of $\hat{n}$, the angle θ^U_{Lab} of the decay baryon B in the up-going decay is related to the angle θ^D_{Lab} of the down-going hyperon decay by $\theta^D_{\text{Lab}} = \pi - \theta^U_{\text{Lab}}$.

The above equation translates the up-down symmetry of the momenta into a relation between the angles $\theta^{U,D}_{\text{Lab}}$ of the decay baryons of the two hyperon decays with respect to the production plane normals in the laboratory frame:

$$\begin{aligned}
\cos\theta^U_{\text{Lab}} &= \hat{n}_U \cdot \vec{p}^{\,U}_B / |\vec{p}^{\,U}_B| = (n_x p_x + n_y p_y + n_z p_z)/|\vec{p}^{\,U}_B| \\
\cos\theta^D_{\text{Lab}} &= \hat{n}_D \cdot \vec{p}^{\,D}_B / |\vec{p}^{\,D}_B| = (-n_x p_x - n_y p_y - n_z p_z)/|\vec{p}^{\,U}_B| \\
\cos\theta^D_{\text{Lab}} &= -\cos\theta^U_{\text{Lab}} \\
\theta^D_{\text{Lab}} &= \pi - \theta^U_{\text{Lab}}
\end{aligned} \tag{7.10}$$

The Lorentz factors of the hyperons in the two symmetric decay processes are equal. Therefore the change of the baryon angles with respect to the production plane normals

is also symmetric, when they are boosted into the particular hyperon rest frames. This means that relation (7.10) also holds for the angles $\theta_y^{U,D}$ in the rest frame of the hyperons:

$$\theta_y^D = \pi - \theta_y^U \quad \text{and thus} \quad \cos\theta_y^D = -\cos\theta_y^U \tag{7.11}$$

Because of the up-down symmetry of the apparatus, the two mirrored decays have the same acceptances:

$$\tilde{A}_U\Big(\cos\theta_y^U;\,\xi\Big) = \tilde{A}_D\Big(-\cos\theta_y^U;\,\xi\Big) \tag{7.12}$$

where eq. (7.11) was used and where $\tilde{A}_{U,D}$ represent the basic acceptances, that depend on the angle $\theta_y^{U,D}$ and on other kinematical variables of the decay, which are subsumed in the symbol ξ and which, due to the symmetry, are equal for the "up" and the "down" decay. In the angular distributions the parameters ξ are integrated out, thereby conserving the symmetry of the acceptance:

$$A_U(\cos\theta_y) = \int \mathrm{d}\xi\, \tilde{A}_U\big(\cos\theta_y;\,\xi\big) = \int \mathrm{d}\xi\, \tilde{A}_D\big(-\cos\theta_y;\,\xi\big) = A_D(-\cos\theta_y) \tag{7.13}$$

According eq. (7.7), (7.8), and (7.13) acceptance effects cancel, when the asymmetry of the up and the down sample is calculated:

$$R_0(\cos\theta_y) = \frac{U(\cos\theta_y) - D(-\cos\theta_y)}{U(\cos\theta_y) + D(-\cos\theta_y)} = \alpha_H\, P_y^H \cos\theta_y \qquad \text{where} \quad \theta_y \in [-\pi, \pi] \tag{7.14}$$

The slope of the acceptance corrected angular distribution $R_0(\cos\theta_y)$ is directly proportional to the polarization.

Eq. (7.14) is only valid, if the assumption of equal numbers of up- and down-going hyperons (eq. (7.8)) is fulfilled, which, due to imperfect alignment of beam and apparatus, is usually not the case. In order to correct also for this kind of asymmetry, the geometric mean concept of Ohlsen and Keaton [Ohl73] is employed: The up and down samples are subdivided once more, but this time with respect to the *sign* of $\cos\theta_y$, which results in four disjoint subsamples:

$$\begin{aligned} U^{\pm}(\cos\theta_y) &= \frac{\mathrm{d}N_U^{\pm}}{\mathrm{d}\cos\theta_y} = \frac{U_0}{2} A_U(\pm\cos\theta_y)\Big(1 \pm \alpha_H\, P_y^H \cos\theta_y\Big) \\ D^{\pm}(\cos\theta_y) &= \frac{\mathrm{d}N_D^{\pm}}{\mathrm{d}\cos\theta_y} = \frac{D_0}{2} A_D(\pm\cos\theta_y)\Big(1 \pm \alpha_H\, P_y^H \cos\theta_y\Big) \\ &\text{where now} \quad \theta_y \in [0, \pi] \end{aligned} \tag{7.15}$$

By taking the geometric mean of the $U^{\pm}$, $D^{\pm}$ pairs with the same sign of $\cos\theta_y$ and by applying the up-down symmetry in the form of eq. (7.13), the absolute numbers of hyperons U_0 and D_0 cancel, when the asymmetry is formed using the geometric means:

$$\begin{aligned}\sqrt{U^+D^+} &= \sqrt{\frac{U_0}{2}\frac{D_0}{2}A_U(\cos\theta_y)A_U(-\cos\theta_y)}\Big(1+\alpha_H\,P_y^H\cos\theta_y\Big)\\ \sqrt{U^-D^-} &= \sqrt{\frac{U_0}{2}\frac{D_0}{2}A_U(-\cos\theta_y)A_U(\cos\theta_y)}\Big(1-\alpha_H\,P_y^H\cos\theta_y\Big)\end{aligned} \tag{7.16}$$

$$\boxed{R(\cos\theta_y)=\frac{\sqrt{U^+D^+}-\sqrt{U^-D^-}}{\sqrt{U^+D^+}+\sqrt{U^-D^-}}=\alpha_H\,P_y^H\cos\theta_y} \quad \text{where} \quad \theta_y\in[0,\pi] \tag{7.17}$$

In order to calculate the acceptance corrected angular distribution $R(\cos\theta_y)$, the distributions $U^{\pm}(\cos\theta_y)$ and $D^{\pm}(\cos\theta_y)$ have to be extracted from the data. The goal is consequently to determine the *number* of hyperons within a certain range of $\cos\theta_y$ with a background as low as possible.

Since an event-by-event identification of the hyperon decays is not necessary, a bin-by-bin method is applied: The hyperon candidates are sorted into N_{θ_y} bins in $\cos\theta_y$. For each $\cos\theta_y$ bin the sample is subdivided further into up- and down-going hyperons and an invariant mass histogram is generated for each subsample. The number of hyperons in the $2\cdot N_{\theta_y}$ subsamples is determined by fitting the hyperon mass peaks, which results in the nearly background free angular distributions $U^{\pm}$ and $D^{\pm}$ (see section 7.4 as well as fig. 7.31 (page 126)). From the angular distributions the background corrected $R(\cos\theta_y)$ distribution is calculated by combining the positive and negative $\cos\theta_y$ bins according to eq. (7.17). The polarization is finally obtained by a linear fit of $R(\cos\theta_y)$.

The uncertainty δR of R is calculated straightforward utilizing Gaussian error propagation:

$$\begin{aligned}\delta R^2 &= \left(\frac{\partial R}{\partial U^+}\delta U^+\right)^2+\left(\frac{\partial R}{\partial U^-}\delta U^-\right)^2+\left(\frac{\partial R}{\partial D^+}\delta D^+\right)^2+\left(\frac{\partial R}{\partial D^-}\delta D^-\right)^2\\ \delta R^2 &= \frac{1}{\left(\sqrt{U^+D^+}+\sqrt{U^-D^-}\right)^4}\left[\frac{U^-D^-}{U^+D^+}\Big(D^{+2}\delta U^{+2}+U^{+2}\delta D^{+2}\Big)+\right.\\ &\qquad\left.\frac{U^+D^+}{U^-D^-}\Big(D^{-2}\delta U^{-2}+U^{-2}\delta D^{-2}\Big)\right]\end{aligned} \tag{7.18}$$

where $\delta U^{\pm}$ and $\delta D^{\pm}$ are the errors on the number of hyperons, obtained from the fit of the invariant mass histograms of the respective subsample. If N_0 is the number of hyperons in a certain $\cos\theta_y$ bin and if the asymmetry is small, the four samples $U^{\pm}$ and $D^{\pm}$ have approximately equal statistics of $N_0/2$ and their uncertainty is given by $\sqrt{N_0/2}$. Consequently the resulting uncertainty of R is $\delta R = 1/\sqrt{2N_0}$. Under similar assumptions the simple bias canceling ratio R_0, as defined in eq. (7.14), has an error of $\delta R_0 = 1/\sqrt{N_0}$. The

error on the extracted hyperon polarization δP_y^H, however, is in both cases the same, since the ratio $R_0(\cos\theta_y)$ is defined in the full angular range from $-\pi$ to π, whereas $R(\cos\theta_y)$ covers only positive angles.

7.4 Background Subtraction

The bin-by-bin bias canceling method, presented in section 7.3, extracts the polarization from the acceptance corrected angular distribution $R(\cos\theta_y)$ and is based on the precise knowledge of the number of hyperons in each $\cos\theta_y$ subsample. To this end an invariant mass histogram is generated for each subsample and the number of hyperons is determined by fitting of the hyperon's mass peak. The challenge is to find a good description of the background and of the hyperon peak, in particular for the Λ ($\bar{\Lambda}$) case, where apart from the combinatorial background contaminations from kaons and converted photons play an important role. Subsection 7.4.1 describes the special fit method, that disentangles these contributions. A simpler method, explained in subsection 7.4.2, is used for the Ξs, whose background is predominantly of combinatorial origin and has a less complex behavior.

7.4.1 Λ Background Subtraction

The invariant mass histogram of the final Λ sample (see fig. 7.33a) shows that the background has a quite complicated structure: One component starts at the kinematical border of $m_p + m_{\pi^-} = 1077.84$ MeV/c^2. On top of it the kaons contribute for invariant masses $m_{p\pi^-} \gtrsim 1094$ MeV/c^2 and produces a rising edge in this mass region. Moreover the shape of the background changes with the kinematical variables including $\cos\theta_y$, which is illustrated by fig. 7.33c and d.

For the extraction of the angular distributions it would be unfavorable to exclude the K^0s by an invariant mass cut, as it is done for the side-band subtracted plots. Firstly, because such a cut would distort the angular distributions, and secondly, it would also remove a non-negligible fraction of the Λs. As will be shown below, the kaon contribution to the background can be disentangled, and it moreover may be used to study the systematic error.

Fig. 7.33a displays the result of a fit of the Λ peak region with the sum of a Gaussian and a third order polynomial:

$$\begin{aligned} f_G(m_{p\pi^-}) =& w_B \cdot N_\Lambda \cdot \mathrm{Gauss}\left[m_{p\pi^-};\, m_\Lambda, \sigma_\Lambda\right] + p_0 + p_1 \cdot m_{p\pi^-} + p_2 \cdot m_{p\pi^-}^2 + p_3 \cdot m_{p\pi^-}^3 \\ \text{with} \quad & \mathrm{Gauss}[x;\, m, \sigma] \equiv \frac{1}{\sqrt{2\pi}\cdot\sigma} \exp\left[-\frac{(x-m)^2}{2\sigma^2}\right] \end{aligned} \tag{7.19}$$

where w_B is the bin width, N_Λ the number of Λs under the Gaussian peak, σ_Λ the width, and m_Λ the mean value of the peak. The fit function has in total seven free parameters.

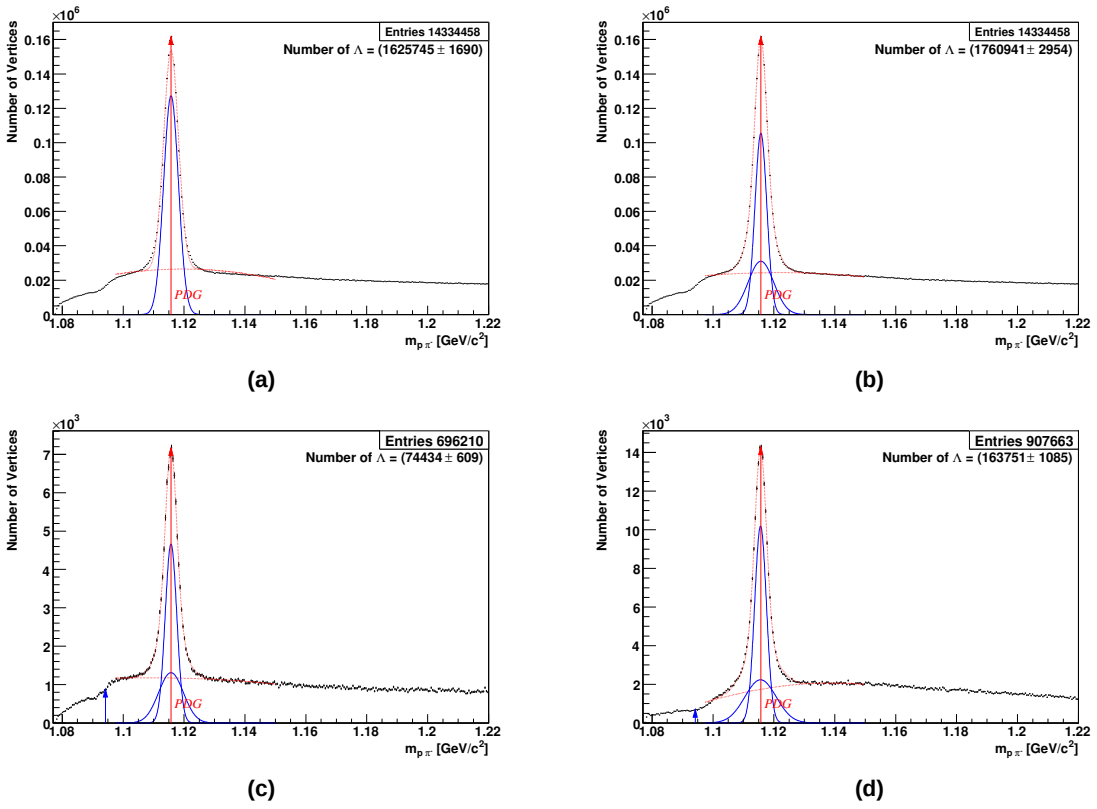

Figure 7.33: (a) $m_{p\pi^-}$ invariant mass spectrum of the Λ sample. The peak region is fitted with the sum of a Gaussian and a third order polynomial (function (7.19)). (b) shows the same $m_{p\pi^-}$ invariant mass spectrum, but fitted with the sum of a double Gaussian and a third order polynomial (function (7.20)). (c) Invariant mass distribution for up-going Λs in the angular bin $\cos\theta_y \in [0, 0.25]$. (d) shows the respective histogram for the bin $\cos\theta_y \in [0.75, 1]$. Note the different shape of the background in the region of the K^0 threshold (indicated by the arrow) in the two plots. In all plots a fit range of $m_{p\pi^-} \in [1097.5, 1150.0]$ MeV/c^2 was used.

From fig. 7.33a it is evident, that neither the background nor the peak is described well by function (7.19), which is also reflected by the large χ^2/n.d.f. value of $11844/103 = 115$. The data exceed the fit function in the center and in the wings of the peak. Due to the incorrect peak shape of the fit function, the background is artificially enhanced under the peak, so that the number of Λs is systematically underestimated.

The fit result improves, if the sum of a double-Gaussian and a third order polynomial if fitted to the data (see fig. 7.33b):

$$\begin{aligned} f_{GG}(m_{p\pi^-}) =& w_B \cdot N_\Lambda \Big(R_N \cdot \text{Gauss}\big[m_{p\pi^-};\, m, \sigma\big] \\ & + (1 - R_N) \cdot \text{Gauss}\big[m_{p\pi^-};\, (m + \Delta m), R_\sigma \cdot \sigma\big] \Big) \\ & + p_0 + p_1 \cdot m_{p\pi^-} + p_2 \cdot m_{p\pi^-}^2 + p_3 \cdot m_{p\pi^-}^3 \end{aligned} \tag{7.20}$$

where w_B again is the bin width and N_Λ the total number of Λs in both Gaussian peaks. The parameters of the second Gaussian are expressed with respect to the ones of the first: R_N is the fraction of Λs, that belong to the first Gaussian peak. Consequently $1 - R_N$ corresponds to the fraction of Λs in the second peak. The second peak has a width of R_σ times the width of the first one and is shifted by Δm with respect to the first Gaussian. In total this fit function has 10 free parameters.

Function (7.20) fits the data much better with a reduced χ^2 value of $719/101 = 7.1$. The fact, that a double-Gaussian improves the peak shape description, may be understood by looking at the resolution of the reconstructed $m_{p\pi^-}$ mass, which depends on the resolution of the momentum and the angle measurement:

$$\begin{aligned} m_{p\pi^-}^2 &= m_p^2 + m_{\pi^-}^2 + 2E_p E_{\pi^-} - 2p_+ p_- \cos\vartheta \\ \delta\Big(m_{p\pi^-}^2\Big)^2 &= 4\left(\frac{E_{\pi^-}}{E_p} p_+ - p_- \cos\vartheta\right)^2 \delta p_+^2 + 4\left(\frac{E_p}{E_{\pi^-}} p_- - p_+ \cos\vartheta\right)^2 \delta p_-^2 \\ &\quad + 4 p_+^2 p_-^2 \sin^2\vartheta\, \delta\vartheta^2 \\ &\text{where} \quad \delta\Big(m_{p\pi^-}^2\Big) = 2 m_{p\pi^-}\, \delta m_{p\pi^-} \quad \text{and} \quad E_{p,\pi^-} = \sqrt{m_{p,\pi^-}^2 + p_\pm^2} \end{aligned} \tag{7.21}$$

The angular resolution $\delta\vartheta$ as well as the momentum resolutions $\delta p_\pm$ are determined by the spatial resolution of the tracking detectors, that measure the particle trajectories. COMPASS employs a staggered tracking system (see subsection 2.2.2), in which the spatial resolution increases for trajectories closer to the beam axis, thereby equalizing the relative resolution in angle and momentum over the acceptance. The various tracking detectors cover different regions of the phase space and define sets of tracks with different precision in the angle and momentum measurement. This means that the mass peak is a sum of many different Gaussians, which reflect the different resolutions of the various sets of measured trajectories. This sum is well approximated already by a double-Gaussian.

Nevertheless the use of a double-Gaussian is problematic, because if the fit parameters are left unconstrained, it may happen, that part of the background is mistaken for signal, which leads to a dilution of the polarization. This ambiguity of signal and background description can possibly be resolved by identifying the track properties, that distinguish the two sets of tracks, that belong to the two Gaussians. With this knowledge one may reduce the number of free parameters of the fit function and consequently make it more robust. Unfortunately no clear correlations of the peak width with simple kinematical parameters like length or position of the track (first or second stage of the spectrometer) or the track momentum were found, so that the precise origin of the two components of the double-Gaussian remains unexplained here.

A different approach to improve the fit, is to improve the description of the background. This is achieved by expanding the $m_{p\pi^-}$ invariant mass distribution with the kaon mass hypothesis $m_{\pi^+\pi^-}$. The resulting two-dimensional plot in fig. 7.34 shows, that the different background contributions are nicely separated: The Λ and the K^0 form two orthogonal bands, that intersect in one region. The remaining background is rather flat and slightly tends to accumulate at the kinematical border.

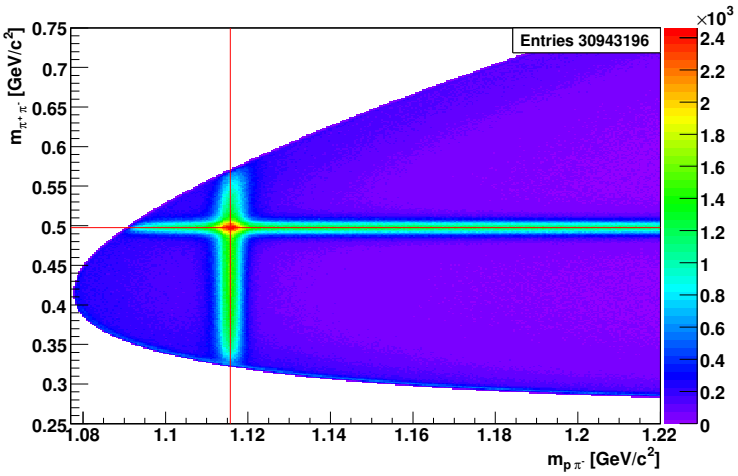

Figure 7.34: Two-dimensional $(m_{p\pi^-}, m_{\pi^+\pi^-})$ invariant mass histogram without cut on $\cos\theta_z$ (cf. fig. 7.35). The vertical Λ band and the horizontal K^0 band intersect in one region, where they add up. The nominal masses of the Λ and K^0 the are indicated by the lines. Part of the background accumulates at the kinematical boundary.

The fit method, employed here, is based on a previous analysis [Wie04], in which the kaon line and the background were first fitted outside the Λ peak region and then subtracted from the data in order to obtain a background free Λ sample. This approach was extended leading to a procedure, in which the number of Λs is extracted by a full two-dimensional fit of the histogram in the $(m_{p\pi^-}, m_{\pi^+\pi^-})$-plane, taking into account the two major background components. The two-dimensional fit function models the shapes of the various components using as few free parameters as possible. The Λ and K^0 bands are described by lines with Gaussian cross sections, that run along the $m_{\pi^+\pi^-}$ and $m_{p\pi^-}$ coordinate, respectively. The amplitudes A_{Λ,K^0}, the widths σ_{Λ,K^0}, and the mean values m_{Λ,K^0}

of the Gaussian cross sections are allowed to vary as the lines run along. They are thus functions of $m_{\pi^+\pi^-}$ and $m_{p\pi^-}$, respectively:

$$\begin{aligned} f_{\mathrm{2D}}(m_{p\pi^-}, m_{\pi^+\pi^-}) = & \underbrace{A_\Lambda(m_{\pi^+\pi^-}) \cdot \mathrm{Gauss}\left[m_{p\pi^-};\, m_\Lambda(m_{\pi^+\pi^-}), \sigma_\Lambda(m_{\pi^+\pi^-})\right]}_{\Lambda \text{ line along } m_{\pi^+\pi^-} \text{ with Gaussian profile}} \\ & + \underbrace{A_{K^0}(m_{p\pi^-}) \cdot \mathrm{Gauss}\left[m_{\pi^+\pi^-};\, m_{K^0}(m_{p\pi^-}), \sigma_{K^0}(m_{p\pi^-})\right]}_{K^0 \text{ line along } m_{p\pi^-} \text{ with Gaussian profile}} \\ & + \underbrace{f_{\mathrm{BG}}(m_{p\pi^-}, m_{\pi^+\pi^-})}_{\text{Background}} \end{aligned} \tag{7.22}$$

where f_{BG} describes the remaining background. From the definition of the Gaussian lines it is evident, that their amplitudes A_{Λ,K^0} correspond to their cross sectional area, which is important for the calculation of the total number of Λs and K^0s (see below).

The two-dimensional fit requires an analytical description of the kinematical boundary, which for a given invariant mass $m_{p\pi^-}$ under Λ hypothesis yields the smallest and largest possible value of the invariant mass $m_{\pi^+\pi^-}$ for the kaon hypothesis. The kaon mass is given by:

$$\begin{aligned} m_{\pi^+\pi^-} &= \sqrt{2m_{\pi^\pm}^2 + 2\sqrt{\left(m_{\pi^\pm}^2 + p_+^2\right)\left(m_{\pi^\pm}^2 + p_-^2\right)} - 2p_+p_-\cos\vartheta} \\ &= f_{\mathrm{B}}(p_\pm, \vartheta) \end{aligned} \tag{7.23}$$

where ϑ is the opening angle between the two daughter particles and $p_\pm$ are the momenta of the positive and negative particles in the laboratory frame. These three variables can be calculated by a boost from the Λ rest frame to the laboratory frame, if the invariant mass $m_{p\pi^-}$ of the two particles under Λ hypothesis, the angle θ_z of the daughters with respect to the z-axis in the rest frame of the Λ, and the Lorentz factor γ_Λ of the Λ are known. The boundary function (7.23) may thus be rewritten as $f_{\mathrm{B}}(m_{p\pi^-}, \cos\theta_z, \gamma_\Lambda)$.

By using eq. (7.3) (page 100) with $m_{V^0} = m_{p\pi^-}$, the breakup momentum p_{Br} of the two daughter particles in the Λ rest frame is calculated. The transverse and longitudinal momentum components $p'_{\perp,\parallel}$ of the daughters in the Λ rest frame are determined by θ_z.

$$p'_\perp = p_{\mathrm{Br}}\,\cos\theta_z \qquad\qquad p'_\parallel = p_{\mathrm{Br}}\,\sin\theta_z \tag{7.24}$$

which boosted to the laboratory frame

$$p_\perp = p'_\perp \qquad\qquad p_{\parallel,\pm} = \pm\gamma_\Lambda\, p'_\parallel + \gamma_\Lambda\,\beta_\Lambda\, E'_\pm \tag{7.25}$$

gives the momenta and the opening angle, that enter in eq. (7.23)

$$p_{\pm}^2 = p_{\perp}^2 + p_{\parallel,\pm}^2 \qquad \vartheta = \arctan\frac{p_{\perp}}{p_{\parallel,+}} + \arctan\frac{p_{\perp}}{p_{\parallel,-}} \tag{7.26}$$

where $E'_{\pm} = \left(m^2_{p\pi^-} \pm m^2_p \mp m^2_{\pi^-}\right)/2m_{p\pi^-}$ is the energy of the daughters in the Λ rest frame.

f_B reaches its maximum and minimum value for $\cos\theta_z = \pm 1$, respectively. Therefore $f_B(m_{p\pi^-}, \cos\theta_z = \pm 1; \gamma_\Lambda)$ describes the kinematical boundary of the invariant mass histogram in the $(m_{p\pi^-}, m_{\pi^+\pi^-})$-plane, which is relevant for the description of the background (see below) and is illustrated in fig. 7.35.

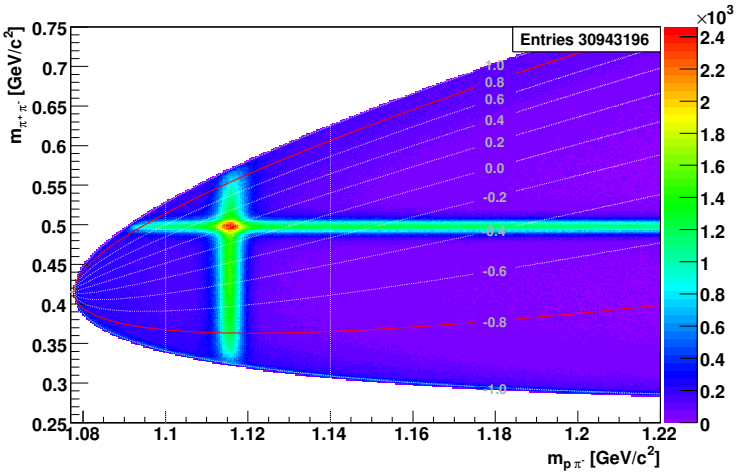

Figure 7.35: Iso-$\cos\theta_z$ lines in the $(m_{p\pi^-}, m_{\pi^+\pi^-})$ invariant mass histogram without cut on $\cos\theta_z$. The kinematical boundary is described by the lines $\cos\theta_z = \pm 1$. The red curves show the effective boundary of the histogram, defined by the cut $|\cos\theta_z| < 0.8$. The vertical lines indicate the position of the slices shown in fig. 7.37

For Lorentz factors γ_Λ larger than about five, f_B depends only weakly on γ_Λ. As the mean Lorentz factors of the Λ ($\langle\gamma_\Lambda\rangle = 14.38$) and the $\bar{\Lambda}$ ($\langle\gamma_{\bar{\Lambda}}\rangle = 14.99$) are much larger (see fig. 7.36), the kinematical boundaries are calculated in both cases with $\gamma_{\Lambda,\bar{\Lambda}}$ set to 15.

According to fig. 7.35 the cut $|\cos\theta_z| < 0.8$, that is applied to suppress the background from converted photons, defines an effective boundary, that determines part of the fit range (see also fig. 7.38). Moreover the binning in $\cos\theta_y$, that is required for the polarization analysis, may limit the fit range as well: As shown in fig. 7.16 (page 114) $\cos\theta_z$ and $\cos\theta_y$ are correlated, so that angular bins with large absolute values of $\cos\theta_y$ cause an implicit cut on $\cos\theta_z$, that is tighter than the one used to suppress the photons. This effect is taken into account for the two-dimensional fit range.

The second ingredient for the fit function is the parameterization of the non-kaonic background represented by f_{BG}. Fig. 7.37 illustrates that the background rises approximately

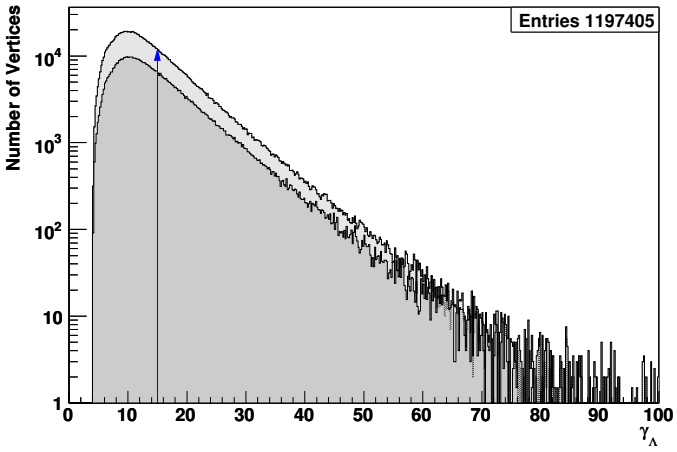

Figure 7.36: Distribution of the Lorentz factors $\gamma_{\Lambda,\bar{\Lambda}}$ for the Λ and the $\bar{\Lambda}$ (darker area). The mean values are virtually the same and are indicated by the arrow.

with $1/m_{\pi^+\pi^-}$ at the upper and lower kinematical borders. The flat part in-between is approximated by an inclined plane:

$$f_{\mathrm{BG}}(m_{p\pi^-}, m_{\pi^+\pi^-}) = \underbrace{b_0 + b_1 \cdot m_{p\pi^-} + b_2 \cdot m_{\pi^+\pi^-}}_{\text{Inclined plane}} + \underbrace{\frac{A^{\mathrm{BG}}_{\mathrm{up}}}{f_{\mathrm{B}}(m_{p\pi^-}, \cos\theta_z = 1; \gamma_\Lambda) - m_{\pi^+\pi^-}} + \frac{A^{\mathrm{BG}}_{\mathrm{low}}}{m_{\pi^+\pi^-} - f_{\mathrm{B}}(m_{p\pi^-}, \cos\theta_z = -1; \gamma_\Lambda)}}_{\text{Poles at kinematical border}} \tag{7.27}$$

where $b_{0,1,2}$ and $A^{\mathrm{BG}}_{\mathrm{up/low}}$ are the five fit parameters. $f_{\mathrm{B}}(\cos\theta_z = \pm 1)$, as defined in eq. (7.23) to (7.26), describes the kinematical border, along which the poles are running.

The fit function is completed with the parameterization of the Λ and K^0 lines: It is desirable, that the total number of Λs and K^0s, N_{Λ,K^0}, are direct fit parameters, like it is the case for the fit functions (7.19) and (7.20). This has the advantage, that no further error propagation is needed, because the uncertainties $\delta N_{\Lambda,K^0}$ can directly be taken from the fit result. In the case of f_{2D} the total number of Λs and K^0s corresponds to the volume under the respective line. The Gaussians, that describe the line profile, were chosen such, that they are normalized to the amplitude functions A_{Λ,K^0}, which represent the cross sectional area. Hence the volume of the Gaussian line can be calculated by integrating the amplitude functions over a certain range. A second order polynomial, extended such, that it has its own integral as a parameter, is employed to parameterize the amplitudes:

$$A_{\Lambda,K^0}(x) = \frac{N_{\Lambda,K^0} \cdot w_B^\Lambda \cdot w_B^{K^0}}{x_2 - x_1} + n_1^{\Lambda,K^0} \cdot \left[x - \frac{x_2^2 - x_1^2}{2(x_2 - x_1)}\right] + n_2^{\Lambda,K^0} \cdot \left[x^2 - \frac{x_2^3 - x_1^3}{3(x_2 - x_1)}\right] \tag{7.28}$$

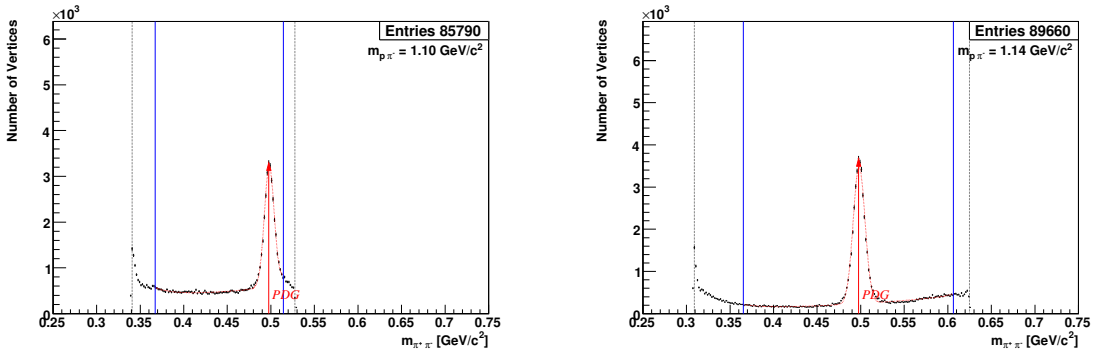

Figure 7.37: (a) Slice of the $(m_{p\pi^-}, m_{\pi^+\pi^-})$ invariant mass histogram taken along the $m_{\pi^+\pi^-}$-axis at $m_{p\pi^-} = 1100$ MeV/c^2 (cf. fig. 7.35) and fitted by a sum of two $1/m_{\pi^+\pi^-}$ poles at the kinematical borders (indicated by the vertical dotted lines) and a first order polynomial. (b) shows a slice at $m_{p\pi^-} = 1140$ MeV/c^2. Both histograms were generated without the cut on $\cos\theta_z$, that is indicated by the blue vertical lines.

where x stands for $m_{p\pi^-}$ and $m_{\pi^+\pi^-}$, respectively. N_{Λ,K^0} is the total number of Λs and K^0s, respectively, in the integration interval $x \in [x_1, x_2]$. w_B^{Λ,K^0} are the bin widths of the $m_{p\pi^-}$- and the $m_{\pi^+\pi^-}$-axis, and $n_{1,2}^{\Lambda,K^0}$ the normal first and second order fit parameters.

The determination of the volume under the Gaussian lines is complicated by the fact, that the boundary of the $(m_{p\pi^-}, m_{\pi^+\pi^-})$ invariant mass plot, described by f_B, is neither parallel to $m_{p\pi^-}$ nor to $m_{\pi^+\pi^-}$ and moreover has a curved shape. Neglecting the curvature of the boundary, a good approximation for the volume under the Λ line is to take the two extremal values of f_B at the nominal Λ mass as the integration limits (see fig. 7.38). The volume of the K^0 line is defined by the fit range along the $m_{p\pi^-}$-axis. The such defined fit parameters N_{Λ,K^0} are only used to get a good approximation for the error on the number of Λs and K^0s from the fit result. A more precise value for the numbers itself is obtained by numerical integration of the respective Gaussian line of the fit result taking f_B as the integration limit.

The widths σ_{Λ,K^0} and centers m_{Λ,K^0} of the Gaussian lines are also parameterized with polynomials:

$$m_{\Lambda,K^0}(x) = m_0^{\Lambda,K^0} + m_1^{\Lambda,K^0} \cdot x$$
$$\sigma_{K^0}(m_{p\pi^-}) = s_0^{K^0} \quad \text{and} \quad \sigma_\Lambda(m_{\pi^+\pi^-}) = s_0^\Lambda + s_1^\Lambda \cdot m_{\pi^+\pi^-} \tag{7.29}$$

where x again stands for $m_{\pi^+\pi^-}$ and $m_{p\pi^-}$, respectively. Both lines are allowed to have an inclination in the $(m_{p\pi^-}, m_{\pi^+\pi^-})$-plane and the width of the Λ line can change with $m_{\pi^+\pi^-}$.

In total the two-dimensional fit function f_{2D} has 18 free parameters: five, that describe the background, plus seven parameters for the Λ and six for the K^0 line. Fig. 7.39 shows the fit result for the total Λ sample.

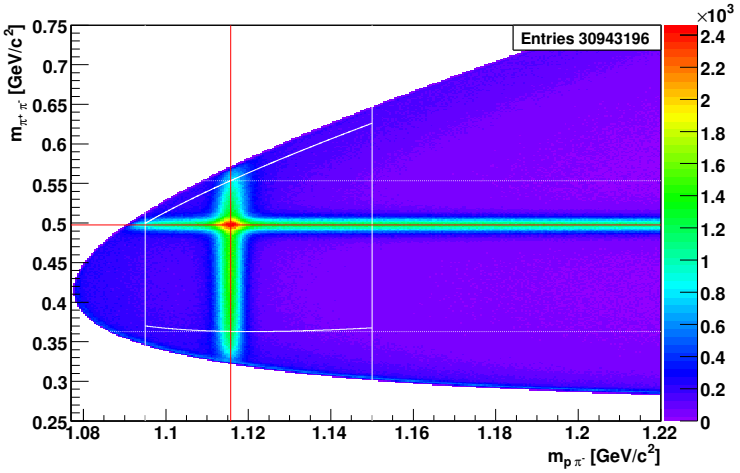

Figure 7.38: $(m_{p\pi^-}, m_{\pi^+\pi^-})$ invariant mass plot showing the boundaries, that determine the fit range (continuous lines). Along the $m_{p\pi^-}$-axis the chosen fit range is $m_{p\pi^-} \in [1095, 1150]$ MeV/c^2. In the $m_{\pi^+\pi^-}$ direction the range is defined by the $\cos\theta_z$ cut and is described by f_B. The dashed lines show the integration limits, used to determine the total number of Λs, which are parameters of the fit function f_2D.

As expected the two-dimensional function f_2D fits the data better than the one-dimensional single Gaussian with a χ^2/n.d.f. value of $50663/13955 = 3.6$. But the available high statistics of the Λ sample also shows, that the chosen method still has shortcomings: The most striking feature is the incorrect peak description of the Λ as well as of the K^0 line. Like in the one-dimensional case (cf. fig. 7.33) the data excess the fit function in the center and in the wings of the Gaussian, which is partly compensated by regions in-between, where the function exceeds the data. As shown above, the fit could be improved by taking double-Gaussian lines, which on the other hand would increase the number of free fit parameters by six to 24. In principle the considerations, that were brought up in the discussion of the one-dimensional double-Gaussian fit, also apply here, but the two-dimensional background parameterization is less ambiguous with respect to the double-Gaussian peak, because the background cannot bend into the peak.

The real problem of the two-dimensional method is, that the fit tends to fail for sparsely populated invariant mass histograms and the increase of the number of free parameters, when going to double-Gaussian peaks, would hamper the fitting of low statistics histograms even more. Although the overall number of Λs is large, the case of low statistics mass histograms is relevant, because the polarization is studied in various kinematical bins. Since already the calculation of a single polarization value requires the subdivision of the Λ sample into $2N_{\theta_y}$ bins (see section 7.3), a further subdivision reduces the number of Λs in the invariant mass histograms, that need to be fitted, easily by two to three orders of magnitude compared to the total sample.

A striking advantage of the two-dimensional fit procedure is, that it allows to extract the angular distribution and thus the polarization of the kaon background in a kinematical

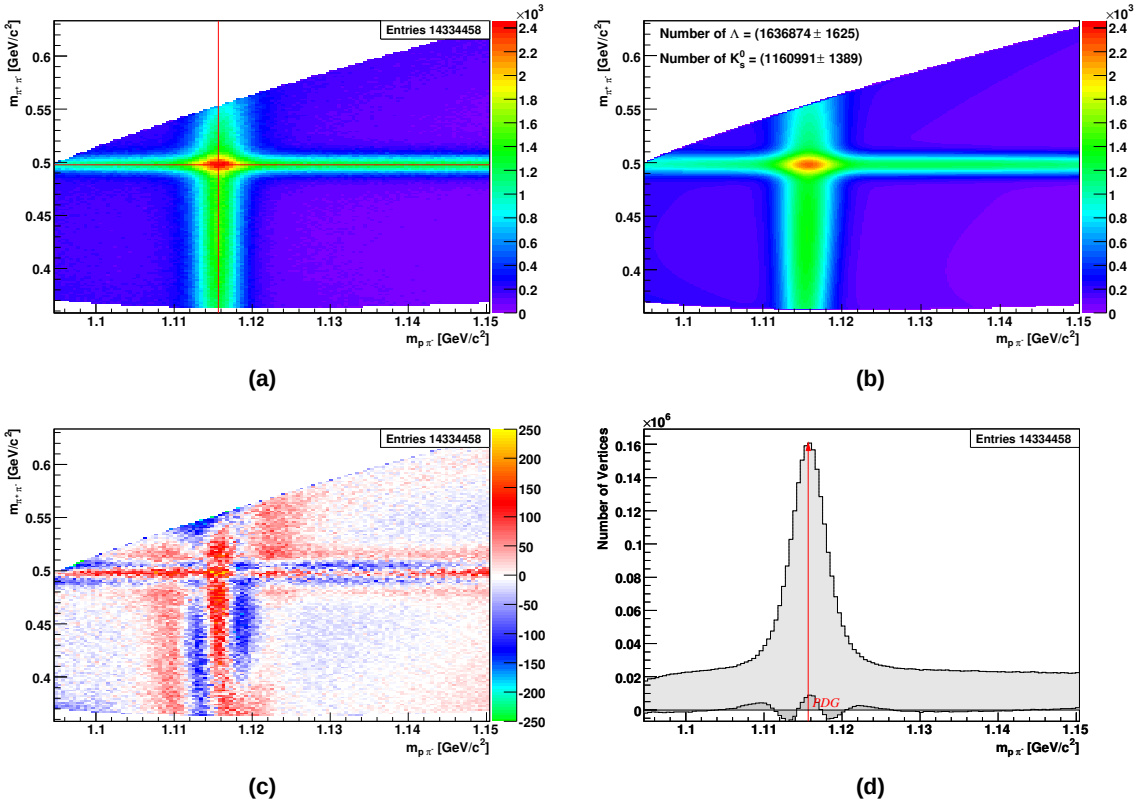

Figure 7.39: Fit result of the $(m_{p\pi^-}, m_{\pi^+\pi^-})$ invariant mass histogram for the total Λ sample: (a) Cut-out of the $(m_{p\pi^-}, m_{\pi^+\pi^-})$ invariant mass histogram, that is fitted by $f_{2\mathrm{D}}$ (function (7.22)). (b) shows the fit result for $f_{2\mathrm{D}}$. (c) Difference of the histogram and the fit result. Note the different color coding and z-scale. (d) Projection of the full mass histogram as shown in (a) and that of the difference histogram (c) (darker area) onto the $m_{p\pi^-}$ axis.

region similar to that of the Λ hyperons. This is used for systematic studies, which are presented in subsection 8.2.1. Therein also the influence of the different fit methods on the final polarization result is discussed in more detail.

7.4.2 Ξ Background Subtraction

As can be seen in the Armenteros plot of the Ξ sample (cf. fig. 7.29 (page 123)), there are no major contributions from other particles with similar signature to the background, which is thus mainly of combinatorial origin. Compared to the Λ the background has no substructure and a simpler behavior in the kinematical variables. The peak region is parameterized in the following way:

$$\begin{aligned} f_t(m_{\Lambda\pi^-}) &= \frac{w_B \cdot N_\Xi}{\sqrt{2\pi}\cdot\sigma_\Xi} \exp\left[-\frac{(m_{\Lambda\pi^-}-m_\Xi)^2}{2\sigma_\Xi^2}\right] \\ &\quad + A\cdot(m_{\Lambda\pi^-}-m_t)^{p_0}\cdot\exp\left[-p_1\cdot(m_{\Lambda\pi^-}-m_t)-p_2\cdot(m_{\Lambda\pi^-}-m_t)^2\right] \\ f_t(m_{\Lambda\pi^-}) &\equiv 0 \quad \text{for} \quad m_{\Lambda\pi^-} < m_t \end{aligned} \tag{7.30}$$

where w_B is the bin width, N_Ξ the number of Ξs in the Gaussian peak, σ_Ξ the width and m_Ξ the mean value of the peak. The background consists of a power-law part with exponent p_0, which is modulated by an exponential part, and has a zero-crossing at the threshold mass m_t. The threshold mass is given by the sum of the daughter masses $m_t = m_\Lambda + m_{\pi^\pm} = 1255.25\ \text{MeV}/c^2$. The fit function has in total seven free parameters and vanishes for invariant masses smaller than m_t.

The peak shape is well described by the Gaussian and the function fits the data successfully with reduced χ^2 values of $319/256 = 1.25$ for the Ξ^- and $276/256 = 1.08$ for the $\bar{\Xi}^+$ sample (see fig. 7.30 (page 124)).

Chapter 8

Results

The previous chapter explained both the selection criteria, that define the hyperon samples, as well as the method to extract their polarization. The following sections present and discuss the results of the analysis: Section 8.1 starts with the polarizations of the Λ, $\overline{\Lambda}$, Ξ^-, and $\overline{\Xi}^+$ hyperons, averaged over the full available kinematical range. Possible systematic errors, introduced by the analysis method or by the setup, are addressed in section 8.2. After this section 8.3 presents the Λ and $\overline{\Lambda}$ polarization in various kinematical bins. Finally section 8.4 summarizes the results and compares them with other experimental data and theoretical models.

Unless explicitly stated otherwise, all distributions, that are shown in the following sections, are background corrected using the methods explained in subsection 7.2.4 for the Λ and in 7.2.5 for the Ξ hyperons, respectively.

8.1 Average transverse Polarization of Λ and Ξ Hyperons

The hyperon polarization is determined from the double bias canceling ratio $R(\cos\theta_y)$ (see section 7.3). $R(\cos\theta_y)$ is calculated from the background corrected angular distributions of the daughter baryon in the hyperon's rest frame, which are obtained by fitting invariant mass histograms, that correspond to certain angular bins (see section 7.4). In this analysis eight bins in $\cos\theta_y$ are used, so that due to the additional up-down subdivision in total 16 mass histograms are generated and fitted. The resulting 16 numbers are combined according to eq. (7.17) (page 129) to four values of $R(\cos\theta_y)$. If the acceptance is symmetric with respect to the mid-plane of the spectrometer, $R(\cos\theta_y)$ is directly proportional to the polarization: $R(\cos\theta_y) = \alpha_H P_y^H \cos\theta_y$. A simple fit of the slope of the four $R(\cos\theta_y)$ points thus determines the transverse polarization P_y^H. Fig. 8.1 and 8.2 show the results for the overall samples of the Λ and the Ξ hyperons. The measured polarizations as well as the mean values of basic kinematical variables are summarized in table 8.1.

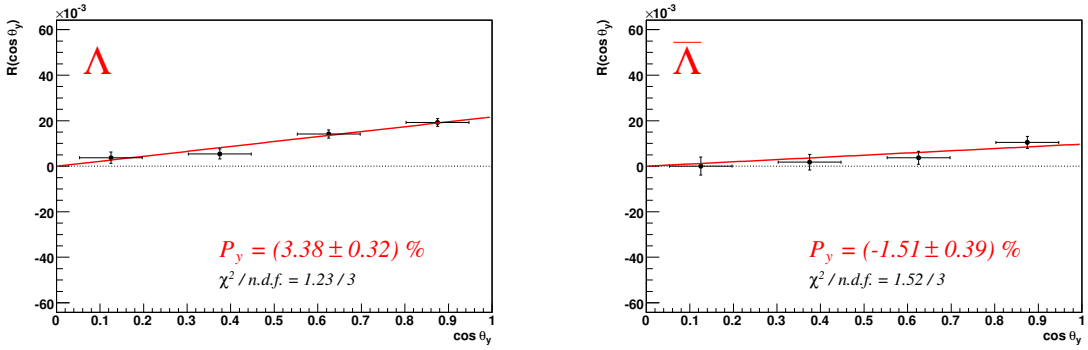

Figure 8.1: Angular distributions $R(\cos\theta_y)$ and polarizations of the overall Λ and $\overline{\Lambda}$ samples: The fitted slopes are directly proportional to the polarizations which in case of the Λ is significantly positive. The $\overline{\Lambda}$ polarization value is 3.9 σ_{stat} below zero. In both cases the straight line fits the data points well with a probability of 74.6 % for the Λ and 67.8 % for the $\overline{\Lambda}$, respectively.

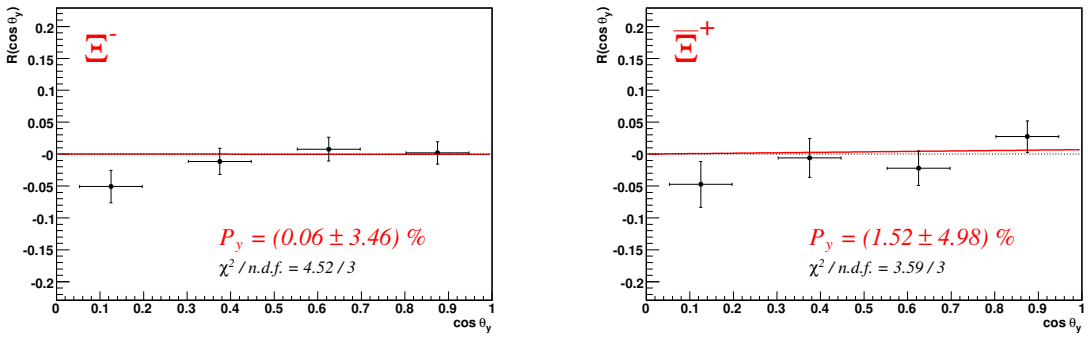

Figure 8.2: Angular distributions $R(\cos\theta_y)$ and polarizations of the overall Ξ^- and $\overline{\Xi}^+$ samples: Both polarizations are compatible with zero. Compared to the Λ the fluctuation of the data points is larger, but with fit probabilities of 21.1 % for the Ξ^- and 30.9 % for the $\overline{\Xi}^+$ still compatible with the straight line hypothesis.

	Λ	$\bar{\Lambda}$	Ξ^-	$\bar{\Xi}^+$
N_H	1645464	867324	24957	14994
P_y^H [%]	$+3.38\pm0.32$	-1.51 ± 0.39	$+0.06\pm3.46$	$+1.52\pm4.98$
Fit χ^2/n.d.f.	0.41	0.51	1.51	1.20
$P_y^{K^0}$ [%]	$+0.13\pm0.28$	$+0.10\pm0.28$	—	—
Fit χ^2/n.d.f.	0.86	4.83	—	—
$\langle x_F \rangle$	0.190	0.183	0.202	0.191
$\langle p_T \rangle$ [GeV/c]	0.563	0.559	0.638	0.637
$\langle y_B \rangle$	0.435	0.460	0.457	0.484
$\langle Q^2 \rangle$ [(GeV/c)^2]	0.402	0.420	0.418	0.433
$\langle z_h \rangle$	0.259	0.249	0.280	0.266

Table 8.1: Measured average hyperon polarizations. The meaning of the K^0 background polarization $P_y^{K^0}$ is explained in subsection 8.2.1.

The $\cos\theta_y$ coordinates of the four $R(\cos\theta_y)$ points correspond to the respective bin centers, the $\cos\theta_y$ error bars are set to $1/\sqrt{12}$ times the bin width. In principle the side-band corrected angular distributions could be used to find better estimates for the respective $\cos\theta_y$ values. Since the $\cos\theta_y$ distributions are rather flat (cf. fig. 7.31) the bin centroids are well approximated by the bin centers, but the errors in $\cos\theta_y$ would get smaller. Consequently the χ^2/n.d.f. values of the fits of the four $R(\cos\theta_y)$ points are underestimated by the used method.

8.2 Study of Systematics

Systematic effects, that may cause false asymmetries, are of manifold origin: The fitting procedure of the invariant mass histograms might introduce biases in particular for the Λ hyperons, where peak and background have a nontrivial shape (see subsection 8.2.1). It also has to be verified, whether the acceptance correction with the double bias canceling method works correctly (see subsection 8.2.2) and whether the polarization results are stable over the various data taking periods (see subsection 8.2.3). Possible systematic effects might in addition be caused by the longitudinal polarization of the target material or might result from the influence of the target solenoid field and its interaction with the fringe field of the first spectrometer magnet, which breaks the mid-plane symmetry of the apparatus. Both issues are addressed in subsection 8.2.4.

A good indicator for false asymmetries are the kaons, which are available in very large numbers and also contribute to the background in the Λ and $\bar{\Lambda}$ invariant mass histograms. As spin-0 particles the K^0s by definition must have zero polarization. Fig. 8.3 shows the average false transverse K^0 polarization extracted from the angular distribution of the positive daughter pion. In the calculation of the K^0 polarization value the same

decay asymmetry parameter as for the Λ decay was used, so that the K^0 polarization can directly compared to the respective Λ and $\overline{\Lambda}$ values.

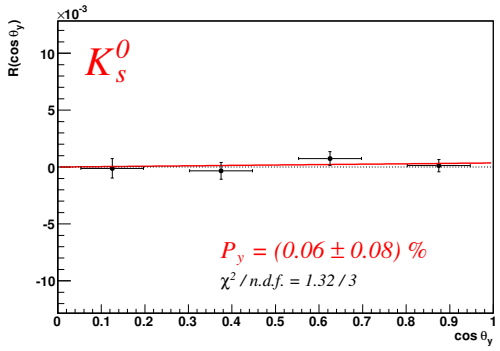

Figure 8.3: Angular distribution $R(\cos\theta_y)$ and polarization for the overall K^0 sample: The polarization is small and compatible with zero. The straight line hypothesis has a probability of 72.4 %.

The measured overall K^0 polarization is about 2 % of the Λ polarization and within the errors compatible with zero. This result already gives some confidence, that possible apparatus effects are small and that the assumptions, made for the bias canceling, are valid, so that the acceptance correction is working properly. Nevertheless the result has to be interpreted with care, as the main fraction of the kaons decays symmetrically with small absolute values of the Armenteros α, thus covering a different kinematical region compared to the Λs and $\overline{\Lambda}$s, that always decay asymmetrically.

8.2.1 Systematics of the Background Subtraction

Unlike the Ξs the Λ hyperons sit on top of a quite complicated background. Subsection 7.4.1 introduced three different methods to fit the Λ invariant mass histograms: The simplest method uses the sum of a Gaussian and a third order polynomial, but is not able to describe the data well. It has the tendency to overestimate the background and to underestimate the number of hyperons. The second method uses a double gaussian on top of a third order polynomial background and agrees much better with the data, but is problematic, because background and signal are partly ambiguous, so that this method tends to overestimate the number of Λs in the invariant mass peak. The ambiguity is reduced by constraining the two Gaussians to have the same mean values. In the third method, that was finally chosen for the analysis, the invariant Λ mass histogram is expanded with the invariant mass for the K^0 hypothesis and fitted with a two-dimensional function (cf. fig. 7.39 (page 139)). This way the kaon contribution to the background is nicely separated and can also be analyzed quantitatively (see further below). Fig. 8.4 shows the results for the Λ and $\overline{\Lambda}$ polarizations, obtained using the three fit methods described above.

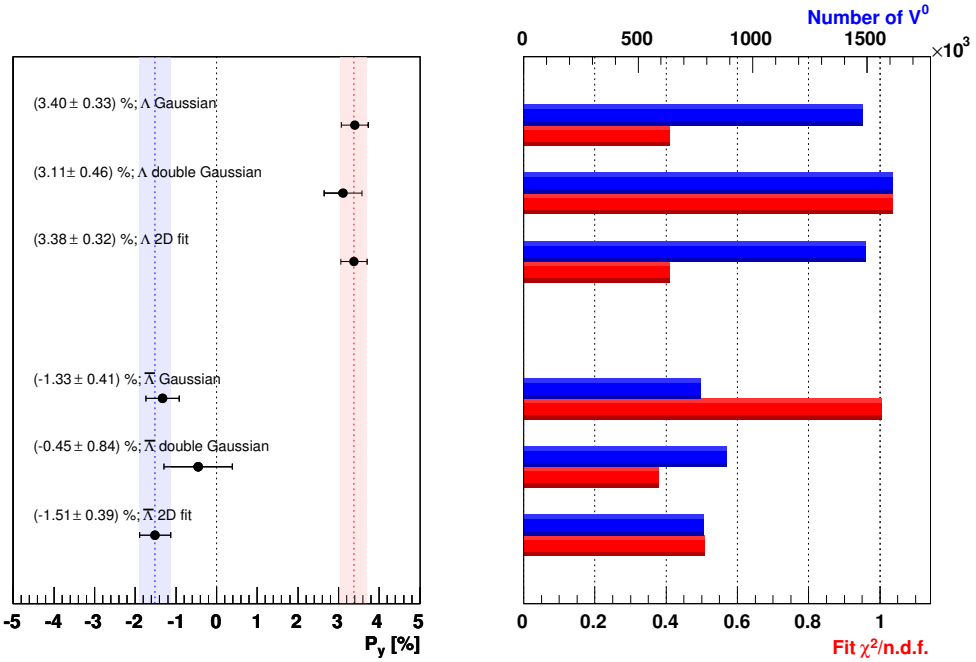

Figure 8.4: Λ and $\bar{\Lambda}$ polarizations obtained with three different fit methods: The upper three points represent the results for the overall Λ sample using the single Gaussian, the double Gaussian, and the two-dimensional fit. The lower three points show the same for the overall $\bar{\Lambda}$ sample. In both cases a band highlights the result of the two-dimensional fit. The graph on the right displays for each point the total number of hyperons (blue bars) and the χ^2/n.d.f. of the straight line fit to the four $R(\cos\theta_y)$ points (red bars). The total number of hyperons is calculated by integrating the background corrected angular distributions, that are obtained from the invariant mass fits.

Within the errors the results from the different fit methods are in agreement. This demonstrates that the employed polarization extraction method is quite robust with respect to the precision, with which the shape of the invariant mass histograms is described. Fig. 8.4 also illustrates the disadvantage of the double Gaussian fit: The number of Λs is overestimated, which potentially leads to a dilution of the polarization by the background, and in addition the signal-background ambiguity increases the error on the extracted number of hyperons resulting in a larger polarization error.

One of the advantages of the two-dimensional fit method is, that it allows to extract the number of background K^0s under the Λ and $\overline{\Lambda}$ peaks. This way it is possible to study the false kaon polarization in the same kinematical region as for the Λs and $\overline{\Lambda}$s (see fig. 8.5). Fig. 8.6 shows the polarization of the K^0 background for the overall Λ and $\overline{\Lambda}$ samples. The expected zero polarization is confirmed by the data. In the further analysis the kaon background polarization will be used as an estimate for the systematic error.

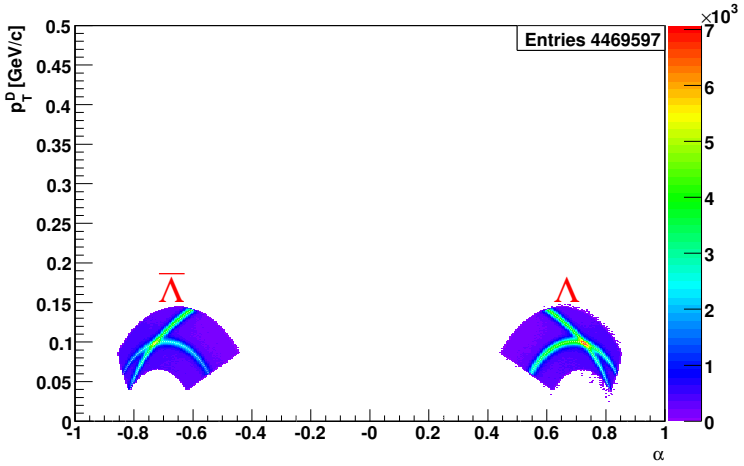

Figure 8.5: Armenteros plot of the two-dimensional fit regions for the overall Λ and $\overline{\Lambda}$ sample (cf. fig. 7.39 (page 139)).

The possible influence of the converted photon background on the Λ, $\overline{\Lambda}$, Ξ^-, and $\overline{\Xi}^+$ polarizations is estimated by disabling the cut, that forbids the decay pion to be associated with the primary vertex (see subsection 7.2.4). This increases the contamination of the hyperon samples by converted photons (cf. fig. 7.15 (page 113) for the Λ and fig. 7.26 (page 121) for the Ξ), which in the two-dimensional Λ and $\overline{\Lambda}$ invariant mass histograms tend to gather at the kinematical border. Fig. 8.7 shows that, apart from an expected increase of the polarization error, the converted photon background has no systematic influence on the results, which means that it is well described by the fit functions.

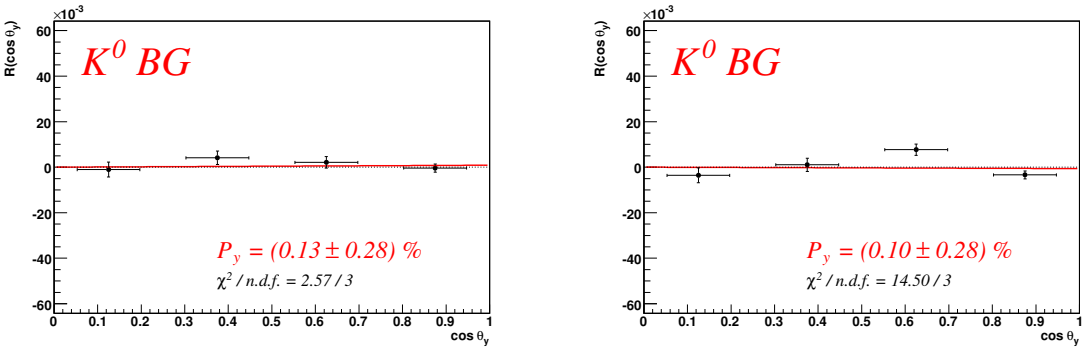

Figure 8.6: (a) Angular distribution $R(\cos\theta_y)$ and polarization of the K^0 background for the overall Λ sample. (b) shows the same for the $\overline{\Lambda}$. In both cases the polarizations are within the errors compatible with zero. The fit probability of the Λ background is 46.3 %, whereas that of the $\overline{\Lambda}$ is only 0.2 %.

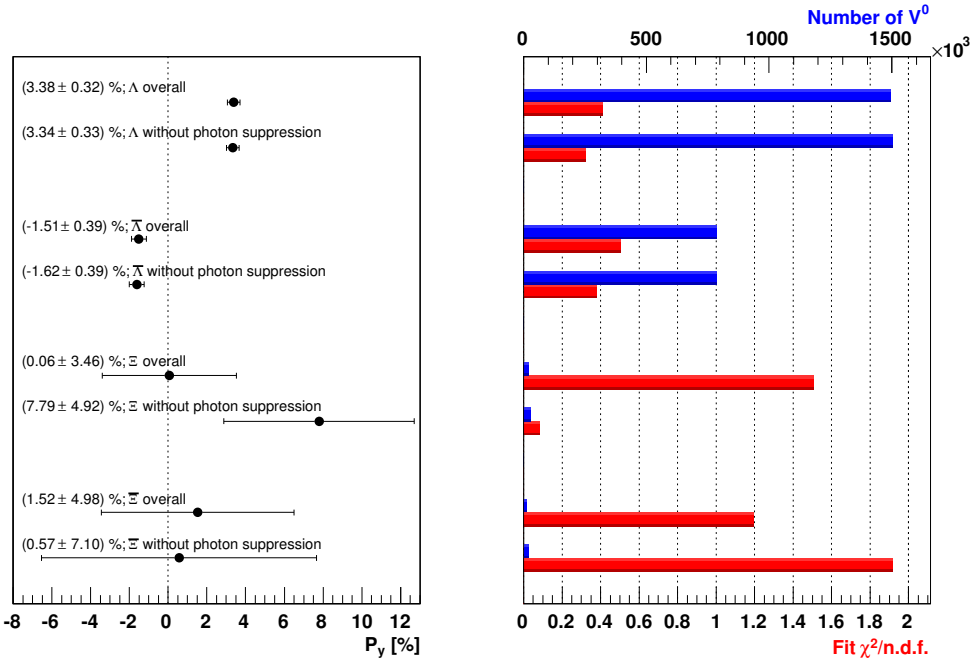

Figure 8.7: Influence of the converted photon background on the measured hyperon polarization: The four groups of points show the Λ, $\overline{\Lambda}$, Ξ^-, and $\overline{\Xi}^+$ polarizations with and without suppression of the converted photon background. The right graph displays for each point the total number of hyperons and the χ^2/n.d.f. of the $R(\cos\theta_y)$ fit.

8.2.2 Systematics of the Bias Canceling

8.2.2.1 Simple vs. Double Bias Canceling

The double bias canceling ratio $R(\cos\theta_y)$ was introduced in section 7.3, because the statistics of the "up" and "down" samples is not equal. Imperfect alignment of beam and apparatus cause a small asymmetry ε between the total numbers of up- and down-going hyperons

$$\varepsilon = \frac{U_0 - D_0}{U_0 + D_0} \tag{8.1}$$

With the above asymmetry the simple bias canceling ratio R_0 as defined in eq. (7.14) (page 128) may be written with eq. (7.7) and (7.13) as:

$$R_0(\cos\theta_y) = \frac{U(\cos\theta_y) - D(-\cos\theta_y)}{U(\cos\theta_y) + D(-\cos\theta_y)} = \frac{\varepsilon + \alpha_H\, P_y^H \cos\theta_y}{1 + \varepsilon\,\alpha_H\, P_y^H \cos\theta_y} \tag{8.2}$$

Both $|\varepsilon|$ and $|\alpha_H\, P_y^H \cos\theta_y|$ are small, which in first order approximation leads to

$$R_0(\cos\theta_y) \approx (1 - \varepsilon\,\alpha_H\, P_y^H \cos\theta_y)(\varepsilon + \alpha_H\, P_y^H \cos\theta_y) \approx \alpha_H\, P_y^H \cos\theta_y + \varepsilon \tag{8.3}$$

This means that the asymmetry in the total number of up- and down-going hyperons manifests itself as an offset in the $R_0(\cos\theta_y)$ distribution.

Fig. 8.8 and 8.9 show the angular distributions $R_0(\cos\theta_y)$ for the overall Λ, $\overline{\Lambda}$, Ξ^-, and $\overline{\Xi}^+$ samples and have to be compared with fig. 8.1 and 8.2, respectively. The $R_0(\cos\theta_y)$ distributions cover the full angular range from $-\pi$ to π and have twice the number of angular bins. According to eq. (8.3) the data are fitted by a linear function with a nonzero offset. The polarizations, that are determined from the slope of the fit, are virtually identical to the ones from the fit of the double bias canceling ratio $R(\cos\theta_y)$. The offsets of the Λ and $\overline{\Lambda}$ fits agree with the asymmetry values $\varepsilon_\Lambda = 21.9 \cdot 10^{-3}$ and $\varepsilon_{\overline{\Lambda}} = 21.6 \cdot 10^{-3}$ from the fit of the invariant mass histograms of up- and down-going Λs and $\overline{\Lambda}$s. This demonstrates that the double bias canceling successfully compensates the different size of the "up" and the "down" samples.

8.2.2.2 Verification of the Left-Right Acceptance Correction

The bias canceling technique exploits the up-down symmetry of the apparatus to compensate the inherent left-right asymmetry of the acceptance, that is caused by the spectrometer magnets. To verify the reliability of this method the Λ, $\overline{\Lambda}$, Ξ^-, and $\overline{\Xi}^+$ samples are subdivided into three disjoint subsamples according to their azimuthal angle in the laboratory frame (similar to [Ada04a]). Each of the three samples combines four 15° segments to an up-down and left-right symmetric configuration (see fig. 8.10). If the

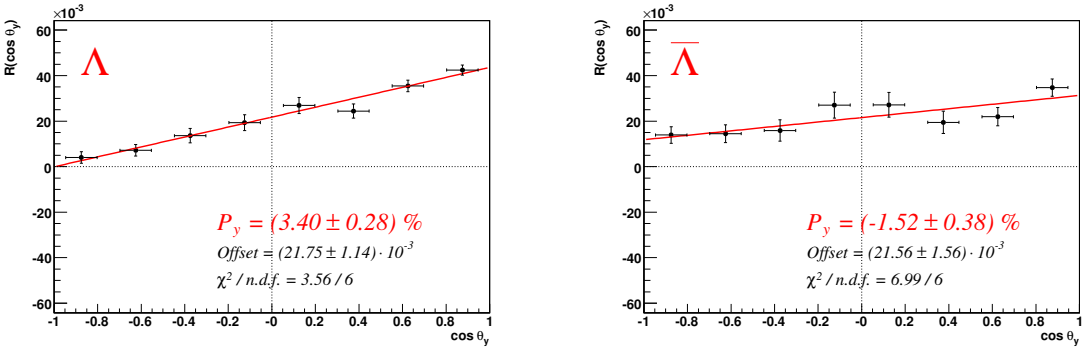

Figure 8.8: Angular distributions $R_0(\cos\theta_y)$ and polarizations of the overall Λ and $\overline{\Lambda}$ samples: The slope of the fits is proportional to the polarization. The offset is a measure for the asymmetry of the number of up- and down-going hyperons. In both cases the straight lines fit the data well with probabilities of 73.6 % for the Λ and 32.2 % for the $\overline{\Lambda}$.

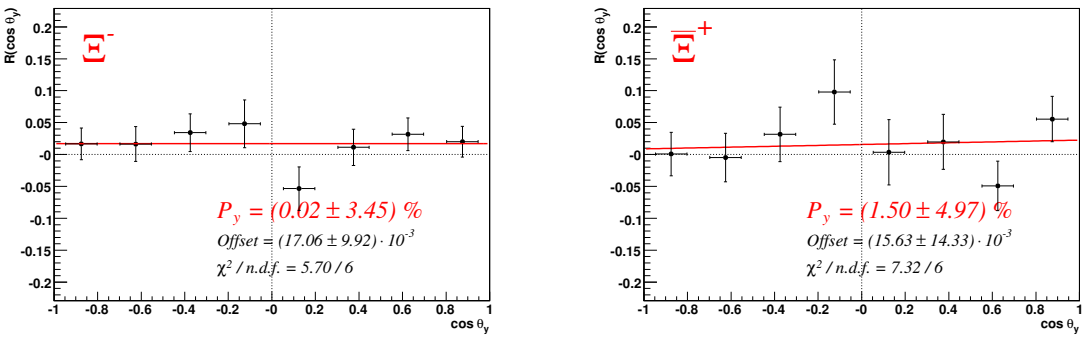

Figure 8.9: Angular distributions $R_0(\cos\theta_y)$ and polarizations of the overall Ξ^- and $\overline{\Xi}^+$ samples: The fit probabilities of 45.8 % for the Ξ^- and 29.2 % for the $\overline{\Xi}^+$ show that the data are described by a straight line.

bias canceling fails to compensate part of the left-right asymmetry of the acceptance, this would cause systematic deviations of the polarizations in the three sectors.

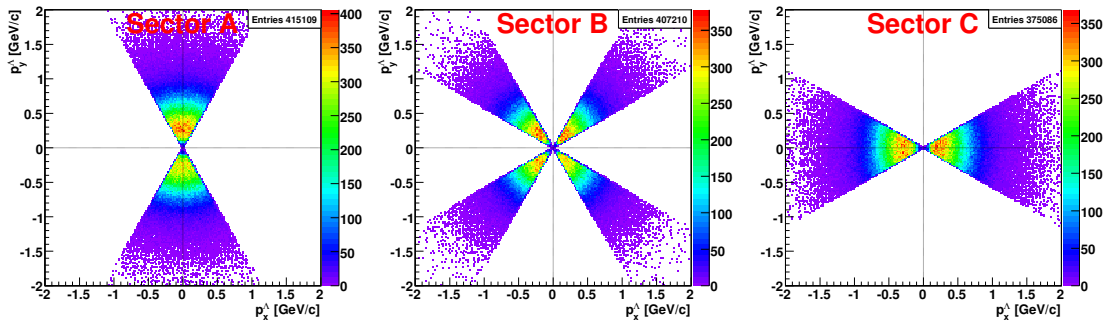

Figure 8.10: Sector definition to verify the left-right acceptance correction: The overall sample is subdivided according to the x_{Lab}- and y_{Lab}-components of the hyperon momentum. Whereas sector A predominantly contains up- and down-going hyperons, that have a y_{Lab}-momentum component larger than the one along x_{Lab}, sector C has a pronounced left-right orientation.

A possible influence of the beam direction on the bias cancelling is checked by determining the polarization in four disjoint subsamples, that correspond to the four quadrants in the (x_{Lab}, y_{Lab}) beam momentum plane.

Fig. 8.11 and 8.12 summarize the results for the Λ, $\overline{\Lambda}$, Ξ^-, and $\overline{\Xi}^+$ hyperons. Neither the hyperon momentum sectors nor the beam momentum quadrants show systematic deviations from the average polarization.

8.2.2.3 Stability under Binning in $\cos\theta_y$

In order to extract the polarization the hyperon samples are subdivided into eight bins in $\cos\theta_y$, which result in four bins in $R(\cos\theta_y)$. Fig. 8.13 shows that this particular choice has no systematic influence on the Λ, $\overline{\Lambda}$, Ξ^-, and $\overline{\Xi}^+$ polarization results. The polarizations remain unchanged within the statistical limits, if the number of angular bins is increased by a factor of two and four. The main reason for using only eight $\cos\theta_y$-bins is, that this way the invariant mass histograms still have reasonable statistics, when the sample is subdivided into several kinematical bins (see section 8.3).

8.2.3 Stability of the Setup

Over the years the spectrometer setup was improved by adding and rearranging some detectors. In parallel the reconstruction software evolved, so that the mDST data of the different periods in the data set were produced by different versions of the reconstruction program. Fig. 8.14 and 8.15 show that these changes have no systematic influence on the

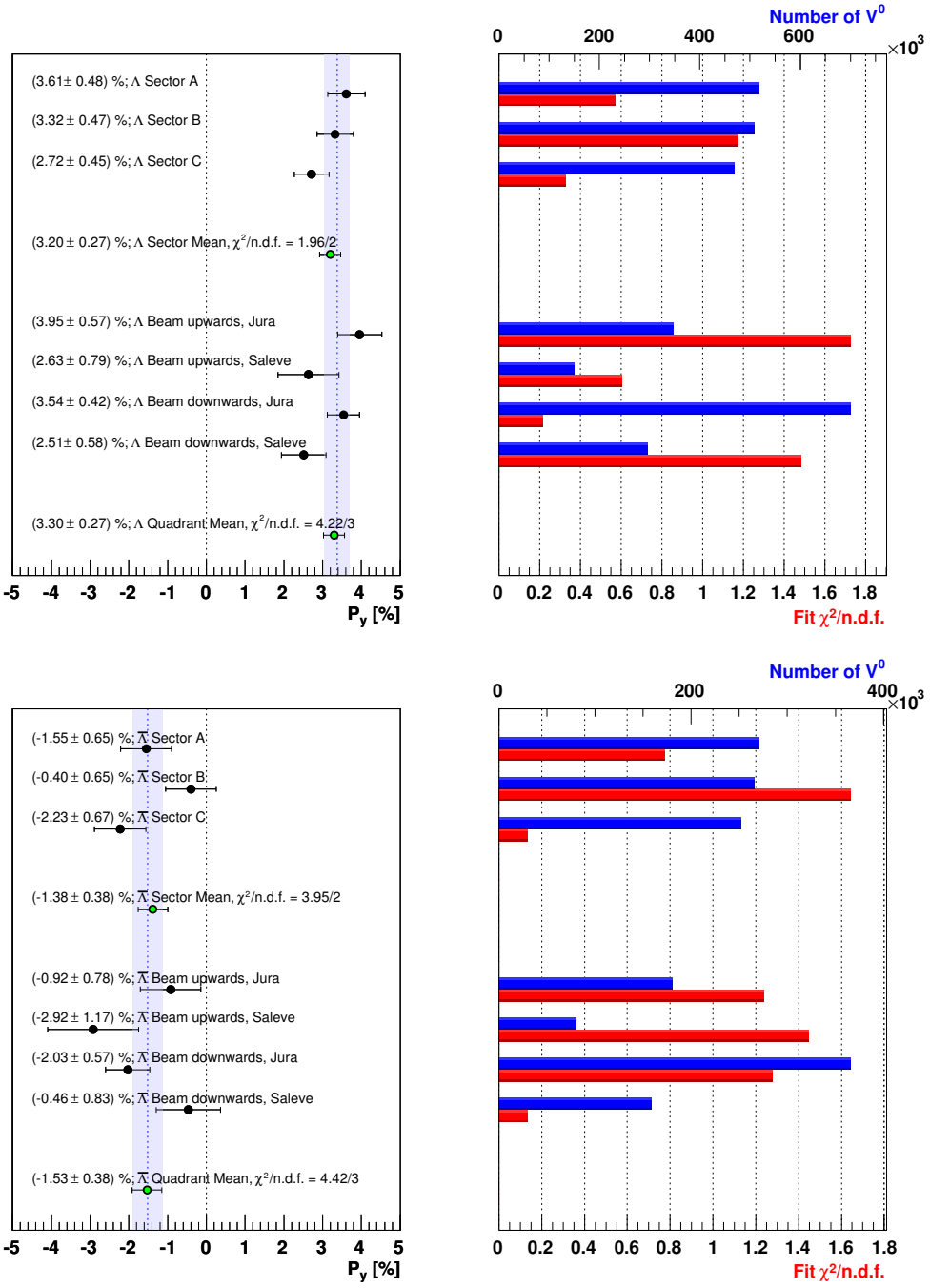

Figure 8.11: Λ and $\overline{\Lambda}$ polarizations in three azimuthal sectors and in dependence on the beam direction: The weighted mean values show that the polarizations of the three sector as well as that of the four quadrant subsamples fluctuate within statistical range and do not exhibit any systematic deviations. The bands indicate the values of the overall Λ and $\overline{\Lambda}$ polarization, respectively. The graph on the right displays for each point the total number of hyperons and the χ^2/n.d.f. of the $R(\cos\theta_y)$ fit.

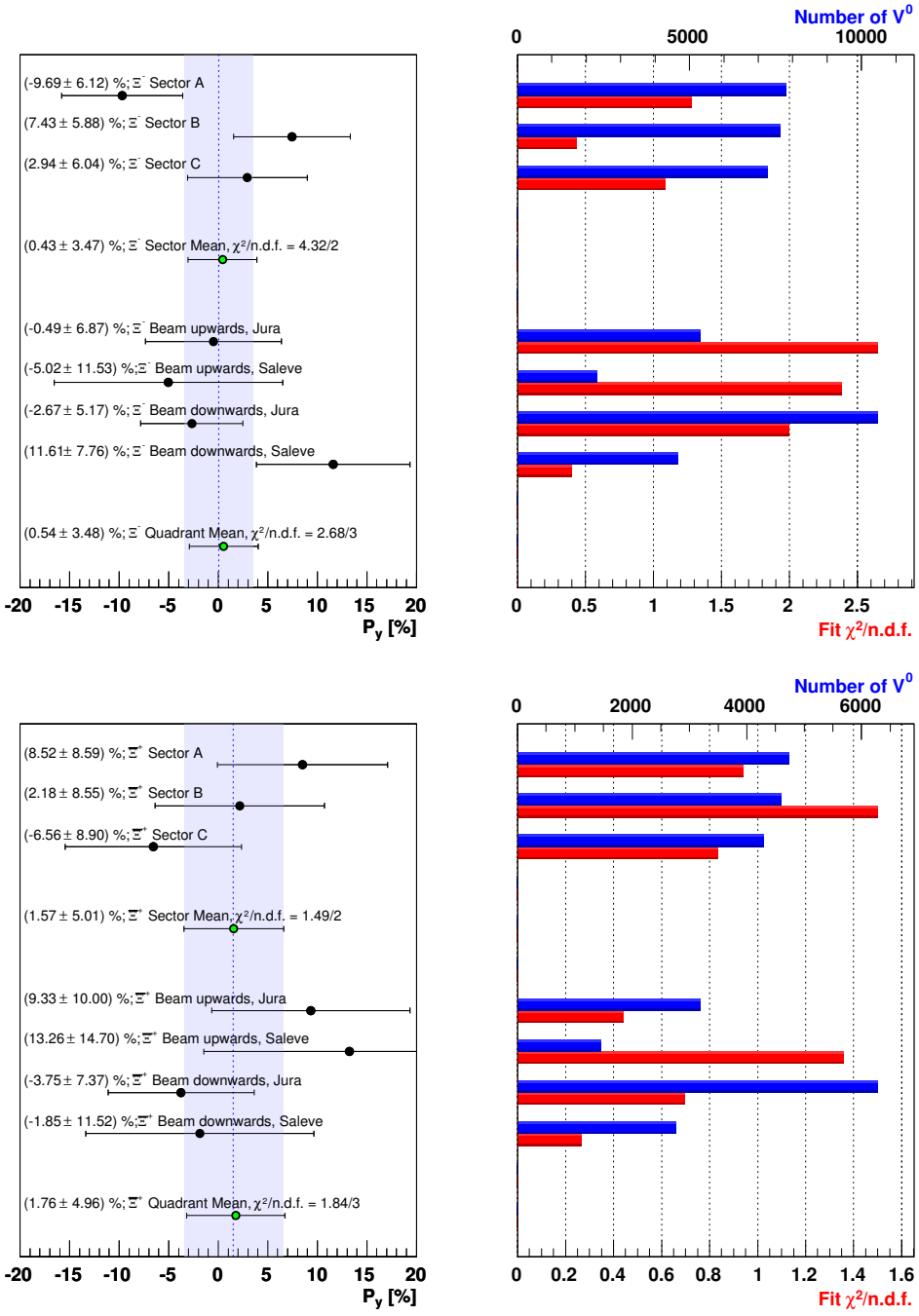

Figure 8.12: Ξ^- and $\bar{\Xi}^+$ polarizations in three azimuthal sectors and in dependence on the beam direction: As for the Λ hyperons the polarizations of the three sector as well as that of the four quadrant subsamples fluctuate within statistical range and do not exhibit any systematic deviations. The bands indicate the values of the overall Ξ^- and $\bar{\Xi}^+$ polarization, respectively.

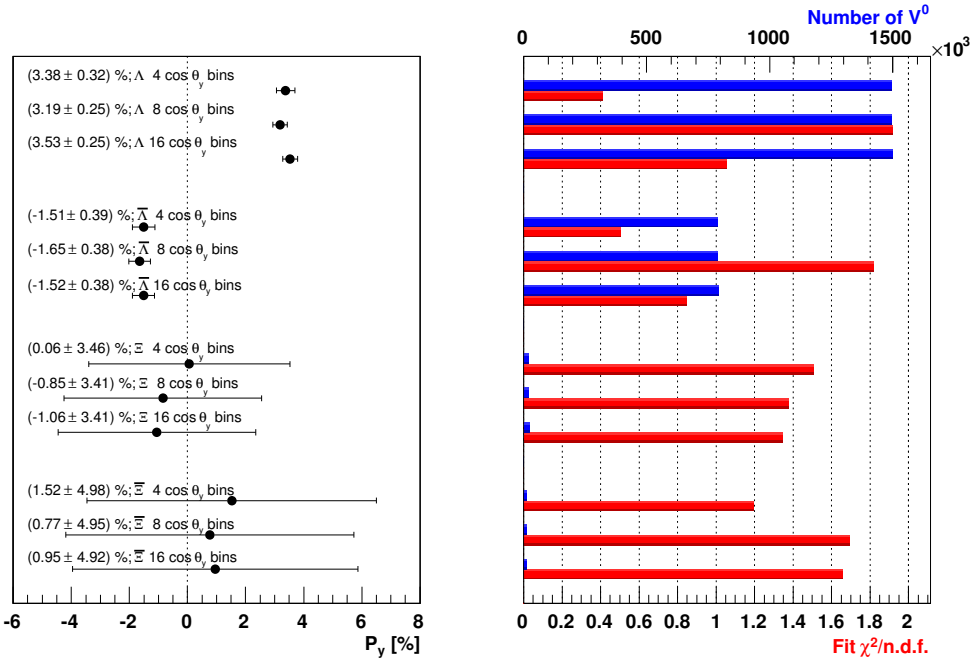

Figure 8.13: Dependence of Λ, $\overline{\Lambda}$, Ξ^-, and $\overline{\Xi}^+$ polarizations on binning in $\cos\theta_y$: In each case the polarization is calculated using four, eight, and sixteen bins for the angular distributions $R(\cos\theta_y)$. The values show that the binning has no systematic effect on the polarization. The graph on the right displays for each point the total number of hyperons and the χ^2/n.d.f. of the $R(\cos\theta_y)$ fit.

Λ and $\bar{\Lambda}$ polarizations. Due to the small number of Ξ hyperons, this check is not possible for the Ξ^- and $\bar{\Xi}^+$ polarizations.

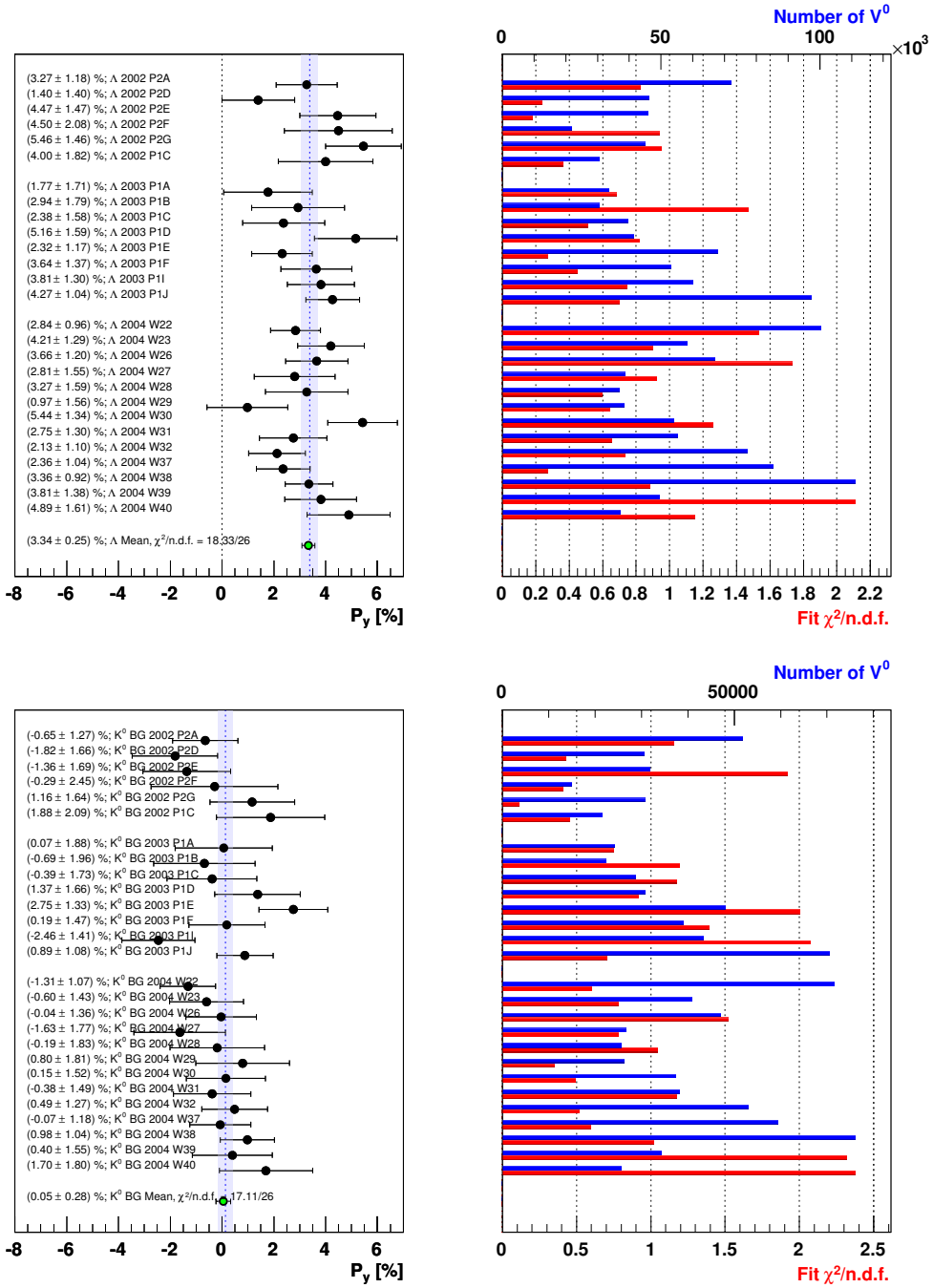

Figure 8.14: Λ and K^0 background polarizations for the various data taking periods: The polarizations fluctuate within the statistical range. The weighted mean of all polarization values agrees with the respective overall polarization, that is indicated by the band. The right graph shows for each point the total number of hyperons and the χ^2/n.d.f. of the $R(\cos\theta_y)$ fit.

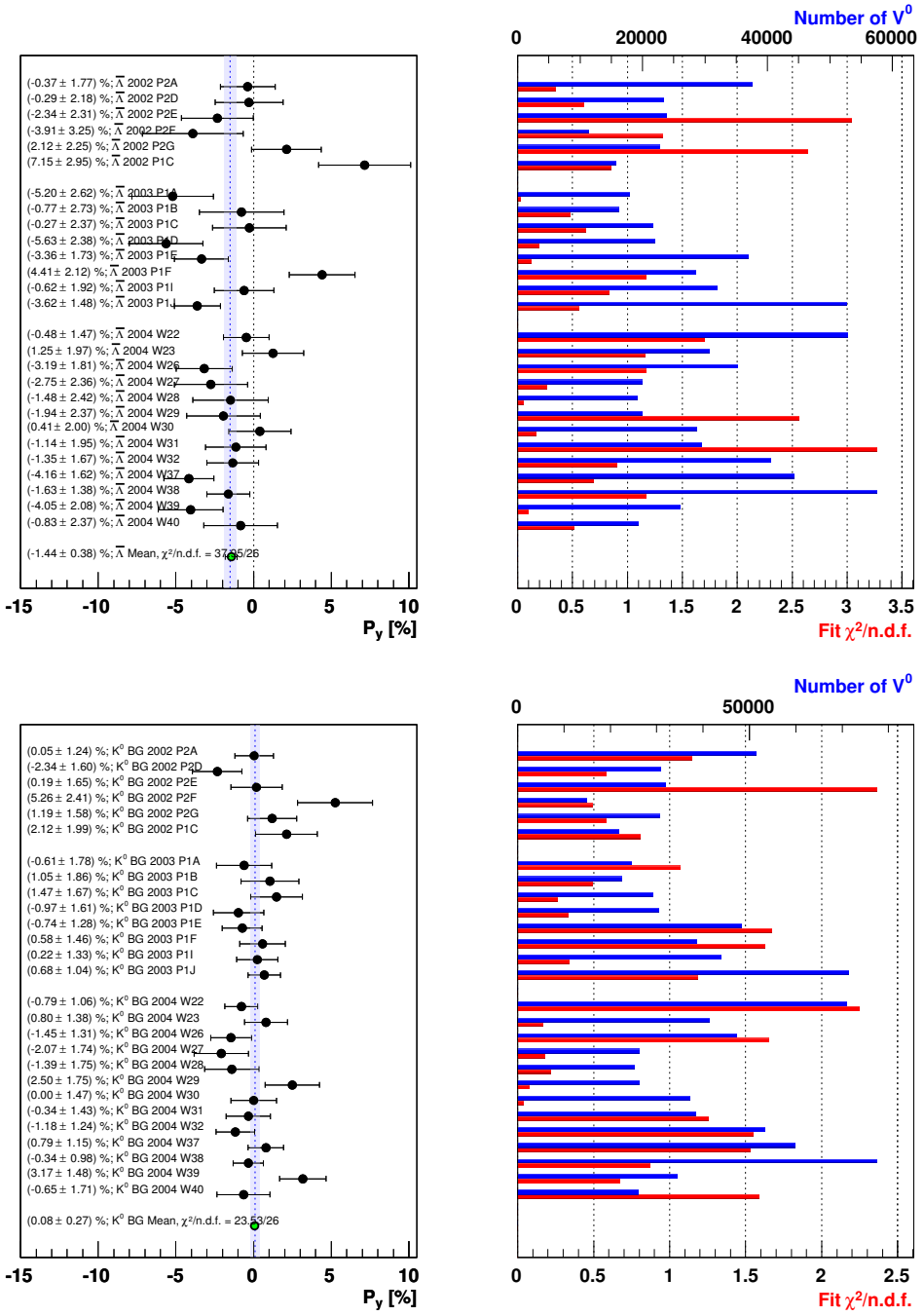

Figure 8.15: $\overline{\Lambda}$ and K^0 background polarizations for the various data taking periods: Compared to the Λ the $\overline{\Lambda}$ polarization exhibits a larger fluctuation in particular in the years 2002 and 2003. A possible reason for this behavior is, that the signal to background ratio of the $\overline{\Lambda}$ is lower than that of the Λ. In combination with the low statistics of the fitted samples this leads to only sparsely populated invariant mass histograms, for which the two-dimensional fit of the $\overline{\Lambda}$ line may become unreliable. The K^0 background polarization shows the expected statistical fluctuation.

8.2.4 Systematics due to the Setup

8.2.4.1 Influence of the Target Polarization

Up to now the target material was considered unpolarized in this analysis, but this is, strictly speaking, only true for those events, where the target polarization vector lies in the production plane. It is possible to estimate an upper limit for the potential influence of the target polarization from the distribution of the angle θ_{γ^*} of the virtual photon with respect to the target polarization axis, which is in good approximation parallel to the z_{Lab}-axis. As the direction of the virtual photon $\vec{\gamma}^*$ is one of the two vectors, that span the production plane (cf. fig. 7.5 (page 103)), the component of the target polarization transverse to the production plane is

$$P_{y,\text{Target}} = \pm P_{\text{Target}} \sin\theta_{\gamma^*} \tag{8.4}$$

Fig. 8.16a shows that the mean angle $\langle\theta_{\gamma^*}\rangle$ of the virtual photon is smaller than 5.2 mrad, so that the mean transverse component of the target polarization is smaller than 0.52 % $\cdot$ P_{Target}, a value that is comparable to the statistical error of the overall Λ polarization.

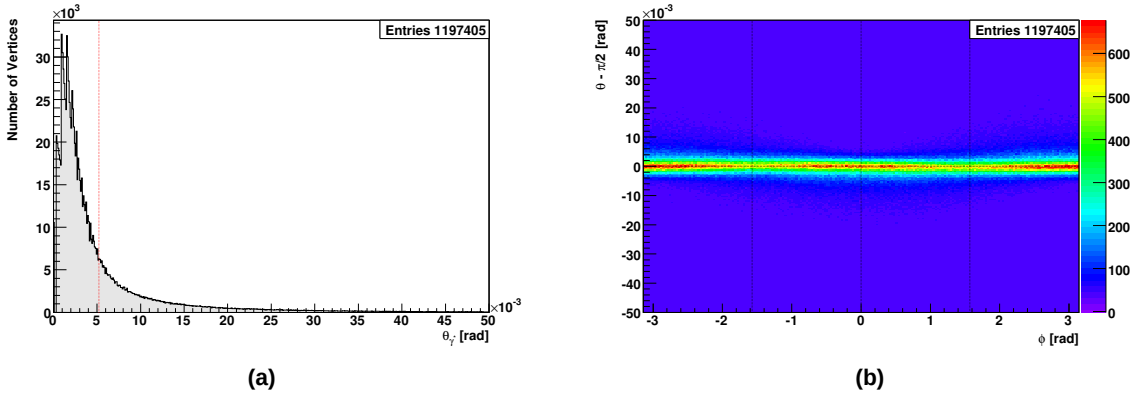

Figure 8.16: (a) Distribution of the polar angle of the virtual photon with respect to the z_{Lab}-axis in the Λ sample. The mean angle is indicated by the vertical line. (b) Angular distribution of the production plane normal with respect to the z_{Lab}-axis in the Λ sample. The azimuthal φ distribution is defined with respect to the x_{Lab}-axis and is modulated according to the rectangular shape of the geometrical acceptance.

The above calculation does not take into account the azimuthal angle of the outgoing hyperon, which rotates the production plane around the virtual photon direction, so that the plane has various orientations with respect to the target polarization. This is illustrated in Fig. 8.16b, which shows the angular distribution of the production plane normal with respect to the z_{Lab}-axis. Due to the small Λ and γ^* angles, the production plane normal is approximately perpendicular to the z_{Lab}-axis, whereas the azimuthal distribution is rather flat. This reduces the magnitude of the effective target polarization component along the production plane normal, since the components along and opposite to the y-axis cancel each other nearly completely. This effect is shown in fig. 8.17, which depicts

the distribution of the target polarization component along the production plane normal, which has a negligible mean value of $-0.0035\ \% \cdot P_{\text{Target}}$.

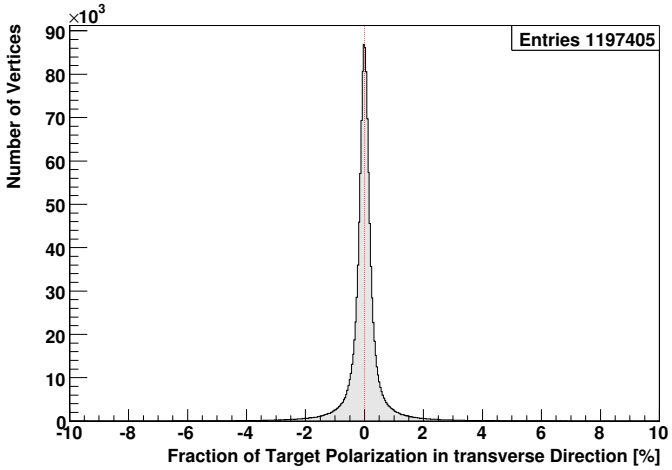

Figure 8.17: Fraction of the target polarization along the production plane normal y.

The above result is supported by the fact, that no influence of the orientation of the target polarization on the hyperon polarization result is found (see fig. 8.18 and 8.19).

8.2.4.2 Precession in the Target Solenoid Field

Another possible systematic effect is the precession of the hyperon spin in the magnetic field of the target solenoid. The precession leads to a systematic underestimation of the polarization, because the direction of the hyperon polarization at its decay vertex is not anymore parallel to the production plane normal as it is the case at the hyperon's production vertex. Consequently only the projection of the real polarization onto the production plane normal is measured.

The equation of motion of the spin in the rest frame of the hyperon is

$$\left[\frac{\mathrm{d}\vec{S}_H}{\mathrm{d}t}\right]_{\text{RF}} = \vec{\mu}_H \times \vec{B}_{\text{RF}} \tag{8.5}$$

$$\text{with} \quad \vec{B}_{\parallel,\text{RF}} = \vec{B}_{\parallel,\text{Lab}}, \quad \vec{B}_{\perp,\text{RF}} = \gamma_H(\vec{B}_{\perp,\text{Lab}} - \vec{\beta}_H \times \vec{E}_{\text{Lab}}/c), \quad \text{and} \quad \vec{E}_{\text{Lab}} \approx 0$$

where $\vec{S}_H$ is the spin vector of the hyperon, $\vec{\mu}_H$ its magnetic moment and $\vec{B}_{\text{RF}}$ the magnetic field in the rest frame, which is calculated from the field in the laboratory frame by a Lorentz transformation, that involves the hyperon's Lorentz factor γ_H and its velocity β_H. The magnetic moment of the hyperon is given by its relative magnetic moment μ_R^H and the nuclear magneton μ_N by $\vec{\mu}_H = g\,\mu_R^H\,\mu_N\,\vec{S}_H/\hbar$.

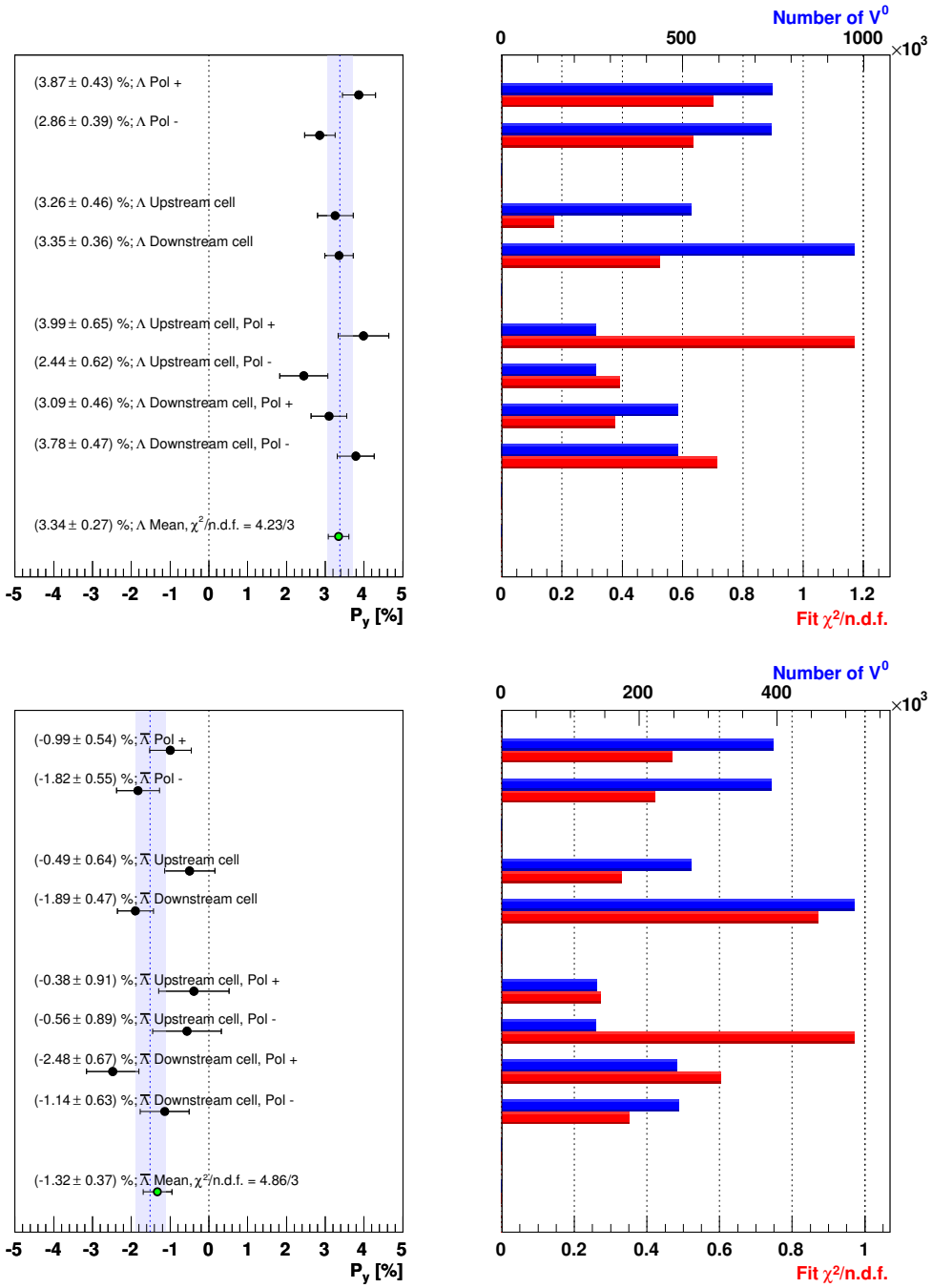

Figure 8.18: Dependence of the Λ and $\bar{\Lambda}$ polarizations on the target polarization: The plot on the top shows the results for the Λ, the lower one for the $\bar{\Lambda}$. In each case the upper two points represent the hyperon polarization for the two possible configurations of the target cell polarizations (cf. subsection 2.2.3), where the sign refers to the state of the upstream cell. Within the statistical errors the polarizations agree with the respective overall polarization, that is indicated by the band. The next two points show, that the polarization does not depend on the target cell in which the hyperon was produced. Similarly the weighted means of the four disjoint subsamples for the two target cells and their polarization indicate no systematic influence of the polarization of the target material. The graphs on the right display for each point the total number of hyperons and the χ^2/n.d.f. of the $R(\cos\theta_y)$ fit.

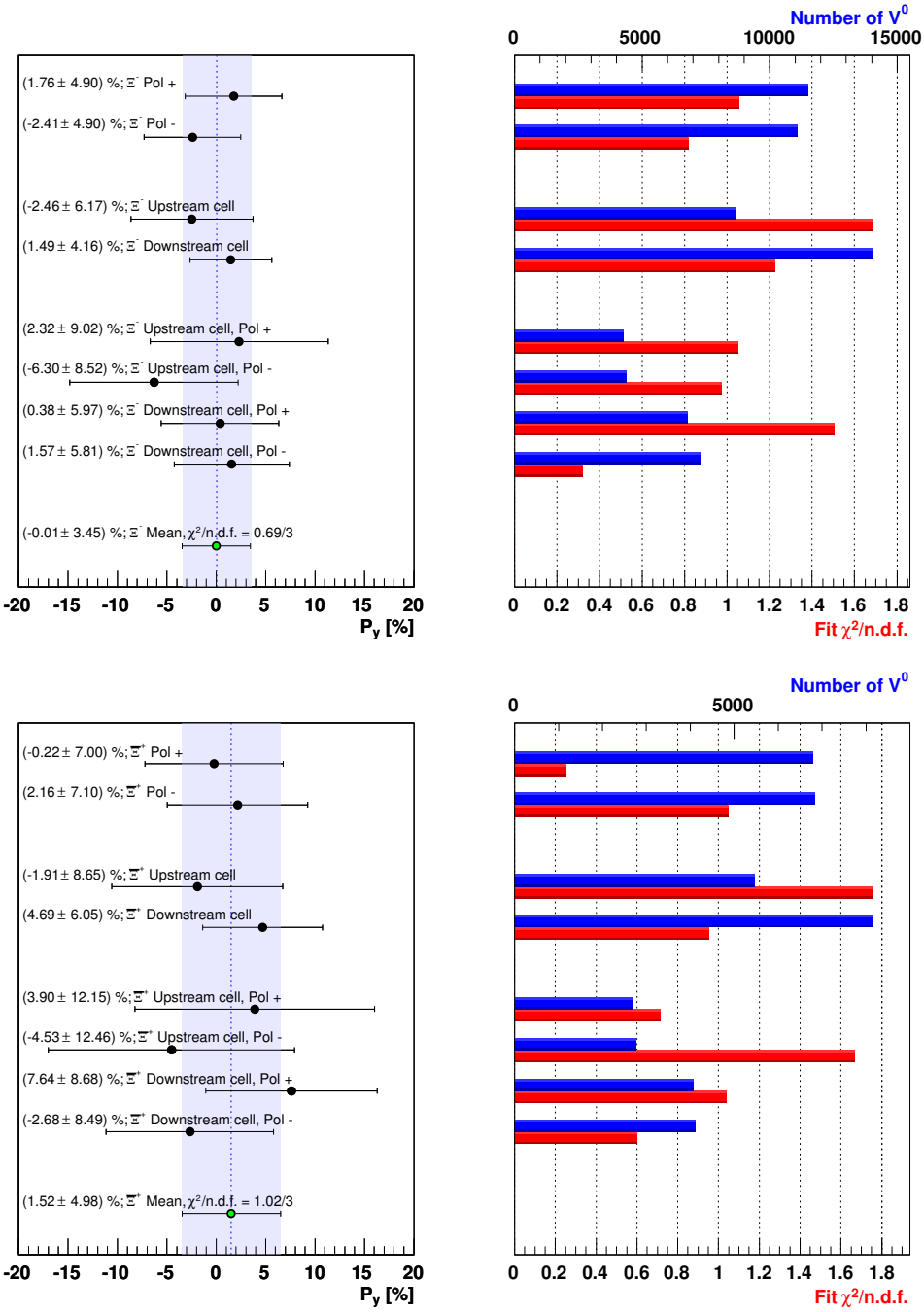

Figure 8.19: Dependence of the Ξ^- and $\overline{\Xi}^+$ polarizations on the target polarization: The upper plot shows the results for the Ξ^-, the lower one for the $\overline{\Xi}^+$. The definition of the points is the same as in fig. 8.18.

A rough upper limit for the total Λ spin precession angle is estimated by assuming, that the solenoid field in the Λ rest frame is perpendicular to the Λ spin direction and that the Λ sees the field for a time of $t_{\mathrm{RF}} = 1\,\mathrm{ns}$ ($\approx 4\ \tau_\Lambda$) before it decays. The solenoid field in the Λ rest frame is certainly smaller than 3 T, which leads to a precession angle of less than 175 mrad. This would correspond to a lowering of the measured polarization with respect to the real one by a factor of 0.98.

Fig. 8.20 shows the distribution of the total precession angles, which are obtained by a simple iterative method [Ye01]: The straight flight path of the hyperon is subdivided into 100 steps, corresponding to a spatial resolution in the order of one centimeter, which is comparable to the resolution of the magnetic field maps. In the center of each trajectory element $\Delta\vec{\ell}_{\mathrm{Lab}}$ the magnetic field vector is boosted from the laboratory frame into the Λ rest frame and the new direction of the spin vector is calculated using eq. (8.5) and assuming constant magnetic field:

$$\vec{S}_{i+1} = \vec{S}_i + \Delta t_{\mathrm{RF}}\,\frac{g\,\mu_R^H\,\mu_N}{\hbar}\vec{S}_i \times \vec{B}_{\mathrm{RF},i} \quad \text{with} \quad \Delta t_{\mathrm{RF}} = \frac{|\Delta\vec{\ell}_{\mathrm{Lab}}|}{c\,\beta_H\,\gamma_H} \tag{8.6}$$

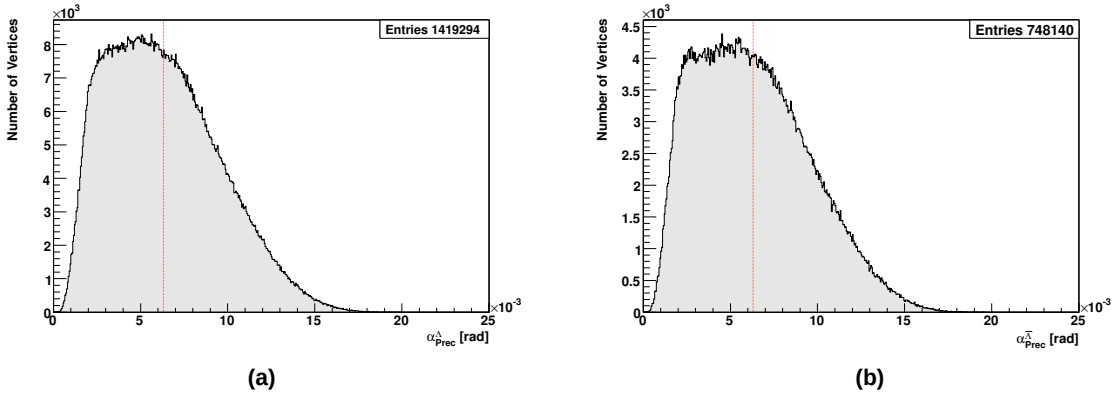

Figure 8.20: Λ and $\bar{\Lambda}$ precession in the target solenoid field: (a) Distribution of the angle between the production plane normal and the calculated Λ spin direction after its precession in the magnetic field. The mean angle is indicated by the vertical line. (b) shows the same for the $\bar{\Lambda}$.

The total mean precession angles are virtually identical for Λ and $\bar{\Lambda}$ and have a value of $\langle\alpha_{\mathrm{Prec}}\rangle = 6.3\,\mathrm{mrad}$, well below the 175 mrad calculated above. As the Ξ hyperons have similar magnetic moment and lifetime their precession angles are of similar magnitude. In principle it is possible to correct the effect of the spin precession by taking instead of the production plane normal the calculated spin direction at the hyperon decay vertex as the analyzer, but since the effect of the spin precession is negligibly small (0.002 % $\cdot\, P_y^H$ on the average), this is not done here.

The influence of a possible longitudinal component of the hyperon polarization, that may be caused by polarization transfer from the target nucleon, on the spin precession can be

neglected, since this component would essentially be parallel to the z_{Lab}-axis and thus to the target solenoid field.

8.2.4.3 Influence of the Target Solenoid Field

The magnetic field of the target solenoid breaks the up-down symmetry of the setup. The solenoidal fringe field interferes with the fringe field of the SM1 dipole magnet. The two fields tend to add up either in the upper half of the spectrometer and cancel in the lower half or vice versa, depending on the sign of the solenoid current. Moreover, since the solenoid field is aligned with the z_{Lab}-axis, it bends the daughter tracks from hyperons, that decay in the target region, in the $(x_{\text{Lab}}, y_{\text{Lab}})$-plane, which also violates the up-down symmetry (see fig. 8.21).

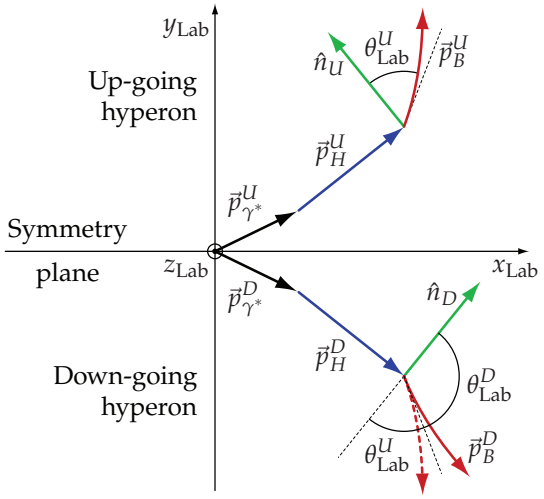

Figure 8.21: Mid-plane symmetry of the apparatus and target solenoid field: Similar to fig. 7.32 (page 127) the figure shows two hyperon decays U and D in the laboratory frame, that are symmetric with respect to the mid-plane of the spectrometer. The solenoid field breaks the symmetry of the decays, because it bends the daughter tracks in the $(x_{\text{Lab}}, y_{\text{Lab}})$-plane. It is possible to restore the up-down symmetry by combining the up- and the down-going hyperon decays from data sets with oppositely oriented solenoid fields (dashed arrow). The same applies to the interference of the solenoid with the SM1 fringe field.

Both effects cancel, if the angular distributions of the up- and down-going hyperons in the double bias canceling ratio $R(\cos\theta_y)$ are taken from data sets with oppositely aligned solenoid fields, so that the rearranged samples are again symmetric with respect to the mid-plane. During the operation of the spectrometer the orientation of the solenoid field is reversed periodically and the data taking is organized in a way, that the data samples with the two different field orientations are equalized with a precision in the order of one percent. This balancing of the samples with opposite solenoid fields leads to an automatic suppression of the solenoid field effects due to the aforementioned cancellation.

Fig. 8.22 and 8.23 illustrate that the disturbance of the up-down symmetry by the solenoid is not negligible for the Λ and $\overline{\Lambda}$ hyperons. The polarization results for positive and negative solenoid currents do not agree. A systematical shift to negative polarizations for positive current and vice versa is observed for the Λ and $\overline{\Lambda}$ as well as for the respective K^0 background polarizations. The fluctuation of the polarization tends to be larger for hyperons, that are produced in the up-stream target cell. The polarization of the target cell has no systematic influence, which is in agreement with the results of subsection 8.2.4.1. The same applies to the z_{Lab} position of the decay vertex, but the effect of the solenoid field seems to be larger (at least for the K^0 background polarization) for particles, that decay closer to the target. Due to the low statistics, the results for the Ξ hyperons, as depicted in fig. 8.22, are not conclusive.

Many polarization values in fig. 8.22 and 8.23 have a very large χ^2/n.d.f. of the $R(\cos\theta_y)$ fit, which indicates that the solenoid field distorts the $R(\cos\theta_y)$ distributions such, that they disagree with the straight line hypothesis. Fig. 8.25 shows how the solenoid field influences on the $R(\cos\theta_y)$ distribution of the Λ sample.

In particular the $R(\cos\theta_y)$ values for the low $\cos\theta_y$-bins depend strongly on the direction of the solenoid current. Fig. 8.26 illustrates that the solenoid field changes the acceptance such, that the angular distributions of the up- and down-going Λs are distorted in a almost anti-symmetric way: If the current changes its direction from negative to positive, the acceptance decreases in the region around $\cos\theta_y = 0.375$ and increases at the same time around $\cos\theta_y = -0.375$ by approximately the same amount, which leads to the observed shift of the $R(\cos\theta_y)$ values in the region of low $|\cos\theta_y|$.

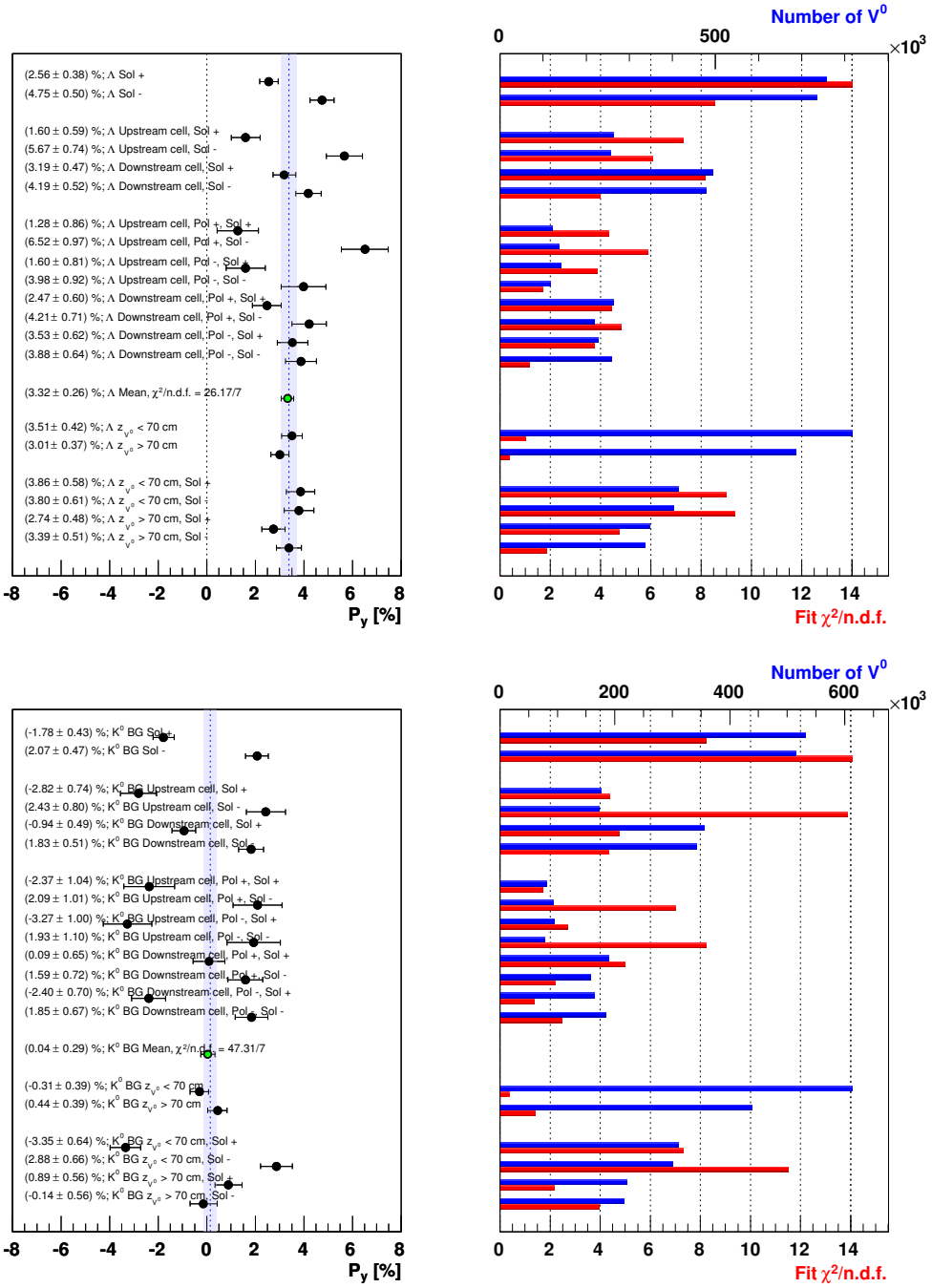

Figure 8.22: Influence of the target solenoid on the Λ polarization: The upper graph shows the Λ polarizations, the lower one that of the respective K^0 background, in each case for various subsamples with respect to the orientation of the solenoid field. The first two points display the results for the two directions of the target solenoid current. The next four points show the effect of an additional subdivision with respect to the target cell in which the Λ was produced. In the following group of eight points the samples are subdivided further with respect to the two polarization directions of each target cell. The last six points illustrate the influence of the position z_{V^0} of the decay vertex. The graphs on the right show for each point the total number of Λs and K^0s, respectively, and the χ^2/n.d.f. of the $R(\cos\theta_y)$ fit.

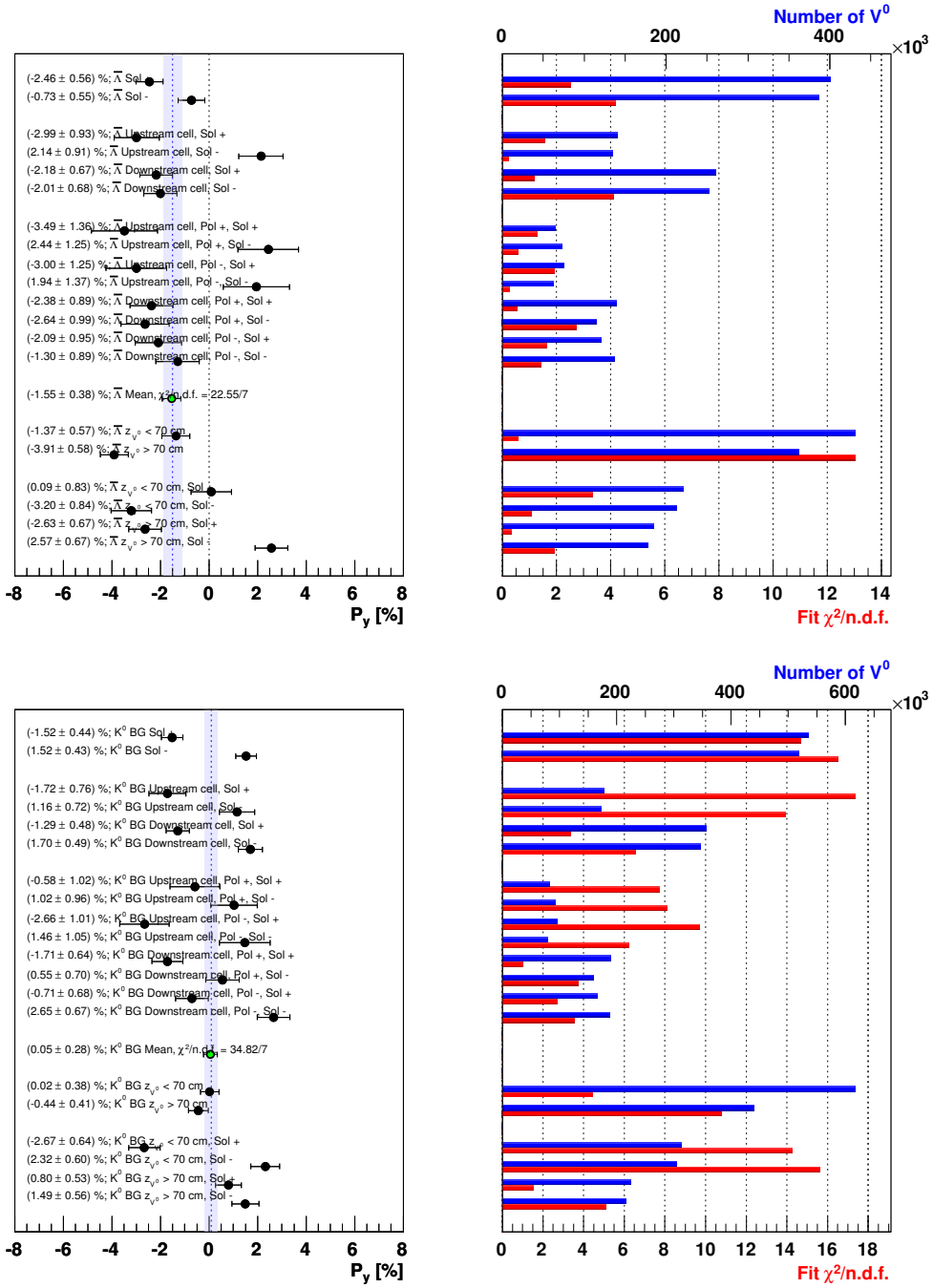

Figure 8.23: Influence of the target solenoid on the $\overline{\Lambda}$ polarization: In the upper graph the $\overline{\Lambda}$ polarization is shown for various subsamples with respect to the orientation of the solenoid field. The lower graph depicts the respective results for the K^0 background polarization. The definition of the bins is the same as in fig. 8.22.

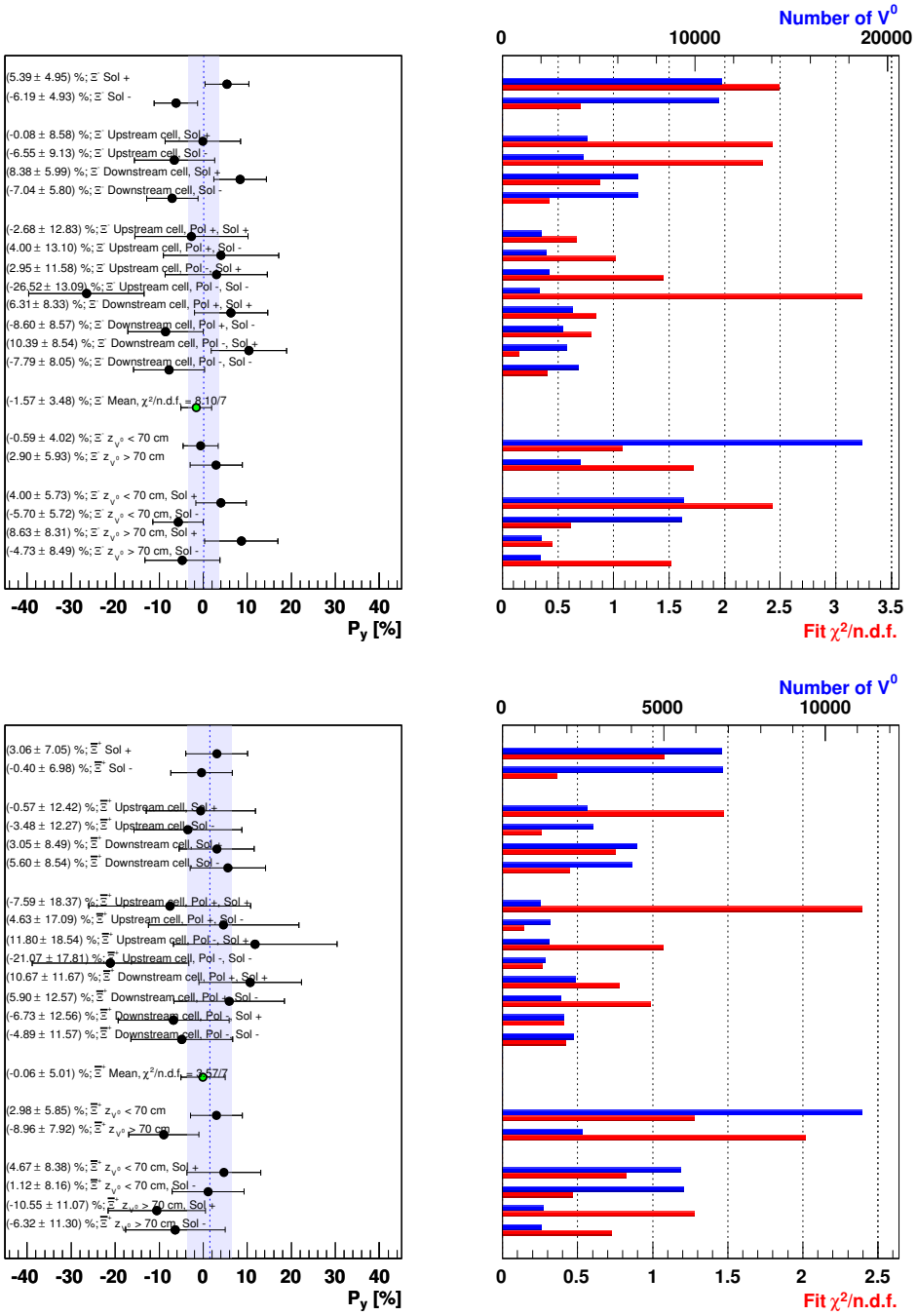

Figure 8.24: Influence of the target solenoid on the Ξ^- and $\overline{\Xi}^+$ polarizations: The upper graph shows the Ξ^- polarization the lower one the results for the $\overline{\Xi}^+$. The definition of the bins is the same as in fig. 8.22.

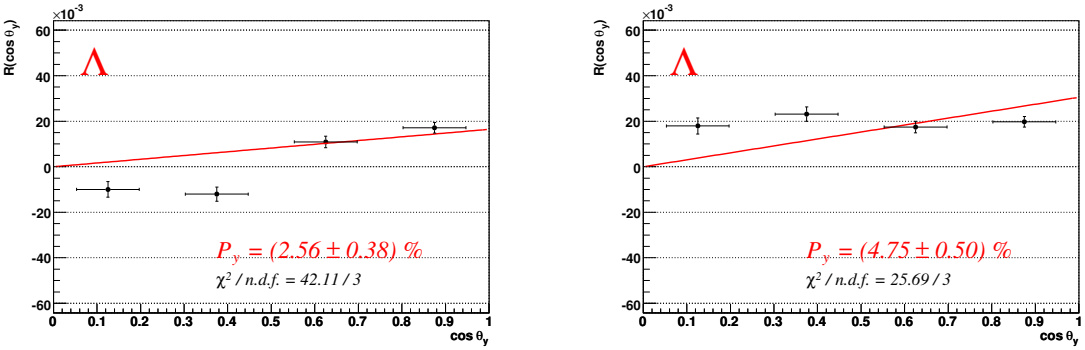

Figure 8.25: Angular distributions $R(\cos\theta_y)$ and polarizations of the Λ hyperon for the two solenoid field orientations: (a) $R(\cos\theta_y)$ distribution for positive solenoid current. (b) shows the same for negative solenoid current. Whereas the value for the highest $\cos\theta_y$ bin changes only by about one σ_{stat}, the other points systematically move with the sign of the solenoid current. Both distributions are not described by a straight line.

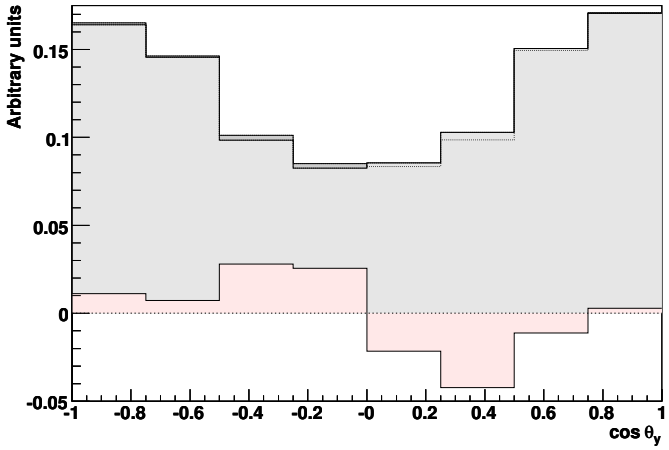

Figure 8.26: Angular distribution of the protons from Λ decays for the two solenoid current directions: The light shaded histogram shows the angular distribution for negative, the darker histogram the one for positive solenoid current, both normalized to their integral. The red histogram depicts the difference of the two, enlarged by a factor of ten.

8.3 Kinematical Study of Λ and $\overline{\Lambda}$ Polarization

8.3.1 x_F and p_T dependence of Λ and $\overline{\Lambda}$ Polarization

The hadro-production data show a clear dependence of the transverse hyperon polarization on the hyperon's longitudinal momentum fraction x_F and on its transverse momentum p_T with respect to the beam (see section 6.1). In the following the x_F and p_T dependence is studied by subdividing the Λ and $\overline{\Lambda}$ samples into nine bins with respect to one of the two variables while leaving the other unconstrained. The bins are chosen such, that they have approximately equal statistics. The results for x_F are shown in fig. 8.27 and 8.28. The respective numerical values can be found in the tables B.1 and B.2. The Λ polarization shows a clear correlation with x_F: It is large in the region around $x_F \approx 0$, where it reaches values of nearly 7 %, and vanishes in the current fragmentation region, where x_F is large. Due to the stronger fluctuation and larger errors, the x_F dependence of the $\overline{\Lambda}$ polarization is less clear: It tends to increase from negative values to zero as x_F increases. In both cases the false K^0 background polarization, that is taken as an estimate for the systematic error, is compatible with zero and does not show any systematic deviations.

The results for the transverse momentum are depicted in fig. 8.29 and 8.30 (cf. also tables B.3 and B.4). Surprisingly the Λ polarization is completely independent from p_T, whereas the $\overline{\Lambda}$ polarization has a slight tendency to grow from negative values to zero with increasing p_T. Again the K^0 background polarization behaves as expected.

Although fig. 8.31 shows that x_F and p_T are only weakly correlated, a true separation of the two dependencies is only achieved, if the Λ and $\overline{\Lambda}$ samples are subdivided into bins in the (x_F, p_T)-plane. Here a 4×4 subdivision was chosen, where again the bin borders are set such, that the statistics of the bins is roughly equalized.

The results, as depicted in fig. 8.32 and 8.33 (cf. also tables B.5 and B.6), mainly confirm the trends, already observed in the one-dimensional binning: For all p_T bins the Λ polarization decreases with increasing x_F. The x_F behavior of the $\overline{\Lambda}$ polarization is less pronounced with a slight trend to lower polarization values with larger x_F. The polarization of the Λ is virtually independent of the transverse momentum. Only in the intermediate x_F region between 0.07 and 0.26 it exhibits a slight positive correlation. The significant positive Λ polarization for the smallest p_T bin in the low x_F region is rather unexpected, since rotational symmetry demands vanishing polarization for $p_T \to 0$ GeV/c. Moreover the four polarization values do not show a tendency to decrease with lower p_T. On the other hand in the Λ selection the transverse momentum was required to be larger than 100 MeV/c, so that the low part of the p_T spectrum does not contribute to the measured polarization. This cut was applied to ensure a good definition of the production plane normal, since the p_T resolution is in the order of 100 MeV/c. Apart from a faint tendency to less negative polarizations with increasing p_T, also the $\overline{\Lambda}$ polarization is found to be independent of p_T.

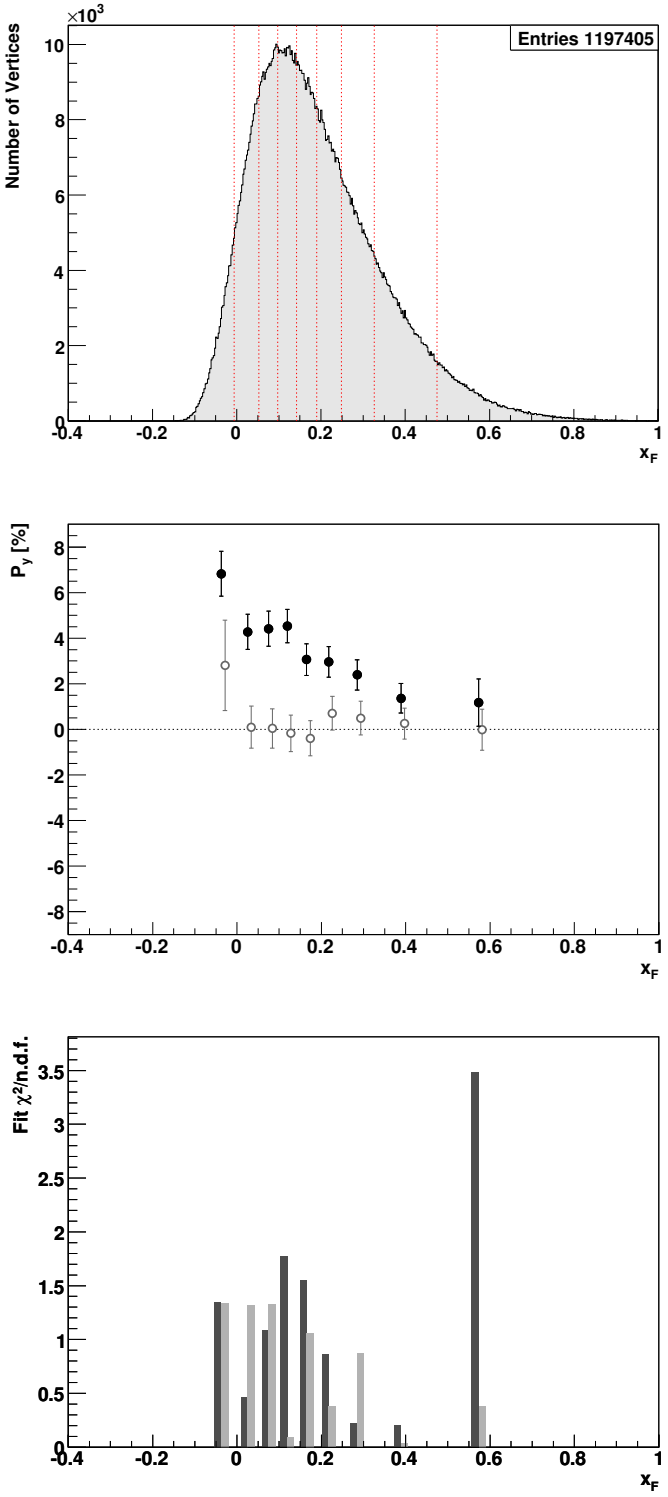

Figure 8.27: Dependence of the Λ polarization on the longitudinal momentum fraction x_F: The upper plot depicts the background corrected x_F distribution. The definition of the bins is illustrated by vertical lines. The graph in the middle shows both the polarization values for the Λ (filled circles) and those of the K^0 background (open circles, right shifted for better visibility) at the average x_F values of the respective bins. The lower plot displays the χ^2/n.d.f. values of the $R(\cos\theta_y)$ fits for the Λ (dark bars) and for the K^0 background (light bars).

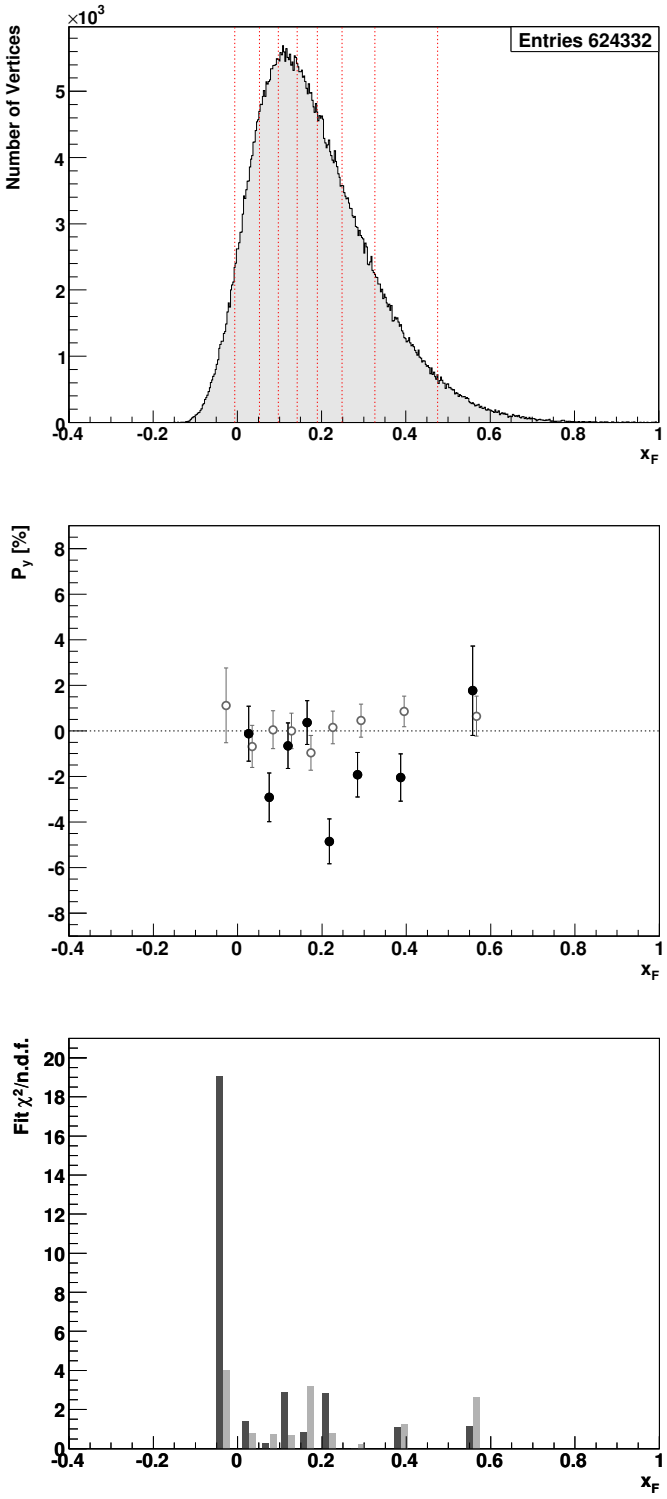

Figure 8.28: Dependence of the $\overline{\Lambda}$ polarization on x_F: The conventions are the same as in fig. 8.27. For the lowest x_F bin the two-dimensional fit procedure partly fails, so that some $R(\cos\theta_y)$ values deviate strongly from the straight line resulting in a strongly negative polarization and a large χ^2/n.d.f. value (see table B.2).

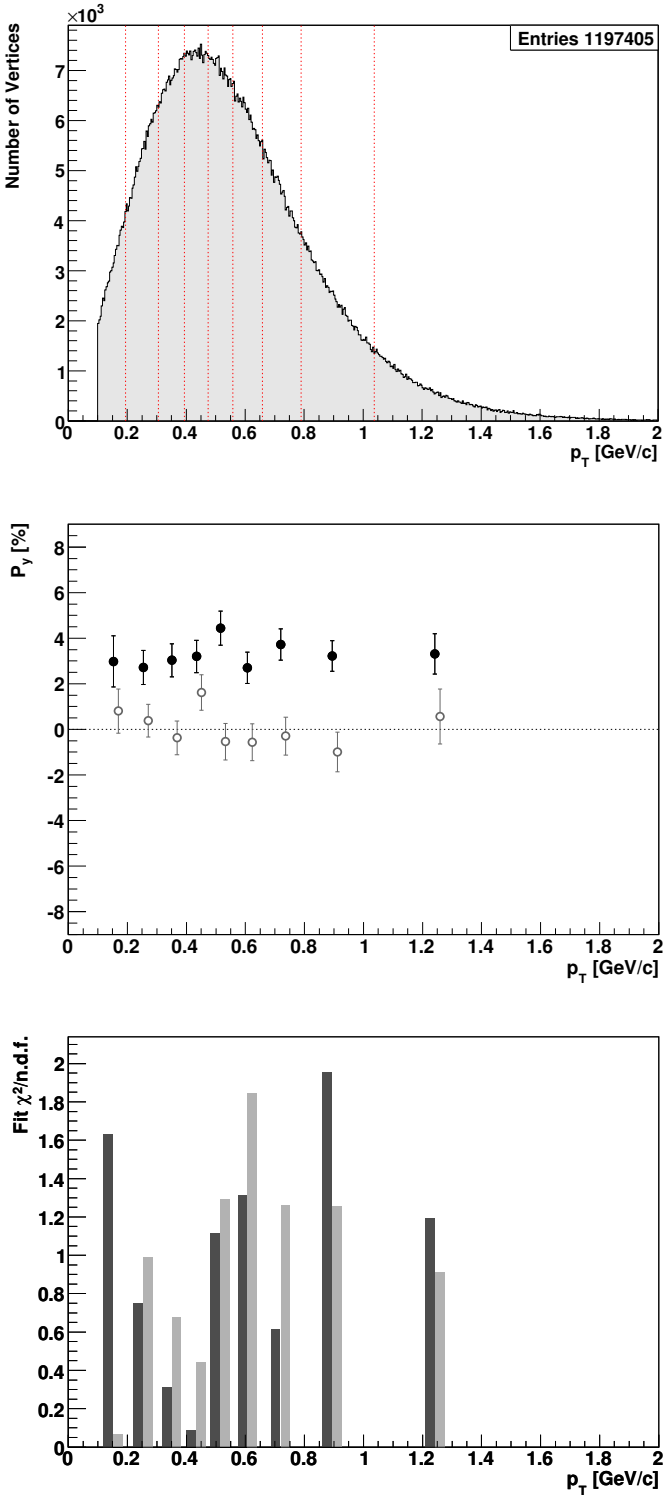

Figure 8.29: Dependence of the Λ polarization on the transverse momentum p_T: The upper plot depicts the background corrected p_T distribution. The definition of the bins is illustrated by vertical lines. The graph in the middle shows both the polarization values for the Λ (filled circles) and those of the K^0 background (open circles, right shifted for better visibility) at the average p_T values of the respective bins. The lower plot displays the χ^2/n.d.f. values of the $R(\cos\theta_y)$ fits for the Λ (dark bars) and for the K^0 background (light bars).

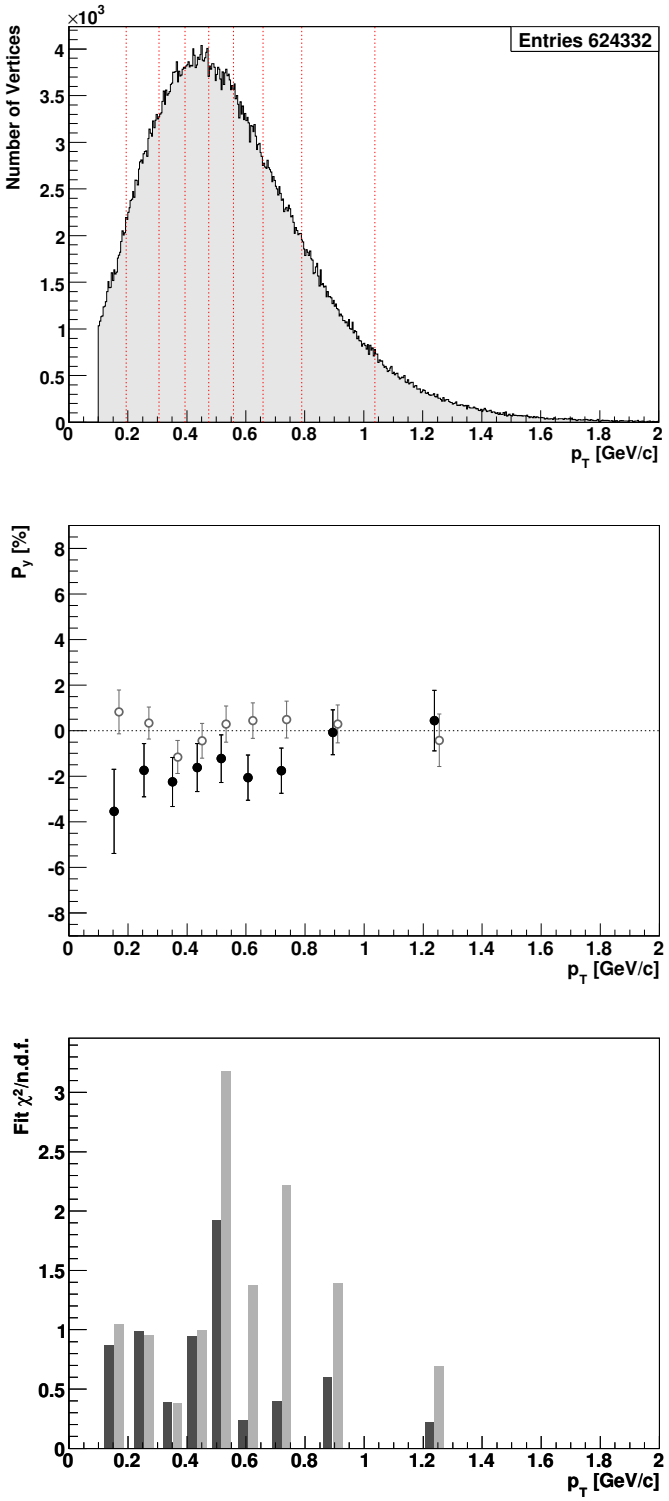

Figure 8.30: Dependence of the $\bar{\Lambda}$ polarization on p_T: The conventions are the same as in fig. 8.29.

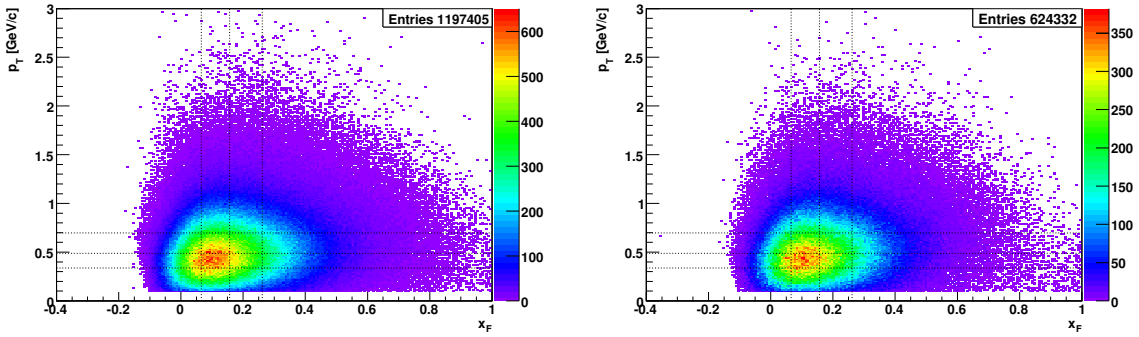

(a) (b)

Figure 8.31: (a) Correlation of p_T and x_F for the Λ. The 4 $\times$ 4 bins are indicated by lines. (b) shows the same for the $\overline{\Lambda}$. The two distributions are very similar, so that in both cases the same binning was applied.

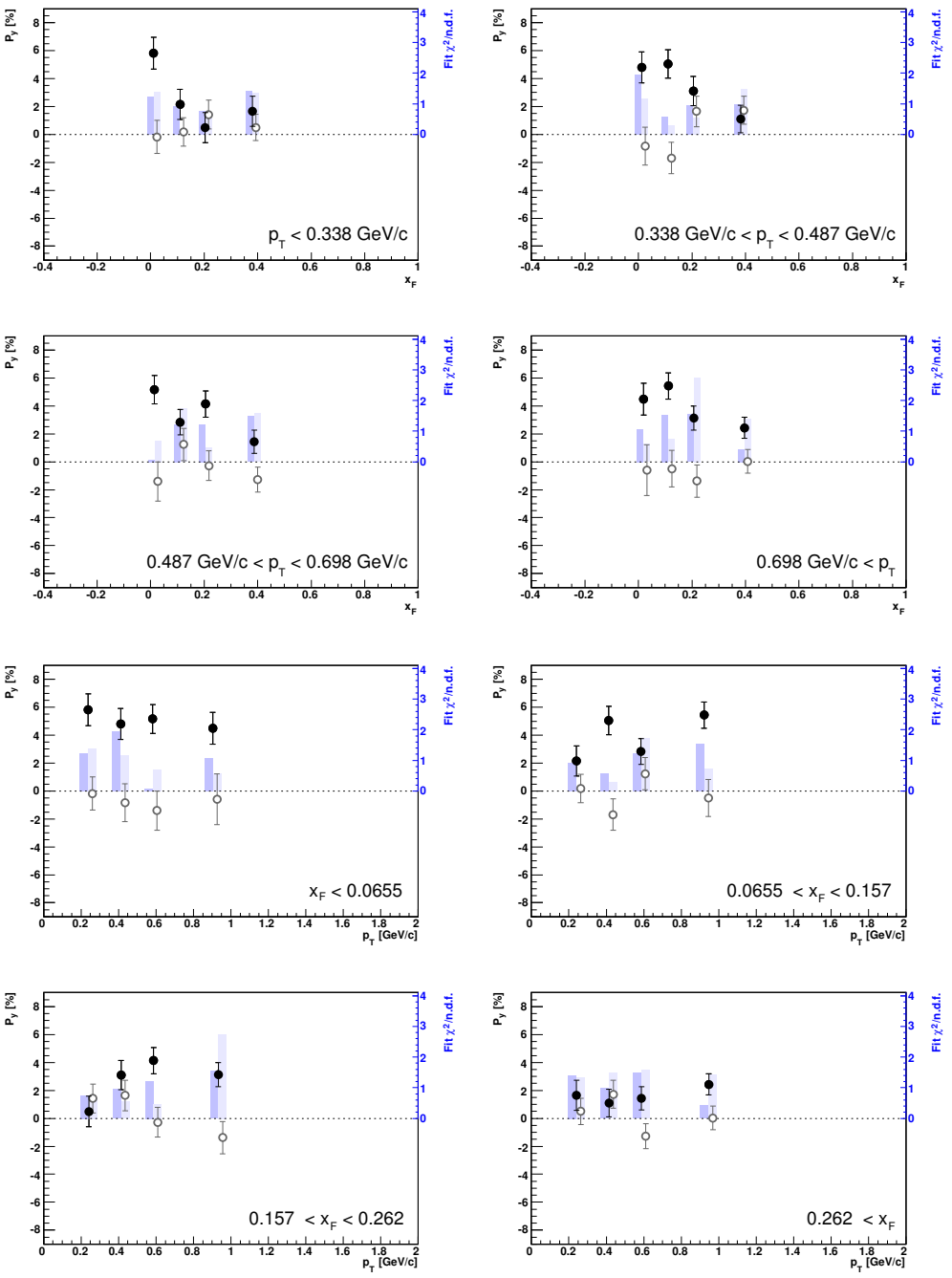

Figure 8.32: Λ polarization as a function of p_T and x_F: The upper four plots depict the x_F dependence of the Λ polarization (full circles) and that of the K^0 background (open circles, right shifted for better visibility) for the four bins in p_T. The lower four graphs show the same 16 data points, but this time their p_T dependence in the four x_F bins. The bars display the χ^2/n.d.f. values of the respective $R(\cos\theta_y)$ fits for the Λ (dark bars) and for the K^0 background (light bars).

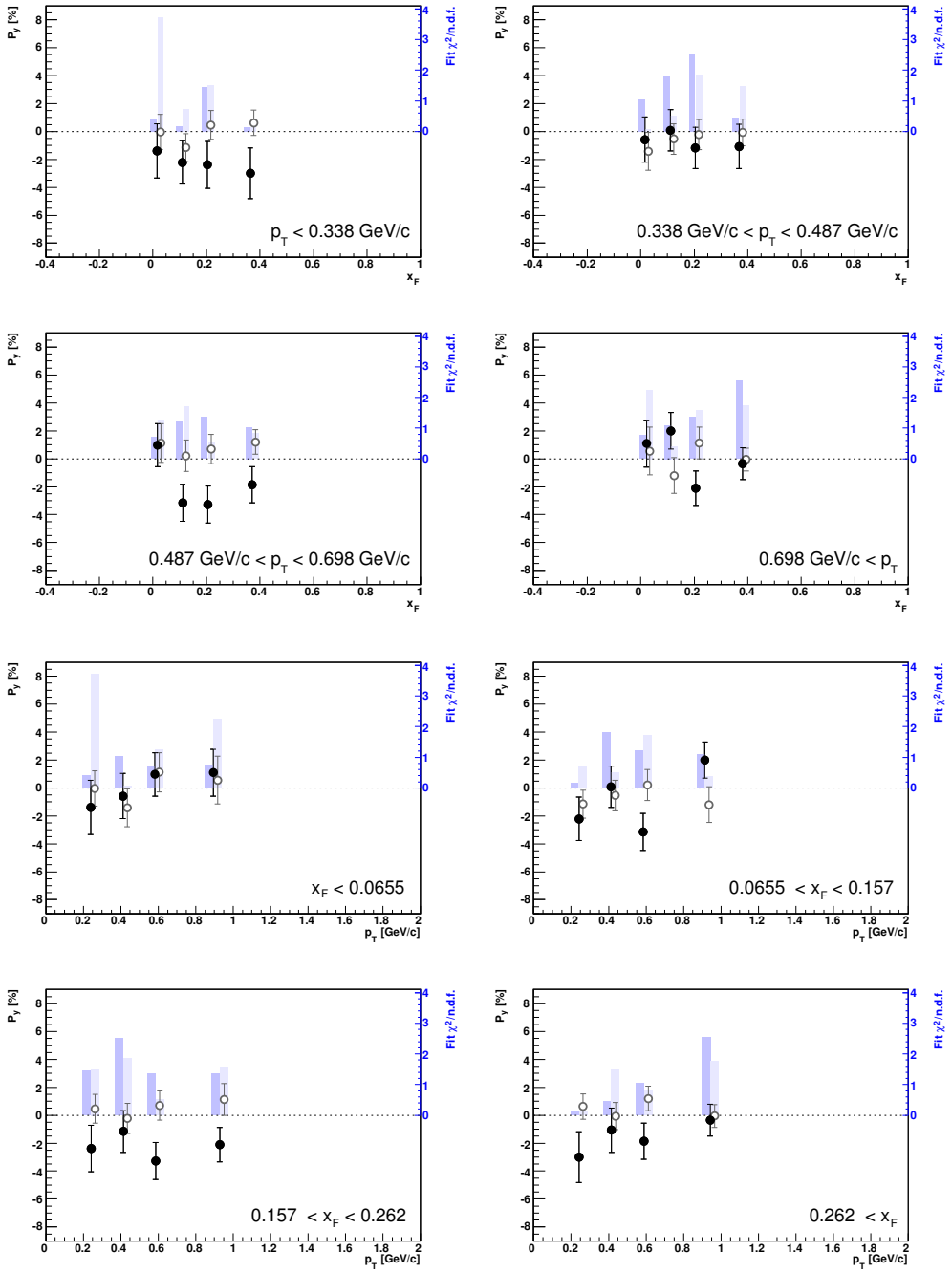

Figure 8.33: $\overline{\Lambda}$ polarization as a function of p_T and x_F: The conventions are the same as in fig. 8.32.

8.3.2 Q^2 and y_B dependence of Λ and $\overline{\Lambda}$ Polarization

In addition to the kinematical variables of the outgoing hyperon the polarization may also depend on the properties of the virtual photon beam, in particular on the squared four-momentum transfer Q^2 of the virtual photon and on its relative energy transfer y_B. Considering that the hadro-production data do not indicate a dependence of the polarization on the center-of-mass energy, one may naïvely expect, that in photo-production Q^2 and y_B have no influence. The dependence on the virtual photon variables is determined in a similar way as for p_T and x_F: Fig. 8.34 and 8.35 show the Λ and $\overline{\Lambda}$ results for nine bins in Q^2 (cf. tables B.9 and B.10). As expected the Λ polarization is not correlated with Q^2, which is also the case for the $\overline{\Lambda}$, although it seems to exhibit a slightly more negative polarization in the low and high Q^2 regions.

As illustrated by fig. 8.36. and 8.37 (cf. tables B.7 and B.8) both the Λ and the $\overline{\Lambda}$ polarization do not show a significant dependence on the relative energy transfer. Only for the $\overline{\Lambda}$ a weak trend to less negative values with increasing y_B is observed.

On the whole the above findings are confirmed by the results of the correlated binning in the (y, Q^2)-plane. Again the Λ and $\overline{\Lambda}$ samples are subdivided into 4×4 bins, that are chosen such, that they have roughly equal statistics (see fig. 8.38). Fig. 8.39 and 8.40 (cf. also tables B.11 and B.12) show that except for the lowest y_B bin neither the Λ nor the $\overline{\Lambda}$ polarization depend strongly on Q^2. For relative energy transfers smaller than about 0.3 the polarizations seem to decrease with Q^2: from about 6 to 0 % for the Λ and from 0 to nearly -7 % for the $\overline{\Lambda}$. The Λ data do not exhibit a clear y_B dependence, which also applies to the $\overline{\Lambda}$ polarization, except for the highest Q^2 bin, in which the polarization rises from about -7 to 0 % with increasing y_B.

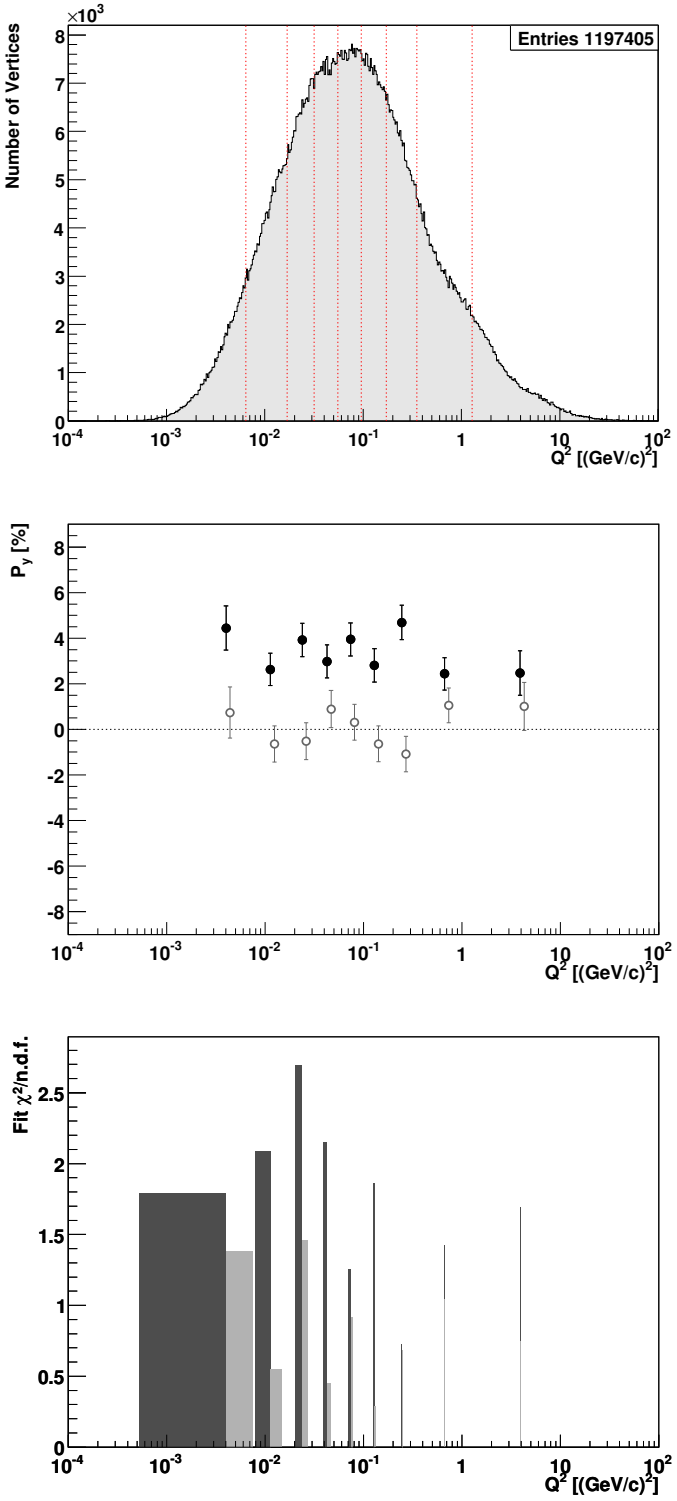

Figure 8.34: Dependence of the Λ polarization on the squared four-momentum transfer Q^2 of the virtual photon: The upper plot depicts the background corrected Q^2 distribution. The definition of the bins is illustrated by vertical lines. The graph in the middle shows both the polarization values for the Λ (filled circles) and those of the K^0 background (open circles, right shifted for better visibility) at the average Q^2 values of the respective bins. The lower plot displays the χ^2/n.d.f. values of the $R(\cos\theta_y)$ fits for the Λ (dark bars) and for the K^0 background (light bars).

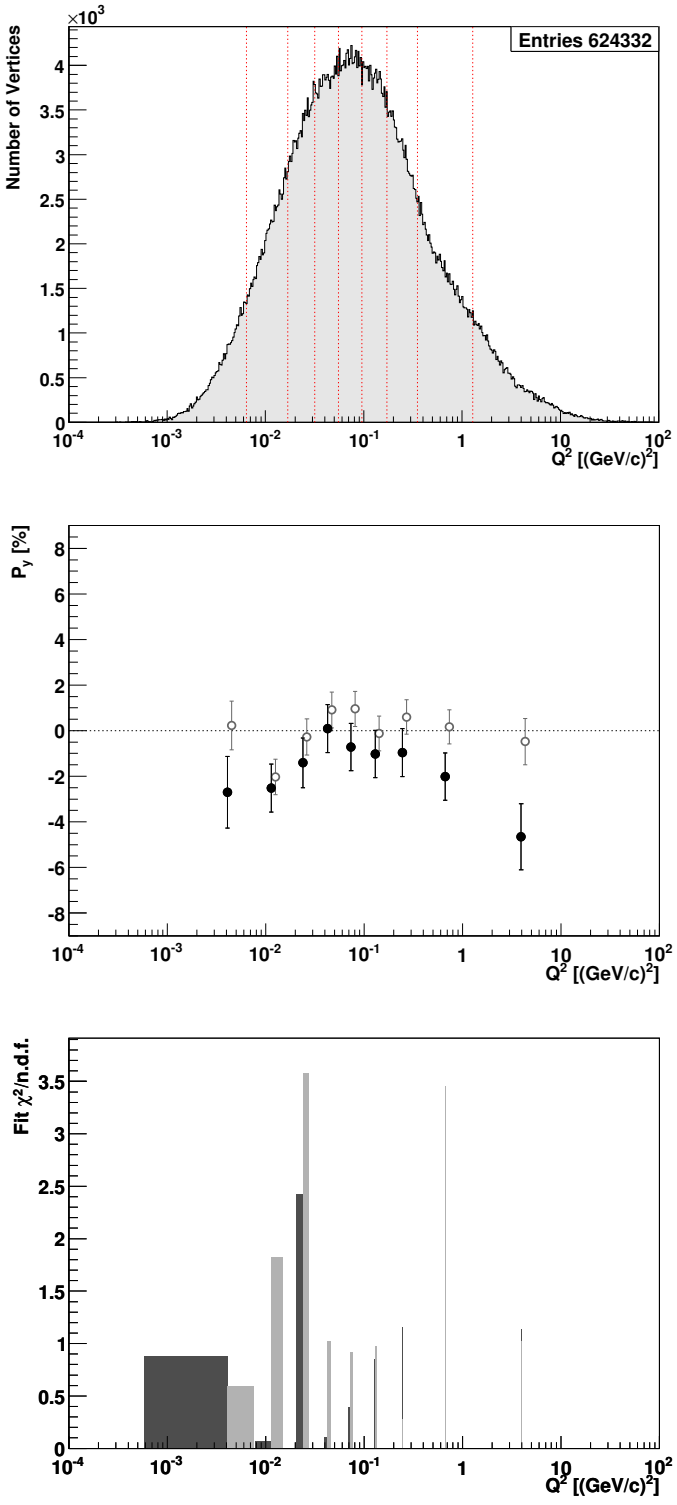

Figure 8.35: Dependence of the $\bar{\Lambda}$ polarization on Q^2: The conventions are the same as in fig. 8.34.

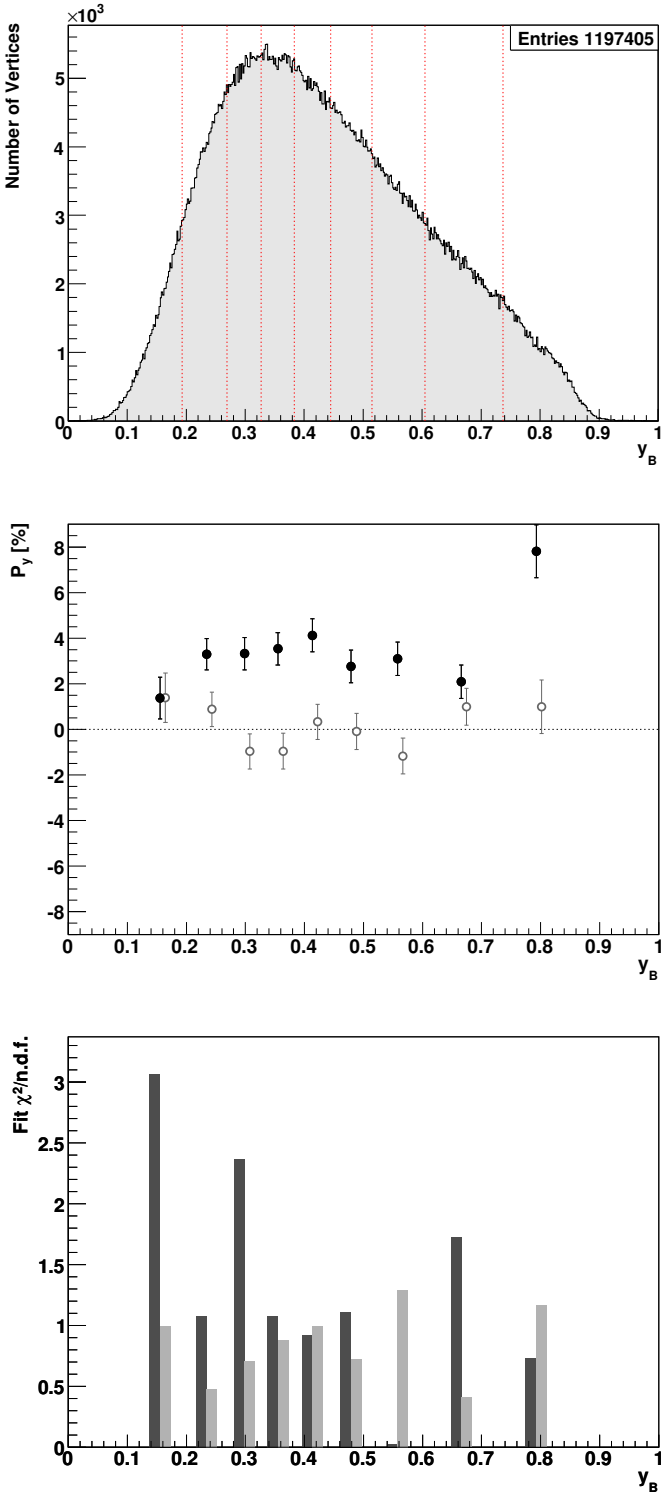

Figure 8.36: Dependence of the Λ polarization on the relative energy transfer y_B of the virtual photon: The upper plot depicts the background corrected y_B distribution. The definition of the bins is illustrated by vertical lines. The graph in the middle shows both the polarization values for the Λ (filled circles) and those of the K^0 background (open circles, right shifted for better visibility) at the average y_B values of the respective bins. The lower plot displays the χ^2/n.d.f. values of the $R(\cos\theta_y)$ fits for the Λ (dark bars) and for the K^0 background (light bars).

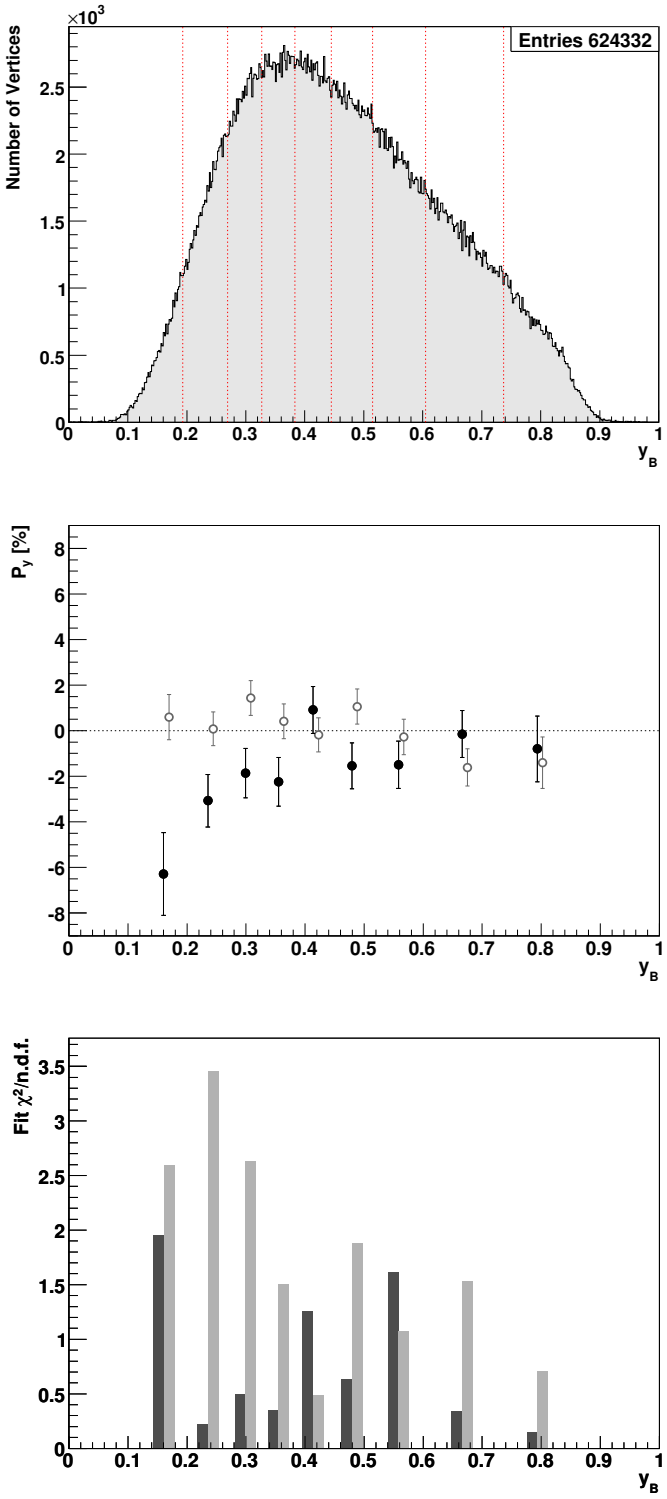

Figure 8.37: Dependence of the $\bar{\Lambda}$ polarization on y_B: The conventions are the same as in fig. 8.36.

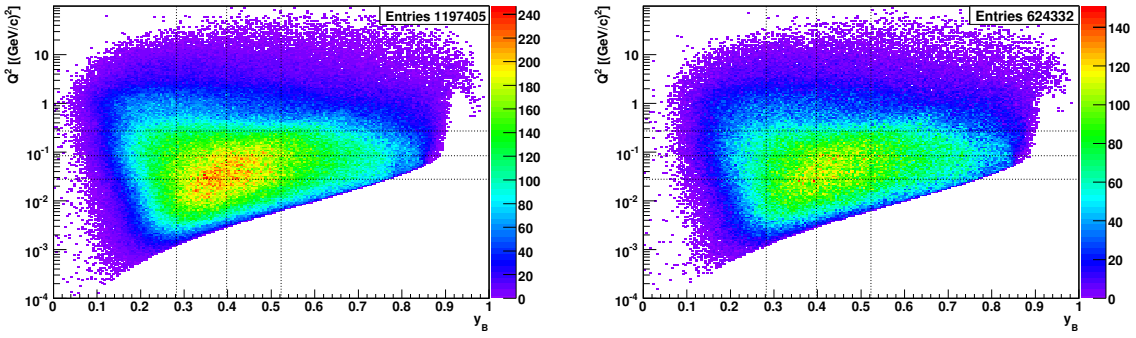

Figure 8.38: (a) Correlation of Q^2 and y_B for the Λ. The 4×4 bins are indicated by lines. (b) shows the same for the $\bar{\Lambda}$. The two distributions are very similar, so that in both cases the same binning was used.

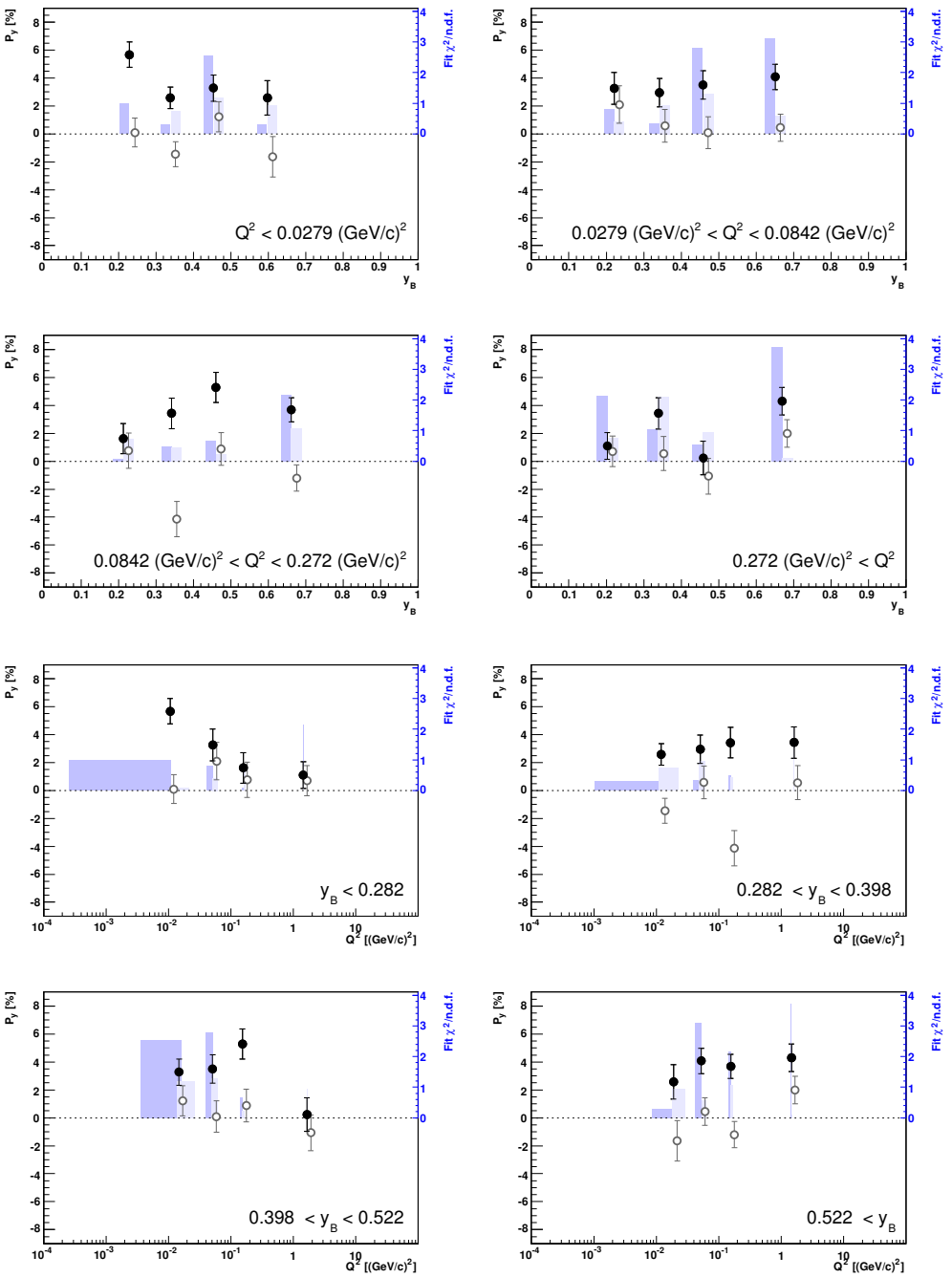

Figure 8.39: Λ polarization as a function of Q^2 and y_B: The upper four plots depict the y_B dependence of the Λ polarization (full circles) and that of the K^0 background (open circles, right shifted for better visibility) for the four bins in Q^2. The lower four graphs show the same 16 data points, but this time the Q^2 dependence for the four y_B bins. The bars display the χ^2/n.d.f. values of the respective $R(\cos\theta_y)$ fits for the Λ (dark bars) and for the K^0 background (light bars).

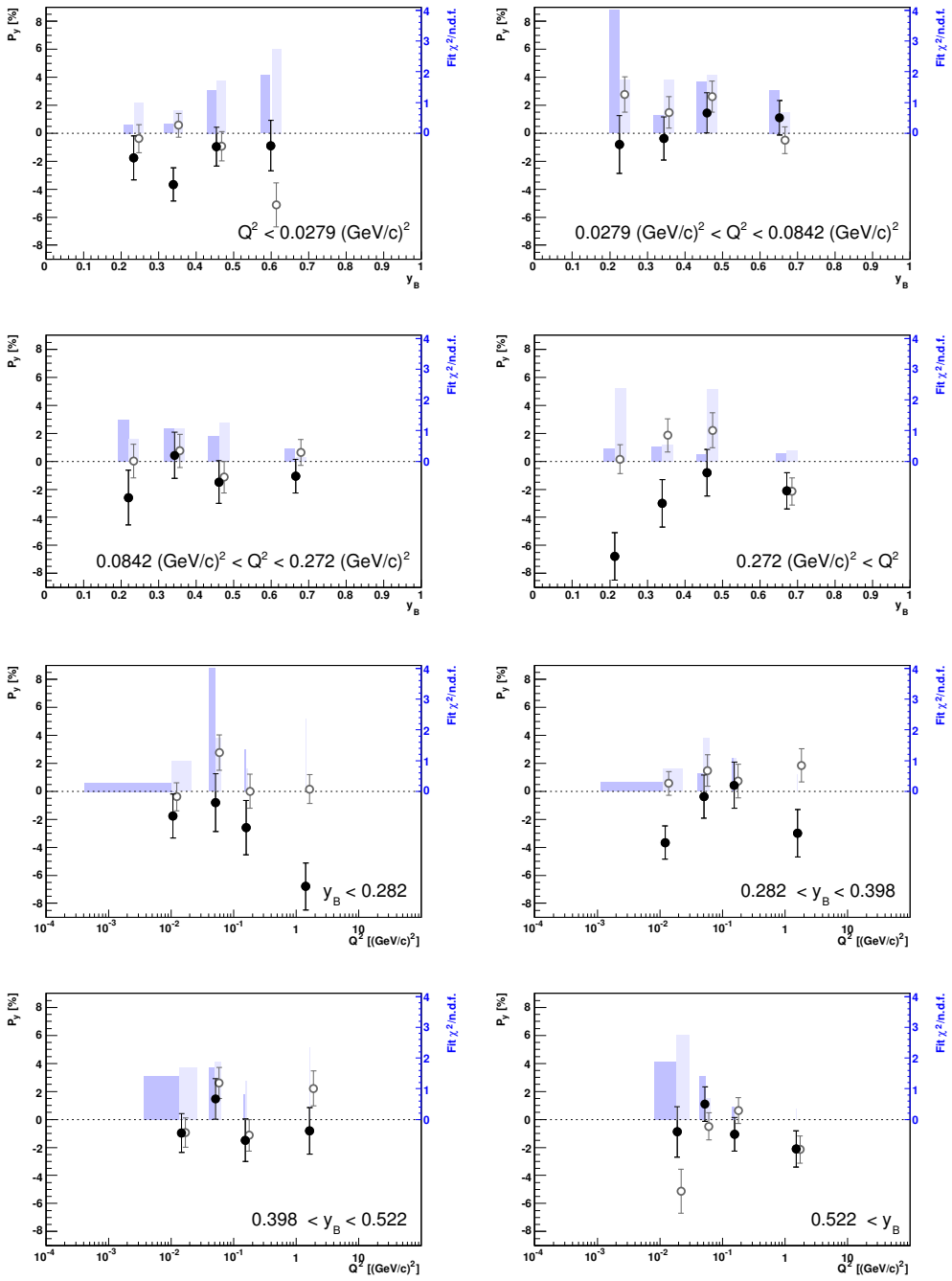

Figure 8.40: $\bar{\Lambda}$ polarization as a function of Q^2 and y_B: The same conventions as in fig. 8.39 are used.

8.4 Summary and Discussion

Based on the COMPASS muon beam data with longitudinally polarized target, taken in the years 2002, 2003, and 2004, the transverse polarization of Λ, $\overline{\Lambda}$, and – for the first time – also that of Ξ^- and $\overline{\Xi}^+$ hyperons was measured in photo-production with predominantly quasi-real virtual photons. The selected sample of V^0 particles contains 1,626,000 Λs and 854,000 $\overline{\Lambda}$s. From the acceptance corrected angular distribution of the decay proton a significantly positive average Λ polarization of $P_T^{\Lambda} = +3.25 \pm 0.32(\text{stat.}) \pm 0.13(\text{sys.})$ % was extracted. The systematic error was estimated by measuring the false polarization of the K^0 background under the Λ invariant mass peak in a kinematical region similar to that of the Λ. The K^0 background polarization has a statistical uncertainty of 0.28 %, which is comparable to that of the Λ polarization. The polarization of the Λ was measured to be *independent* of the transverse momentum p_T with respect to the virtual photon, which is quite astonishing, since so far the hyperon polarization was always found to increase with p_T reaching a plateau around 1 GeV/c. Moreover in the low x_F region even the lowest p_T bins show significantly non-zero polarizations. The Λ polarization shows a clear dependence on the longitudinal momentum fraction x_F, reaching values of up to 6 % for $x_F \approx 0$ and vanishing in the current fragmentation region where x_F is large. The squared four-momentum transfer Q^2 of the virtual photon as well as its relative energy transfer y_B were found to have no strong influence on the Λ polarization.

In a similar way the overall $\overline{\Lambda}$ polarization was measured resulting in an average value of $P_T^{\overline{\Lambda}} = -1.51 \pm 0.39(\text{stat.}) \pm 0.10(\text{sys.})$ %, which is 3.9 σ_{stat} below zero. Also here the K^0 background polarization serves as a rough estimate for the systematic error and has itself a statistical uncertainty of 0.28 %. None of the four kinematical variables shows a clear correlation with the polarization of the $\overline{\Lambda}$, except for a few kinematical regions in Q^2 and y_B, in which the polarization exhibits some dependence at the limit of the statistical accuracy.

Based on a slightly modified Λ and $\overline{\Lambda}$ selection Ξ^- and $\overline{\Xi}^+$ samples were extracted from the data by requiring an additional pion track in the event. In total the sample contains 24,900 Ξ^-s and 14,900 $\overline{\Xi}^+$s. Using the same methods as for the Λ hyperons both the Ξ^- and the $\overline{\Xi}^+$ were found to be unpolarized with measured values of $P_T^{\Xi^-} = 0.06 \pm 3.46(\text{stat.})$ % and $P_T^{\overline{\Xi}^+} = 1.52 \pm 4.98(\text{stat.})$ %.

At present the COMPASS results constitute the most precise data set on hyperon polarization in quasi-real photo-production. COMPASS also made a first direct measurement of the x_F, p_T, Q^2, and y_B dependence of the Λ and $\overline{\Lambda}$ polarizations in this kinematical domain.

8.4.1 Comparison with HERMES Results

The HERMES experiment is in its basic features quite similar to COMPASS: A longitudinally polarized high energy lepton beam, in this case positrons, is shot on an internal gas target, that is as well polarized longitudinally. HERMES measured the transverse Λ and $\overline{\Lambda}$ polarizations also in the domain of quasi-real photo-production, but with a lower beam energy of 27.5 GeV, so that the kinematical region is slightly different. But since the hadro-production data as well as the results of this analysis indicate, that the transverse polarization, if at all, depends only weakly on the center-of-mass energy, the results are expected to be similar.

The HERMES results [Brü02, Gre02, Bel01] for the overall Λ and $\overline{\Lambda}$ polarizations of $P_T^{\Lambda} = +5.5 \pm 0.6(\text{stat.}) \pm 1.6(\text{sys.})$ % and $P_T^{\overline{\Lambda}} = -4.3 \pm 1.3(\text{stat.}) \pm 1.2(\text{sys.})$ % are based on a data set, that contains 386,000 Λs and 72,000 $\overline{\Lambda}$s. Both polarizations have larger magnitudes, but are within the errors compatible with the COMPASS results. The systematic error was estimated from the false transverse polarization of K^0s and of hadron-hadron pairs, that do not originate from Λ and $\overline{\Lambda}$ decays, which is comparable to the measurement of the false K^0 background polarization in this analysis.

Due to the small scattering angles of the beam positron in quasi-real kinematics, the scattered positron cannot be detected in the HERMES spectrometer. The transverse polarization at small Q^2 is measured in the inclusive reaction $e^+ N \longrightarrow \Lambda^{\uparrow} X$, where the kinematics of the virtual photon cannot be reconstructed, so that HERMES has no direct access neither to the x_F- nor to the p_T dependence of the polarization. Instead of x_F HERMES studies the polarization in dependence on the fraction $\zeta \equiv (E_H + p_{z,H})/(E_{e^+} + p_{z,e^+})$ of the light-cone momentum, that the hyperon carries with respect to the beam positron. Monte-Carlo simulations show that ζ is correlated with x_F (see fig. 8.41a), which allows to distinguish between target ($\zeta \lesssim 0.25$) and beam fragmentation region ($\zeta \gtrsim 0.25$). The ζ dependence of the Λ polarization (see fig. 8.41b) agrees well with the results of this analysis: Not only the general behavior of decreasing polarization with increasing x_F and ζ, respectively, but also the actual polarization values are similar. The $\overline{\Lambda}$ polarizations measured by HERMES tend to be more negative in the low ζ- and x_F-region which is not seen in the COMPASS data.

As the transverse momentum of the hyperon with respect to the virtual photon is not measured, HERMES studies the polarization instead in dependence on the transverse momentum p_T^B of the hyperon with respect to the beam positron. HERMES measures a pronounced increase of the Λ polarization with p_T^B both in the beam and in the target fragmentation region (see fig. 8.42). Contrary to this the COMPASS results for the direct p_T dependence do not show any correlation of the Λ polarization with the transverse momentum (cf. fig. 8.32 and 8.29).

Taking into account the limited comparability of the different measured kinematical dependences the COMPASS results are on the whole compatible with the HERMES measurements. Only the p_T dependence of the Λ polarization seems to exhibit a different behavior.

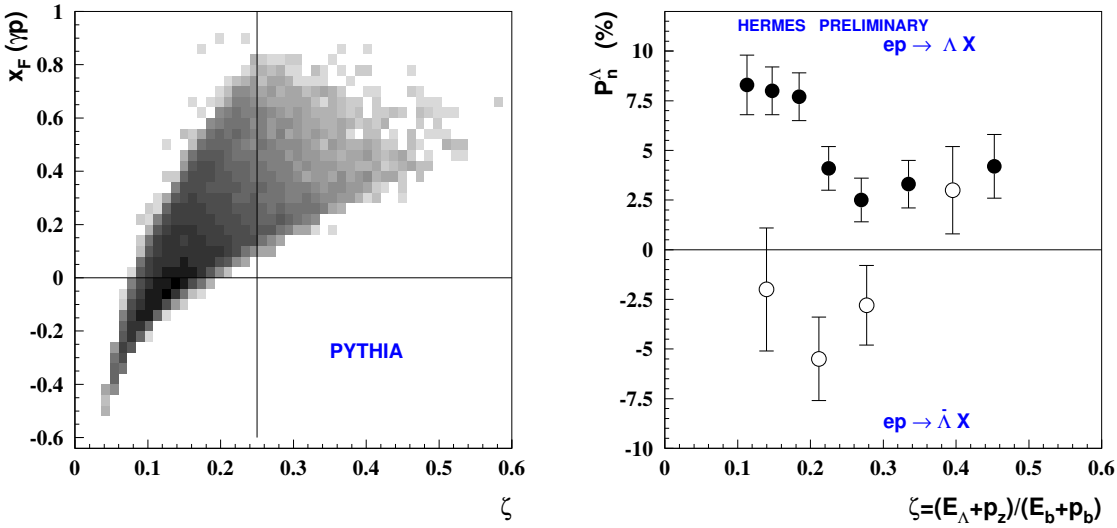

Figure 8.41: HERMES results: (a) Correlation of the longitudinal momentum fraction x_F with the light-cone momentum fraction ζ. For events with $\zeta \gtrsim 0.25$ the hyperons are produced in the forward hemisphere with $x_F > 0$. (b) Λ and $\bar{\Lambda}$ polarizations as function of ζ. This plot should be compared to the x_F dependence of the Λ and $\bar{\Lambda}$ polarizations that are illustrated in fig. 8.27, 8.28, 8.32, and 8.33. (from [Brü02])

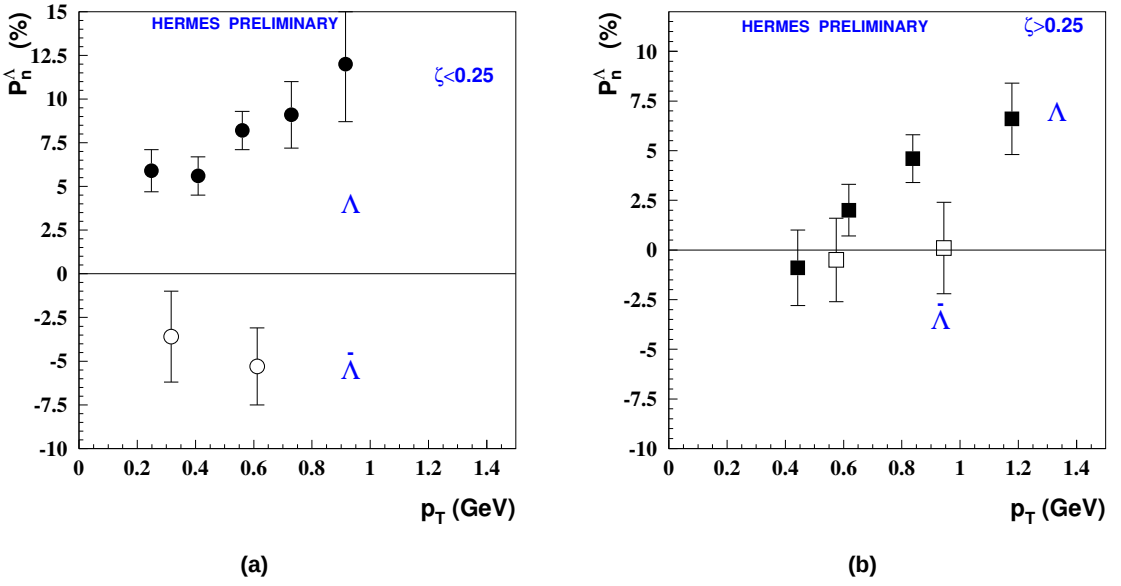

Figure 8.42: HERMES measurement of the Λ and $\bar{\Lambda}$ polarizations as a function of p_T^B for (a) the target and (b) the current fragmentation region. (from [Brü02])

8.4.2 Comparison with Hadro-Production Data

In hadro-production a positive Λ polarization in the beam fragmentation region is only observed in the reaction $K^- \longrightarrow \Lambda$. The polarization shows the typical rise with x_F and p_T, reaches values larger than $+50$ % and is independent of the beam momentum in a range from 8.25 to 176 GeV/c (see fig. 8.43).

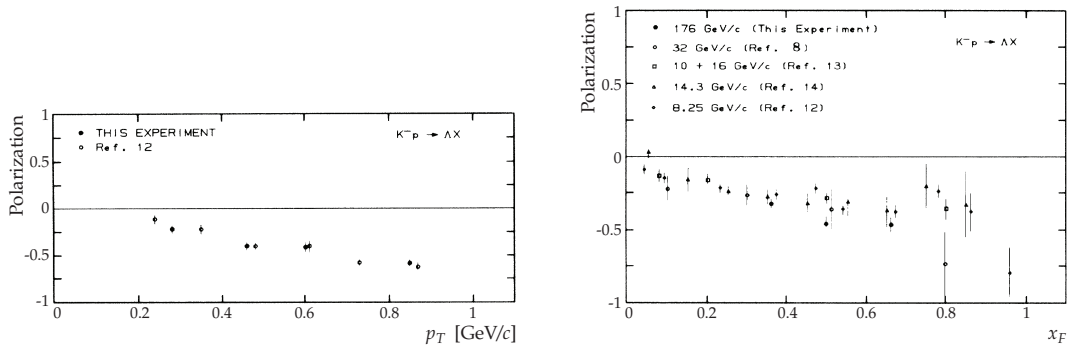

Figure 8.43: Polarization of Λs produced by K^- beams in various experiments as a function of p_T and x_F: Note that in contrast to the convention used throughout this text, here the production plane normal is defined to point in the opposite direction $\hat{n} \propto \vec{p}_\Lambda \times \vec{p}_{K^-}$, so that the polarization has the opposite sign. (from [Gou86])

Fig. 8.44a shows the Λ polarization in the full x_F range. If the s quark in the outgoing Λ stems from the beam kaon ($K^- p \longrightarrow \Lambda + (\pi)_n$), the polarization changes sign in the target fragmentation region around $x_F \approx -0.5$. If on the other hand the production of the s quark from the sea is forced by requiring an additional $K\bar{K}$ pair in the final state ($K^- p \longrightarrow \Lambda K\bar{K} + (\pi)_n$), a positive polarization like in proton and pion production is observed in the target fragmentation region (see fig. 8.44b). This is consistent with the expectation, that in the target fragmentation region the production of the Λ should be dominated by the target properties. As long as the s quark is produced from the sea the Λ polarization should be independent of the beam type.

The COMPASS data cover a x_F range from about -0.1 to 0.6. Due to the limited acceptance the interesting target fragmentation region is not accessible. The observed Λ polarization is in general much lower, but shows the same sign as in K^- production. The dependence on the kinematical variables x_F and p_T is, however, quite different.

In hadro-production the Ξ^- polarization is approximately equal to that of the Λ and also the $\bar{\Xi}^+$ exhibits a polarization with the same sign and comparable in magnitude. Due to the limited statistics of the Ξ samples the statistical errors of the measured polarizations of > 3.5 % are of the same magnitude as the measured Λ polarization itself, so that the above relations can neither be excluded nor verified for the quasi-real photo-production.

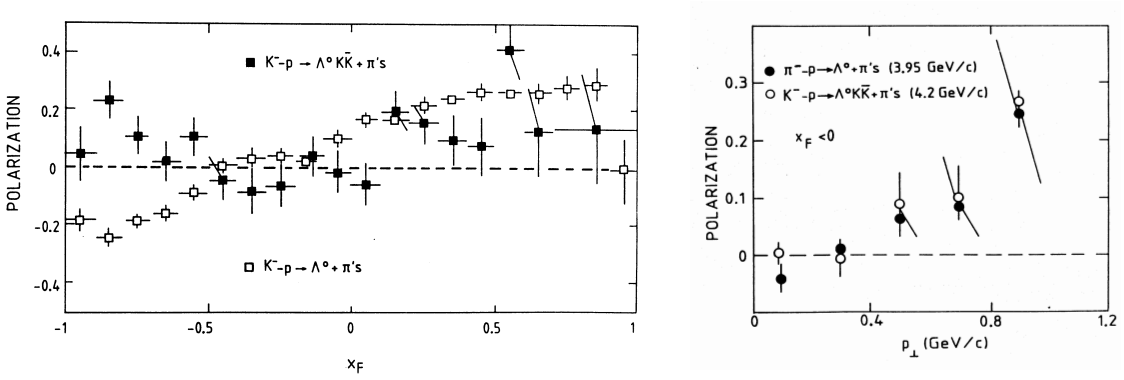

Figure 8.44: (a) Λ polarization in a 4.2 GeV/c K^- beam measured over the full x_F range: Depending on whether the s quark in the Λ stems from the beam ($K^- p \longrightarrow \Lambda + (\pi)_n$) or from the sea ($K^- p \longrightarrow \Lambda K \bar{K} + (\pi)_n$), the polarization exhibits a different behavior in the target fragmentation region. (from [Gan78]) (b) p_T dependence of the Λ polarization in the target fragmentation region: If the s quark of the Λ stems from the sea the polarization is independent of the beam particle. (from [Ade84])

8.4.3 Comparison with theoretical Predictions

8.4.3.1 Quark Recombination Model of DeGrand and Miettinen

The previous subsection showed, that in quasi-real photo-production the Λ polarization has the same sign as in K^- production. In the region of low Q^2 the interaction of high energy photons with the target nucleon is dominated by the quark sub-structure of the photons, which arises from fluctuations into quark-antiquark pairs (ρ, ω, ϕ mesons). These so-called resolved photons act like mesons, hence the quark recombination model is applicable in the current fragmentation region of photo-production and the Λ polarization is related to that in meson production processes like $\pi^\pm p \longrightarrow \Lambda X$ and $K^\pm p \longrightarrow \Lambda X$. In the quark recombination model the polarization is dominated by the valence quark content of the beam particle. Therefore the polarization of Λ and $\bar{\Lambda}$ hyperons at large x_F should be equal, since in the photon quarks and anti-quarks appear on an equal footing. The other way around Λ and $\bar{\Lambda}$ polarization should differ in the target fragmentation region, because the interaction with the target distinguishes between quarks and anti-quarks. As illustrated by fig. 8.45 and 8.46, which show the x_F and p_T dependence of the Λ and $\bar{\Lambda}$ polarizations in the low Q^2 region, both trends are confirmed by the data.

Fig. 8.45 and 8.46 also show the x_F and p_T dependence of the Λ and $\bar{\Lambda}$ polarizations in the large Q^2 region, where in addition the direct point-like interaction of the photon with the quarks inside the nucleon becomes important. In this region the Λ polarization goes to zero for large x_F and p_T. The $\bar{\Lambda}$ polarization drops for large p_T as well, but increases in magnitude if x_F becomes large.

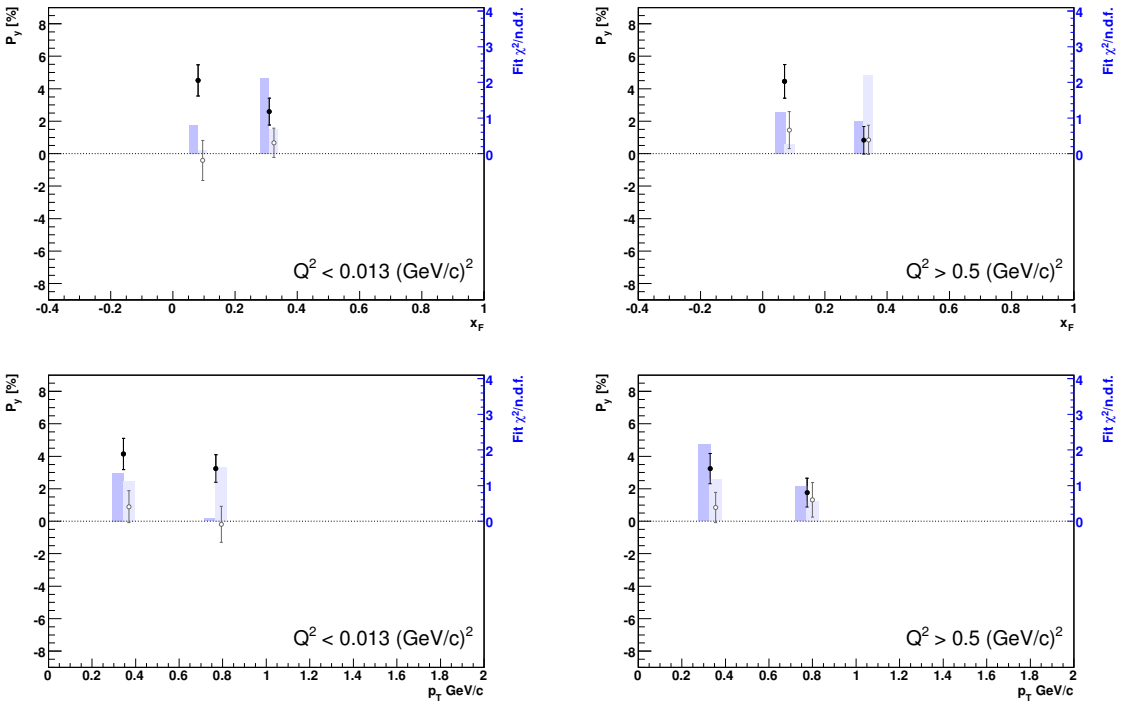

Figure 8.45: x_F and p_T dependence of the Λ polarization for small and large Q^2

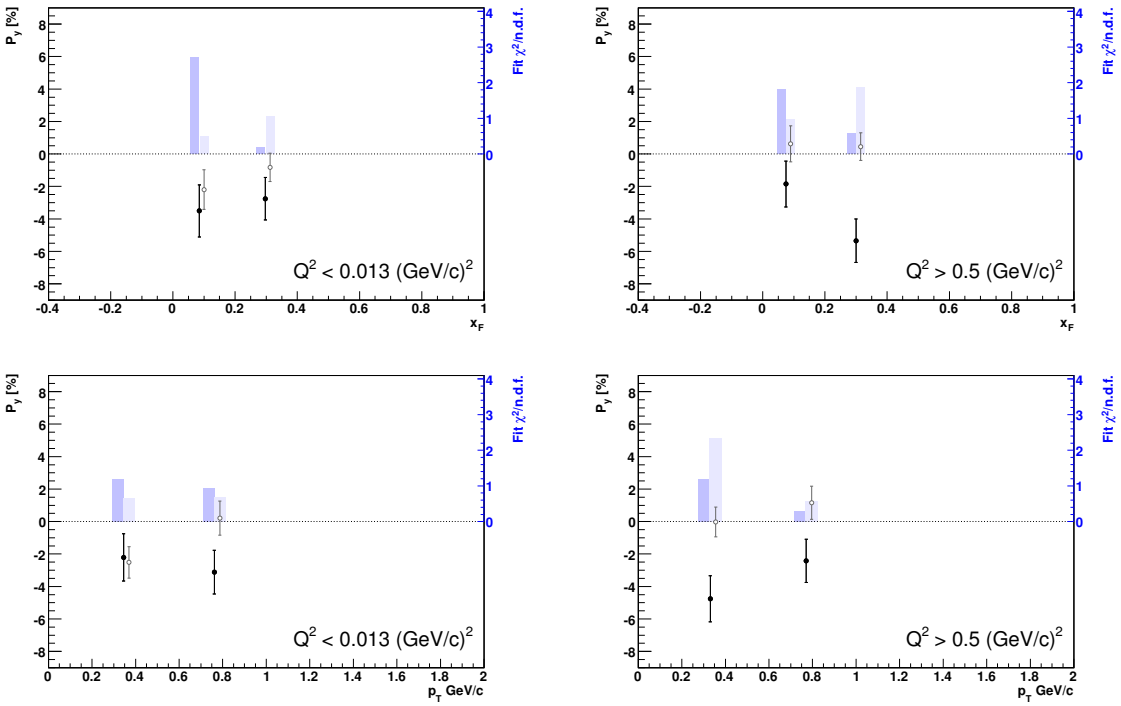

Figure 8.46: x_F and p_T dependence of the $\overline{\Lambda}$ polarization for small and large Q^2

8.4.3.2 Polarizing Fragmentation Functions

Based on a model for the polarizing fragmentation functions Anselmino *et al.* [Ans02b] predict negative polarizations for Λ and $\bar{\Lambda}$ hyperons with a momentum fraction z_h larger than about 0.3 in the current fragmentation region of deeply inelastic scattering (see subsection 6.2.2 and fig. 6.7 (page 89)). For lower z_h the polarization is expected to vanish. The calculations are based on the kinematical region of the HERMES experiment with $0.023 < x_B < 0.4$, $y_B < 0.85$, $1 < Q^2 < 10$ GeV/c^2, and $E_\Lambda > 4.5$ GeV. This is similar to the COMPASS kinematics in the DIS region with $0.004 < x_B < 0.3$, $0.2 < y_B < 0.8$, $1 < Q^2 < 20$ GeV/c^2, and $E_\Lambda > 5$ GeV.

Table 8.2 shows the polarization results for Λ and $\bar{\Lambda}$ in the DIS region, where in addition $x_F > 0$ was required. The mean z_h is in both cases below 0.3, so that the hyperons are expected to be unpolarized. The polarization of the Λ deviates by $+2.4\ \sigma_{\text{stat}}$ from zero, that of the $\bar{\Lambda}$ by $-3.1\ \sigma_{\text{stat}}$. Taking into account the K^0 background polarization as a measure for the systematic uncertainty, both values are compatible with the prediction.

	Λ	$\bar{\Lambda}$
N_H	105676	61410
P_y^H [%]	$+2.40 \pm 1.00$	-4.44 ± 1.43
Fit χ^2/n.d.f.	1.22	0.15
$P_y^{K^0}$ [%]	$+0.82 \pm 1.04$	-0.00 ± 1.01
Fit χ^2/n.d.f.	0.46	0.56
$\langle x_F \rangle$	0.216	0.200
$\langle p_T \rangle$ [GeV/c]	0.537	0.534
$\langle y_B \rangle$	0.437	0.458
$\langle Q^2 \rangle$ [(GeV/c)^2]	3.399	3.393
$\langle z_h \rangle$	0.277	0.261

Table 8.2: Λ and $\bar{\Lambda}$ polarizations in deeply inelastic scattering: The DIS subsample was selected by requiring $Q^2 > 1$ (GeV/c)^2, $0.2 < y_B < 0.8$, and $x_F > 0$.

8.4.4 Outlook

In 2006 COMPASS will again take data with the muon beam and longitudinally polarized target. Based on the numbers of the 2004 run this will increase the statistics by about 50 % thereby decreasing the statistical error of the Λ polarization down to 0.27 % and that of the Ξ^- to 2.8 %.

On the analysis side some systematical studies, in particular the change of the acceptance by the solenoid field and the robustness of the bias canceling method, should be verified by Monte-Carlo simulations.

To improve the mass resolution one could implement a kinematic refit of the secondary vertices according to the V^0 hypothesis. This way it would also be possible to calculate the error on the reconstructed invariant mass on an event-by-event basis, which could be used to exclude badly defined vertices. If the acceptance corrections would be taken from Monte-Carlo simulations, the refit would also allow to perform a V^0 identification event by event.

Moreover it would be interesting to study the Λ polarization in reactions with associated strangeness production like $\mu N \rightarrow \mu' \Lambda^{\uparrow} K^{+} X$. After 2006 it is planned, that COMPASS runs with different hadron beams, which would offer the opportunity to study the hyperon polarization in hadro-production as well.

Appendix A

TCS Controller VME Registers

The following sections give a complete overview over the configuration registers of the TCS controller which are accessible via the VMEbus. The address space for the configuration registers has a granularity of four so that the last nibble of the address is either 0x0, 0x4, 0x8, or 0xC.

A.1 Basic Registers

Address	Description	Width	Default
0x24	Run[0], pause[4], long broadcast[8], reset[12]	—	0xFE0100
	LEMO output mode for SubDAQs[23..17]		
0x28	Slow command FIFO	20	0x00000
0x2C	Configuration FIFO	20	0x00000
0x120	VME test register	32	0x00000000

Table A.1: Basic registers: The run bit in register 0x24 activates the TCS controller, the pause bit blocks external FLTs, the long broadcast bit determines whether the controller always sends out two consecutive broadcast commands to transmit the full 20 bit event number or whether the high part is sent only when it changed. The LEMO output mode defines whether the LEMO jacks for the SubDAQs put out all vetoed and synchronized first level triggers ('0') or only the artificial triggers ('1').

A.2 Read-only Status Registers

Address	Description	Width
0x30	Run[0], spill[4], configuration FIFO full[8], slow command FIFO full[12] running DAQ mask[23..16], firmware version[31..24]	32
0xC4	Spill #[30..20] and event #[19..0] of MainDAQ	31
0xC8	Spill #[30..20] and event #[19..0] of SubDAQ 1	31
0xCC	Spill #[30..20] and event #[19..0] of SubDAQ 2	31
0xD0	Spill #[30..20] and event #[19..0] of SubDAQ 3	31
0xD4	Spill #[30..20] and event #[19..0] of SubDAQ 4	31
0xD8	Spill #[30..20] and event #[19..0] of SubDAQ 5	31
0xDC	Spill #[30..20] and event #[19..0] of SubDAQ 6	31
0xE0	Spill #[30..20] and event #[19..0] of SubDAQ 7	31

Table A.2: Read-only status registers: The run bit of register 0x30 indicates whether the TCS is running, the spill bit indicates on-spill ('1') and off-spill ('0') periods. Bits 16 to 23 contain a mask in which each bit indicates whether the respective SubDAQ is running ('1') or not ('0').

A.3 MultiDAQ Time Slices

Address	Description	Width	Unit	Default
0x44	Time slice MainDAQ	20	CLK	0x00000
0x48	Time slice SubDAQ 1	20	CLK	0x00000
0x4C	Time slice SubDAQ 2	20	CLK	0x00000
0x50	Time slice SubDAQ 3	20	CLK	0x00000
0x54	Time slice SubDAQ 4	20	CLK	0x00000
0x58	Time slice SubDAQ 5	20	CLK	0x00000
0x5C	Time slice SubDAQ 6	20	CLK	0x00000
0x60	Time slice SubDAQ 7	20	CLK	0x00000

Table A.3: Registers for the eight time slices that determine the time division.

A.4 Variable Dead-Time

Address	Description	Width	Unit	Default
0x84	Number of FLTs for MainDAQ	8	—	0x0F
0x100	2nd number of FLTs for MainDAQ	8	—	0x0F
0x88	Number of FLTs for SubDAQ 1	8	—	0x0F
0x8C	Number of FLTs for SubDAQ 2	8	—	0x0F
0x90	Number of FLTs for SubDAQ 3	8	—	0x0F
0x94	Number of FLTs for SubDAQ 4	8	—	0x0F
0x98	Number of FLTs for SubDAQ 5	8	—	0x0F
0x9C	Number of FLTs for SubDAQ 6	8	—	0x0F
0xA0	Number of FLTs for SubDAQ 7	8	—	0x0F
0xA4	Time window for MainDAQ	16	CLK	0x97E0
0x104	2nd time window for MainDAQ	16	CLK	0x97E0
0xA8	Time window for SubDAQ 1	16	CLK	0x97E0
0xAC	Time window for SubDAQ 2	16	CLK	0x97E0
0xB0	Time window for SubDAQ 3	16	CLK	0x97E0
0xB4	Time window for SubDAQ 4	16	CLK	0x97E0
0xB8	Time window for SubDAQ 5	16	CLK	0x97E0
0xBC	Time window for SubDAQ 6	16	CLK	0x97E0
0xC0	Time window for SubDAQ 7	16	CLK	0x97E0
0x108	Dead-time at beginning of next spill (throttle)	8	200 ms	0x00

Table A.4: Configuration registers for the variable dead-time which is defined by the number of triggers within a time window. The MainDAQ has a second independent variable dead-time generator that is combined with the first one by a logical “or”.

A.5 Fixed Dead-Time

Address	Description	Width	Unit	Default
0x64	Fixed DT MainDAQ	16	CLK	0x0184
0x68	Fixed DT SubDAQ 1	16	CLK	0x0184
0x6C	Fixed DT SubDAQ 2	16	CLK	0x0184
0x70	Fixed DT SubDAQ 3	16	CLK	0x0184
0x74	Fixed DT SubDAQ 4	16	CLK	0x0184
0x78	Fixed DT SubDAQ 5	16	CLK	0x0184
0x7C	Fixed DT SubDAQ 6	16	CLK	0x0184
0x80	Fixed DT SubDAQ 7	16	CLK	0x0184

Table A.5: Fixed dead-times for the eight SubDAQs.

A.6 Artificial Trigger Sequencer

Address	Description	Width	Unit	Default
0x220	Period for event type 1	8	3.371 msec	0xFF
⋮	⋮	⋮	⋮	⋮
0x284	Period for event type 26	8	3.371 msec	0xFF
0x2A0	Mode for event type 1	2	—	0x0
⋮	⋮	⋮		⋮
0x304	Mode for event type 26	2	—	0x0
0x320	Fine delay for event type 1	8	1/256 CLK	0x00
⋮	⋮	⋮	⋮	⋮
0x384	Fine delay for event type 26	8	1/256 CLK	0x00
0x3C	SubDAQ activation mask for sequencer	8	—	0x00

Table A.6: The artificial trigger sequencer is configured by specifying the period, the mode, and the fine delay for each of the 26 calibration and monitoring triggers. In case the TCS receivers are equipped with a delay chip the fine delay allows to define the timing of the pre-trigger pulse with a precision of 1/256 CLK. The activation map defines for which SubDAQs the sequencer generates calibration and monitoring triggers.

A.7 Pulse Sequencer

Address	Description	Width	Unit	Default
`0x34`	Period of regular pulses	20	CLK	`0x097E0`
`0x38`	Downscale parameter for random pulses	24	—	`0x009C40`
`0x41C`	(Length - 1) of pulse pattern	14	CLK	`0x001F`
`0x420`	1st row of pattern RAM	32	—	`0x00000000`
⋮	⋮	⋮		⋮
`0xC1C`	512th row of pattern RAM	32	—	`0x00000000`

Table A.7: Configuration registers for the pulse sequencer.

Appendix B

Λ and $\overline{\Lambda}$ Polarization in kinematical Bins

The following tables detail the results of the analysis of the Λ and $\overline{\Lambda}$ polarizations in various kinematical bins, as presented in the subsections 8.3.1 and 8.3.2. Apart from the numerical polarization values they also specify the kinematical bins and the respective mean values of additional kinematical parameters.

x_F	N_H	P_y^H [%]	Fit χ^2/n.d.f.	$P_y^{K^0}$ [%]	Fit χ^2/n.d.f.	$\langle x_F \rangle$	$\langle p_T \rangle$ [GeV/c]	$\langle Q^2 \rangle$ [(GeV/c)^2]	$\langle y_B \rangle$	$\langle z_h \rangle$
<-0.007	95692	$+6.82 \pm 0.98$	1.35	$+2.81 \pm 1.98$	1.34	-0.037	0.478	0.429	0.567	0.083
$-0.007 \ldots 0.052$	195490	$+4.28 \pm 0.77$	0.47	$+0.10 \pm 0.93$	1.31	0.026	0.515	0.369	0.528	0.118
$0.052 \ldots 0.097$	205909	$+4.42 \pm 0.77$	1.09	$+0.04 \pm 0.86$	1.33	0.075	0.538	0.350	0.494	0.154
$0.097 \ldots 0.142$	215794	$+4.53 \pm 0.74$	1.77	-0.17 ± 0.80	0.09	0.119	0.554	0.360	0.463	0.190
$0.142 \ldots 0.189$	211782	$+3.06 \pm 0.69$	1.55	-0.39 ± 0.77	1.06	0.165	0.565	0.377	0.434	0.229
$0.189 \ldots 0.248$	217345	$+2.96 \pm 0.67$	0.86	$+0.71 \pm 0.74$	0.38	0.218	0.577	0.388	0.405	0.277
$0.248 \ldots 0.327$	212128	$+2.39 \pm 0.67$	0.22	$+0.49 \pm 0.74$	0.87	0.285	0.590	0.436	0.376	0.340
$0.327 \ldots 0.475$	209958	$+1.36 \pm 0.65$	0.20	$+0.25 \pm 0.68$	0.03	0.389	0.607	0.477	0.343	0.440
>0.475	88534	$+1.18 \pm 1.04$	3.48	-0.01 ± 0.90	0.38	0.573	0.636	0.513	0.298	0.621

Table B.1: Dependence of the Λ polarization on its longitunal momentum fraction x_F (cf. fig. 8.27 (page 168)).

x_F	N_H	P_y^H [%]	Fit χ^2/n.d.f.	$P_y^{K^0}$ [%]	Fit χ^2/n.d.f.	$\langle x_F \rangle$	$\langle p_T \rangle$ [GeV/c]	$\langle Q^2 \rangle$ [(GeV/c)^2]	$\langle y_B \rangle$	$\langle z_h \rangle$
<-0.007	55693	-15.60 ± 2.42	19.08	$+1.12\pm1.65$	4.03	-0.036	0.479	0.476	0.577	0.082
$-0.007\ldots0.052$	99179	-0.12 ± 1.20	1.41	-0.68 ± 0.92	0.81	0.026	0.511	0.410	0.545	0.116
$0.052\ldots0.097$	113162	-2.92 ± 1.07	0.28	$+0.05\pm0.83$	0.72	0.075	0.531	0.414	0.514	0.151
$0.097\ldots0.142$	122270	-0.65 ± 1.00	2.90	-0.00 ± 0.78	0.70	0.119	0.547	0.409	0.483	0.187
$0.142\ldots0.189$	120252	$+0.36\pm0.97$	0.85	-0.96 ± 0.77	3.20	0.165	0.560	0.400	0.454	0.226
$0.189\ldots0.248$	123062	-4.85 ± 0.99	2.85	$+0.15\pm0.72$	0.82	0.218	0.573	0.416	0.428	0.274
$0.248\ldots0.327$	114956	-1.92 ± 0.98	0.02	$+0.45\pm0.72$	0.21	0.284	0.588	0.427	0.402	0.336
$0.327\ldots0.475$	102300	-2.05 ± 1.04	1.11	$+0.85\pm0.67$	1.26	0.387	0.610	0.442	0.379	0.433
>0.475	33238	$+1.76\pm1.97$	1.13	$+0.65\pm0.88$	2.60	0.558	0.651	0.441	0.357	0.598

Table B.2: Dependence of the $\bar{\Lambda}$ polarization on its longitunal momentum fraction x_F (cf. fig. 8.28 (page 169)).

p_T [GeV/c]	N_H	P_y^H [%]	Fit χ^2/n.d.f.	$P_y^{K^0}$ [%]	Fit χ^2/n.d.f.	$\langle x_F \rangle$	$\langle p_T \rangle$ [GeV/c]	$\langle Q^2 \rangle$ [(GeV/c)^2]	$\langle y_B \rangle$	$\langle z_h \rangle$
<0.194	97568	$+2.98\pm1.12$	1.63	$+0.81\pm0.97$	0.07	0.164	0.153	0.541	0.431	0.229
0.194...0.306	200468	$+2.72\pm0.75$	0.75	$+0.39\pm0.72$	0.99	0.167	0.254	0.476	0.431	0.232
0.306...0.394	203243	$+3.03\pm0.72$	0.31	-0.37 ± 0.74	0.68	0.174	0.351	0.435	0.429	0.240
0.394...0.474	196747	$+3.20\pm0.71$	0.09	$+1.62\pm0.78$	0.44	0.179	0.434	0.391	0.428	0.246
0.474...0.558	200069	$+4.44\pm0.75$	1.12	-0.54 ± 0.81	1.29	0.186	0.515	0.379	0.430	0.254
0.558...0.658	209318	$+2.70\pm0.69$	1.31	-0.56 ± 0.81	1.85	0.194	0.606	0.369	0.431	0.263
0.658...0.790	209914	$+3.73\pm0.69$	0.61	-0.30 ± 0.84	1.26	0.204	0.720	0.362	0.435	0.275
0.790...1.038	214933	$+3.22\pm0.67$	1.95	-0.99 ± 0.87	1.25	0.216	0.894	0.354	0.445	0.290
>1.038	118131	$+3.31\pm0.89$	1.19	$+0.56\pm1.21$	0.91	0.234	1.242	0.368	0.470	0.318

Table B.3: Dependence of the Λ polarization on its transverse momentum p_T (cf. fig. 8.29 (page 170)).

p_T [GeV/c]	N_H	P_y^H [%]	Fit χ^2/n.d.f.	$P_y^{K^0}$ [%]	Fit χ^2/n.d.f.	$\langle x_F \rangle$	$\langle p_T \rangle$ [GeV/c]	$\langle Q^2 \rangle$ [(GeV/c)^2]	$\langle y_B \rangle$	$\langle z_h \rangle$
$<$0.194	51881	-3.54 ± 1.85	0.87	$+0.82 \pm 0.96$	1.05	0.160	0.152	0.551	0.454	0.222
0.194...0.306	106864	-1.73 ± 1.17	0.99	$+0.33 \pm 0.70$	0.95	0.163	0.254	0.490	0.453	0.225
0.306...0.394	108254	-2.25 ± 1.08	0.40	-1.15 ± 0.72	0.39	0.166	0.351	0.459	0.452	0.229
0.394...0.474	105060	-1.61 ± 1.05	0.95	-0.45 ± 0.76	1.00	0.172	0.434	0.411	0.452	0.235
0.474...0.558	106867	-1.23 ± 1.05	1.92	$+0.29 \pm 0.79$	3.18	0.178	0.516	0.407	0.455	0.242
0.558...0.658	111037	-2.06 ± 1.00	0.24	$+0.44 \pm 0.78$	1.37	0.186	0.606	0.375	0.458	0.251
0.658...0.790	110911	-1.76 ± 0.99	0.40	$+0.49 \pm 0.81$	2.22	0.195	0.720	0.385	0.463	0.262
0.790...1.038	110831	-0.07 ± 0.98	0.60	$+0.29 \pm 0.83$	1.40	0.209	0.894	0.370	0.474	0.279
$>$1.038	57966	$+0.44 \pm 1.33$	0.23	-0.42 ± 1.15	0.70	0.228	1.238	0.387	0.500	0.307

Table B.4: Dependence of the $\overline{\Lambda}$ polarization on its transverse momentum p_T (cf. fig. 8.30 (page 171)).

x_F	p_T [GeV/c]	N_H	P_y^H [%]	Fit χ^2/n.d.f.	$P_y^{K^0}$ [%]	Fit χ^2/n.d.f.	$\langle x_F \rangle$	$\langle p_T \rangle$ [GeV/c]	$\langle Q^2 \rangle$ [(GeV/c)^2]	$\langle y_B \rangle$	$\langle z_h \rangle$
<0.066	<0.338	93565	+5.82±1.13	1.23	−0.19±1.19	1.38	0.011	0.238	0.400	0.518	0.105
<0.066	0.338...0.487	84626	+4.80±1.11	1.95	−0.84±1.36	1.16	0.012	0.412	0.360	0.524	0.108
<0.066	0.487...0.698	92788	+5.15±1.02	0.06	−1.41±1.40	0.68	0.014	0.583	0.368	0.537	0.114
<0.066	>0.698	78629	+4.49±1.13	1.07	−0.60±1.81	0.59	0.019	0.903	0.402	0.569	0.126
0.066...0.157	<0.338	100974	+2.14±1.08	0.93	+0.17±1.02	0.08	0.110	0.241	0.411	0.452	0.175
0.066...0.157	0.338...0.487	98101	+5.04±1.02	0.58	−1.69±1.13	0.28	0.111	0.413	0.357	0.456	0.179
0.066...0.157	0.487...0.698	117466	+2.84±0.92	1.22	+1.24±1.16	1.73	0.111	0.585	0.340	0.468	0.183
0.066...0.157	>0.698	116284	+5.43±0.94	1.54	−0.50±1.32	0.73	0.112	0.922	0.334	0.498	0.194
0.157...0.262	<0.338	85935	+0.49±1.09	0.75	+1.42±1.04	0.65	0.204	0.241	0.493	0.398	0.257
0.157...0.262	0.338...0.487	87206	+3.10±1.04	0.95	+1.64±1.09	0.55	0.205	0.414	0.405	0.399	0.261
0.157...0.262	0.487...0.698	110379	+4.14±0.94	1.22	−0.28±1.07	0.47	0.205	0.587	0.348	0.408	0.265
0.157...0.262	>0.698	119862	+3.12±0.87	1.56	−1.38±1.16	2.75	0.206	0.933	0.336	0.436	0.276
>0.262	<0.338	88006	+1.65±1.08	1.40	+0.50±0.93	1.34	0.381	0.241	0.672	0.335	0.425
>0.262	0.338...0.487	94372	+1.11±0.99	0.98	+1.73±1.00	1.48	0.382	0.415	0.501	0.334	0.429
>0.262	0.487...0.698	128182	+1.44±0.83	1.48	−1.28±0.90	1.57	0.388	0.588	0.424	0.339	0.438
>0.262	>0.698	158446	+2.43±0.75	0.41	+0.03±0.85	1.41	0.396	0.947	0.375	0.364	0.456

Table B.5: Λ polarization as a function of p_T and x_F(cf. fig. 8.32).

x_F	p_T [GeV/c]	N_H	P_y^H [%]	Fit χ^2/n.d.f.	$P_y^{K^0}$ [%]	Fit χ^2/n.d.f.	$\langle x_F \rangle$	$\langle p_T \rangle$ [GeV/c]	$\langle Q^2 \rangle$ [(GeV/c)^2]	$\langle y_B \rangle$	$\langle z_h \rangle$
$<$0.066	$<$0.338	46909	-1.39 ± 1.93	0.41	-0.05 ± 1.26	3.71	0.015	0.239	0.440	0.533	0.105
$<$0.066	0.338...0.487	42605	-0.58 ± 1.62	1.05	-1.41 ± 1.35	0.08	0.015	0.412	0.410	0.538	0.108
$<$0.066	0.487...0.698	46098	$+0.97 \pm 1.55$	0.72	$+1.12 \pm 1.39$	1.27	0.018	0.583	0.403	0.551	0.113
$<$0.066	$>$0.698	37148	$+1.09 \pm 1.68$	0.77	$+0.56 \pm 1.72$	2.24	0.022	0.894	0.461	0.584	0.125
0.066...0.157	$<$0.338	58250	-2.21 ± 1.56	0.18	-1.16 ± 0.99	0.73	0.110	0.241	0.477	0.472	0.173
0.066...0.157	0.338...0.487	56167	$+0.09 \pm 1.48$	1.84	-0.54 ± 1.09	0.50	0.111	0.413	0.404	0.476	0.176
0.066...0.157	0.487...0.698	66786	-3.15 ± 1.32	1.22	$+0.21 \pm 1.12$	1.72	0.111	0.584	0.372	0.486	0.181
0.066...0.157	$>$0.698	62214	$+2.00 \pm 1.31$	1.09	-1.20 ± 1.27	0.40	0.112	0.914	0.380	0.520	0.191
0.157...0.262	$<$0.338	49200	-2.39 ± 1.67	1.44	$+0.46 \pm 1.03$	1.49	0.204	0.242	0.528	0.419	0.255
0.157...0.262	0.338...0.487	50385	-1.17 ± 1.48	2.51	-0.23 ± 1.08	1.85	0.204	0.414	0.426	0.420	0.258
0.157...0.262	0.487...0.698	62713	-3.27 ± 1.32	1.36	$+0.69 \pm 1.06$	0.51	0.205	0.586	0.383	0.432	0.262
0.157...0.262	$>$0.698	65717	-2.10 ± 1.23	1.36	$+1.12 \pm 1.14$	1.59	0.206	0.929	0.346	0.460	0.272
$>$0.262	$<$0.338	42165	-2.99 ± 1.82	0.15	$+0.62 \pm 0.90$	0.14	0.364	0.242	0.579	0.371	0.405
$>$0.262	0.338...0.487	45244	-1.07 ± 1.58	0.45	-0.07 ± 0.97	1.48	0.368	0.415	0.469	0.371	0.411
$>$0.262	0.487...0.698	62809	-1.86 ± 1.29	1.03	$+1.20 \pm 0.87$	0.82	0.371	0.589	0.406	0.379	0.417
$>$0.262	$>$0.698	77385	-0.35 ± 1.14	2.53	-0.05 ± 0.82	1.75	0.381	0.943	0.363	0.405	0.435

Table B.6: $\overline{\Lambda}$ polarization as a function of p_T and x_F(cf. fig. 8.33).

y_B	N_H	P_y^H [%]	Fit χ^2/n.d.f.	$P_y^{K^0}$ [%]	Fit χ^2/n.d.f.	$\langle x_F \rangle$	$\langle p_T \rangle$ [GeV/c]	$\langle Q^2 \rangle$ [(GeV/c)^2]	$\langle y_B \rangle$	$\langle z_h \rangle$
<0.193	101103	$+1.38\pm0.92$	3.07	$+1.39\pm1.08$	0.99	0.360	0.526	0.580	0.156	0.455
0.193...0.269	204229	$+3.30\pm0.69$	1.08	$+0.88\pm0.76$	0.48	0.269	0.543	0.405	0.234	0.349
0.269...0.327	205031	$+3.32\pm0.70$	2.37	-0.97 ± 0.78	0.71	0.228	0.552	0.346	0.298	0.301
0.327...0.383	202740	$+3.54\pm0.71$	1.08	-0.96 ± 0.78	0.88	0.201	0.558	0.338	0.355	0.270
0.383...0.445	208378	$+4.13\pm0.73$	0.92	$+0.33\pm0.77$	1.00	0.179	0.564	0.349	0.413	0.246
0.445...0.515	205808	$+2.76\pm0.72$	1.11	-0.09 ± 0.79	0.72	0.159	0.570	0.369	0.479	0.223
0.515...0.605	209073	$+3.10\pm0.73$	0.02	-1.17 ± 0.79	1.29	0.140	0.576	0.396	0.558	0.202
0.605...0.737	209141	$+2.09\pm0.74$	1.73	$+0.99\pm0.80$	0.41	0.119	0.581	0.442	0.665	0.179
>0.737	101041	$+7.81\pm1.16$	0.73	$+0.99\pm1.17$	1.16	0.100	0.587	0.568	0.793	0.158

Table B.7: Dependence of the Λ polarization on the relative energy transfer y of the virtual photon (cf. fig. 8.36 (page 178)).

y_B	N_H	P_y^H [%]	Fit χ^2/n.d.f.	$P_y^{K^0}$ [%]	Fit χ^2/n.d.f.	$\langle x_F \rangle$	$\langle p_T \rangle$ [GeV/c]	$\langle Q^2 \rangle$ [(GeV/c)^2]	$\langle y_B \rangle$	$\langle z_h \rangle$
$<$0.193	32723	-6.29 ± 1.82	1.96	$+0.59 \pm 1.00$	2.60	0.320	0.492	0.549	0.160	0.415
0.193...0.269	86021	-3.07 ± 1.15	0.22	$+0.08 \pm 0.74$	3.46	0.256	0.530	0.423	0.235	0.336
0.269...0.327	97553	-1.87 ± 1.09	0.50	$+1.43 \pm 0.76$	2.63	0.223	0.545	0.370	0.299	0.296
0.327...0.383	104305	-2.25 ± 1.07	0.36	$+0.41 \pm 0.77$	1.51	0.202	0.553	0.348	0.355	0.271
0.383...0.445	112795	$+0.91 \pm 1.03$	1.26	-0.18 ± 0.75	0.49	0.185	0.561	0.365	0.414	0.250
0.445...0.515	116336	-1.54 ± 1.01	0.64	$+1.06 \pm 0.77$	1.88	0.165	0.564	0.388	0.479	0.227
0.515...0.605	123542	-1.50 ± 1.04	1.61	-0.28 ± 0.78	1.07	0.149	0.571	0.428	0.558	0.209
0.605...0.737	128441	-0.15 ± 1.03	0.34	-1.61 ± 0.81	1.53	0.131	0.579	0.457	0.666	0.188
$>$0.737	64712	-0.80 ± 1.44	0.15	-1.41 ± 1.13	0.71	0.114	0.585	0.610	0.793	0.169

Table B.8: Dependence of the $\overline{\Lambda}$ polarization on the relative energy transfer y of the virtual photon (cf. fig. 8.37 (page 179)).

Q^2 [(GeV/c)^2]	N_H	P_y^H [%]	Fit χ^2/n.d.f.	$P_y^{K^0}$ [%]	Fit χ^2/n.d.f.	$\langle x_F \rangle$	$\langle p_T \rangle$ [GeV/c]	$\langle Q^2 \rangle$ [(GeV/c)^2]	$\langle y_B \rangle$	$\langle z_h \rangle$
$<$0.006	102573	$+4.45 \pm 0.97$	1.79	$+0.73 \pm 1.12$	1.38	0.229	0.559	0.004	0.300	0.305
0.006...0.017	203901	$+2.63 \pm 0.70$	2.09	-0.64 ± 0.80	0.55	0.196	0.565	0.011	0.379	0.267
0.017...0.032	200775	$+3.92 \pm 0.73$	2.70	-0.52 ± 0.81	1.46	0.182	0.569	0.024	0.430	0.251
0.032...0.055	201451	$+2.98 \pm 0.72$	2.15	$+0.89 \pm 0.81$	0.45	0.177	0.570	0.042	0.457	0.246
0.055...0.096	209672	$+3.95 \pm 0.73$	1.26	$+0.31 \pm 0.79$	0.92	0.177	0.571	0.074	0.471	0.245
0.096...0.171	208238	$+2.81 \pm 0.73$	1.86	-0.64 ± 0.79	0.29	0.179	0.568	0.129	0.472	0.247
0.171...0.352	205748	$+4.69 \pm 0.76$	0.73	-1.08 ± 0.78	0.69	0.185	0.566	0.245	0.466	0.253
0.352...1.288	205889	$+2.44 \pm 0.72$	1.42	$+1.05 \pm 0.77$	1.04	0.202	0.550	0.669	0.442	0.271
$>$1.288	106870	$+2.47 \pm 0.98$	1.69	$+1.01 \pm 1.05$	0.75	0.216	0.525	3.901	0.423	0.286

Table B.9: Dependence of the Λ polarization on the squared four-momentum transfer Q^2 of the virtual photon (cf. fig. 8.34 (page 176)).

Q^2 [(GeV/c)^2]	N_H	P_y^H [%]	Fit χ^2/n.d.f.	$P_y^{K^0}$ [%]	Fit χ^2/n.d.f.	$\langle x_F \rangle$	$\langle p_T \rangle$ [GeV/c]	$\langle Q^2 \rangle$ [(GeV/c)^2]	$\langle y_B \rangle$	$\langle z_h \rangle$
$<$0.006	46106	-2.70 ± 1.58	0.88	$+0.22 \pm 1.07$	0.60	0.220	0.547	0.004	0.309	0.294
0.006...0.017	100522	-2.52 ± 1.06	0.07	-2.03 ± 0.78	1.82	0.193	0.561	0.011	0.393	0.262
0.017...0.032	104428	-1.41 ± 1.09	2.42	-0.28 ± 0.80	3.58	0.180	0.567	0.024	0.448	0.246
0.032...0.055	106426	$+0.09 \pm 1.05$	0.11	$+0.91 \pm 0.78$	1.03	0.176	0.567	0.043	0.478	0.241
0.055...0.096	112564	-0.72 ± 1.04	0.40	$+0.96 \pm 0.77$	0.92	0.173	0.568	0.074	0.494	0.237
0.096...0.171	113119	-1.02 ± 1.04	0.85	-0.12 ± 0.76	0.98	0.173	0.566	0.129	0.496	0.237
0.171...0.352	111481	-0.96 ± 1.06	1.15	$+0.60 \pm 0.75$	0.28	0.177	0.560	0.246	0.492	0.241
0.352...1.288	113324	-2.01 ± 1.04	1.64	$+0.17 \pm 0.75$	3.46	0.187	0.548	0.667	0.476	0.252
$>$1.288	58362	-4.66 ± 1.46	1.14	-0.48 ± 1.02	1.02	0.192	0.524	3.945	0.462	0.258

Table B.10: Dependence of the $\bar{\Lambda}$ polarization on the squared four-momentum transfer Q^2 of the virtual photon (cf. fig. 8.35 (page 177)).

y_B	Q^2 [(GeV/c)^2]	N_H	P_y^H [%]	Fit χ^2/n.d.f.	$P_y^{K^0}$ [%]	Fit χ^2/n.d.f.	$\langle x_F \rangle$	$\langle p_T \rangle$ [GeV/c]	$\langle Q^2 \rangle$ [(GeV/c)^2]	$\langle y_B \rangle$	$\langle z_h \rangle$
<0.282	<0.028	113688	+5.68±0.92	0.98	+0.10±1.02	0.08	0.273	0.552	0.011	0.230	0.355
<0.282	0.028...0.084	66073	+3.26±1.14	0.80	+2.10±1.34	0.41	0.286	0.550	0.051	0.221	0.369
<0.282	0.084...0.272	72331	+1.61±1.08	0.06	+0.76±1.26	0.74	0.299	0.550	0.158	0.213	0.382
<0.282	>0.272	98658	+1.10±0.95	2.13	+0.70±1.09	0.76	0.312	0.507	1.442	0.203	0.398
0.282...0.398	<0.028	165429	+2.57±0.77	0.29	−1.45±0.89	0.73	0.203	0.562	0.012	0.338	0.275
0.282...0.398	0.028...0.084	92572	+2.95±1.02	0.32	+0.59±1.17	0.94	0.205	0.562	0.050	0.342	0.276
0.282...0.398	0.084...0.272	78940	+3.43±1.09	0.47	−4.14±1.26	0.44	0.210	0.558	0.154	0.342	0.280
0.282...0.398	>0.272	76061	+3.43±1.13	1.05	+0.56±1.22	2.09	0.221	0.538	1.601	0.339	0.290
0.398...0.522	<0.028	116488	+3.28±0.94	2.55	+1.23±1.07	1.18	0.162	0.572	0.015	0.453	0.228
0.398...0.522	0.028...0.084	102663	+3.50±1.01	2.79	+0.09±1.13	1.30	0.163	0.571	0.051	0.458	0.228
0.398...0.522	0.084...0.272	92138	+5.30±1.07	0.67	+0.88±1.16	0.23	0.165	0.568	0.153	0.460	0.230
0.398...0.522	>0.272	71546	+0.23±1.19	0.53	−1.07±1.28	0.95	0.176	0.557	1.657	0.459	0.239
>0.522	<0.028	66250	+2.57±1.23	0.29	−1.64±1.45	0.93	0.127	0.582	0.019	0.597	0.190
>0.522	0.028...0.084	145353	+4.08±0.91	3.11	+0.44±0.98	0.59	0.120	0.585	0.052	0.651	0.181
>0.522	0.084...0.272	156513	+3.69±0.87	2.16	−1.20±0.94	1.08	0.120	0.583	0.155	0.661	0.180
>0.522	>0.272	131405	+4.30±0.99	3.71	+1.99±0.99	0.11	0.127	0.572	1.455	0.669	0.186

Table B.11: Λ polarization as a function of Q^2 and y (cf. fig. 8.39).

y_B	Q^2 [(GeV/c)^2]	N_H	P_y^H [%]	Fit χ^2/n.d.f.	$P_y^{K^0}$ [%]	Fit χ^2/n.d.f.	$\langle x_F \rangle$	$\langle p_T \rangle$ [GeV/c]	$\langle Q^2 \rangle$ [(GeV/c)^2]	$\langle y_B \rangle$	$\langle z_h \rangle$
$<$0.282	$<$0.028	44745	-1.76 ± 1.57	0.28	-0.39 ± 1.01	0.98	0.258	0.540	0.011	0.234	0.340
$<$0.282	0.028...0.084	26314	-0.80 ± 2.06	4.01	$+2.77 \pm 1.28$	1.72	0.267	0.537	0.051	0.226	0.349
$<$0.282	0.084...0.272	28872	-2.59 ± 1.95	1.34	$+0.01 \pm 1.20$	0.74	0.272	0.529	0.158	0.220	0.355
$<$0.282	$>$0.272	39479	-6.79 ± 1.68	0.40	$+0.16 \pm 1.03$	2.36	0.276	0.489	1.425	0.213	0.361
0.282...0.398	$<$0.028	80609	-3.66 ± 1.20	0.31	$+0.57 \pm 0.85$	0.74	0.205	0.557	0.012	0.340	0.275
0.282...0.398	0.028...0.084	46447	-0.37 ± 1.53	0.57	$+1.48 \pm 1.12$	1.72	0.206	0.559	0.050	0.344	0.275
0.282...0.398	0.084...0.272	40136	$+0.43 \pm 1.65$	1.07	$+0.74 \pm 1.20$	1.06	0.206	0.551	0.155	0.343	0.276
0.282...0.398	$>$0.272	40986	-3.00 ± 1.69	0.47	$+1.85 \pm 1.19$	0.53	0.214	0.531	1.598	0.340	0.283
0.398...0.522	$<$0.028	63215	-0.97 ± 1.38	1.40	-0.93 ± 1.04	1.70	0.170	0.568	0.015	0.454	0.233
0.398...0.522	0.028...0.084	55984	$+1.46 \pm 1.44$	1.67	$+2.60 \pm 1.11$	1.89	0.171	0.567	0.051	0.459	0.234
0.398...0.522	0.084...0.272	51939	-1.48 ± 1.53	0.82	-1.13 ± 1.12	1.25	0.171	0.564	0.154	0.461	0.234
0.398...0.522	$>$0.272	42180	-0.81 ± 1.67	0.23	$+2.21 \pm 1.25$	2.35	0.177	0.550	1.642	0.459	0.239
$>$0.522	$<$0.028	38911	-0.89 ± 1.81	1.88	-5.12 ± 1.57	2.75	0.138	0.578	0.019	0.599	0.197
$>$0.522	0.028...0.084	87188	$+1.09 \pm 1.23$	1.40	-0.49 ± 0.96	0.69	0.133	0.582	0.053	0.652	0.190
$>$0.522	0.084...0.272	95471	-1.05 ± 1.20	0.42	$+0.65 \pm 0.92$	0.15	0.132	0.581	0.156	0.665	0.189
$>$0.522	$>$0.272	83802	-2.11 ± 1.29	0.24	-2.15 ± 0.97	0.36	0.136	0.570	1.510	0.671	0.192

Table B.12: $\bar{\Lambda}$ polarization as a function of Q^2 and y (cf. fig. 8.40).

List of Figures

The COMPASS Experiment

2.1 Inclusive lepton scattering in Born approximation 5
2.2 The photon-gluon fusion diagram 7
2.3 Definition of Collins and Sivers angle 9
2.4 The M2 beam line at the CERN SPS as used for the muon program 14
2.5 Top view of the COMPASS muon beam setup as of 2004 16
2.6 Dynamic nuclear polarization in an electron-proton spin system 21
2.7 The COMPASS polarized ^{6}LiD target 23

Data Acquisition System

3.1 General structure of the COMPASS data acquisition system 26
3.2 Schematic view of CATCH and GeSiCA concentrator modules 30
3.3 Spillbuffer card 31
3.4 The event building network 33
3.5 Architecture of the online filter 35

Trigger System

4.1 Top view of the trigger hodoscope setup 39
4.2 Selection of DIS events with geometrical trigger 40
4.3 Determination of the scattered muon energy with segmented hodoscopes 41
4.4 HCAL1 cluster summation in the hadronic trigger 43
4.5 The veto hodoscope system 44

Trigger Control System

5.1 Architecture of the trigger control system 48
5.2 Two-channel time division multiplexing using a biphase mark code 51
5.3 TTCex encoder circuitry 51
5.4 Data transferred via channel A and B 52
5.5 Schematic view of the TCS controller 54
5.6 Trigger synchronization and veto logic 55
5.7 The TCS controller module 56
5.8 Schematic view of the TCS receiver 58

5.9 Decoding of the time division multiplexed bit stream in the TCS receiver . 59
5.10 The TCS receiver card 61
5.11 Tagging of the SPS spill structure by artificial events 65

Transverse Hyperon Polarization

6.1 Hyperon polarization and parity conservation 72
6.2 Weak decay of the Λ and the Ξ^- hyperon 72
6.3 Polarization of various hyperons and anti-hyperons in proton induced inclusive reactions 76
6.4 Schematic illustration of some VVS and VSS recombination processes . . 80
6.5 Thomas precession in the semi-classical parton recombination model . . . 83
6.6 Λ production in SIDIS at leading order and leading twist 85
6.7 Numerical results for the p_T-averaged transverse Λ and $\overline{\Lambda}$ polarization as a function of z_h 89

Data Analysis

7.1 Background corrected momentum distributions of protons and pions from Λ decays 99
7.2 V^0 and Ξ event signature 100
7.3 Armenteros-Podalanski plot of the V^0 sample 101
7.4 Definition of the coordinate system in the laboratory frame 102
7.5 Definition of the coordinate system in the hyperon rest frame 103
7.6 Target cut 104
7.7 Definition of the V^0 vertex 105
7.8 Suppression of halo muons 106
7.9 V^0 sample after selection 106
7.10 Removal of fringe field tracks 108
7.11 V^0 decay vertex position 109
7.12 Vertex Separation 110
7.13 Collinearity cut 111
7.14 Definition of the production plane 112
7.15 Cut on pion association with the primary vertex 113
7.16 Suppression of converted photons 114
7.17 Λ sample after selection 115
7.18 Final Λ and $\overline{\Lambda}$ samples after event selection 116
7.19 Definition of Ξ vertex 118
7.20 Suppression of halo muons 118
7.21 Ξ decay topology 118
7.22 Pion passes through SM1 119
7.23 Definition of Λ vertex 119

7.24 DCA of Ξ vertex . . . 120
7.25 Definition of production plane . . . 121
7.26 Cut on pion association with the primary vertex . . . 121
7.27 Suppression of converted photons for Λ daughter . . . 122
7.28 Cut on invariant mass of the Λ daughter . . . 122
7.29 Ξ sample after selection . . . 123
7.30 Final Ξ^- and $\bar{\Xi}^+$ samples after event selection . . . 124
7.31 Background corrected $\cos\theta_y$ distributions for Λ and Ξ^- hyperons . . . 126
7.32 Mid-plane symmetry of the apparatus and hyperon decay . . . 127
7.33 Fit of the $m_{p\pi^-}$ invariant mass spectrum . . . 131
7.34 Two-dimensional $(m_{p\pi^-}, m_{\pi^+\pi^-})$ invariant mass histogram . . . 133
7.35 Kinematical boundary of the $(m_{p\pi^-}, m_{\pi^+\pi^-})$ invariant mass histogram . . . 135
7.36 Distribution of the Lorentz factors $\gamma_{\Lambda,\bar{\Lambda}}$ for Λ and $\bar{\Lambda}$ . . . 136
7.37 Slices of the $(m_{p\pi^-}, m_{\pi^+\pi^-})$ invariant mass histogram . . . 137
7.38 Fit range in the $(m_{p\pi^-}, m_{\pi^+\pi^-})$ invariant mass plot . . . 138
7.39 Fit of the $(m_{p\pi^-}, m_{\pi^+\pi^-})$ invariant mass histogram . . . 139

Results

8.1 Angular distributions $R(\cos\theta_y)$ and polarizations of Λ and $\bar{\Lambda}$ . . . 142
8.2 Angular distributions $R(\cos\theta_y)$ and polarizations of Ξ^- and $\bar{\Xi}^+$ . . . 142
8.3 Angular distribution $R(\cos\theta_y)$ and polarization for the K^0 . . . 144
8.4 Λ and $\bar{\Lambda}$ polarizations with three different fit methods . . . 145
8.5 Armenteros plot of the two-dimensional fit regions . . . 146
8.6 Angular distributions $R(\cos\theta_y)$ and polarizations of the K^0 background . . . 147
8.7 Influence of the converted photon background on the polarization . . . 147
8.8 Angular distributions $R_0(\cos\theta_y)$ and polarizations of Λ and $\bar{\Lambda}$ . . . 149
8.9 Angular distributions $R_0(\cos\theta_y)$ and polarizations of Ξ^- and $\bar{\Xi}^+$ . . . 149
8.10 Sector definition to verify the left-right acceptance correction . . . 150
8.11 Λ and $\bar{\Lambda}$ polarizations in three azimuthal sectors and in dependence on the beam direction . . . 151
8.12 Ξ^- and $\bar{\Xi}^+$ polarizations in three azimuthal sectors and in dependence on the beam direction . . . 152
8.13 Dependence of Λ, $\bar{\Lambda}$, Ξ^-, and $\bar{\Xi}^+$ polarizations on binning in $\cos\theta_y$ . . . 153
8.14 Λ and K^0 background polarizations for the various data taking periods . . . 154
8.15 $\bar{\Lambda}$ and K^0 background polarizations for the various data taking periods . . . 155
8.16 Angular distributions of virtual photon and production plane normal with respect to the z_{Lab}-axis . . . 156
8.17 Fraction of the target polarization along the production plane normal . . . 157
8.18 Dependence of the Λ and $\bar{\Lambda}$ polarizations on the target polarization . . . 158

8.19 Dependence of the Ξ^- and $\overline{\Xi}^+$ polarizations on the target polarization . . . 159
8.20 Λ and $\overline{\Lambda}$ precession in the target solenoid field 160
8.21 Mid-plane symmetry of the apparatus and target solenoid field 161
8.22 Influence of the target solenoid on the Λ polarization 163
8.23 Influence of the target solenoid on the $\overline{\Lambda}$ polarization 164
8.24 Influence of the target solenoid on the Ξ^- and $\overline{\Xi}^+$ polarizations 165
8.25 Angular distributions $R(\cos\theta_y)$ and polarizations of the Λ hyperon for the two solenoid field orientations 166
8.26 Angular distribution of the protons from Λ decays for the two solenoid current directions 166
8.27 Dependence of the Λ polarization on x_F 168
8.28 Dependence of the $\overline{\Lambda}$ polarization on x_F 169
8.29 Dependence of the Λ polarization on p_T 170
8.30 Dependence of the $\overline{\Lambda}$ polarization on p_T 171
8.31 Correlation of p_T and x_F for Λ and $\overline{\Lambda}$ 172
8.32 Λ polarization as a function of p_T and x_F 173
8.33 $\overline{\Lambda}$ polarization as a function of p_T and x_F 174
8.34 Dependence of the Λ polarization on Q^2 176
8.35 Dependence of the $\overline{\Lambda}$ polarization on Q^2 177
8.36 Dependence of the Λ polarization on y_B 178
8.37 Dependence of the $\overline{\Lambda}$ polarization on y_B 179
8.38 Correlation of Q^2 and y_B for Λ and $\overline{\Lambda}$ 180
8.39 Λ polarization as a function of Q^2 and y_B 181
8.40 $\overline{\Lambda}$ polarization as a function of Q^2 and y_B 182
8.41 HERMES measurement of the Λ and $\overline{\Lambda}$ polarizations as a function of ζ . . 185
8.42 HERMES measurement of the Λ and $\overline{\Lambda}$ polarizations as a function of p_T^B . 185
8.43 Polarization of Λs produced by K^- beams in various experiments as a function of p_T and x_F 186
8.44 Λ polarization in K^- and π^- beams 187
8.45 x_F and p_T dependence of the Λ polarization for small and large Q^2 188
8.46 x_F and p_T dependence of the $\overline{\Lambda}$ polarization for small and large Q^2 188

List of Tables

Trigger Control System

5.1 Byte format of the event label generated by the TCS receiver 59
5.2 Definition of the TCS error byte 60
5.3 Read-only status registers in the TCS receiver 60
5.4 TCS event types 65
5.5 Supported option strings in the TCS server configuration file 67
5.6 Socket based remote interface provided by the TCS server 68

Transverse Hyperon Polarization

6.1 Decay asymmetry parameters of some hyperon decay channels 73
6.2 Comparison of the DeGrand and Miettinen model with data 82

Data Analysis

7.1 Summary of the dataset used for the analysis 98
7.2 Summary of the V^0 selection cuts 107
7.3 Summary of the cuts, that define the Λ and $\overline{\Lambda}$ sample 115
7.4 Summary of the cuts, that define the Ξ^- and $\overline{\Xi}^+$ sample 123

Results

8.1 Measured average hyperon polarizations 143
8.2 Λ and $\overline{\Lambda}$ polarizations in DIS 189

TCS Controller VME Registers

A.1 Basic registers 191
A.2 Read-only status registers 192
A.3 Time slice registers 192
A.4 Variable dead-time registers 193
A.5 Fixed dead-time registers 194
A.6 Artificial trigger sequencer registers 194
A.7 Pulse sequencer registers 195

Λ and $\overline{\Lambda}$ Polarization in kinematical Bins

B.1 Dependence of the Λ polarization on x_F 198
B.2 Dependence of the $\overline{\Lambda}$ polarization on x_F 199

B.3 Dependence of the Λ polarization on p_T 200
B.4 Dependence of the $\overline{\Lambda}$ polarization on p_T 201
B.5 Λ polarization as a function of p_T and x_F 202
B.6 $\overline{\Lambda}$ polarization as a function of p_T and x_F 203
B.7 Dependence of the Λ polarization on y 204
B.8 Dependence of the $\overline{\Lambda}$ polarization on y 205
B.9 Dependence of the Λ polarization on Q^2 206
B.10 Dependence of the $\overline{\Lambda}$ polarization on Q^2 207
B.11 Λ polarization as a function of Q^2 and y 208
B.12 $\overline{\Lambda}$ polarization as a function of Q^2 and y 209

Bibliography

[Abe84] K. Abe et al. Inclusive photoproduction of neutral strange particles at 20 GeV . *Phys. Rev.* **D29**, 1877 (1984). (Cited on page 76.)

[Abr76] H. Abramowicz et al. Λ polarization in the reaction $K^- p \to \Lambda +$ anything at 14.3 GeV/c. *Nucl. Phys.* **B105**, 222 (1976). (Cited on page 76.)

[Abr78] A. Abragam and M. Goldman. Principles of dynamic nuclear polarisation. *Rep. Prog. Phys.* **41**, 395–467 (1978). (Cited on page 21.)

[Ada95] M. I. Adamovich et al. Measurement of the polarization of Λ, $\bar{\Lambda}$, Σ^+ and Ξ^- produced in a Σ^- beam of 330 GeV/c. *Z. Phys.* **A350**, 379–386 (1995). (Cited on page 126.)

[Ada00] D. Adams et al. Measurement of the SMC muon beam polarisation using the asymmetry in the elastic scattering off polarised electrons. *Nucl. Inst. Meth.* **A443**, 1–19 (2000). (Cited on page 14.)

[Ada04a] M. I. Adamovich et al. A measurement of Λ polarization in inclusive production by Σ^- of 340 GeV/c in C and Cu targets. *Eur. Phys. J.* **C32**, 221–228 (2004). (Cited on pages 76 and 148.)

[Ada04b] M. I. Adamovich et al. A measurement of Ξ^- polarization in inclusive production by Σ^- of 340 GeV/c in C and Cu targets. *Eur. Phys. J.* **C36**, 315–321 (2004). (Cited on page 76.)

[Ade84] B. Adeva, M. Aguilar-Benitez, J. A. Rubio, J. A. Garzon, and C. Pajares. Study of strange particle inclusive reactions in $\pi^- p$ interactions at 3.95 GeV/c. *Z. Phys.* **C26**, 359–372 (1984). (Cited on page 187.)

[Age05] E. S. Ageev et al. Search for the $\Phi(1860)$ pentaquark at COMPASS. *Eur. Phys. J.* **C41**, 469–474 (2005). (Cited on page 117.)

[Aji83] I. V. Ajinenko et al. Inclusive $\bar{\Lambda}$ polarization in $K^+ p$ interactions at 32 and 70 GeV/c. *Phys. Lett.* **B121**, 183 (1983). (Cited on page 76.)

[Alb03] E. Albrecht et al. COMPASS RICH-1. *Nucl. Inst. Meth.* **A502**, 112 (2003). (Cited on page 99.)

[Alb04] E. Albrecht et al. First performances of COMPASS RICH-1. *Nucl. Inst. Meth.* **A518**, 586 (2004). (Cited on page 15.)

[Ald85] D. Alde et al. Acquisition system for the hodoscope spectrometer GAMS-4000. *Nucl. Inst. Meth.* **A240**, 343 (1985). (Cited on page 19.)

[Ale00] A. N. Aleev et al. The measurement of the transverse polarization of Λ hyperons produced in nC reactions in the EXCHARM experiment. *Eur. Phys. J.* **C13**, 427–432 (2000). (Cited on pages 75 and 126.)

[Ale01] V. Alexakhin et al. Vertex reconstruction in the COMPASS spectrometer. *COMPASS Note* **2001-17** (2001).

[And83] Bo Andersson, G. Gustafson, G. Ingelman, and T. Sjostrand. Parton fragmentation and string dynamics. *Phys. Rept.* **97**, 31 (1983). (Cited on page 77.)

[Ang05a] H. Angerer, `heinz.angerer@e18.physik.tu-muenchen.de`. Private communication, 2005. (Cited on pages 30 and 55.)

[Ang05b] H. Angerer et al. The silicon vertex detector of COMPASS with sub-ns time resolution. *submitted to Nucl. Inst. Meth.* **A** (2005). (Cited on pages 17, 28, and 52.)

[Ans00a] M. Anselmino, M. Boglione, and F. Murgia. Λ and $\bar{\Lambda}$ polarization in polarized DIS. *Phys. Lett.* **B481**, 253–262 (2000). (Cited on page 11.)

[Ans00b] M. Anselmino and F. Murgia. Spin effects in the fragmentation of a transversely polarized quark. *Phys. Lett.* **B483**, 74–86 (2000). (Cited on page 9.)

[Ans01a] M. Anselmino, D. Boer, U. D'Alesio, and F. Murgia. Λ polarization from unpolarized quark fragmentation. *Phys. Rev.* **D63**, 054029 (2001). (Cited on page 84.)

[Ans01b] M. Anselmino, D. Boer, U. D'Alesio, and F. Murgia. Λ polarization in unpolarized hadron reactions. *Czech. J. Phys.* **51**, A107–A113 (2001). (Cited on page 84.)

[Ans01c] M. Anselmino, D. Boer, U. D'Alesio, and F. Murgia. Transverse Λ polarization in unpolarized semi-inclusive DIS. In *9th International Workshop on Deep Inelastic Scattering (DIS 2001)*, Bologna, Italy, April 2001. (Cited on page 84.)

[Ans01d] M. Anselmino, M. Boglione, U. D'Alesio, E. Leader, and F. Murgia. Parton densities and fragmentation functions from polarized Λ production in semi-inclusive DIS. *Phys. Lett.* **B509**, 246–252 (2001). (Cited on page 11.)

[Ans02a] M. Anselmino. Transversity and Λ polarization. In *Workshop on future Physics @ COMPASS*, CERN, Geneva, Switzerland, September 2002. CERN-2004-011. (Cited on page 12.)

[Ans02b] M. Anselmino, D. Boer, U. D'Alesio, and F. Murgia. Transverse Λ polarization in semi-inclusive DIS. *Phys. Rev.* **D65**, 114014 (2002). (Cited on pages 84, 88, 89, and 189.)

[Ans03] M. Anselmino, D. Boer, U. D'Alesio, and F. Murgia. Transverse Λ polarization in inclusive processes. *Int. J. Mod. Phys.* **A18**, 1237–1246 (2003). (Cited on page 84.)

[Ant90] Yu. M. Antipov et al. Drift tubes for the SAMUS muon spectrometer of the D∅ detector at FNAL. *Nucl. Inst. Meth.* **A297**, 121 (1990). (Cited on page 20.)

[Ast82] D. Aston et al. Inclusive production of Λs and $\bar{\Lambda}$s in γp interactions for photon energies between 25 GeV and 70 GeV. *Nucl. Phys.* **B195**, 189 (1982). (Cited on page 76.)

[Ath80] H. W. Atherton et al. Precise measurements of particle production by 400 GeV protons on beryllium targets. *CERN Yellow Report* **80-07** (1980). (Cited on page 13.)

[Bar92] R. Barni, G. Preparata, and P. G. Ratcliffe. A simple explanation of hyperon polarization at high p_T. *Phys. Lett.* **B296**, 251–255 (1992). (Cited on page 77.)

[Bar94] S. Barlag et al. A study of the transverse polarization of Λ and $\bar{\Lambda}$ hyperons produced in π^-Cu interactions at 230 GeV/c. *Phys. Lett.* **B325**, 531–535 (1994). (Cited on page 76.)

[Bar98] P. Barberis et al. Test of front-end chip for COMPASS MWPC. *COMPASS Note* **1998-9** (1998). (Cited on page 19.)

[Bar02] V. Barone, A. Drago, and P. G. Ratcliffe. Transverse polarisation of quarks in hadrons. *Phys. Rept.* **359**, 1–168 (2002). (Cited on page 9.)

[Bau03] G. Baum et al. The COMPASS RICH-1 read-out system. *Nucl. Inst. Meth.* **A502**, 246 (2003). (Cited on page 27.)

[Bed04] Y. Bedfer et al. COMPASS's track reconstruction algorithm. *COMPASS Note* **2004-1** (2004). (Cited on page 93.)

[Bel01] S. L. Belostotski and O. Grebenyuk. Transverse polarization of Λ hyperons produced inclusively in eN-scattering at hermes. In *9th Workshop on High Energy Spin Physics*, Dubna, Russia, August 2001. (Cited on pages 76 and 184.)

[Ben83] J. Bensinger et al. Inclusive Λ production and polarization in 16 GeV/c $\pi^- p$ interactions. *Phys. Rev. Lett.* **50**, 313–316 (1983). (Cited on page 76.)

[Ben85] J. Bensinger et al. Measurement of decay parameters and polarization in inclusive Ξ^- production from $K^- p$ interactions. *Nucl. Phys.* **B252**, 561–577 (1985). (Cited on page 76.)

[Ber05a] C. Bernet et al. The $40 \times 40\,\mathrm{cm}^2$ gaseous microstrip detector Micromegas for the high-luminosity COMPASS experiment at CERN. *Nucl. Inst. Meth.* **A536**, 61–69 (2005). (Cited on page 18.)

[Ber05b] C. Bernet et al. The COMPASS trigger system for muon scattering. *Nucl. Instrum. Meth.* **A550**, 217–240 (2005). (Cited on pages 37 and 43.)

[Bin86] F. Binon et al. Hodoscope multiphoton spectrometer GAMS-2000. *Nucl. Inst. Meth.* **A248**, 86 (1986). (Cited on page 19.)

[Bis02] J. Bisplinghoff et al. A scintillating fibre hodoscope for high rate applications. *Nucl. Inst. Meth.* **A490**, 101–111 (2002). (Cited on page 18.)

[Bra76] F. W. Brasse et al. Construction of a large drift chamber and test measurements. *DESY* **F21-76-02** (1976). (Cited on page 19.)

[Bra98a] A. Brandt et al. Measurements of inclusive $\overline{\Lambda}$ production with large x_F at the S$p\bar{p}$S collider. *Nucl. Phys.* **B519**, 3–18 (1998). (Cited on page 75.)

[Bra98b] A. Bravar. Experimental overview of spin effects in hadronic interactions at high energies. In *13th International Symposium on High-Energy Spin Physics (SPIN 98)*, Protvino, Russia, September 1998. (Cited on pages 75 and 76.)

[Bra98c] A. Bravar, D. v. Harrach, and A. Kotzinian. Gluon polarization from correlated high-p_T hadron pairs in polarized electroproduction. *Phys. Lett.* **B421**, 349–359 (1998). (Cited on page 8.)

[Bru97] R. Brun and F. Rademakers. ROOT: An object oriented data analysis framework. *Nucl. Inst. Meth.* **A389**, 81 (1997). (Cited on page 92.)

[Brü02] A. Brüll. Transverse polarisation of Λ and $\overline{\Lambda}$ hyperons in quasi-real photon nucleon scattering. In *Presented at the 15th International Spin Physics Symposium (SPIN02)*, Brookhaven National Lab, New York, USA, September 2002. (Cited on pages 76, 184, and 185.)

[Bun76] G. Bunce et al. Λ hyperon polarization in inclusive production by 300 GeV protons on beryllium. *Phys. Rev. Lett.* **36**, 1113–1116 (1976). (Cited on pages 74 and 75.)

[CAS] CASTOR. Home page, `http://castor.web.cern.ch`. (Cited on page 33.)

[Cer02] L. Cerini et al. Fast front-end electronics for the large drift chambers W4-W5 at COMPASS experiment. *COMPASS Note* **2002-9** (2002). (Cited on page 19.)

[CHE95] Y. Alexandrov et al. The CHEOPS letter of intent. **CERN-SPSLC-95-22** (1995). (Cited on page 3.)

[Chu75] S. U. Chung, R. L. Eisner, S. D. Protopopescu, and R. D. Field. Polarization study of inclusive Λ production in $K^- p$ interactions. *Phys. Rev.* **D11**, 1010 (1975). (Cited on page 76.)

[CMS] CMS. Home page, `http://cmsinfo.cern.ch`. (Cited on page 28.)

[COM96] The COMPASS collaboration. A proposal for a Common Muon and Proton Apparatus for Structure and Spectroscopy. **CERN-SPSLC-96-14** (1996). (Cited on pages 3 and 4.)

[COM05a] E. S. Ageev et al. Gluon polarization in the nucleon from quasi-real photoproduction of high-p_T hadron pairs. *submitted to Phys. Lett.* **B** (2005). (Cited on page 8.)

[COM05b] V. Yu. Alexakhin et al. First measurement of the transverse spin asymmetries of the deuteron in semi-inclusive deep inelastic scattering. *Phys. Rev. Lett.* **94**, 202002 (2005). (Cited on pages 9 and 11.)

[COR] CORAL: COmpass Reconstruction and AnaLysis program, `http://coral.web.cern.ch/coral`. (Cited on pages 67 and 92.)

[DAT01] CERN ALICE DAQ group. DATE 3.7, ALICE DATE user's guide. *CERN* **ALICE Internal Note/DAQ ALICE-INT-200-31 v.2** (2001). (Cited on page 33.)

[DeG81a] T. A. DeGrand and H. I. Miettinen. Models for polarization asymmetry in inclusive hadron production. *Phys. Rev.* **D24**, 2419–2427 (1981). Erratum ibid. D31:661, 1985. (Cited on page 77.)

[DeG81b] T. A. DeGrand and H. I. Miettinen. Quark dynamics of polarization in inclusive hadron production. *Phys. Rev.* **D23**, 1227–1230 (1981). (Cited on page 77.)

[DeG85] T. A. DeGrand, J. Markkanen, and H. I. Miettinen. Hyperon polarization asymmetry: Polarized beams and Ω^- production. *Phys. Rev.* **D32**, 2445–2448 (1985). (Cited on pages 77 and 82.)

[Del00] E. Delagnes et al. SFE16, a low noise front-end integrated circuit dedicated to the read-out of large Micromegas detectors. *IEEE Trans. Nucl. Sci.* **47**, 1447–1453 (2000). (Cited on page 27.)

[DeM04] R. De Masi. *Development of a cryogenic silicon detector system and study of strange particle production in deep inelastic scattering*. Ph.D. thesis, Technische Universität München, November 2004. (Cited on page 117.)

[Dob94] N. Doble et al. The upgraded muon beam at the SPS. *Nucl. Inst. Meth.* **A343**, 351–362 (1994). (Cited on page 13.)

[Duk87] E. C. Dukes et al. Polarization of Σ^0 hyperons in inclusive production from 28.5 GeV/c protons on beryllium. *Phys. Lett.* **B193**, 135–139 (1987). (Cited on page 75.)

[Dur91] J. Duryea et al. Polarization of Ξ^- hyperons produced by 800 GeV protons. *Phys. Rev. Lett.* **67**, 1193–1196 (1991). (Cited on page 75.)

[DvH] D. v. Harrach et al. The fast readout of HCAL1 and HCAL2 for the COMPASS muon trigger, `http://wwwcompass.cern.ch/compass/detector/trigger/muon-trigger/HCAL.ps.gz`. (Cited on page 43.)

[Ell74] J. Ellis and R. Jaffe. Sum rule for deep inelastic electroproductions from polarized protons. *Phys. Rev.* **D9**, 5 (1974). (Cited on page 4.)

[EMC89] J. Ashman et al. An investigation of the spin structure of the proton in deep inelastic scattering of polarized muons on polarized protons. *Nucl. Phys.* **B328**, 1 (1989). (Cited on page 4.)

[Erh79] S. Erhan et al. Λ polarization in proton-proton interactions at $\sqrt{s} = 53$ and 62 GeV. *Phys. Lett.* **B82**, 301 (1979). (Cited on page 75.)

[Fan99] V. Fanti et al. A measurement of the transverse polarization of Λ-hyperons produced in inelastic pN-reactions at 450 GeV proton energy. *Eur. Phys. J.* **C6**, 265–269 (1999). (Cited on page 75.)

[Fel99] J. Felix. On theoretical studies of Λ polarization. *Mod. Phys. Lett.* **A14**, 827–842 (1999). (Cited on page 77.)

[Fil01] B. W. Filippone and Xiang-Dong Ji. The spin structure of the nucleon. *Adv. Nucl. Phys.* **26**, 1 (2001). (Cited on page 6.)

[Fis99] H. Fischer et al. $\mathcal{F}1$: An eight channel time-to-digital converter chip for high rate experiments. In *5th Workshop on Electronics for the LHC Experiments (LEB '99)*, Snowmass, Colorado, USA, September 1999. (Cited on page 27.)

[Fis00] H. Fischer et al. Implementation of the dead-time free $\mathcal{F}1$ TDC in the COMPASS detector readout. In *8th Pisa Meeting Advanced Detectors 2000*, La Biodola, Isola d'Elba, Italy, May 2000. Nucl. Inst. Meth. A461:507. (Cited on pages 27 and 30.)

[Fis03] H. Fischer et al. The COMPASS online data format – version 4. *COMPASS Note* **2002-8** (2003). (Cited on page 29.)

[Fre01] M. J. French et al. Design and results from the APV25, a deep sub-micron CMOS front-end chip for the CMS tracker. *Nucl. Instrum. Meth.* **A466**, 359–365 (2001). (Cited on page 28.)

[Frü87] R. Frühwirth. Application of Kalman filtering to track and vertex fitting. *Nucl. Inst. Meth.* **A262**, 444–450 (1987). (Cited on page 94.)

[Gan78] S. N. Ganguli et al. Inclusive production of lambda in the proton fragmentation region from $K^- p \to \Lambda X$ at 4.2 GeV/c. *Nuovo Cim.* **A44**, 345 (1978). (Cited on page 187.)

[Gav04] O. P. Gavrishchuk et al. Calorimeter for hadron detection in the energy range 10-100 GeV. *COMPASS Note* **2004-20** (2004). (Cited on page 19.)

[Glü88] M. Glück and E. Reya. Spin dependent parton distributions in polarized deep inelastic lepton nucleon scattering. *Z. Phys.* **C39**, 569 (1988). (Cited on page 7.)

[Gon01] F. Gonella et al. 'The MAD', a full custom ASIC for the CMS barrel muon chambers front end electronics. In *7th Workshop on Electronics for LHC Experiments (LEB '01)*, Stockholm, Sweden, September 2001. (Cited on page 27.)

[Gou86] S. A. Gourlay et al. Polarization of Λ's and $\overline{\Lambda}$'s in pp, $\bar{p}p$, and $K^- p$ interactions at 176 GeV/c. *Phys. Rev. Lett.* **56**, 2244–2247 (1986). (Cited on pages 75, 76, and 186.)

[Gre02] O. Grebenyuk. Transverse polarization of Λ and $\overline{\Lambda}$ produced inclusively in eN scattering at hermes. In *10th International Workshop on Deep Inelastic Scattering and QCD (DIS 2002)*, Cracow, Poland, May 2002. (Cited on pages 76 and 184.)

[Gru01a] B. Grube. *The Trigger Control System and the common GEM and Silicon Readout for the COMPASS Experiment*. Diploma thesis, Technische Universität München, December 2001. (Cited on pages 28, 30, 49, 52, 61, 69, and 229.)

[Gru01b] B. Grube et al. Architecture of a common GEM and silicon readout for the COMPASS experiment. In *7th International Conference on Advanced Technology and Particle Physics (ICATPP-7)*, Como, Italy, October 2001. World Scientific. (Cited on page 30.)

[Grü02] A. Grünemaier. *Eine universelle Ausleseschnittstelle für das COMPASS-Experiment*. Ph.D. thesis, Albert-Ludwigs-Universität Freiburg, September 2002. (Cited on page 30.)

[Hel78] K. J. Heller et al. Polarization of Λs and $\overline{\Lambda}$s produced by 400 GeV protons. *Phys. Rev. Lett.* **41**, 607 (1978). (Cited on pages 75 and 77.)

[Hel83] K. J. Heller et al. Polarization of Ξ^0 and Λ hyperons produced by 400 GeV protons. *Phys. Rev. Lett.* **51**, 2025–2028 (1983). (Cited on page 75.)

[Hel96] K. J. Heller. Spin and high energy hyperon production, results and prospects. In *12th International Symposium on High-energy Spin Physics (SPIN 96)*, Amsterdam, Netherlands, September 1996. (Cited on page 75.)

[Hen92] T. Henkes et al. Further evidence for pomeron-quark interactions: Observation of large Λ polarization in $pp \to (\Lambda K^+)p$. *Phys. Lett.* **B283**, 155–160 (1992). (Cited on page 75.)

[HMC95] E. Nappi et al. The HMC letter of intent. **CERN-SPSLC-95-27** (1995). (Cited on page 3.)

[Ho91] P. M. Ho et al. Measurement of the polarization and magnetic moment of $\overline{\Xi}^+$ anti-hyperons produced by 800 GeV/c protons. *Phys. Rev.* **D44**, 3402–3418 (1991). (Cited on page 75.)

[Hod02] M. Frhr. v. Hodenberg. *A first Reconstruction of COMPASS Data*. Diploma thesis, Albert-Ludwigs-Universität Freiburg, 2002. (Cited on page 14.)

[Hor02] S. Horikawa et al. A scintillating fiber tracker with high time resolution for high-rate experiments. *IEEE Trans. Nucl. Sci.* **49**, 950–956 (2002). (Cited on page 18.)

[Iar83] E. Iarocci et al. Plastic streamer tubes and their application in high energy physics. *Nucl. Inst. Meth.* **A217**, 30 (1983). (Cited on page 20.)

[IEE] IEEE. Home page, `http://www.ieee.org`. (Cited on pages 29 and 30.)

[Ilg03] Ch. Ilgner. *Fertigung und Inbetriebnahme einer Strohdriftkammerstation für das COMPASS Experiment*. Ph.D. thesis, Ludwig-Maximilians-Universität München, 2003. (Cited on page 18.)

[Jac99] J. D. Jackson. *Classical Electrodynamics*. John Wiley & Sons Inc., 3rd edition, 1999. (Cited on page 82.)

[JED] JEDEC. Home page, `http://www.jedec.org`. (Cited on page 31.)

[Jon99] L. L. Jones et al. The APV25 deep submicron readout chip for CMS detectors. In *5th Workshop on Electronics for the LHC Experiments (LEB '99)*, Snowmass, Colorado, USA, September 1999. (Cited on page 28.)

[Kan] D. Kang. Status report lambda polarization study, `http://pccosrv1.cern.ch/compass/software/analysis/transparencies/2004/am_040729/Kang_29-07-2004.pdf`. COMPASS Analysis Meeting July 2004. (Cited on page 111.)

[Kan78] G. L. Kane, J. Pumplin, and W. Repko. Transverse quark polarization in large-p_T reactions, e^+e^- jets, and leptoproduction: a test of QCD. *Phys. Rev. Lett.* **41**, 1689 (1978). (Cited on page 74.)

[Ket02] B. Ketzer et al. Triple GEM tracking detectors for COMPASS. *IEEE Trans. Nucl. Sci.* **49**, 2403 – 2410 (2002). (Cited on page 18.)

[Kob] S. Koblitz and A. Korzenev. Data stability and grouping for asymmetry studies, `http://wwwcompass.cern.ch/compass/software/offline/input/stab/index.html`. (Cited on page 97.)

[Kon05] I. Konorov, `igor.konorov@cern.ch`. Private communication, 2005. (Cited on pages 29, 30, and 55.)

[Kuh05] R. Kuhn, `rkuhn@ph.tum.de`. Private communication, 2005. (Cited on page 35.)

[Kuh06] R. Kuhn. Ph.D. thesis in preparation, Technische Universität München, 2006. (Cited on pages 29 and 34.)

[Lac92] J. Lach. Hyperon polarization: An experimental overview. In *International Workshop on Flavor and Spin in Hadronic and Electromagnetic Interactions*, Turin, Italy, September 1992. FERMILAB-Conf-92/378. (Cited on page 75.)

[Leb02] M. Leberig. *Das COMPASS-Triggersystem zur Messung des Gluonbeitrags ΔG zum Protonspin*. Ph.D. thesis, Universität Mainz, November 2002. (Cited on pages 37, 39, 40, 41, and 44.)

[Leb03] M. Leberig et al. The trigger system of the COMPASS experiment. *Nuclear Science Symposium Conference Record, 2003 IEEE* **1**, 297–301 (2003). (Cited on page 37.)

[Leo94] W. R. Leo. *Techniques for Nuclear and Particle Physics Experiments*. Springer, 2nd edition, 1994. (Cited on page 45.)

[Luk93] K. B. Luk et al. Polarization of Ω^- hyperons produced in 800 GeV proton-beryllium collisions. *Phys. Rev. Lett.* **70**, 900–903 (1993). (Cited on page 75.)

[Lun89] B. Lundberg et al. Polarization in inclusive Λ and $\bar{\Lambda}$ production at large p_T. *Phys. Rev.* **D40**, 3557–3567 (1989). (Cited on page 75.)

[Mal96] G. K. Mallot. *The spin structure of the nucleon from the SMC Experiments*. Habilitationsschrift, Johannes Gutenberg Universität Mainz, 1996. (Cited on page 21.)

[Mor93] A. Morelos et al. Polarization of Σ^+ and $\bar{\Sigma}^-$ hyperons produced by 800 GeV/c protons. *Phys. Rev. Lett.* **71**, 2172–2175 (1993). (Cited on page 75.)

[Mul96] P. J. Mulders and R. D. Tangerman. The complete tree-level result up to order $1/Q$ for polarized deep-inelastic leptoproduction. *Nucl. Phys.* **B461**, 197–237 (1996). Erratum ibid. B484:538-540, 1997. (Cited on page 84.)

[Nag05] T. Nagel. *Cinderella: an Online Filter for the COMPASS Experiment*. Diploma thesis, Technische Universität München, January 2005. (Cited on page 34.)

[New93] F. M. Newcomer et al. A fast, low power, amplifier-shaper-discriminator for high rate straw tracking systems. *IEEE Trans. Nucl. Sci.* **40**, 630–636 (1993). (Cited on page 27.)

[Ohl73] G. Ohlsen and P. W. Keaton. Techniques for measurement of spin-1/2 and spin-1 polarization analyzing tensors. *Nucl. Inst. Meth.* **109**, 41 (1973). (Cited on pages 126 and 128.)

[Pan90] A.D. Panagiotou. Λ polarization in hadron-nucleon, hadron-nucleus and nucleus-nucleus interactions. *Int. J. Mod. Phys.* **A5**, 1197 (1990). (Cited on page 75.)

[PCI] PCI SIG. Home page, `http://www.pcisig.com/home`. (Cited on page 30.)

[PDG04] S. Eidelman et al. Review of particle physics. *Phys. Lett.* **B592**, 1–1109 (2004). (Cited on pages 73 and 105.)

[Per87] D. H. Perkins. *Introduction to High Energy Physics*. Addison Wesley, 3rd edition, 1987. (Cited on page 71.)

[Per01] H. Pereira da Costa. *Développement de chambres à derive pour les hauts flux dans l'expérience COMPASS*. Ph.D. thesis, University Paris-Sud, November 2001. (Cited on page 18.)

[PHA] S. Gerassimov. PHAST: PHysics Analysis Software Tool, `http://ges.home.cern.ch/ges/phast`. (Cited on page 95.)

[Pla05] K. Platzer et al. Mapping the large area Straw detectors of the COMPASS experiment with X-rays. *IEEE Trans. Nucl. Sci.* **52**, 793–798 (2005). (Cited on page 18.)

[Ram86] R. Rameika et al. Measurements of production polarizations and decay asymmetry for Ξ^- hyperons. *Phys. Rev.* **D33**, 3172–3179 (1986). (Cited on page 75.)

[Ram94] E. J. Ramberg et al. Polarization of Λ and $\bar{\Lambda}$ produced by 800 GeV protons. *Phys. Lett.* **B338**, 403–408 (1994). (Cited on page 75.)

[ROO] R. Brun, F. Rademakers, et al. ROOT home page, `http://root.cern.ch`. (Cited on page 92.)

[San94] J. C. Santiard et al. Gasplex: A low noise analog signal processor for readout of gaseous detectors. In *6th Pisa Meeting on Advanced Detectors*, La Biodola, Isola d'Elba, Italy, May 1994. (Cited on page 27.)

[Sch02] T. Schmidt. *A common readout driver for the COMPASS Experiment*. Ph.D. thesis, Albert-Ludwigs-Universität Freiburg, May 2002. (Cited on page 30.)

[Sch04] L. Schmitt et al. The DAQ of the COMPASS experiment. *IEEE Trans. Nucl. Sci.* **51**, 439–444 (2004). (Cited on pages 25, 31, 33, and 35.)

[Sch05] L. Schmitt, `lschmitt@ph.tum.de`. Private communication, 2005. (Cited on page 67.)

[SEL02] M. Mattson et al. First observation of the doubly charmed baryon ξ_{cc}^+. *Phys. Rev. Lett.* **89**, 112001 (2002). (Cited on page 13.)

[Siv90] D. W. Sivers. Single spin production asymmetries from the hard scattering of point-like constituents. *Phys. Rev.* **D41**, 83 (1990). (Cited on page 10.)

[Smi87] A. M. Smith et al. Λ polarization in proton-proton interactions from $\sqrt{s} = 31$ to 62 GeV. *Phys. Lett.* **B185**, 209 (1987). (Cited on page 75.)

[Sof92] J. Soffer and N. A. Törnqvist. Origin of the polarization for inclusive Λ production in pp collisions. *Phys. Rev. Lett.* **68**, 907–910 (1992). (Cited on page 77.)

[Sof99] J. Soffer. Is the riddle of the hyperon polarizations solved? In *Hyperon '99: Hyperon Physics Symposium*, Batavia, Illinois, USA, September 1999. (Cited on pages 74 and 77.)

[Soz03] F. Sozzi. *Identificazione di particelle con il RICH di COMPASS al Superprotosincrotrone del CERN*. Diploma thesis, University of Trieste, 2003. (Cited on page 99.)

[Szw81] J. Szwed. Hyperon polarization at high energies. *Phys. Lett.* **B105**, 403 (1981). (Cited on page 77.)

[Tak02] N. Takabayashi. *Polarized target for the measurement of the gluon contribution to the nucleon spin in the COMPASS exeriment*. Ph.D. thesis, Nagoya University, 2002. (Cited on page 23.)

[Tay] B. G. Taylor. TTC laser transmitter (TTCex, TTCtx, TTCmx) user manual, v2.0, `http://ttc.web.cern.ch`. (Cited on page 50.)

[Tay98] B. G. Taylor. TTC distribution for LHC detectors. *IEEE Trans. Nucl. Sci.* **45**, 821–828 (1998). (Cited on page 51.)

[Tay02] B. G. Taylor. Timing distribution at the LHC. In *8th Workshop on Electronics for the LHC Experiments (LEB '02)*, Colmar, France, September 2002. (Cited on page 49.)

[TTC] RD12 Collaboration. TTC website, `http://ttc.web.cern.ch`. (Cited on page 51.)

[vdB97] H. C. van der Bij et al. S-LINK a data link interface specification for the LHC era. *IEEE Trans. Nucl. Sci.* **44**, 398–402 (1997). (Cited on page 29.)

[Wah85] Y. W. Wah et al. Measurement of Σ^- production polarization and magnetic moment. *Phys. Rev. Lett.* **55**, 2551 (1985). (Cited on page 75.)

[Web04] R. Webb. *First measurement of transverse spin asymmetries through single pion production at the COMPASS experiment*. Ph.D. thesis, Friedrich-Alexander-Universität Erlangen-Nürnberg, 2004. (Cited on page 18.)

[Wei03] Q. Weitzel. *Triple GEM detectors in COMPASS*. Diploma thesis, Technische Universität München, 2003. (Cited on page 18.)

[Wie04] M. Wiesmann. *A Silicon Microstrip Detector for COMPASS and a first Measurement of the transverse Polarization of Λ-Hyperons from quasi-real Photo-Production*. Ph.D. thesis, Technische Universität München, February 2004. (Cited on pages 107, 133, and 229.)

[Wik] Wikipedia, `http://www.wikipedia.org`.

[Wil87] C. Wilkinson et al. Polarization and magnetic moment of the Σ^+ hyperon. *Phys. Rev. Lett.* **58**, 855–858 (1987). (Cited on page 75.)

[Wol93] E. J. Wolin et al. Covariance matrices for track fitting with the Kalman filter. *Nucl. Inst. Meth.* **A329**, 493–500 (1993). (Cited on page 94.)

[Woo96] D. M. Woods et al. Polarization of Ξ^- and Ω^- hyperons produced from neutral beams. *Phys. Rev.* **D54**, 6610–6619 (1996). (Cited on page 76.)

[Xil] Xilinx Inc. Data sheets, `http://www.xilinx.com/xlnx/xweb/xil_publications_index.jsp`. (Cited on page 25.)

[Yam97] Y. Yamamoto, K. Kubo, and H. Toki. Quark recombination model for spin polarization in high energy inclusive hadron reactions. *Prog. Theor. Phys.* **98**, 95–128 (1997). (Cited on page 83.)

[Ye01] Y. Ye, H. Lv, T. Ruan, J. Shen, W. Dong, and Z. Ye. The spin precession and polarization correction for Λ hyperon. *Nucl. Inst. Meth.* **A463**, 350–353 (2001). (Cited on page 160.)

Own contributions

I started to work on the TCS six years ago, when I still was a student trainee. Based on prototypes of the TCS controller and receiver, made by Igor Konorov and Wolfgang Liebl, I implemented the digital logic in the FPGAs in the context of my diploma and Ph.D. thesis. In close teamwork with Igor Konorov and Lars Schmitt I tested and debugged the components and commissioned and maintained the system. Lars Schmitt integrated the TCS into the DAQ software and also wrote the TCS Server software.

In parallel I was involved in the development, commissioning, and operation of the high speed readout system for the COMPASS silicon and GEM detectors [Gru01a] and also contributed to the development of a fast sampling ADC card for the ECAL2 readout.

During the beam times in 2002, 2003, and 2004 I took part in the regular shifts and I was in addition "expert on call" for the DAQ, the GEM and the Silicon detectors.

Based on the the work of Michael Wiesmann [Wie04] and under the supervision of Prof. Stephan Paul and Jan Friedrich I continued the analysis of the transverse hyperon polarization. I completely restructured the analysis code and extended it to the case of Ξ hyperons. In addition the analysis procedure was adapted to utilize the OpenPBS batch system.

Acknowledgments

Foremost I would like to thank Prof. Stephan Paul for giving me the opportunity to work in the COMPASS collaboration and letting me study this interesting topic as well as for his guidance and support.

I am also very indebted to Jan Friedrich for his continuous support not only during the data analysis. He was always open to all kinds of questions and many ideas arose in discussions with him. I learned a lot from him and it was fun too. Thanks!

On the hardware side my mentor was Igor Konorov. I want to thank him for introducing me into the FPGA business, for being a good and patient teacher and for his support during the development and the debugging of the system.

Further thanks go to Lars Schmitt for his support in the development of the TCS and the readout system as well as for the helpful discussions and comments.

Of course also Roland Kuhn, aka "the man page", deserves many thanks for his kind help with all my TEX, C++, and Linux questions, for his good company over all the years, for the discussions and, not to forget, for the barbecues.

In addition I am grateful to Michael Wiesmann, who started this analysis and laid the foundations for me. Thanks also for chocolate and tea!

For his help and advice in practical things, in particular in soldering, Heinz Angerer deserves many thanks.

Additional thanks go to my room mates, Anne-Marie Dinkelbach, Steffi Grabmüller, and Alexander Mann as well as to all the E18 members for the cooperative, friendly and motivating atmosphere.

Also the colleagues from the COMPASS group at CERN deserve thanks for their support and discussions.

Ganz besonders möchte ich mich bei meinen Eltern bedanken. Sie haben mir das Studium ermöglicht, mich immer unterstützt und gefördert und mir in den entscheidenden Momenten den Rücken frei gehalten.

Last but not least I would like to thank Suh-Urk Chung, who gave me a good reason to finish this thesis in time.